UNIVERSIDADE FEDERAL DO MARANHÃO

Centro de Ciências Exatas e Tecnología

Departamento de Física

Programa de Pós-Graduação em Física

Gopal Niraula

Engenharia de Arquitetura de Nanopartículas de Vórtice à Base de Óxido de Ferro para Aplicações Terapêuticas Direcionadas

São Luís-MA, Brasil

Fevereiro-2022

FEDERAL UNIVERSITY OF MARANHÃO

Center for Exact Sciences and Technologies

Department of Physics

Post-Graduate Research Program in Physics

Gopal Niraula

Architecture Engineering of Iron Oxide-Based Vortex Nanoparticles for Targeted Therapeutic Applications

São Luís-MA, Brazil

February-2022

Gopal Niraula

Architecture Engineering of Iron Oxide-Based Vortex Nanoparticles for Targeted Therapeutic Applications

This Doctoral Thesis is Presented to the Post-Graduate Research Program in Physics (PPGF), Federal University of Maranhão (UFMA) as a Fulfillment of Partial Requirement for Obtaining the Doctorate Degree in Physics.

(Esta Tese de Doutorado é Apresentada ao Programa de Pesquisa de Pós-Graduação em Física (PPGF) da Universidade Federal do Maranhão (UFMA) como Cumprimento de Requisito Parcial para Obtenção do Título de Doutor em Física).

Supervisor:
Prof. Dr. Surender Kumar Sharma
Functional Nanomaterial Laboratory
Post-Graduate Program in Physics (PPGF)
Federal University of Maranhão, São Luís, Brazil

Co-supervisor:
Prof. Dr. Alan Silva de Menezes
Department of Physics-CCET
Federal University of Maranhão
São Luís, Brazil

Ficha gerada por meio do SIGAA/Biblioteca com dados fornecidos pelo(a) autor(a).
Diretoria Integrada de Bibliotecas/UFMA

Niraula, Gopal.
Architecture Engineering of Iron Oxide-Based Vortex Nanoparticles for Targeted Therapeutic Applications / Gopal Niraula. - 2022.
254 f.

Coorientador(a): Alan Silva de Menezes.
Orientador(a): Surender Kumar Sharma.
Tese (Doutorado) - Programa de Pós-graduação em Física/ccet, Universidade Federal do Maranhão, Sao Luis-MA, 2022.

1. Anisotropy/Stoichiometry/Switching Fields. 2. Magnetic Fluid Hyperthermia. 3. Magnetic Nanorings/Nanodisks/Nanotubes/Nanorods. 4. Magnetic Vortex Nanoparticles. 5. Mechanical Force Therapy. I. Menezes, Alan Silva de. II. Sharma, Surender Kumar. III. Título.

Gopal Niraula

Architecture Engineering of Iron Oxide-Based Vortex Nanoparticles for Targeted Therapeutic Applications

(Engenharia de Arquitetura de Nanopartículas de Vórtice à Base de Óxido de Ferro para Aplicações Terapêuticas Direcionadas)

This Doctoral Thesis is Presented to the Post-Graduate Research Program in Physics (PPGF), Federal University of Maranhão (UFMA) as a Fulfillment of Partial Requirement for Obtaining the Doctorate Degree in Physics.

(Esta Tese de Doutorado é Apresentada ao Programa de Pesquisa de Pós-Graduação em Física (PPGF) da Universidade Federal do Maranhão (UFMA) como Cumprimento de Requisito Parcial para Obtenção do Título de Doutor em Física).

Approved on
18/02/2022

Board of Examiners

Prof. Dr. Surender Kumar Sharma
Functional Nanomaterial Laboratory
Post-Graduate Program in Physics (PPGF)
Federal University of Maranhão, São Luís, Brazil

Prof. Dr. Alan Silva de Menezes
Department of Physics-CCET
Federal University of Maranhão
São Luís, Brazil

Prof. Dr. Giorgio Zoppellaro
Regional Center for Advanced Technology and Materials
Palacký University, Olomouc, Czech Republic

Prof. Dr. Gerardo Fabián Goya Rossetti
Institute of Nanoscience and Materials of Argon (INMA)
University of Zaragoza, Zaragoza, Spain

Prof. Dr. Diego Muraca
"Gleb Wataghin" Institute of Physics
University of Campinas, São Paulo, Brazil

Prof. Dr. José Antonio Huamaní Coaquira
Laboratory of Magnetic Materials, NFA
Institute of Physics,
University of Brasília, Brasília, Brazil

This thesis is fully dedicated to…….

"My Parents and All Family Members
for All The
Blessing, Continuous Care, Unconditional Love,
Endless Motivation
And Always Being There for Me to
Support and Encouragement
in Every Adventurous Journey I Choose in My Life"

The word 'EVERYTHING' is more-enough to describe the word 'FAMILY'.

Gopal Niraula

ACKNOWLEDGEMENT

It is my great pleasure to express profound gratitude and indebtedness to my advisor Prof. (Dr.) Surender Kumar Sharma, Post-Graduate Department of Physics (PPGF), Federal University of Maranhão (UFMA), São Luís, Brazil for continuous and relentless guidance, fruitful discussions, motivation, and providing all the research facilities throughout the project and invaluable time for all the direction in my Ph.D. research journey without which the present work would not have been accomplished. My heartfelt thanks goes to Prof. (Dr.) José Antonio Huamaní Coaquira, Laboratory of Magnetic Materials, Institute of Physics, University of Brasília (UnB), Brasília, Brazil for great encouragement, research facilities and allowing me to work at his laboratory independently. I highly acknowledge Prof. (Dr.) Manoel Messias Ferreira, PPGF, Coordinator; Former Head, Department of Physics, Prof. (Dr.) Alan Silva de Menezes; Prof. (Dr.) Adalto Rodrigues G. Dos Santos; and Prof. (Dr.) Rodolfo Alvan C. Sifuentes for a huge support to conduct my research in the institute, and the routine administrative work throughout my journey at PPGF-UFMA.

I would like to express my immense sincerity to Prof. (Dr.) Gerardo Fabián Goya Rossetti and Prof. (Dr.) Ricardo Ibarra from Institute of Nanoscience and Materials of Argon (INMA), University of Zaragoza, Zaragoza, Spain; Prof. (Dr.) Giorgio Zoppellaro from Regional Centre of Advanced Technologies and Materials, Palacký University, Olomouc, Czech Republic; Prof. (Dr.) Flavio Garcia from Brazilian Centre for Research in Physics (CBPF), Rio de Janeiro, Brazil; Prof. (Dr.) Diego Muraca and Prof. (Dr.) Marcelo Knobel from "Gleb Wataghin" Institute of Physics, University of Campinas, São Paulo, Brazil; Prof. (Dr.) João Paulo Figueiró Longo from Department of Biological Sciences, University of Brasília (UnB); Prof. (Dr.) Andris F. Bakuzis from Institute of Physics, Federal University of Goias (UFG), Goiania, Brazil; Prof. (Dr.) Francisco Sávio M. Sinfrônio from Department of Electrical Engineering, Federal University of Maranhão (UFMA); Dr. Trevor P. Almeida from School of Physics & Astronomy, University of Glasgow, United Kingdom; Prof. Nguyen T. K. Thanh from Department of Physics & Astronomy, University College London (UCL), London; Prof. Juliano C. Denardin from Department of Physics, University of Santiago in Chile, Santiago; Prof. Cristina Gomez Polo and Prof. Eneko Garayo Urabayen from Institute of Advanced Materials and Mathematics, Public University of Navarre (UPNA), Pamplona, Spain

for their indispensable assistance to carry-out my experimental work and discussions in an ambient research atmosphere.

I am thankful to Dr. Mohan Chandra Mathpal, Mahes Chand, Dr. Fermin H. Aragon, Dr. Jason Jerry A. Medrano, Dr. Beatriz Sanz Sagué, Dr. Jesus A. Fuentes, Dr. Richard J. Caraballo-Vivas, Dr. Evelyn C. S. Santos, and Bianca M. G. Villar Dr. Kunal Ranjan, Mr. Suresh Bhattarai, Ashok Timsina, Ms. Manisha Dwa, Ms. Heena Joshi, Mr. Dileep Kumar, Shashi Jaiswal, Mr. Harish Raza, Mr. Marcus Vinícius-Araújo, Carlos A. Vilca-Huayhua, Karla J. Paz-Corrales, Ana C. Moreno Maldonado, Melik Maksem, Yessica A. Urian for a constant encouragement, motivation and fruitful discussions throughout my research journey so far.

Finally, I wish to extend my utmost sense of respect to my grandmother Late Manamaya Niraula. I am always grateful and indebted to my loving mother Ms. Hem Kumari Niraula and caring father Mr. Lal Bahadur Niraula whose unconditional and endless love and blessings are always on the top of my head that energize me to continue my work anywhere in the world in any situations. I express my intense thank to my younger brother Mr. Bhupal Niraula, elder sister Ms. Indira Poudel, brother-in-law Mr. Durga Mani Poudel and my sincere nephew Mr. Satyam Shree Poudel; these people are my real motivator, source of inspiration, and great elevator in my journey wherever I go and whatever I do, they are always there in back-support either hand-by-hand or side-by-side due to which I stand here today.

ABSTRACT

The targeted therapy-based approach such as magnetic fluid hyperthermia (MFH) as thermal therapy and magneto-mechanical as a mechanical force therapy (MFT) have been clinically launched as an alternative treatment of cancer tumors. In both approaches magnetic nanoparticles (MNPs) are at the center; are used as 'heat generators' in MFH whereas the same is used as 'mechanotransducers' in MFT when they are subjected to an alternating magnetic field. Utilizing the MNPs, mainly superparamagnetic iron oxide nanoparticles (SPIONs), both therapeutic techniques are emerging as a cornerstone approach in view of impractical scenarios and are becoming a topic of great interest in the cancer therapies because of their several advantages to the effectual antitumor therapy for instance high biosafety, deep tissue penetration, and targeted selective tumor killing. However, the SPIONs display weak magnetic responses, i.e., low magnetization, due to which a large dosage of SPIONs need to be injected inside the body for complete destruction of the tumors; this is a kind of challenge for surrounding healthy cells that need to be overcome. Thus, a new generation of magnetic nanoparticles with excellent properties is immediately needed to face the therapeutic challenges in advancing cancer therapies and subsequent treatment. The engineering of topological iron oxide nanoparticles (NPs) with novel vortex-domain structures offers an exciting avenue for probing their efficacy in targeted therapy in cancer treatment overcoming the limitation of conventional superparamagnetic iron oxide NPs. The main reasons for the appropriateness of these NPs in cancer therapy are high dispersion ability, colloidal stability biocompatibility, and easy manipulation in the application of magnetic fields. Thus, the design of such magnetic nanomaterials with vortex-domain structure may serve as versatile candidates in therapeutic-based cancer treatments.

The present work aims to design the iron oxide-based vortex NPs for targeted therapeutic applications. This thesis is divided into two main parts: (a) control synthesis and characterization of iron oxide magnetic vortex nanoparticles and (b) their utilization in magnetic hyperthermia and mechanotransduction for cancer cell destruction, under biologically safe conditions using experimental, theoretically and micromagnetic simulations. The interest in the magnetic vortex nanoparticles over simple single-domain in the biological applications is due to negligible dipole-dipole interactions and thus low/zero magnetic remanence, allowing the magnetic nanosystems to remain well dispersed in colloidal formulations in the absence of an external magnetic field. The spin structures are produced in NPs due to the confinement of spins imposed by geometrical restrictions; thus it is challenging to control the geometry of nanoparticles to preserve the vortex configuration. In the first part, we have successfully synthesized magnetic vortex nanorings (NRs), nanodisks (NDs), nanospheres (NSs), nanorods (NRDs), and nanotubes (NTs) via microwave-assisted hydrothermal (MAH) route and characterized as-obtained NPs thoroughly by X-ray diffraction (XRD), Fourier transforms infrared spectroscopy (FTIR), electron microscopy (EM), Mossbauer spectroscopy (MS), X-ray photoelectron spectroscopy (XPS), cryostat-based resistivity measurement, magnetometry, and calorimetry-based MFH to examine their structural, morphological, magnetic properties and MFH efficacy. In addition, theoretical analysis and micromagnetic simulation were performed as supportive tools to confirm the experimental outcomes specially to provide evidence of geometry-based vortex-domain structure in iron oxide NPs. In the second part, we have performed the MFH experiment to evaluate the thermal efficiency and in vitro cytotoxicity test in different cell lines: (i) 4T1 cells (murine mammary adenocarcinoma cell line), (ii) CT26 (murine colorectal carcinoma cell line), and (iii) J774A.1 (a murine

monocyte/macrophage). Through the complete characterization, we revealed that stoichiometry does not need to be preserved for the existence of magnetic vortex-domain structure in NPs. Further, the key findings on MFH of NDs is that the heating efficiency is better for stoichiometry magnetite (Fe_3O_4) NDs as compared with the nonstoichiometric one owing to charge ordering between Fe^{2+} and Fe^{3+}, which is further tuned by controlling the switching field-mediated shape, size, and orientation of nanodiscs in the direction of applied field in a controlled way revealing that the existence of magnetic vortex configuration is not only a factor to enhance heating capability but switching field mediated by shape, size, and orientation are also key factors to be considered. The specific absorption rate (SAR) and intrinsic loss power (ILP) in NRs and NTs at maximum clinical field 450 Oe and under the frequency of 107 kHz were evaluated. The NTs exhibited the highest SAR value among those reported so far in the hollow iron-oxide family accounting for the importance of magnetic shape anisotropy. The reported SAR values and their excellent cell viability tests strongly suggest NRs and NTs as potential candidates in targeted therapy-based cancer treatments. Further, we moved towards the magneto-mechanical approach for MFT-based cancer treatments. Taking in-depth analysis by means of theoretical and micromagnetic simulation, we proposed the iron oxide NRs as a mechanotransducer providing evidence on the magnetic stability of the curling ground states in NRs and opens the possibility of applying these systems to magneto-mechanical actuation on single cells for therapeutics in biomedicine, such as cancer cell destruction by low-frequency torque transduction.

Keywords: Magnetic Nanorings/Nanodisks/Nanotubes/Nanorods, Magnetic Vortex Nanoparticles, Anisotropy, Stoichiometry, Switching Fields, Magnetic Fluid Hyperthermia, Cytotoxicity, Mechanical Force Therapy

RESUMO

A abordagem baseada em terapia direcionada, como a hipertermia do fluido magnético (HFM) como terapia térmica e a abordagem magneto-mecânica como terapia de força mecânica (TFM) foram lançadas clinicamente como um tratamento alternativo de tumores cancerígenos. Em ambas as abordagens, as nanopartículas magnéticas estão no centro, essas nanopartículas magnéticas são usadas como 'geradores de calor' em HFM enquanto os mesmos são usados como 'mecanotransdutores' em TFM quando são submetidos à um campo magnético alternado. Utilizando as nanopartículas magnéticas, principalmente nanopartículas de óxido de ferro superparamagnéticas, ambas as técnicas terapêuticas estão surgindo como uma abordagem fundamental diante de cenários impraticáveis e estão se tornando um tópico de grande interesse nas terapias contra o câncer devido às suas várias vantagens para a terapia antitumoral eficaz, por exemplo, alta biossegurança, penetração tecidual profunda e morte seletiva direcionada de tumores. No entanto, os óxido de ferro superparamagnéticas apresentam respostas magnéticas fracas, ou seja, baixa magnetização devido a uma grande dose de óxido de ferro superparamagnéticas que precisa ser injetada dentro do corpo para destruição completa dos tumores, este é um tipo de desafio para as células saudáveis circundantes que precisam ser superados. Assim, uma nova geração de nanopartículas magnéticas com excelentes propriedades é imediatamente necessária para enfrentar os desafios terapêuticos no avanço das terapias contra o câncer e no tratamento subsequente. A engenharia de nanopartículas topológicas de óxido de ferro com novas estruturas de domínio de vórtice oferece um caminho interessante para testar sua eficácia na terapia direcionada no tratamento do câncer, superando a limitação das nanopartículas superparamagnéticas de óxido de ferro convencionais. As principais razões para a adequação desses nanopartículas na terapia do câncer são a alta capacidade de dispersão, biocompatibilidade de estabilidade coloidal e fácil manipulação na aplicação de campos magnéticos. Assim, o modelo de tais nanomateriais magnéticos com estrutura de domínio de vórtice pode servir como candidatos versáteis em tratamentos de câncer de base terapêutica.

O presente trabalho tem como objetivo projetar as nanopartículas de vórtice à base de óxido de ferro para aplicação terapêutica direcionada. Esta tese está dividida em duas partes principais: (a) controle da síntese e caracterização de nanopartículas de vórtice magnético de óxido de ferro e (b) sua utilização em hipertermia magnética e mecanotransdução para destruição de células cancerígenas, sob condições biologicamente seguras usando simulações experimentais, teóricas e micromagnéticas. O interesse nas nanopartículas de vórtice magnético sobre simples domínio único na aplicação biológica é devido às interações dipolo-dipolo desprezíveis e, portanto, à remanência magnética baixa/zero, permitindo que os nanosistemas magnéticos permaneçam bem dispersos em formulações coloidais na ausência de um campo magnético externo. As estruturas de spin são produzidas em NPS devido ao confinamento de spins imposto por restrições geométricas, assim, é um desafio controlar a geometria das nanopartículas para preservar a configuração do vórtice. Na primeira parte, sintetizamos com sucesso nanoanéis de vórtice magnético (NRs), nanodiscos (NDs), nanoesferas (NSs), nanobastões (NRDs) e nanotubos (NTs) via rota hidrotermal assistida por micro-ondas (HAM) e caracterizados como obtidos NPs completamente por difração de raios-X (DRX), espectroscopia infravermelha por transformadas de Fourier (FTIR), microscopia eletrônica de transmissão (MET), espectroscopia Mössbauer (EM), espectroscopia de fotoelétrons de raios-X (EFX), medição de resistividade baseada em criostato, magnetometria e calorimetria baseado em HFM para examinar suas propriedades estruturais, morfológicas,

magnéticas e eficácia de HFM. Além disso, análises teóricas e simulação micromagnética foram realizadas como ferramentas de suporte para confirmar os resultados experimentais, especialmente para fornecer evidências de estrutura de domínio de vórtice baseada em geometria de NPs de óxido de ferro. Na segunda parte, realizamos o experimento HFM para avaliar a eficiência térmica e o teste de citotoxicidade in vitro em diferentes linhagens celulares: (i) células 4T1 (linhagem celular de adenocarcinoma mamário murino), (ii) CT26 (linhagem celular de carcinoma colorretal murino) e (iii) J774A.1 (um monócito/macrófago murino). Através da caracterização completa, revelamos que a estequiometria não precisa ser preservada para a existência de estrutura de domínio de vórtice magnético em nanopartículas. Além disso, as principais descobertas sobre HFM de NDs é que a eficiência de aquecimento é melhor para NDs de magnetita estequiométrica (Fe_3O_4) em comparação com a não estequiométrica devido à ordenação de carga entre Fe^{2+} e Fe^{3+}, que é ajustada ainda mais controlando a forma mediada por campo de comutação , tamanho e orientação dos nanodiscos na direção do campo aplicado de forma controlada, revelando que a existência de configuração de vórtices magnéticos não é apenas um fator para aumentar a capacidade de aquecimento, mas o campo de comutação mediado por forma, tamanho e orientação também são fatores-chave para ser considerados. A taxa de absorção específica e a perda de potência intrínseca em NRs e NTs no campo clínico máximo de 450 Oe e na frequência de 107 kHz foram avaliadas. Os NTs exibiram o maior valor de taxa de absorção específica entre os relatados até agora na família de óxido de ferro oco, explicando a importância da anisotropia de forma magnética. Os valores de taxa de absorção específica relatados e seus excelentes testes de viabilidade celular sugerem fortemente NRs e NTs como potenciais candidatos em tratamentos de câncer baseados em terapia direcionada. Além disso, avançamos para a abordagem magneto-mecânica para tratamentos de câncer baseados em TFM. Aprofundando a análise por meio de simulação teórica e micromagnética, propusemos o óxido de ferro NRs como um mecanotransdutor fornecendo evidências sobre a estabilidade magnética dos estados fundamentais de curling em NRs e abrindo a possibilidade de aplicação desses sistemas para atuação magneto-mecânica em células únicas para terapia em biomedicina, como destruição de células cancerosas por transdução de torque de baixa frequência.

Palavras-chave: Nanorings Magnéticos/Nanodiscos/Nanotubos/Nanorods, Nanopartículas de Vórtice Magnético, Anisotropia, Estequiometria, Campos de Comutação, Hipertermia de Fluido Magnético, Citotoxicidade, Terapia de Força Mecânica

List of Figures

List of Tables

List of Publications

Articles:

1. **NIRAULA**, **GOPAL**; DENILSON TONETO; GERARDO F. GOYA; GIORGIO ZOPPELLARO; JOSE A. H. COAQUIRA; DIEGO MURACA; JULIANO C. DENARDIN; TREVOR P. ALMEIDA; MARCELO KNOBEL AND SURENDER K. SHARMA, "Evidence of Magnetic Vortex Configuration and Loss of Stoichiometry in Submicrometer Fe_3O_4 Nanospheres" **Submitted**.

2. **NIRAULA, GOPAL**; TONETO, DENILSON; JOSHY, ELMA; COAQUIRA, JOSE AH; FLAVIO; MURACA, DIEGO; AYESH, AHMAD I.; DENARDIN, JULIANO; GOYA, GERARDO F.; SHARMA, SURENDER K, "Energy Evolution, Stabilization, and Mechanotransducer Properties of Fe_3O_4 Vortex Nanorings and Nanodiscs" **Physical Review Applied**, **v. 16, p.024002, 2021** (10.1103/PhysRevApplied.16.024002) [IF= 4.985, Quartile = Q1]

3. **NIRAULA, GOPAL**; COAQUIRA, JOSE AH; ZOPPELLARO, GIORGIO; VILLAR, BIANCA MG; GARCIA, FLAVIO; BAKUZIS, ANDRIS F.; LONGO, JOÃO PF; RODRIGUES, MOSAR C.; MURACA, DIEGO; AYESH, AHMAD I.; SINFRÔNIO, FRANCISCO SÁVIOM.; DE MENEZES, ALAN S.; GOYA, GERARDO F.; SHARMA, SURENDER K. Engineering Shape Anisotropy of Fe_3O_4 -γ-Fe_2O_3 Hollow Nanoparticles for Magnetic Hyperthermia. **ACS Applied Nano Materials, v.4, 3, 3148–3158, 2021.** [IF= 5.097, Quartile = Q1, Citation = 7]

4. **NIRAULA, GOPAL**; COAQUIRA, JOSE AH; ARAGON, FERMIN H.; BAKUZIS, ANDRIS F.; VILLAR, BIANCA MG; GARCIA, FLAVIO; MURACA, DIEGO; ZOPPELLARO, GIORGIO; AYESH, AHMAD I.; SHARMA, SURENDER K. Stoichiometry and Orientation and Shape-Mediated Switching Field Enhancement of the Heating Properties of Fe_3O_4. **Physical Review Applied, v. 15, p.014056, 2021.** [IF= 4.985, Quartile = Q1, Citation = 2]

5. **NIRAULA, GOPAL**; COAQUIRA, JOSE AH; ARAGON, FERMIN H.; GALEANO VILLAR, BIANCA M.; MELLO, ALEXANDRE; GARCIA, FLAVIO; MURACA, DIEGO; ZOPPELLARO, GIORGIO; VARGAS, JOSE M.; SHARMA, SURENDER K. Tuning the shape, size, phase composition and stoichiometry of iron oxide nanoparticles: The role of phosphate anions. **Journal of Alloys and Compounds, v. 856, p. 156940, 2021.** [IF= 5.316, Quartile = Q1, Citation = 2]

Book Chapters:

1. **NIRAULA, GOPAL**; JASON J. A. MEDRANO; MOHAN C. MATHPAL; JERO-R MAZE; JOSE A. H. COAQUIRA AND SURENDER K. SHARMA, "X-rays Based Bioimaging Techniques and Scintillating Materials", (**in production).**

2. FAEZEH, MOZAFARI; HAMID, RASHIDZADEH; MURAT, BARSBAY; MOHAMMADREZA, GHAFFARLOU; MARZIYEH, SALEHIABAR; ALI, RAMAZANI; MORTEZA, ABAZARI; MOHAMMAD-AMIN, RAHMATI; **NIRAULA, GOPAL**, SHARMA, SURENDER K. AND HOSSEIN DANAFAR, "Application of Nanoradioprotective Agents in Cancer Therapy", (**in production)**

3. **NIRAULA, GOPAL**; MATHPAL, MOHAN C.; HERRERA, EDHER Z.; SOLER, MARIA A.G.; COAQUIRA, JOSE A.H.; SHARMA, SURENDER K. Magnetic Nanoflowers: Synthesis, Formation Mechanism and Hyperthermia Application. Accepted in Springer Nature, Switzerland: Springer International Publishing, S.K. Sharma Eds., 2021. [ISBN: 978-3-030-79959-5; https://doi.org/10.1007/978-3-030-79960-1_6]

4. **NIRAULA, GOPAL**; MATHPAL, MOHAN C.; HERRERA, EDHER Z.; SOLER, MARIA A.G.; COAQUIRA, JOSE A.H.; VERMA, RAMESH; SHARMA, SURENDER K. Superparamagnetic Iron Oxide Based Nanomaterials for Magnetic Resonance Imaging. Accepted in Springer Nature, Switzerland: Springer International Publishing, S.K. Sharma Eds., 2021. [ISBN: 978-3-030-79959-5; https://doi.org/10.1007/978-3-030-79960-1_7]

5. MATHPAL, MOHAN C.; **NIRAULA, GOPAL**; CHAND MAHESH; KUMAR, PRAMOD; SINGH, MANISH K.; SHARMA, SURENDER K.; SOLER, MARIA A.G.; SWART, H. C. Ferrite as an Alternative Source of Renewable Energy for hydroelectric cell. Springer International Publishing, S.K. Sharma Eds., 2021. [ISBN: 978-3-030-79959-5; https://doi.org/10.1007/978-3-030-79960-1_13]

6. MATHPAL, MOHAN C.; **NIRAULA, GOPAL**; CHAND MAHESH; KUMAR, PRAMOD; SINGH, MANISH K.; SHARMA, SURENDER K.; SOLER, MARIA A.G.; SWART, H. C. State of Art of Spinel Ferrites Enabled Humidity Sensor. Accepted in Springer Nature, Switzerland: Springer International Publishing, S.K. Sharma Eds., 2021. [ISBN: 978-3-030-79959-5; https://doi.org/10.1007/978-3-030-79960-1_14]

7. **NIRAULA, GOPAL**; SHRIVASTAVA, NAVADEEP; AKHTAR, KANWAL; JAVED, YASIR; COAQUIRA, JAH; SHARMA, SURENDER K. Liquid-Phase Synthesis of Multifunctional Nanomaterials: A Recent Update. Nanomedicine and Nanotoxicology. First ed. Switzerland: Springer International Publishing, 2020, v., P. 1-56 [Citation = 2]

Table of Content

Chapter 1

Introduction and General Background

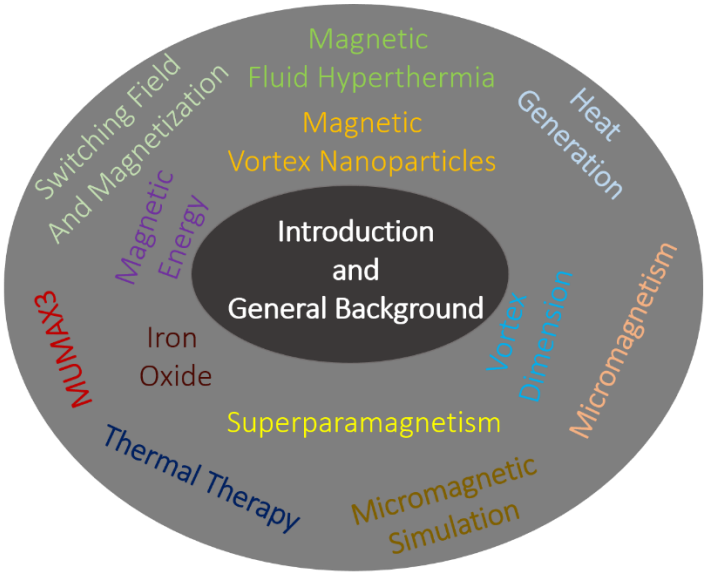

The literature review and general background of a particular research problem is significant ingredient for its proper understanding, finding gaps, plan/execute experiment and making hypotheses. This thesis is devoted to engineered iron oxide vortex NPs for thermal therapeutic applications and therefore, this chapter provides a general overview, background, loophole, and the way to overcome those loophole prior to conduct this research. This chapter gives a necessary background of iron oxide NPs, superparamagnetism, magnetic vortex NPs and their magnetic energy, heat generation, hysteresis loss, and their importance in magnetic fluid hyperthermia and magneto-transducers therapeutics.

1.1 Iron Oxide Nanoparticles

In magnetism, iron oxides are well-known particles, which are ubiquitously found in nature (soils and bacteria) as well as they can be artificially synthesized in a control way. Generally, three types of iron oxides are usually found/prepared (hematite-α-Fe_2O_3, magnetite-Fe_3O_4 and maghemite-γ-Fe_2O_3) considering their important applications from industrial technology to nanomedicine. The name hematite (α-Fe_2O_3) originated from Greek word 'haima' which means blood. The α-Fe_2O_3 consists iron 3+ cations whose crystal structure is a hexagonal (rhombohedral) with unit cell dimensions of a=5.034 Å and c=13.752 Å and belongs to the space group R3c [1]. In addition, they are weak ferromagnetic at room temperature, which can be turned onto antiferromagnetic below Morin temperature (T_M), usually T_M = 260 K and behaves as paramagnetic above Curie temperature (T_C), usually 950 K [2].

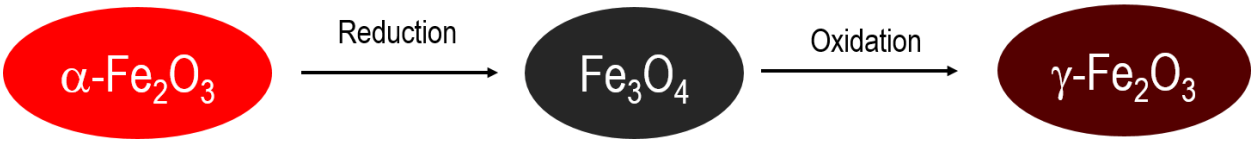

Figure 1.1: Schematic representation of different phases of iron oxide NPs. The box color itself represents the actual color of each phase (Source: self-made).

The name magnetite (Fe_3O_4) itself originated from the Turkish word 'Magnesia'. The Fe_3O_4 NPs consist of Fe^{3+} and Fe^{2+} in two different environment of the crystal structure, i.e., tetrahedral (A-site) and octahedral (B-site), where tetrahedral site contains only Fe^{3+} and octahedral site consist of both cations i.e., Fe^{3+} and Fe^{2+}. The unit cell lattice parameter of Fe_3O_4 is, a=b=c=8.396 Å, which belongs to Fd3m space group. The unit cell of magnetite comprises a 32 cubically face centered oxygen atom, and iron atoms occupy 16 octahedral sites (Fe^{3+}: Fe^{2+} = 1:1) and 8 tetrahedral sites (Fe^{3+}). In bulk Fe_3O_4, the distributions of Fe^{3+} and Fe^{2+} cation at the tetrahedral and octahedral sites is in ratio of 1:2. The crystal structure of Fe_3O_4 is largely dependent on temperature since its structure is inverse cubic spinel above Verwey temperature (T_V), usually T_V = 120 K, which can be changed onto monoclinic structure below T_V; this structural transition from inverse cubic spinel to monoclinic is also referred as metal-insulator transition [3]. The 'Verwey transition' is widely discussed in magnetite since its origin whose exact phenomena is still mysterious and under debate. In brief, T_V is associated with the stoichiometry of magnetite and the signal of bulk magnetite, which can be obtained only if the electron hopping is possible in between

Fe^{2+} and Fe^{3+} cations at the octahedral sites that gives rise to extremely conductive magnetite. The magnetization in magnetite origins due the opposing nature of the spins with different magnitudes. The magnetic behavior of magnetite turned onto paramagnetic above Curie temperature (T_C), usually at T_C = 850 K.

Further, maghemite (γ-Fe_2O_3) is the oxidized form of magnetite with a similar inverse cubic spinel structure suffering from defect arises owing to presence of cation vacancy at the octahedral site. Unlike the presence of Fe^{2+} in magnetite, octahedral contains two-third of Fe^{3+} with one-third of cation vacancy; the general chemical formula is $[Fe^{3+}]_A[Fe^{3+}_{5/3}\square_{1/3}]_B$, where $\square$ represents the defect at the octahedral site. The unit cell lattice parameter of γ-Fe_2O_3 is a=b=c= 8.346Å and belongs to $P4_332$ space group [1]. The nature of γ-Fe_2O_3 is considered as a ferrimagnetic because of the Fe^{3+} cation distribution to the different environment of tetrahedral and octahedral sites. The Curie temperature of γ-Fe_2O_3 lies within the range of 820-986 K, whereas it turns onto α-Fe_2O_3 at ~ 600 K [4].

1.2 Superparamagnetism

Superparamagnetism (SPM) is a special magnetic phase exist in tiny ferro/ferrimagnetic NPs around the size of few nanometer to a couple of a tenth nanometer [5,6]. Here, the total magnetic moment of the NPs is composed of all the individual magnetic moments of the atoms that constitute the NPs and can be considered as one giant magnetic moment. As per rule, an assembly of non-interacting single-domain (i.e., size above SPM, but below single-domain size of ferromagnetic) isotropic materials exhibit a classical paramagnetic with very larger ($\sim 10^3$ - 10^4 μ_B) magnetic moment μ per particle, but real particles can be complex (not uniform) in magnetic structure/behavior. Generally, albeit, the properties shown by a single-domain NPs are not considering an isotropic. The morphology and crystal composition (magnetocrystalline anisotropy) are important physical factors that contribute anisotropically to their energy. In the presence an external magnetic field, the magnetic NPs show quick response to change of magnetic field without remanence (M_R) and coercive field (H_C). Under the influence of temperature, the magnetization of sufficiently small NPs can randomly flip its direction with uniaxial anisotropy. This is due to the fact that below certain critical dimension, the anisotropy barrier energy (ΔE) of a magnetic nanoparticle is decreased to the edge point where this energy can be prevailed by

thermal energy k_BT (here k_B is the Boltzmann constant and T is the absolute temperature) [7]; this phenomenon collectively shown in Figure 1.2(a, b).

The single-domain particle has anisotropy energy, and depends upon the volume of the magnetic NPs. For the uniaxial anisotropy, the energy barrier E_{an} proportionally varies to KV; here K is anisotropy constant. This anisotropy energy depends on the size, and decreases with decrease in the particle size that leads the anisotropy energy very small, either comparable or lower, than the thermal energy k_BT if the nanoparticle size is lower than a characteristic value.

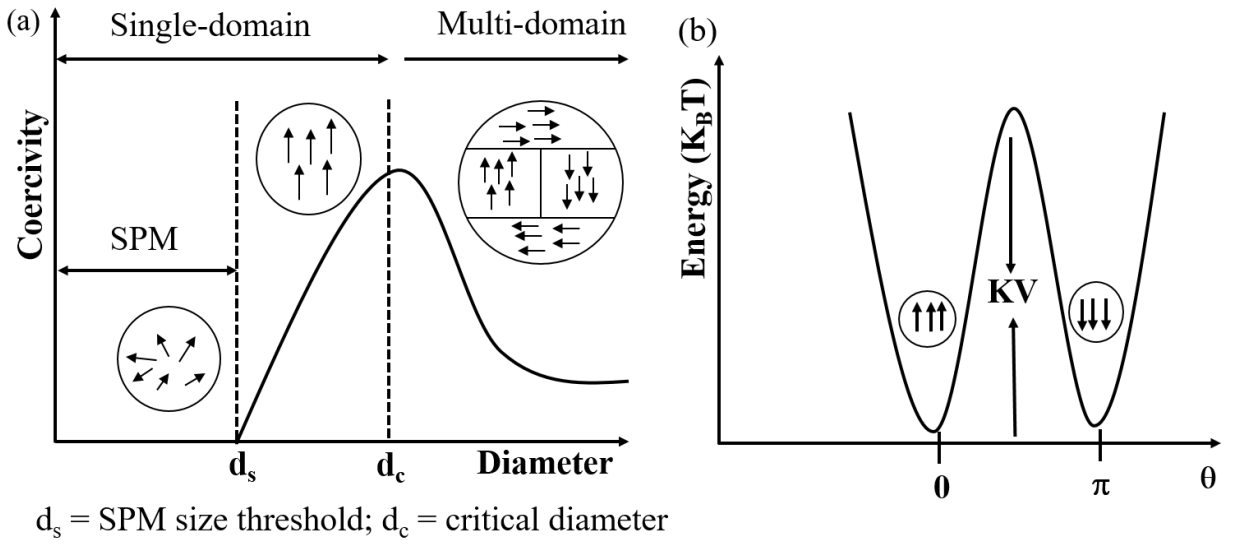

Figure 1.2: (a) Schematic picture showing the coercivity (H_c) behavior of magnetic NPs and its relation with diameter and (b) energy barrier for magnetization reversal (Source: self-made).

As a results, the magnetic reversal can be overcome by this energy reinforcing the thermal fluctuation of total magnetic moment and such magnetic moment is plainly rotated, but remain magnetically coupled (ferromagnetically or antiferromagnetically) within the particle. In such case, if external magnetic field or temperature changes it results in the rapid assembly of NPs approaching to thermal equilibrium. At H = 0, the two minima are detached by an energy barrier of height $\Delta E = KV$. The system exhibits like a 'permanent' ferromagnet; if $KV >> k_BT$, then the moment cannot switch spontaneously. However, if $KV \sim k_BT$ or less, then the natural switching of the 'superspins' can exist on the time-scale of the experiment and the NPs are in SPM state. The magnetic properties of NPs are affected by the measuring time (τ_m) of the specific experimental approach with respect to the relaxation time (τ) that is related with the overcoming of the energy

barriers. Magnetic NPs having uniaxial anisotropy can randomly overturn their magnetization direction induced by the thermal energy. The average time required to overturn can be given by the relaxation time [8,9],

$$\tau = \tau_o \, e^{-\Delta E/k_B T} \tag{1.1}$$

where $\Delta E = KV\sin^2\theta$ is the energy barrier, $\tau_o \sim 10^{-9}$ s to 10^{-12} s is the length of time characteristic of the material, θ is angle between the magnetization and easy axis, and T is absolute temperature[10]. When field is applied then above equation (1.1) becomes,

$$\tau = \tau_o \, e^{-\Delta E(H,\theta)/k_B T} \tag{1.2}$$

with $\Delta E(H, \theta)$ is the field dependent energy barrier, which can be derived as

$$\Delta E(H, \theta) = \Delta E_o \left(1 - \frac{H}{H_{SW}^0}\right)^{\kappa} \tag{1.3}$$

Where $\kappa = 0.86 + \frac{1.14\, H_{SW}^0}{H}$, $H_{SW}^0 = \frac{H_a}{(\sin^{2/3}\theta + \cos^{2/3}\theta)^{3/2}}$ and $H_a = \frac{2K}{M_S}$

The magnetization, in superparamagnetic phase, is zero in the absence of external magnetic field which is linearly varies with the application of the field. Every experimental technique has its own measurement time scale τ_m, which can vary from 10^{-8} s to 100 s. There are two conditional state that may explain with relating τ_m and τ, i.e., superparamagnetic and blocking state. The first is when $\tau_m >> \tau$, if the average time between the spin overturns (flips) smaller than the measurement time, the magnetization appears to fluctuate unless the external field applied. The magnetization appears to be zero and this magnetic arrangement is known as a superparamagnetic state, whereas $\tau_m << \tau$ when the average time between flips is much larger than the measurement time, the system appear to be stuck and given magnetic field have a fixed magnetization in the field direction. The NPs in this situation are in defined state, known as a blocking state due to the blockage of magnetization in one direction and stop flipping. Simply, the blocking temperature is the transition temperature between blocking state and superparamagnetic state. If $T > T_B$, then nanoparticle is in superparamagnetic state and if $T < T_B$, then is in blocking state [11] .

The energy required to form the domain walls is an important factor that determines the favorable state; if the energy required in the formation of the domain walls is less than the difference between the magnetostatic energies of the single-domain and multi-domain states, then the multi-domain state is energetically most favorable. When the dimensions of the particles are shrink, the resultant

energy of the ferromagnetic particles are changed due to the parallel contributions of the several energies that account the surface energy of domain walls is more important as compared to the magnetostatic volume energy. As already mentioned above that the particle size in between superparamagnetic and ferromagnetic is single-domain particles. The magnetic behavior of a single-domain particle strongly depends on the particle's shape and magnetic anisotropy; for instance, the total magnetic moment of the spherical particle is zero due to negligible anisotropic properties. It is expected that magnetic moment align towards the easy direction if the magnetocrystalline anisotropy is relatively high. The combined contribution from the energy parameters; exchange stiffness constant 'A', anisotropy constant 'K', and particle volume energy; introduces characteristic length scales, for example, the exchange length $l_{ex} = (A/M_S)^{1/2}$, the Bloch wall thickness $l_w = (A/|K_1|)^{1/2}$. The relative ordering of the quantities l_{ex}, l_w, and the particle size 'l' is of great importance for the critical properties (i.e., exchange coupling/interaction and magnetic properties, etc.) of the nanoparticle. For $l << l_w < l_{ex}$, the particle is dominated by the exchange interaction. Finite-size effect arises from the geometric restriction of the particle volume originating due to cutoff of the characteristic length i.e., exchange length, domain size, etc. As the specimen characteristic dimension "l" approach to nanosized value and the magnetic correlation length deviates at the critical temperature (T_C), the correlated fluctuating magnetic moments are controlled by the finite size of the specimen [12–14]. With the decrease in the particle size, the Curie temperature also decreases. However, the change in the crystallography could mask and even inverse this effect [15,16].

Surface effects have a sort of finite-size effects since the surface influence is highly significant in small NPs. Because of the small size of NPs, a large fraction of all the atoms in a nanoparticle are surface atoms, which prompt surface effect. The surface contribution to the magnetization becomes significant when there is an increase in the ratio of surface atom to the bulk atom. The surface atoms have different environment than core atoms because these have been affected by the existence of different types of defect, for instance changes in the atomic coordination, dangling bonds, atomic vacancies, and lattice disorder. In particular, the reduced atomic coordination at the surface leads to a reduction in the Curie temperature 'T_C' and significant deviation of the temperature dependence of the magnetization in the thermodynamic limit [17]. The cluster of NPs demonstrated a significant change in physical/magnetic properties of the surface atoms give rises a surface anisotropy that obviously enhances the overall magnetic anisotropy of the system[18,19].

For example, thermal measurements revealed that the strength of their surface anisotropy and the structure of NPs control their magnetic properties[20]. The magnetization of oxide NPs decreases for some oxide NPs due to the existence of a magnetically dead layer, canted spins, or the existence of a spin-glass-like behavior of the surface spins on the particle's surface [15]. On the other hand, the magnetization of some metallic NPs (cobalt) was reported to increase [21]. A number of experimental studies reported an increase in the effective magnetic anisotropy due to surface effects [18,21–23].

1.3 Magnetic Vortex Nanoparticles

The vortex structural configuration allows an efficient dissipation of energies. This typical phenomenon is widely found in nature involving in several physical process such as wind, water velocity in turbulent flows, electrical charges in eddy currents, matter density in black holes, sea, plume of smoke, tornado and magnetization in 2-D/3-D ferromagnets. The common physical parameter in all these phenomena is a curling-configuration throughout a central singularity point energy diverged. However, vortex core continuously maintains this divergence through its distinct structure. The conventional trend of research is on uniformly magnetized NPs and thin films, recently, however, large interest is attained towards the designation and manipulation of non-uniform spin-configurations at nanoscale in the form of vortices and skyrmions [24]. The stability of these non-uniform configuration, referred as '**topological defects**' can be traced to topological arguments. The basic arguments rely on the existence of topological defects is once the physical parameter are vanished either at the centre or at the edge [25]. As an example of topological magnetic defect [26], a vortex-structure is evolved in in-plane curling magnetization in XY-axis and an out-of-plane core magnetization towards Z-axis; it worth to note that the rises of out-of-plane magnetization is depends on geometry of particle structure and mainly appeared on NDs/dots and nanospheres (NSs).

The pioneered work on magnetic vortices was done by Feldtkeller E. and co-worker in 1965 A.D. calculating the micromagnetic structure of their samples[27]. Thereafter, magnetic vortices have been intensively studied as a particular topological solution of the phase transition in the 2-D XY model [28]. The several transition occurs on the system having vortex-configuration, thus the complete vortex-formation is linked with a topological phase transition between topologically trivial phenomena, for instance, non-superconducting, non-superfluid, disordered liquid crystals etc. and

topologically rich enough to support vortices, such as, superconducting, superfluid, nematic or smectic liquid crystals, and symmetry-broken vacuum etc. In some cases, vortex-configuration appears as a function of temperature once it crossed the phase transition temperature; conversely, existing vortex/antivortex pairs may disappears because of being dominant at lower temperature.

Figure 1.3: Examples of vortex formation in natural phenomena; (a) sea, (b) plume of smoke, (c) spiral galaxy, and (d) tornado (Source: www.google.com).

In thermal transition, the Kibble Zurek model predicts the existence of vortices/antivortices at low temperatures depending upon the quenching rate; following the relation, the existence of same vortex-configuration was observed in the hexagonal manganites [29–31]. The 2-D XY model is a system of spins constrained to rotate in the plane of the lattice. Since the ground state is unstable against low-energy spin-wave excitations, the Hamiltonian avoids any long-range order in such systems [32,33]. However, the system could have a phase transition at certain temperature which may emerges an unusual magnetization behavior below curie temperature (T_C) [34,35]. The metastable states corresponding to the vortices are bounded in a pair below some T_C whereas they become free above the T_C. The phase transition can be observed through change in magnetic response by applying the magnetic field. The spin-wave excitation is responsible for destroying long-range order, whereas the interaction energy of the vortices cause the phase transition in the system. The energy of an isolated vortex configuration in the XY model increases logarithmically with the size

of the system [28]. This general model provides in-depth interplay of classical magnetization confined in a plane of ferro/antiferromagnetism or any spin physics. Magnetic vortex-configuration allow to reduce the energy of the system by the interaction of vortex-antivortex pair. These geometry restricted vortex-configuration generally appears for a sizes larger than exchange length of the material and stable within a few tens of nanometer to few tens-micrometer [36–44]. The lowest total energy configuration, also known as ground state, of soft ferro/ferrimagnetic particles in remanence is a vortex state. The stability of magnetic vortices depends on the external magnetic field and particles geometry. Moreover, along with these factor, the magnetostatic interaction plays an important role in the vortex state stability and dynamic excitations in finite magnetic NPs, for instance disks/dots. Although it is predicted several decades ago, the magnetic vortex state has received special attention for practical implication only few years back since it is found to be the ground state of magnetic NPs.

In three dimension, the strongly inhomogeneous vortex state magnetization cannot be reduced to the uniform magnetization by any finite deformation. The vortex-state magnetization distribution modifies the nature of spin excitation significantly as compared to those in the uniform (saturated/single domain) state [45,46]. The magnetization reversal process for micron and sub-micron of different shaped/morphologies is determined by successive nucleation, displacement and annihilation of magnetic vortices. The hysteresis loops exhibit characteristic fields related to the nucleation and annihilation of magnetic vortices. The evolution of the magnetic vortex state is studied as functions of in-plane geometry, i.e., thickness, diameter, length, width as per the nature of NPs and the competition between the magnetostatic, anisotropic, and the exchange energies [38,39,41,42,47]. For example, circular magnetic disks at sufficiently larger radius give rise to vortex state having neither magnetic poles nor stray field at all at the expense of dominant exchange energy over magnetostatic one [37,48,49]. However, centered vortex core tries to destroy the overall vortex-configuration with decrease in radius (r) [36]. In vortex-disks, the magnetization often points out-of-the plane at the vortex core to satisfy unfavorable exchange and dipole interactions even with strong planar anisotropy [37].

Interesting geometry magnetic NRs favors the vortex-configuration avoiding the vortex core because of the presence of hole, which allows vortex-configuration in NRs can be preserved for very small 'r' [36,50–58]. The remnant state at H = 0 of magnetic NPs (NDs, NRs, and NTs etc.) consist

of two domains of different helicity parted by two domain walls (DWs) on the opposite sides of the NPs. If two DWs starts to move towards each other, they will continuously be driven by the external magnetic field until the annihilation that consequently forces to retained the vortex-configuration. On the other hand, if the two DWs starts to move in opposite directions, they will continue to do so until the onion state is fully reversed. These two typical processes are called vortex-formation process (V-process) and the onion rotation process (O-process), respectively. The probability of the V-process was found to be dependent on geometrical factor such as radius, thickness, width, length and the wall width of NPs. For example, nanoring with radius in the micrometer (μm) range, V-process is dominating. On the other hand, for radius 'r' within 50 nm, the both V-and O-reversal processes occurs; it was found that about 40 % undergo through V-process whereas 60 % through the O-process [59]. The bi-stable occurred between the V-process and the O-process in NRs whereas it is between the single domain state and the vortex state in NDs [60]. Thus, the understanding of the movement of DWs is crucial to the vortex-spin-configuration in magnetic NPs.

1.4 Magnetic Vortex Nanoparticles in Different Dimensions

Low dimensional vortex NPs, such as nanowires (NWs) are considered as 1-D when its radius is in the range of the DWs width or less and corresponding length is larger than DWs width, are getting attention significantly because of attainable physical properties and their manipulation varying the shape and size [61–67]. The dimensional parameters of NWs can be controlled precisely with a high precision. Consequently, for example one can tune the superconducting magnetic response of superconductors in regards of their respective applications. The condensate and its vortex-configuration of NWs are inevitably influenced by the confining potential of the boundaries. For example, if the boundary effect overcome the stray field one can expect the NWs made of a material remains same irrespective of its thickness. Being quasi1-D systems, they are comparable with the theoretical/analytical solutions of coherent reversal such as Stoner-Wohlfarth and curling models [68]. The magnetic properties of iron- and nickel-NWs are strongly influenced by the shape anisotropy [69,70] whereas, the magnetic properties cobalt-wires can be controlled by tuning the temperature and size dependent shape anisotropy and magnetocrystalline anisotropy. The competition between these anisotropies (shape and magnetocrystalline) can be tuned by the radius of the wires, i.e., smaller the radius, larger the effect of shape anisotropy even at a low

temperatures [70]. The angular dependence of the switching field, an effect of large anisotropic field, cannot be accounted for by uniform mode (i.e., Stoner-Wohlfarth model) and curling mode. This is consistent with the irreversible reversal nucleates in a volume much smaller than the NWs volume. In this case, the choosing low anisotropy field allows the curling mode to describes the direction-dependent switching field [71]. The several experimental evidences show that the reversal of the magnetization is governed by the nucleation of a reverse domain at the wire extremities and its subsequent propagation along the wire [71–73]. For wires with diameters equal and/or larger than twice the exchange length l_{ex}, the nucleation occurs at several nearly degenerate fields values close to the curling instability; whereas the wires of diameters close to the l_{ex}, the Stoner-Wohlfarth model becomes relevant. In such case, the switching time and switching field measurements reveal that only a single energy barrier is dominated and the reversal process could described by an Arrhenius law [73]. W.Y. Córdoba-Camacho et al. [61] have demonstrated the formation of quasi-1D vortex NPs in a single NWs and studied the magnetic response of the NWs with thickness. It is observed that when the NWs thickness decreases, vortices tend to arrange themselves in a regular chain (1D Abrikosov lattice). Adequately thin NWs diverge from type I material in favor of the intertype (IT) regime with multiquantum vortices and vortex clusters were found in mixed state. In such a regular chain, vortices were observed in the mixed state only when the field was close to its upper critical value. When decreasing the NWs thickness further, signatures of the IT regime was gradually disappeared. However, the regime of type II superconductivity was not reached; instead, ultrathin NWs re-enter to the type I regime. Although the analysis was done for a single NWs, the results were relevant for arrays of NWs when they were far away from one-another in an insulating template. This opens prospects of creating composite superconducting materials with widely tunable magnetic properties.

Similarly, when we pass through 1D NPs to 2D and 3D, with different morphologies, for instance nanodiscs (NDs)/microdiscs (MDs)/nanorings (NRs) as 2D, whereas, nanocubes (NCs)/nanospheres (NSs) as 3D, can be found in the literatures. In case of ferromagnetic NDs/MDs, a well-defined vortex-spin-configuration are occurred.

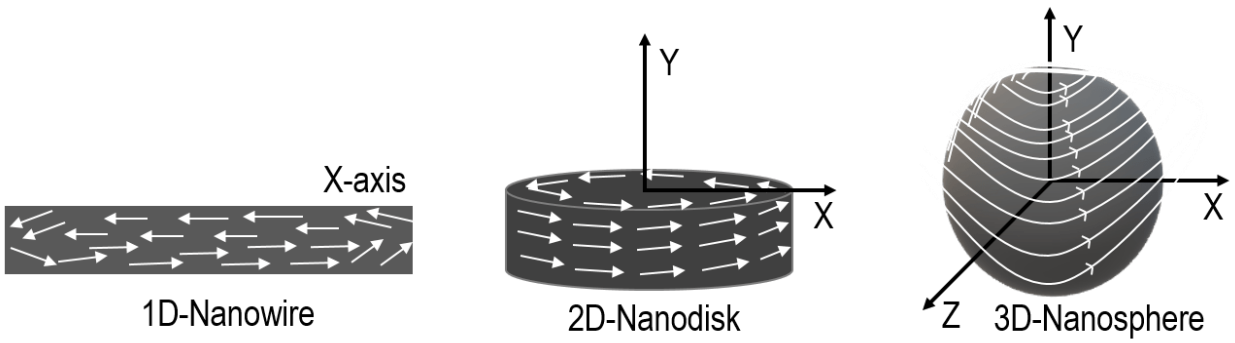

Figure 1.4: Examples of dimension-based vortex NPs (Source: self-made).

With the field, these spins tend to align in-plane if the thickness of NDs/MDs is much smaller than the diameter that contributes the loss of exchange energy to cancel/balance the dipole energy. Simultaneously at the core of the NDs/MDs, the magnetization evolves out-of- plane and parallel to the plane normal. Nevertheless, they avoid the out-of-plane magnetization if the thickness is too small. A vortex core with out-of-plane (perpendicular) magnetization is therefore expected to occur if the geometry, i.e., shape, size, and thickness of the NDs/MDs are appropriate [36,37]. Recently, the time-resolved response to applied magnetic field pulses is extensively reported in broad aspect which studied the dynamics of vortex in NDs/MDs, demonstrating the time-dependence of the size, shape, and polarity deviations of the vortex cores, Eigen frequencies and damping of time-harmonic trajectories of the cores, the switching processes, and the spin waves involved. In case of NRs, the absence of a central vortex core substantially reduces the exchange energy, making their vortex state energetically favorable, i.e., the lowest energy state (ground state), without out-of-plane magnetization (M_R = 0), which avoids possible clusters due aggregation [41,74]. Moreover, the vortex NRs have lower energy than NDs and do not produce surface magnetostatic charges, thus becoming more stable.

1.5 Magnetic Energy in Nanorings/Nanodisks

1.5.1 Exchange energy: The magnetic vortex state can be energetically preferable only when the particle size beats the exchange length, l_{ex}. In case of vortex state, the magnetostatic energy is zero, and the only energy value is the exchange energy, that in this structure has cylindrical symmetry. The exchange energy, E_{ex}^{V}, in the vortex state is given by [75,76]

$$E_{ex}^{V} = \frac{\mu_O M_S^2 2l_{ex}^2}{2(R_{out}^2 - R_{in}^2)} \ln\frac{R_{in}}{R_{out}} \text{ for NRs} \quad (1.4)$$

$$E_{ex}^{V} = \frac{\mu_O M_S^2 2l_{ex}^2}{2(R_{out}^2 - R_{in}^2)} \ln\frac{R_{out}}{R_{in} + 0.5l_{ex}} \text{ for NDs} \quad (1.5)$$

where R_{out} and R_{in} are the outer and inner radii, respectively.

Since the extra exchange energy, E_{ex}^{r}, term appears from the edge roughness, which is proportional to the ratio between the perimeter as well as the volume of the ring,

$E_{ex}^{r} \alpha \frac{2\pi(R_{out}+R_{in})t\sigma}{\pi(R_{out}^2 - R_{in}^2)t} = \frac{2\sigma}{W}$, which can be further written as

$$E_{ex}^{r} = \frac{\mu_O M_S^2 C_O^{ex} R_{out} t}{2L_{ex}^2} \frac{2\sigma}{W} \quad (1.6)$$

where $C_O^{ex} = 9.2\times10^{-6}$ is a characteristic energy for such nanostructures, $w=R_{out} - R_{in}$ is the width, and σ is the roughness amplitude. For a disc, $w=R_{out} - R_{in} = R_{out}$ since $R_{in} = 0$. Therefore, the total exchange energies of ring and disc elements with the edge roughness energy contribution become

$$E_{ex}^{tot} = E_{ex}^{V} + E_{ex}^{er} = \frac{\mu_O M_S^2 2L_{ex}^2}{2(R_{out}^2 - R_{in}^2)} \ln\frac{R_{out}}{R_{in}} + \frac{\mu_O M_S^2 C_O^{ex} R_{out} t}{2L_{ex}^2} \frac{2\sigma}{W} \quad \text{for NRs} \quad (1.8)$$

$$E_{ex}^{tot} = E_{ex}^{V} + E_{ex}^{er} = \frac{\mu_O M_S^2 2L_{ex}^2}{2(R_{out}^2 - R_{in}^2))} \ln\frac{R_{out}}{R_{in} + 0.5L_{ex}} + \frac{\mu_O M_S^2 C_O^{ex} R_{out} t}{2L_{ex}^2} \frac{2\sigma}{W} \quad \text{for NDs} \quad (1.9)$$

1.5.2 Magnetostatic energy: The magnetostatic energy of the system is considered to be an effect of the roughness of the surface and induced from the outer part (face and side surface) only. In this case, the energy expression of the roughness contribution term to the magnetostatic energy of the vortex state [75] is given by

$$E_{ms} = \frac{E_O^{ms} \xi t}{t+\sigma} \frac{2\sigma}{w} \text{ for NRs} \quad (1.10)$$

In case of NDs, the extra magnetostatic energy due to the out-of-plane magnetization at the vortex core, referred to as the vortex core magnetostatic energy, E_{ms}^{vc}, is quantitatively calculated by $E_{ms}^{vc} = \left(\frac{L_{ex}}{R_{Out}}\right)^2$. Thus, the total magnetostatic energy of NDs, E_{ms}^{tot}, is

$$E_{ms} = E_{ms}^{vc} + E_{ms} = \left(\frac{L_{ex}}{R_{out}}\right)^2 + \frac{E_o^{ms} \xi t}{t+\sigma} \frac{2\sigma}{w} \quad \text{for NDs} \quad (1.11)$$

where E_o^{ms}= 0.36 ± 0.01, ξ=2σ/λ, λ is a roughness correlation length of the order $\sqrt{2}$c, c = 5 nm is the cell size, and σ = $\sqrt{2}$c/4 is the roughness amplitude. This empirical equation should describe the edge roughness effect of magnetic states for that the magnetostatic energy term dominates.

1.6 Magnetic Energy in Nanospheres

1.6.1 Exchange Energy: The exchange energy of vortex area is,

$$E_A^v = \frac{J_s^2 l_s^2 R(2-\ln\frac{b}{R_v})}{2\mu_o} \tag{1.12}$$

The anisotropy energy of the vortex area in the case of uniaxial anisotropy in the (x, y) plane,

$$E_A^v = \frac{K_1 V^v\{1+(3-4\ln 2)(\frac{b}{R_v})^2\}}{2} \tag{1.13}$$

Where, $V^v = 2\pi R_v^2 R$ is the volume of vortex region in NSs since vortex evolve in the cylindrical form. Further, the stray field energy of the vortex area can be written for the case R > l_s,

$$E_S^v = \frac{2\pi J_s^2 b^3\{0.083-(\ln 2-\frac{1}{2})^2(\frac{b}{R})\}}{\mu_o} \tag{1.13}$$

Here, R_v is the radius of vortex region, and b = R_v/2 is the radius of the vortex core obtained by minimizing the total energy of the vortex region for soft magnetic materials [77].

$$b = 0.68 l_s(\frac{R}{l_s})^{0.33} \tag{1.14}$$

The energy of the curling region (volume V^{curl}) is composed of exchange energy (E_A^c) and magnetocrystalline energy (E_K^c) and is given as,

$$E_A^c = 4\pi AR\ln\frac{2R}{R_v}$$

$$E_K^c = \frac{KV^c}{2} \tag{1.15}$$

Where, $V^c = \frac{4}{3}\pi R^3 - 2\pi R_v^2 R$ is the volume of curling region.

1.7 Magnetic Fluid Hyperthermia as a Thermal Therapeutics

The word 'Hyperthermia' defines its meaning itself where 'hyper' means excessive and 'thermia' signifies the reflection of heat or heat generation. The idea to induce heat in the specific part of the body is to kill the unhealthy cells, mainly the cancer cells keeping safe healthy tissue at normal body temperature. Briefly, cancer is an abnormal and uncontrollable cell proliferation, with the

potential to metastasize to throughout the body, including the brain, liver, breast and bones, through blood or lymph circulation. It has given a great threat to our health system being a largest cause of the death worldwide. According to the Global Burden of Cancer Study 2012, 14.1 million new cancer cases and 8.2 million cancer deaths were reported. In this scenario, the hyperthermia therapeutic technique involves the enhancing body temperature or a specific part above a threshold temperature. The temperature range generally utilize in between 42°- 48°C until the complete destruction of tumors [78]. Usually, the limit temperature at which normal enzymatic forms can be annihilated, and the cells could slaughter, is 42°C. In brief, NPs with improved heating capabilities, along with the strategies for testing them have significantly changed the way in that hyperthermia based treatments are organized, driving to an energizing modern concept in cancer treatment. The local hyperthermia is utilized for tiny tumors and is the foremost dedicated treatment. Heat needs to be applied to tiny/little regions of the body whereas the encompassing zones are kept up at the typical body temperature of 37°C. As of now, modest microwave antennas or ultrasound is utilized to convey the heat to the tumor, which contains a most extreme estimate of almost 5 cm in size.

In 1957, Gilchrist et al. [79] has introduced the magnetic NPs in thermal therapy as heat generators in the application of ac magnetic field and frequency. With the efforts of several years in the development of nanotechnology, the magnetic NPs (MNPs) based hyperthermia technique, called magnetic fluid hyperthermia (MFH) is now widely attentive and rising as an efficient and effective research field in thermal therapeutic cancer treatments along with diagnosis and imaging. MFH technique directly transports therapeutic heating to the tumor cells that aids the realization of intracellular MFH, which can be further refined by attaching the cell-targeting ligands with MNPs. This advantage of control uniform localization heat leads to the greater selectivity and effectiveness of the treatment. Once the magnetic NPs are exposed to an ac magnetic field, the electromagnetic energy converts into heat which provides a great advantage in the deep tissue penetration and selectively destruction of tumor cells without harming the surrounding healthy tissues. The magnitude of converted heat energy largely depends on size, shape, types of NPs, composition, anisotropy, stoichiometry, application of the frequency, and the ac magnetic field. The application of magnetic field and the frequency need to be set in the inverse order. For instance, if the frequency is fixed, the amount of energy released by the MNPs, or the specific absorption rate (SAR), is dependent on the amplitude. Higher the amplitude of the ac magnetic field (AMF), the higher the SAR will be. This principle is the same for a fixed magnetic field;

higher the frequency, the higher the SAR [80]. The complete overview on how MNPs-based MFH works from physical system and its translation onto clinical setup is given in Figure 1.5. Here, SAR is a terminology of heat measurement generated by the magnetic particles, whose details is given in the experimental section (Chapter 2).

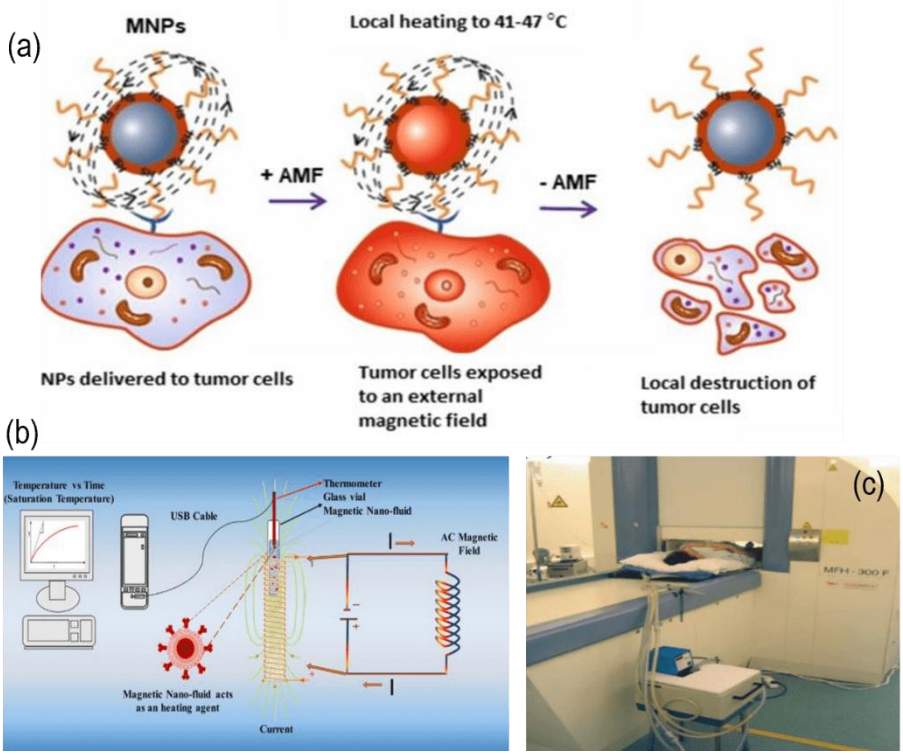

Figure 1.5: Schematic representation of MFH for selective tumor cell destruction [81], (b) Schematic experimental setup for MFH [82], and (c) first AC magnetic field applicator used in humans (MFH300F, MagForce Nanotechnologies GmbH, Berlin) with an external field strength of 0–18 kA/m and a frequency of 100 kHz. The temperature is recorded by using Fibre-optic thermometry which are placed in different parts, such as prostate, urethra, rectum, perineum, scrotum and left ear, to adjust the desired steady-state temperature in the tumor [83].

Of course, once the MNPs gets inside the body, great care has to be taken since the prompt generation of heat at the nanoscale level cause the significant functional changes in organisms along with direct synchronization of the physio-biochemical properties of the molecules. Such significant changes in the biological environment that may introduce the novel topics into the improvement of therapeutic efficacy in MNPs base thermal therapy. As an example, when an external field is applied to the lysosome-accumulated MNPs, lysosomal cell death can be arised due to increase in temperature and the possibility of larger reactive oxygen species (ROS) production within the lysosomes [84]. Thus, the biological effects of induced local heat in

cellular/subcellular death and its fine administration mechanisms needs in-depth further investigation.

1.7.1 Heat Loss Mechanism

With the application of field and frequency to the MNPs, the induced electromagnetic (EM) energy exhibit their response in the form of heat. Such conversion of EM into heat during magnetization reversal is, in principle, called magnetic loss, which is usually called as heat loss. The induced heat largely depends on size of the NPs since the mechanism of heat loss is varied with the size-dependent magnetic states. There are different magnetic states such as superparamagnetic, single-domain, ferro/ferrimagnetic (vortex, and multi-domain) with increase in size (Figure 1.6 (c)). Within the superparamagnetic range, the heat loss is mainly granted from Néel and/or Brownian relaxation mechanism when the thermal energy overcomes the rotational energy barrier under the application of magnetic field. In case of Néel relaxation, the rotations should overcome the induce friction in between magnetization easy axis and atomic lattices, whereas such rotation need to overcome the friction induce in between MNPs and their surroundings for Brownian relaxation and lead to the loss of EM energy and the production of thermal energy (Figure 1.6(a)). Néel mechanism in MNPs exponentially depends on magnetic anisotropy and volume of the particle. Néel relaxation is generally occurs in smaller particle sizes, i.e., superparamagnetic, whereas Brownian relaxation is not restricted within the superparamagnetic regime and largely depends on the viscosity of the medium if the particles can rotate or not even for larger particles, for instance single-domain or multi-domain particles [85,86].

On the other hand, the internal magnetic structure of ferromagnetic system is an assemble of several domains separated by domain walls. The uniform magnetization emerges in each domain aligning all spin in the same direction. However, an accumulation heat loss mechanism in single-domain and ferro/ferrimagnetic (vortex/multi-domain) NPs always occurs from the magnetization hysteresis (MH) losses in the application of external field and the nature of hysteresis loss largely depends on the particles response with increase/decrease of the applied field.

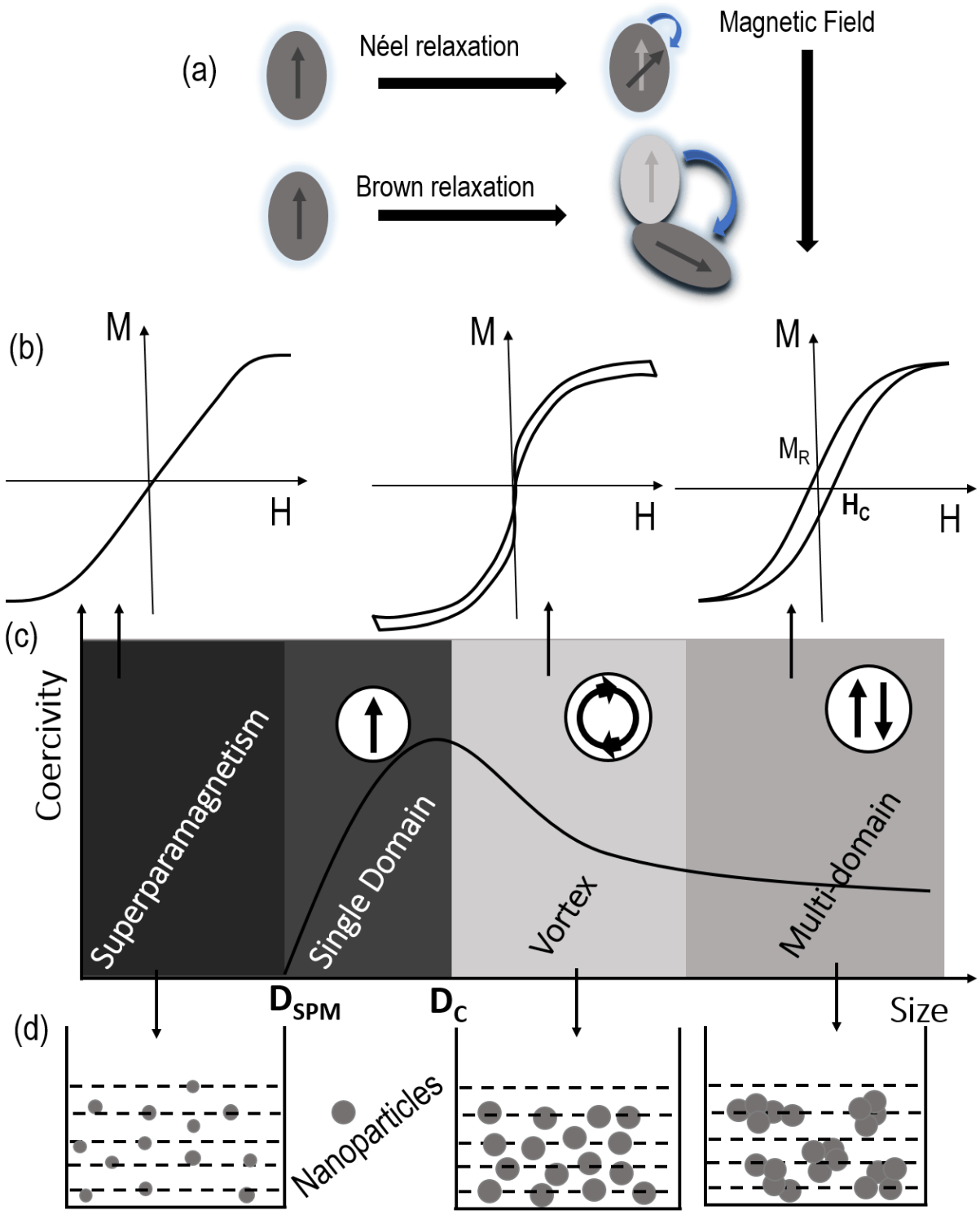

Figure 1.6: A complete overview of size-dependent heating mechanism at different region of NPs from superparamagnetic to multi-domain with Néel and Brownian mechanism, general magnetization hysteresis behavior (a-c) and dispersion of NPs in solution at their respective regions (d) (Source: self-made).

The complete hysteresis loss cycle provides three major information about the magnetic behavior of the system, namely coercive field (H_C), magnetic remanance (M_R) and the magnetic saturation (M_S). These three physical parameter can predict the nanoparticle interactions and heating efficiency for magnetic fluid hyperthermia. The total heat induced by the MNPs approximately equals to the area of the magnetization hysteresis loss in a complete cycle of the applied magnetic field, which is given by relation [87,88].

$$A = \oint_{-H}^{+H} \mu_0 M(H) H dH \quad (1.16)$$

Where A is area of hysteresis loss, μ_0 is permeability, $+H$ to $-H$ is the application of magnetic field in a complete cycle, and $M(H)$ is magnetization as a function of magnetic field.

1.8 Magnetic Vortex Nanoparticles in Magnetic Fluid Hyperthermia

The MNPs-based MFH is the most promising supplementary techniques to the chemotherapy/radiotherapy for a cancer treatment. This technique has several achievements in terms of heating properties depending upon the NPs size, shape, crystallinity, dopant material etc. which are still under continuous improvement and is currently going through clinical trials[89–92]. The technique involves magnetic NPs subject to an external ac magnetic field and frequency to generate the heat and allows to target a specific tumor location and deliver toxic doses of heat only to the tumor area without damaging the surrounding healthy tissues [91,93].

In particular, iron oxide based NPs are promising in MFH as a heat inducer. Superparamagnetic magnetite (Fe_3O_4) has been widely optimized in terms of shape, size, saturation magnetization (M_S) and magnetic anisotropy in order to enhance heating response under the application ac magnetic field and frequency[91,94]. Unfortunately, the heat induced by SPM iron oxide NPs has reached its limit [95]. Since last decades, on one hand, the focus is to design ferro/ferrimagnetic iron oxide NPs due to their larger hysteresis loss, which gives higher heating performance since heating efficiency depend on hysteresis loss of MNPs; on the other hand, high coercive field (Hc) and magnetic remanance (M_R) give rise to agglomeration in the suspension [42,89,96]. In this regard, NPs based on different geometry such as magnetic nanodiscs and nanorings with negligible H_C and M_R, but significant hysteresis loss, called magnetic vortex NPs, can be an alternative nanoheaters on combining the properties of SPM and FM/FiM [41,42,57,97,98]. These properties reduce the long-range magnetostatic forces (dipole-dipole interactions) responsible for particle agglomeration; the complete scenario on advantage of vortex NPs is shown in Figure 1.6. The hysteresis loss nature

of these NPs are quite different as usually observed in ferro/ferromagnetic NPs governed by the transition of different state (vortex to onion, c-state and s-state). The nucleation (H_n) and annihilation field (H_{an}), also called switching field (H_S), are responsible for the nucleation and annihilation of such different state occurred on the NPs [39,99]. Although stoichiometry of NPs does not affect the magnetic configuration of vortex NPs, different switching field (H_S) can be observe for different NPs depending upon the shape, size and orientation with respect to application of field that provides different hysteresis loss on which the final heating efficiency (SAR, specific absorption rate) is depended. Thus, the heating properties of magnetic vortex NPs can be enhanced by tuning the several physical properties such as switching field (H_S), shape and size, a.c. magnetic field and frequency, orientation of NPs etc. and this thesis is mainly devoted to study these physical parameters and their effects on MFH.

1.9 Magneto-mechanical Approach

In cell biology, the living cells generate force and sense often via proteins, since proteins are generally force sensor in biological phenomena, which react to the mechanical influence with a conformational change (i.e., change in the shape of molecule produced by external factors) that triggers a biochemical signaling cascade. Every cells are influenced by a mechanical stimulation caused by muscle contraction, arterial pressure, and change in internal dynamics/mechanics. All the cellular process such as cell migration/motion, cell division, transportation of vesicle, and formation/shaping of cell membrane are monitored via intracellular mechanosensors and actuators; and their mechanical regulation are surveilled through the receptor-ligand interactions between cells and their extracellular environment [100]. During such interactions, mechanical force imparted from the extracellular to the intracellular side and vice versa allows cells to record/examine the physical/mechanical properties of their surroundings and provides all the mechanical information. This mechanical information is converted into biochemical signals via adhesion assemblies/cytoskeleton and serves as mechanical input for intracellular signaling cascades influencing all the physiological response called mechanotransduction [101]. The mechanical forces are of course generated by cells itself; besides it, such force can be generated by externally, for example through the application of magnetic field on MNPs.

The shape-and size-dependent MNPs embedding the molecules onto their surface/shell are allowed to be remotely activated by applied magnetic field and promotes their interaction with cells,

viruses, proteins and DNA. The mechanical force, unlike the MFH, induced by mechanically actuated (by oscillation/rotation) MNPs after applying magnetic field remotely is widely attracted in the field of cell mechanobiology. The physical action inside the tumor arises by means of magnetic torque (τ) and hence induced mechanical force allows us to study the cellular functions/response within the tumor cells and their death. Thus, remote sensing magneto-mechanical transduction approach, combined properties of magnetism and mechanical force, could shape the new therapeutical methods in the field of cancer treatment [102].

1.10 An Overview of Micromagnetism

The theory of micromagnetism, widely known as 'continuum theory of micromagnetism' was developed in the early 20th century, which helps to understand the phenomena of magnetization processes/hysteresis loops in magnetic materials connecting the Maxwell's theory of electromagnetic fields and quantum theory based on atomic backgrounds since both theories are unable to explain the magnetic phenomenon of spin order structures themselves. The Maxwell's theory subjected to the permeabilities and susceptibilities of materials that valid for macroscopic dimensions; whereas, the quantum theory describes the magnetic properties on the atomistic level. The properties of magnetic materials can be understood by analytical solutions derived from these two theories. The purpose of the theory is to predict the energy and magnetization distribution as function of the applied field/current considering the several morphologies based material and their mutual interactions. The 'continuum theory of micromagnetism' became crucial after Barkhausen's jumps and Sixtus K. J. and Tonks L. experiment on the domain wall velocity[103–106]. The exchange energy of materials induces the long range magnetic order leading to the parallel alignment of neighboring atomic spins. This fundamental problem on origin of the long range magnetic order is extensively studied by means of theoretically and experimentally. However, the exact correlation of the atomic properties to magnetization structures and magnetization reversal mechanisms in bulk materials is still under huge debate. Although micromagnetism theory explains the materials properties based on the exchange energy arises by means of the boundary of materials, it is not recommended to avoid any of the three major energy terms, exchange, anisotropy, and magnetostatic because of the fact that the detailed magnetic behavior of a given material depends on the balance between these energies.

Heisenberg describes the ferromagnetism[107] on the basis of exchange interactions and derives the micromagnetic equations from which two major assumptions are made: (i) micromagnetism is a quasi-classical theory and Heisenberg spin operators are replaced by classical vectors and (ii) the energy terms are derived either by the transition from an atomistic model to a continuum model. Further, the micromagnetism assumes that the direction of the spin changes by a small angle from one lattice point to other, whose direction angles can be estimated by a continuous function of position vector, $\mathbf{x}= (x, y, z)^T$. In this case, the continuous vector field, i.e., the magnetization **M(x)** describes the ferromagnetic state; the direction of **M(x)** varies continuously with the coordinates x, y, and z [108].

1.10.1 Exchange energy

The exchange energy in ferromagnetic NPs, which behaves a quantum mechanical in nature, depends on the relative direction of their spins. In such case, the energy of two parallel spins is lower as compared to their antiparallel state. Once the spins get parallel to each other, the electrons favor to move apart lowering the electrostatic energy. The corresponding gain in energy can be large enough so that the parallel state is preferred. This energy is very crucial in the formation of covalent bond of solids materials and is responsible for ferromagnetic exchange coupling, also refereed as 'direct exchange coupling'. This direct exchange coupling is potentially applicable to very limited materials since several models, including itinerant electron ferromagnetism and indirect exchange interaction or Ruderman-Kittel-Kasuya-Yoshida (RKKY) interaction, exist which covers wide range of materials. To provide the continuum equation of the exchange energy, Landau and Lifshitz[109] have demonstrated for tiny deviations of the magnetization from a uniformly magnetized low energy state. For non-uniform magnetic states, which increases the exchange energy, the first deviations $\nabla\gamma$ of the direction cosines γ must occur quadratically in the energy equation. Both assumptions are fulfilled by the differential operators **(**grad J)^2, (div J)^2 and (curl J)^2. Among them, (grad J) is considered as the accurate and precise illustration of the excess exchange energy because div J and curl J would lead to zero exchange energies although both cases non-uniform magnetization exists[110]. The exchange energy density for any materials, i.e., amorphous and crystals,

$$\phi_{ex} = A\{(\nabla\gamma_1)^2 + (\nabla\gamma_2)^2 + (\nabla\gamma_3)^2\} \quad (1.17)$$

The exchange stiffness constant A is related to the exchange integral J_{ij} between spin S_i and S_j at position r_i and r_j. From the Heisenberg exchange Hamiltonian[111], the exchange energy for two localized spins,

$$H_{ex} = -2\sum_{i\neq j} J_{ij}(r_{ij})S_i(r_i).S_j(r_j) \quad (1.18)$$

where J_{ij} denotes the exchange integral between the ions of spin S_i and S_i with distance $r_{ij} = r_i - r_j$. The exchange interactions tend to keep the magnetization uniform. However, external fields could give rise to a locally confined non-uniform magnetization depending on the geometry of NPs.

1.10.2 Magnetocrystalline Anisotropy Energy

The 'anisotropy' signifies the dependence of magnetic properties of a material with the direction axes. The magnetocrystalline anisotropy has intrinsic contribution to the material with the origin at the atomic level interacting between the ions and the crystal field. The strong coupling between the spin and orbital angular momenta within an atom may lead to induce the different physical properties, for instance hysteresis loop in a magnetic measurement. Depending upon the shape of materials, the spin–orbit coupling (L-S coupling) prefers toward their crystallographic directions for the magnetization, which is referred as easy direction. In this state, anisotropy energy, need to rotate the magnetization away from the easy axis, is small as compares to the exchange energy depends on the lattice structural origins. For examples, (i) uniaxial anisotropy occurs in hexagonal crystals such as cobalt with energy $E = KV \sin^2\theta$ + higher terms, where θ is the is the angle between the easy direction and the magnetization, K is the anisotropy constant, and V is the volume of the materials. Usually 'higher terms' are very small and hence can be neglected; (ii) cubic anisotropy usually found in iron and nickel with energy $E = K_0V + K_1V(\alpha_1^2\alpha_2^2 + \alpha_1^2\alpha_3^2 + \alpha_2^2\alpha_3^2)$, where α is direction cosine between the magnetization axis and the crystal axis.

1.10.3 Magnetostatic Energy

The total magnetostatic energies, includes the non-local dipolar interactions, are contributed from two different magnetic fields, i.e., external magnetic field, H_{ext}, and the dipolar fields, H_S, resulting from magnetization M_S. The magnetostatic energy of the external field, introduced as Zeeman energy, which is the sum of the interaction energies of local moments $\mu_i = g\mu_B S_i(r_i)$, can be written as,

$$\phi = g\mu_B\mu_0 \sum_i S_i(r_i).H_{ext} \quad (1.19)$$

Where "g" is Lande's splitting factor, μ_B is Bohr magnetron and μ_0 is permeability in free space. On the other hand, the dipolar field is very important for the formation of domain patterns in the magnetic materials[109]. Brown W. F.[112] discussed magnetostatic principle extensively within the atomistic description of magnetization in which the macroscopic stray field is determined by summing all dipole fields of the magnetization,

$$H_S(r)=\frac{1}{4\pi}\sum_i \frac{\mu_i r_i}{R^3}+\frac{3(\mu_i(r_i).R).R}{R^5} \tag{1.20}$$

Where $R = r - r_i$

1.11 Landau-Liftshitz-Gilbert Equation of Motion

The theory of micromagnetism in a dynamic magnetization processes describes the many problems regarding reduced energy losses in particles/thin-films, the estimation of resonance frequencies and spin-wave spectra. Bloch [113] gave the time-dependent motion of magnetizations considering uncoupled and undamped magnetic moments. Further, Landau and Lifshitz[109] revealed the equation of damped motion of the magnetic polarization. Classically, let P is the angular momentum and L is torque acting on the rigid body, then equation of the rotational motion of a rigid body can be given by linking P and L, i.e., $L = dP/dt$. Further, let magnetic torque $L = J_s \times H_{eff}$, where $J_s = \gamma P$, then the undamped rotational motion can be obtained as,

$$\frac{dJ_s}{dt} = \gamma\,(J_s \times H_{eff}) \tag{1.21}$$

Where, $\gamma = -1.1151$ g $(Am/s)^{-1}$ is gyromagnetic ratio.

Landau and Lifshitz (LL) have expanded equation adding damping term $-\frac{\alpha_L}{J_s}[J_s \times [J_s \times H_{eff}]]$ and divided obtained equation by μ_0 and replace J_s by magnetization, M_s which finally gives the equation of magnetization,

$$\frac{dM_s}{dt} = \gamma_L\,(M_s \times H_{eff}) - \frac{\alpha_L}{M_s}[M_s \times [M_s \times M_{eff}]] \tag{1.22}$$

Where, H_{eff} is an effective field which can be defined as a negative variational derivative of the free magnetic energy with respect to the magnetization. The first term on the right-hand side of equation (1.22) describes a precessional rotation of M_s with frequency $\omega = -\gamma H_{eff}$. The minus sign in ω signifies the anticlockwise precessional motion if a positive effective magnetic field considered. Similarly, the second term denotes the rotational magnetization, Ms toward the

direction of the effective field. The above equation is valid for a small damping only, thus the equation is modified by Gilbert [114] for strong damping in thin films as,

$$\frac{dM_s}{dt} = \gamma_G (M_s \times H_{eff}) - \frac{\alpha_G}{M_s}[M_s \times \frac{dM_s}{dt}]) \quad (1.23)$$

On combining the above equations, we get

$$\frac{dM_s}{dt} = \frac{\gamma_G}{(1+\alpha_G^2)M_s} (M_s \times H_{eff}) - \frac{\gamma_G \alpha_G}{(1+\alpha_G^2)M_s}[M_s \times [M_s \times M_{eff}]]) \quad (1.24)$$

Where, $\gamma_L = \frac{\gamma_G}{(1+\alpha_G^2)}$ and $\alpha_L = \frac{\gamma_G \alpha_G}{(1+\alpha_G^2)}$

This is called Landau-Lifshitz-Gilbert equation. The interaction in between the precession (Figure 1.7(a)) and the damping (Figure 1.7(b)) term leads to damped oscillations of the magnetization around its equilibrium state. In LLG, the precessional term $M_s \times H_{eff}$ decreases, which remains same in LL equations. Similarly, the damping factor increases linearly with α_L in case of the LL equation which goes through a maximum value for the LLG equation. For larger values of α_G, the precession and damping terms are vanished.

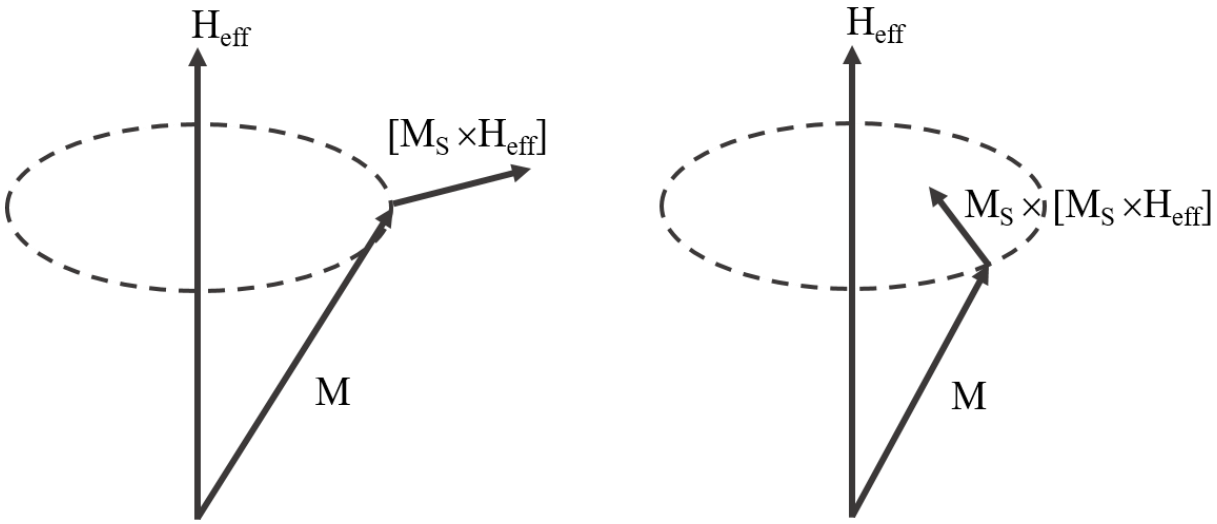

Figure 1.7: Dynamical motion of a single magnetization vector: (a) precession and (b) damping.

The LL and LLG equations are basic but fundamental to investigate the complex magnetization dynamics in ferromagnetic materials. This equation widely takes place to understand the nonlinearity effect in magnetization dynamics, magnetization switching behavior, oscillation in spin wave dynamics and force-precession regime etc. Although the both equations seems equivalent, LLG is more crucial in view of physics of magnetization since the magnetization

direction is space-dependent for ferromagnetic NPs (multi-domain particles). Even in small NPs, where the domain wall formation is energetically unfavorable, the uniform magnetization dynamics realized itself as a single domain state and LLG equation describes the coherent rotational magnetization.

1.12 Micromagnetic Simulation: Overview of Mumax3.9

As discussed in the previous section, the micromagnetic theory is an extensive approach to extend the magnetization reversal/structural and/or hysteresis effects of ferro/ferrimagnetic materials whose strong theoretical foundation is LLG equation described above (Eq. 1.24).

Since the late 19th century, large scale computer has opened up the study of materials physical behavior through computerized simulation which becomes highly impacted tools on not only to understanding/predicting the materials properties but also on the development of advanced technology based on magnetic materials. In this regard, the dynamic micromagnetic simulation allows us to study the time evolution of the magnetization depending upon the value of damping parameter (α) since α depends nonlinearly on the magnetization of ferromagnetic materials. Usually, α is used to take in the range of 0.1-1 (mostly 0.5), which allows to reduce the simulation time. Such numerical micromagnetic modelling can be performed in two well-develop methods, i.e., the finite difference (FD)[115] and finite element (FE)[116]. These two approaches describe the connection between the local spin-configuration arrangement of the magnetizations and the micro/nanostructural properties on a length scale of several nanometers. In addition, the quantitative influence of the size, shape and orientation of magnetic nano/microstructure on the magnetization reversal and hysteresis processes can be observed and/or speculated[42,117]. In particular, the FD approach use the method of discrete values on the grid to speculate the field quantities, whereas in FE approach, the magnetic domain is fragmented into several elements, and nodal basis functions are used to estimate the field quantities. The LLG based micromagnetic simulations is a challenging technique in numerical micromagnetism due to difficulties in obtaining the effective magnetic field. This effective magnetic field is derived mainly from three energies, i.e., the magnetostatic, exchange, and magnetocrystalline anisotropy field contributions to the magnetization dynamics[109]. Among these three, the magnetostatic energy is the most challenging contribution to the magnetization dynamics because of its origin from long-range-interaction in which the effect of the magnetization at any point on the magnetization at every

other point should be accounted. This magnetostatic energy obtaining from a magnetostatic field is the most time-consuming in the micromagnetic problem. Along with this, strong stray field arises from these interaction could make a drastic change in magnetization reversal process that affects switching field of the system, i.e., the angular dependence of nucleation field NPs deviates considerably[118]. Another magnetic simulation study reported the effects of inter-grain exchange and magnetostatic interactions on remanence and coercivity cubic magnetic particles which revealed that inter-grain exchange interactions increase the magnetic remanence and reduce the coercive field [119]. The long-range-magnetostatic interaction between plethora of grains in the system would result a magnetic cluster that can be associated with the final magnetization reversal process.

The impractical importance and the motivation to perform micromagnetic simulation can be summarized specifically (i) to confirm and interpret experimental results, (ii) to test and/or predict/optimize for a new experimental design, and (iii) for an approximate validation of analytical solutions. While designing an expensive and time-consuming new experiment, micromagnetic simulations can be performed in advance in order to navigate the parameter required and the feasibility in practices. In addition, such simulations permit one to quick screen that are not available experimentally, for example individual micromagnetic energy which allows a profound understanding of the complete phenomena under investigation. Sometime recently the appearance of present day computers, micromagnetic investigation was constrained to analytic derivations of equilibrium magnetization states strong solid assumptions and to the simplification of the LLG elements to effective equations of motion, pertinent to one particular framework, for instances domain wall motion [109] and ferromagnetic resonance [120]. In any case, this approach is restricted to exceptionally particular cases and isn't adequately common to complement the outcomes of complex experimental systems. The another way is to utilize numerical methods to minimize the free magnetic energy and to resolve the LLG equation to simulate the magnetization dynamics. Thus, numerical micromagnetic simulation is strong tool to investigate the static and dynamic behavior in micromagnetic systems. This tool helps to solve and predict the damped equation for a continuous magnetic system, involving all the interactions in three-dimensional regions of arbitrary geometry, polycrystalline grain structure and physical properties.

There are several micromagnetic simulation program based on FD (Mumax, GPMagnet, Micromagus, Fidimag etc.) and FE (FEMME, Finmag, Fastmag, Nmag, Magpar, and tetramag etc.) systems. We use an open-source graphics processing unit (GPU)-accelerated Mumax3 program throughout our research to investigate the time and field dependent magnetization dynamics in nano to micro scale iron oxide NPs and compare all the results with their theoretical and experimental counterparts. Mumax3 is an open access software under the GPLv3 license on http://mumax.github.io, which is written in Go[121] and CUDA[122]. An NVIDIA GPU driver is compulsory to run it in a Linux, Windows or Mac platform. No further additional support is required.

To run the required micromagnetic simulation, we need to script the required simulation in txt file in which following physical quantity must be defined:

- **Mesh size and Geometry**: Mesh size, cell size and cell geometry should be defined at the beginning of the script. It is recommended the number of cells to be in the powers of two, or at least have small prime factors. It should be noted that mesh size must be smaller than the exchange length (l_{ex}) of NPs [123].
- **Shape/morphology**: The shape/morphology of the NPs should be defined. For examples sphere, disks, rings, cuboids, square, cylinder etc.
- **Material Regions**: If the NPs contain several regions (for instance core shell) and someone want to simulate those systems then one has to define the number of regions along with their own parameters since each cell is assigned to a single region.
- **Initial Magnetization**: The initial magnetization is set by assigning a Config to m, setting it in separate regions, or by loading a file directly.
- **Material Parameters**: Material parameters should be defined which are assigned to the 256 regions. There are vectors and scalar material parameters
- **Excitation**: The magnetic field or current excitation should be defined, likewise the material parameters.
- **Output**: There are several output, which can be obtained.
- **Scheduling Output**: It gives the required output that one defines as per our needed while scripting.
- **Running**: It runs the simulation for a given time in seconds.

```
// Initial parameters

// Discritization parameters
Cell_x := 5e-9
Cell_z := 5e-9

// ------------------------------------------------------------

Nx := D_ext/Cell_x
Nz := height/Cell_z


SetGridsize(Nx, Nx, Nz)
SetCellsize(Cell_x,Cell_x,Cell_Z)

//Geometric
height := 220e-9 // whole height of the sample
D_int :=  70e-9 // hole diameter
D_ext := 140e-9   // outer diameter
//t_shell := 10e-9  // thickness of the shell


// Magnetic parameters of the core - magnetite
//Mag_shell := 480e3
//Aex_shell := 1.2e-11
//Kc1_shell := -1.36e4
//Kc2_shell := -0.44e4

// Magnetic parameters of the shell - magnetite
Mag_core := 480e3
Aex_core := 1.2e-11
Kc1_core := -1.36e4
Kc2_core := -0.44e4

// Measurement parameter
Bmax  :=0.3
Bstep :=  0.005


TableAddVar(D_int, "Int diameter", "m")
TableAddVar(D_ext, "Ext diameter", "m")
TableAddVar(height, "Height", "m")
//TableAddVar(t_shell, "Shell thickness", "m")
//TableAddVar(Vol_sample, "Vol_sample", "m^3")
//TableAddVar(Vol_core, "Vol_core", "m^3")
//TableAddVar(Vol_shell, "Vol_shell", "m^3")
Tableadd(m_full.comp(2))
//TableAdd(m.Region(1))
TableAdd(m.Region(2))
TableAdd(B_ext)
Tableadd(Edens_demag)
Tableadd(Edens_anis)
Tableadd(Edens_exch)
Tableadd(Edens_total)
Tableadd(E_total)


//Kc1.SetRegion(1,Kc1_shell)
//Kc2.Setregion(1,Kc2_shell)
Kc1.SetRegion(2,Kc1_core)
Kc2.Setregion(2,Kc2_core)

//AnisC1.SetRegion(1, vector(0,0,1))
//AnisC2.SetRegion(1, vector(1,0,0))
AnisC1.SetRegion(2, vector(1,0,1))
AnisC2.SetRegion(2, vector(0,1,0))



SnapshotFormat

alpha =0.5
//m.SetRegion(1, vortex(1, 1))
m.SetRegion(2, vortex(-1, 1))


save(m)
```

```
EdgeSmooth = 2

hole := Cylinder(D_int, height)
//shell_int := Cylinder(D_int + 2*t_shell, height).sub(hole)
core := Cylinder(D_ext, height).sub(hole)

//shell_ext := Cylinder(D_ext, height).sub(core).sub(hole)

//shell := core.add(shell_ext)
Sample := core


//Vol_shell := (((D_int/2) + t_shell)*((D_int/2) + t_shell) - (D_int/2)*//(D_int/2))*PI*(height-2*t_shell)+((D_ext/2)*
//Vol_core := (D_ext/2)*(D_ext/2)*PI*height - Vol_shell - (D_int/2)*//(D_int/2)*PI*height
//Vol_sample := PI*height*((D_ext*D_ext)-(D_int*D_int))/4
//Mag_sample := (Vol_core*Mag_core + Vol_shell*Mag_shell)/Vol_sample


Setgeom(Sample)

//DefRegion(1, shell)
DefRegion(2, core)

save(regions)



Msat.SetRegion(0, 0)
Aex.SetRegion(0, 0)
//Msat.SetRegion(1, Mag_shell)
//Aex.SetRegion(1, Aex_shell)
Msat.SetRegion(2, Mag_core)
Aex.SetRegion(2, Aex_core)
MMagZ := m_full.Comp(2)
//print("<m> for d/lex=30: ", m.average(), "teste =", MMagZ)
//Vol_universe := Nx*Nx*Nz*Cell_x*Cell_x*Cell_z


relax()        // high-energy states best minimized by relax()


MinimizerStop = 1e-6


for B:=0.0; B<=Bmax; B+=Bstep{
   B_ext = vector(B, 0, 0)
   minimize()   // small changes best minimized by minimize()
   tablesave()
            save(m)

}


for B:=Bmax; B>=-Bmax; B-=Bstep{
   B_ext = vector(B, 0, 0)
   minimize()   // small changes best minimized by minimize()
   tablesave()
            save(m)
}


for B:=-Bmax; B<=Bmax; B+=Bstep{
   B_ext = vector(B, 0, 0)
   minimize()   // small changes best minimized by minimize()
   tablesave()
            save(m)
}
```

Figure 1.8: Snapshot of script for the simulation of iron oxide hollow nanotubes.

Based upon above simulation tools, script (Figure 1.8) can be written for hollow nanotubes (as an example). Further, the script can be changed slightly based upon the geometry of the NPs. We have performed micromagnetic simulation for different shapes, such as nanorings, nanodisks, nanospheres and nanotubes with circular vortex-spin-configuration are shown in Figure 1.9.

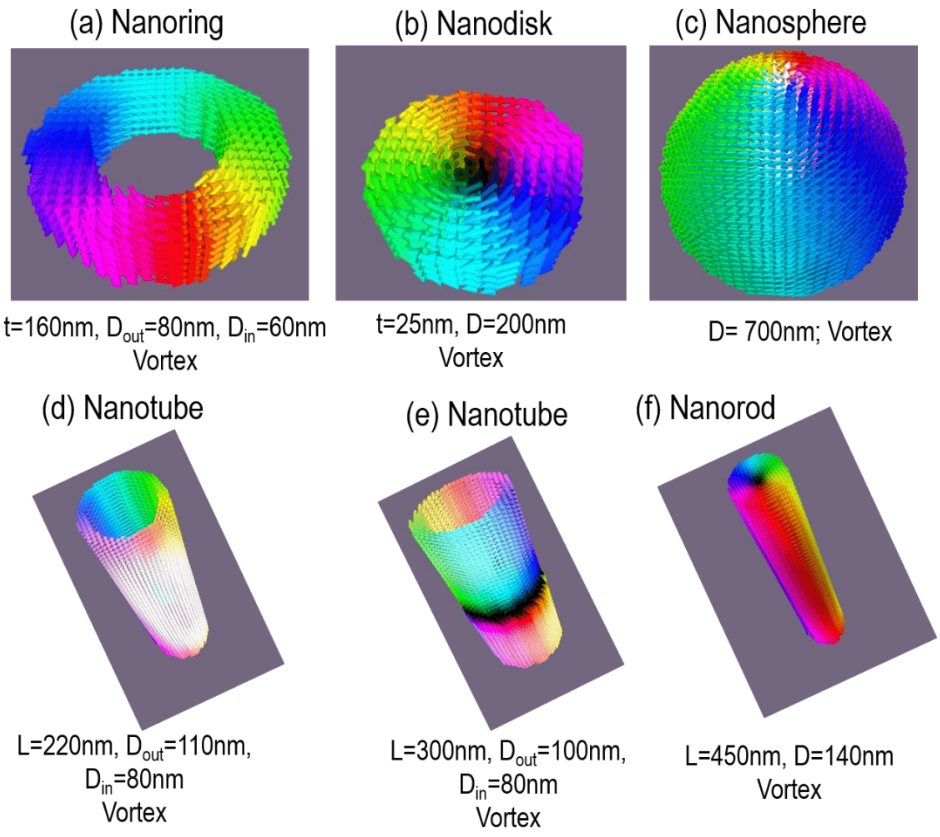

Figure 1.9: Images of shape-dependent vortex NPs obtained via micromagnetic simulation.

1.13 Magnetization Behavior: Hysteresis Reversal Modes and Switching Field Dynamics

In general, magnetic hysteresis (MH) loops are straightforward experimental probe of particle interactions in which the domain-wall and behavior of domains are mainly responsible to reproduce the different nature of hysteresis loop. Moreover, intra-particle effects for instance, thermal fluctuations significantly influence the net magnetization of NPs leading towards the different magnetic environment in a core and a shell which has a key role to reduce energy barrier distributions. Although, a large number of efforts have been made over several decades performing

low temperature dependence magnetic measurement, the impact of intrinsic and extrinsic factor on MH loop is poorly understood. The understanding on MH process becomes more complex when the materials exhibit the unusual properties, i.e., so-called vortex configuration at remanance above the single-domain. The complex phenomena of MH loop are due the distribution of the magnetization to the in-plane and out-of-plane and switching dynamics of the magnetization curve depending on the shape, size, orientation, anisotropy and external field since each case has its own magnetic spin-configurations. The well understanding magnetic behavior of the materials plays an important role in the development of various devices in nanotechnology. The magnetization and switching of the magnetic states from vortex-to-vortex, vortex-to-onion, and onion-to-onion are crucial for technological applications [124,125].

margin[127]

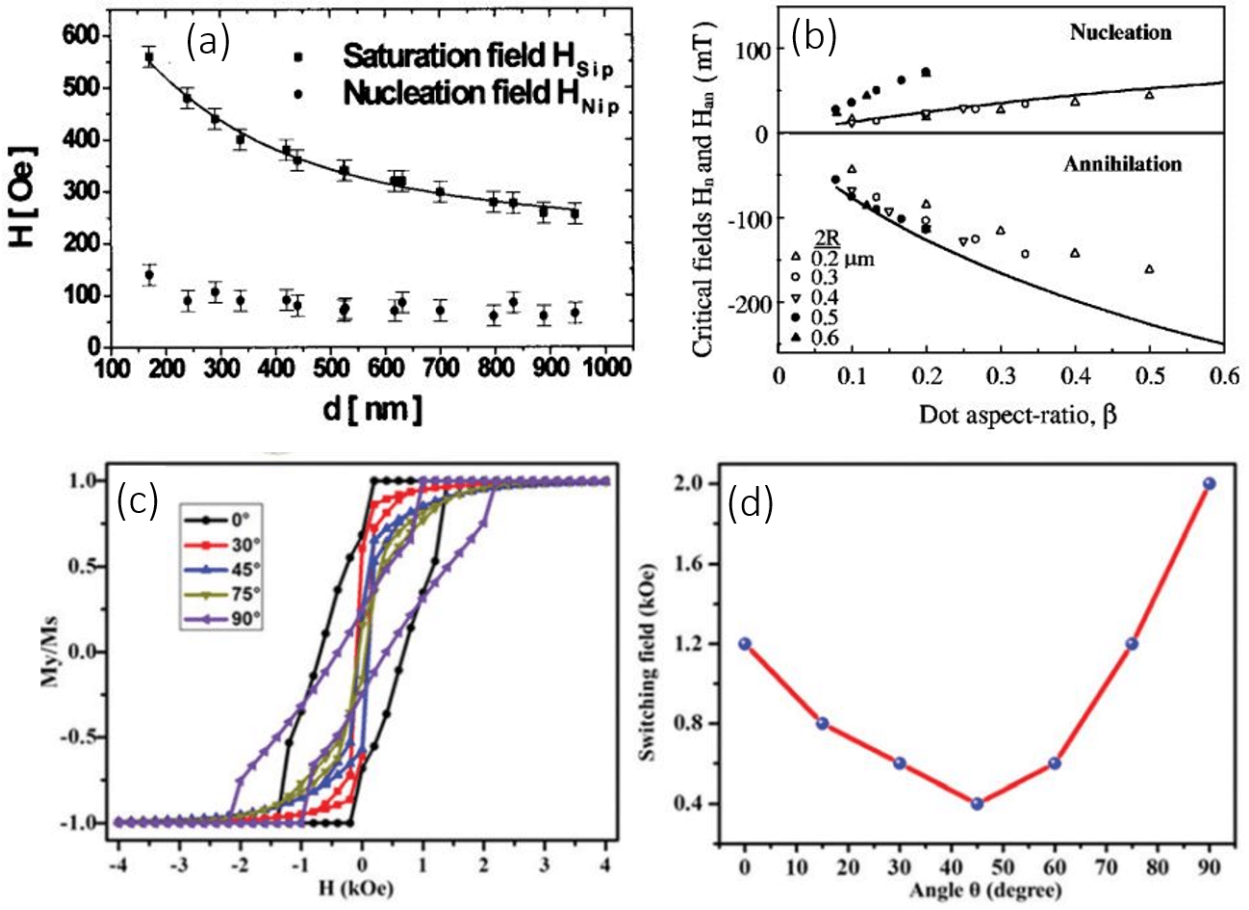

Figure 1.10: (a) Diameter dependent switching field of permalloy disk [127]; (b) aspect ratio dependent switching field of permalloy disks [39], and (c, d) angle-dependent hysteresis loop and switching field of magnetite ellipsoid [44].

To receive the uttermost pliability in a device in a convenient way, the control and reliable switching of the magnetic states is possible, i.e., the two vortex-state chiralities, the two onion-state orientations, and even between these vortex-to-onion states. However, the switching in between two possible vortex states having an opposite chirality is not easy tasks. This can be achieved via nucleation of the onion states immediate followed by the auto-motion of vortex walls (VWs). In any case, the nature of the resulting relaxed vortex state, whether it is clockwise or anticlockwise, depends on the direction of the onion-states while nucleating [126]. Experimentally, these complex switching phenomena of magnetic states can be understood critically by time-resolved scanning-transmission x-ray imaging technique.

The nucleation and annihilation/saturation field can be referred as a switching field of the system since both fields are responsible for the switching of different magnetic states. Figure 1.10 (a) shows the clear dependence of the in-plane (ip) switching field in permalloy disks with its diameter at constant thickness of 35 nm. It looks that saturation field ($H_{S\text{-}ip}$) strongly depends on the disk diameter, whereas the nucleation field ($H_{N\text{-}ip}$) seems remains almost constant within the error. Figure 1.10 (b) shows the analytical and simulated evolution of switching field with aspect ratio ($\beta = t/d$) for an isolated circular dot with variable dimeter at fixed thickness 30 nm. It is clear that nucleation field increases with increase in aspect ratio which in contrast of annihilation field [39]. Gao et al. [44] have studied the orientation dependent hysteresis loops and switching fields of single ellipsoidal NPs with length and width of 140 nm and 90 nm, respectively. Figure 1.10(c) shows the hysteresis loop at different angle 0^0, 30^0, 45^0, 75^0, and 90^0. The obtained hysteresis loops of the ellipsoidal NPs are different at different orientation which is possibly due to the evolution anisotropic magnetization and existence of different spin-configuration influences by the tilt particles. In addition, the switching field for the same particles is extracted from the obtained hysteresis loop and plotted as a function of angle as shown in Figure 1.10 (d). It is noticed that the switching field is significantly influenced by the orientation of the ellipsoidal NPs which first decreases until 45^0 giving a minimum switching field of 400 Oe and then increases until 90^0. Thus, these discussions over different shapes, size, orientation and switching field effect on magnetization behaviors have provided an overview of magnetic reversal and switching dynamics of the vortex NPs.

1.13.1 Effect of the Size, Shape and Orientation

Cowburn and co-workers have investigated the different magnetization dynamics varying the size of permalloy disk[36]. Figure 1.11 (a) shows the experimentally measured hysteresis loops of varying diameter and thickness of the permalloy disks at different magnetic field. The magnetic field was applied in the plane of the disks in the easy axis direction. Figure 1.11 (a) shows the non-coherent hysteresis loss having switching field (nucleation field) nearly 250 Oe. Once the applied field started to decreases/increases from saturation (positive/negative), the disks magnetization remains constant until a switching field (annihilation field) close to zero from which single domain state switch towards vortex state and hence lost all the magnetization.

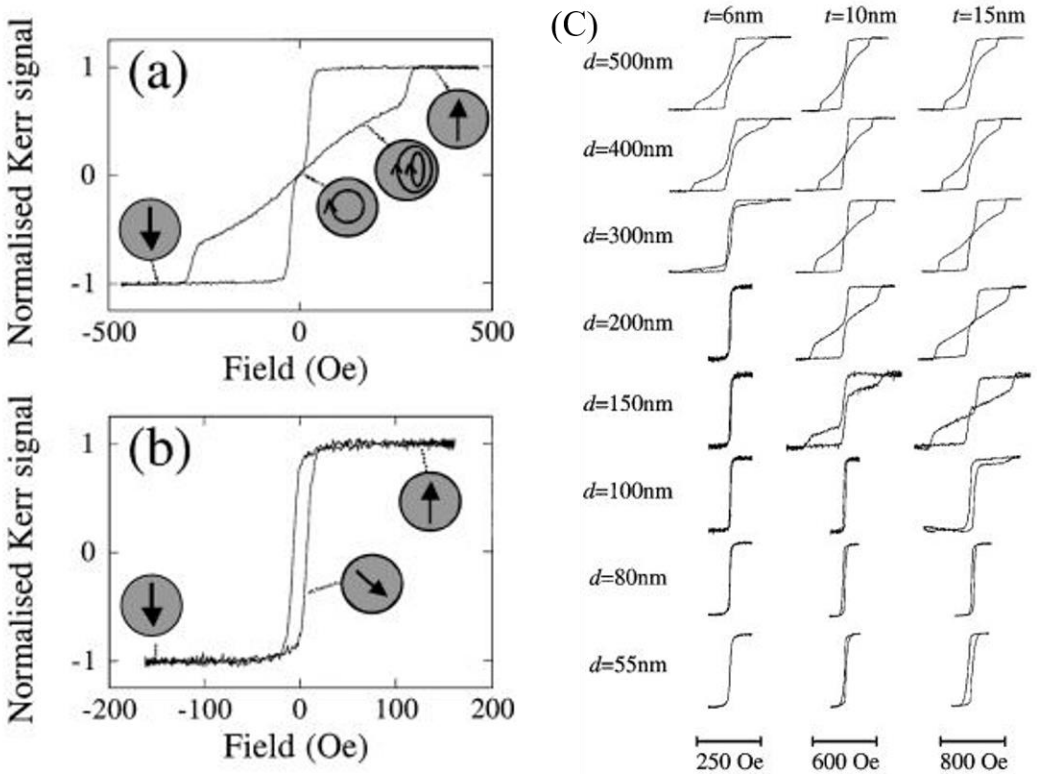

Figure 1.11: MH Hysteresis loops measured from disks of diameter d and thickness t at different magnetic fields. (a) d=300 nm, t =10 nm and (b) d =100 nm, t=10 nm represent the hysteresis loop with schematic spin configurations. (c) Hysteresis loops measured varying diameter d and thickness t of disks[36].

The complete loss of magnetization close to zero field is a key evidence of the formation of a flux-closure-configuration. In such disks system, vortex core formation is a complex field induced structural phenomenon that induces the out-of-plane magnetization. The vortex state can be annihilated by applying the high magnetic field that reinforces the vortex core towards the edge from center of disks and becomes unstable and eventually annihilated leaving single-domain state

as a final spin configuration state. Figure 1.11 (b) shows the hysteresis loop when field applied in direction of easy axis. It seems that the magnetization retains a high remanence nearly 80% and switch at a very low field of 5 Oe which is a behavior of single-domain particles. Further, it was observed zero magnetic remanence when the field was applied parallel to the hard axis instead of the easy axis which reports the effect of field direction on magnetization. Figure 1.11 (c) shows the magnetization reversal hysteresis loop varying the diameter and thickness at different external magnetic field which gives clear visualization regarding the size/shape and field effect on magnetization reversal loop and switching dynamics.

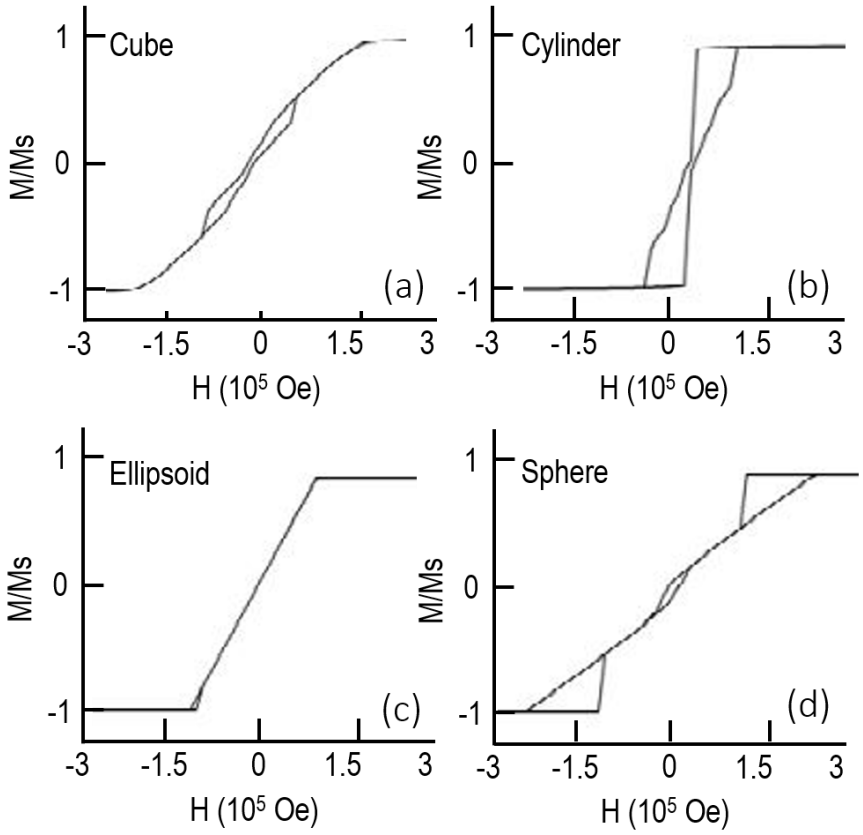

Figure 1.12: MH hysteresis loops for permalloy NPs of different shapes in the application of external field along the easy-axis [128]. (a) cube with size, l = 85.6 nm; (b) cylinder with size, l = 100 nm, w = 20 nm; (c) ellipsoid with size, l = 100 nm, w = 38 nm; (d) sphere with size, d = 53 nm.

Recently, Dimian Mihai and co-workers [128] studied on how NPs of various shapes and orientation affects their MH loop in an external magnetic field. and the how magnetization vortices are formed and propagated in NPs. Figure 1.12 shows the effect of nanoparticle shape on magnetization hysteresis loop for the four different shapes such as cube, cylinder, ellipsoid, and sphere in the

application of external magnetic field from 100 kA/m to -100 kA/m in steps of 1 kA/m on the easy-axis. The comparative study concluded that the cylinder exhibits larger hysteresis loop area indicating the most efficient shape, among four, to use in the hysteresis loop based application. The larger hysteresis loop in cylinder is might be due to the strong contribution of shape anisotropy.

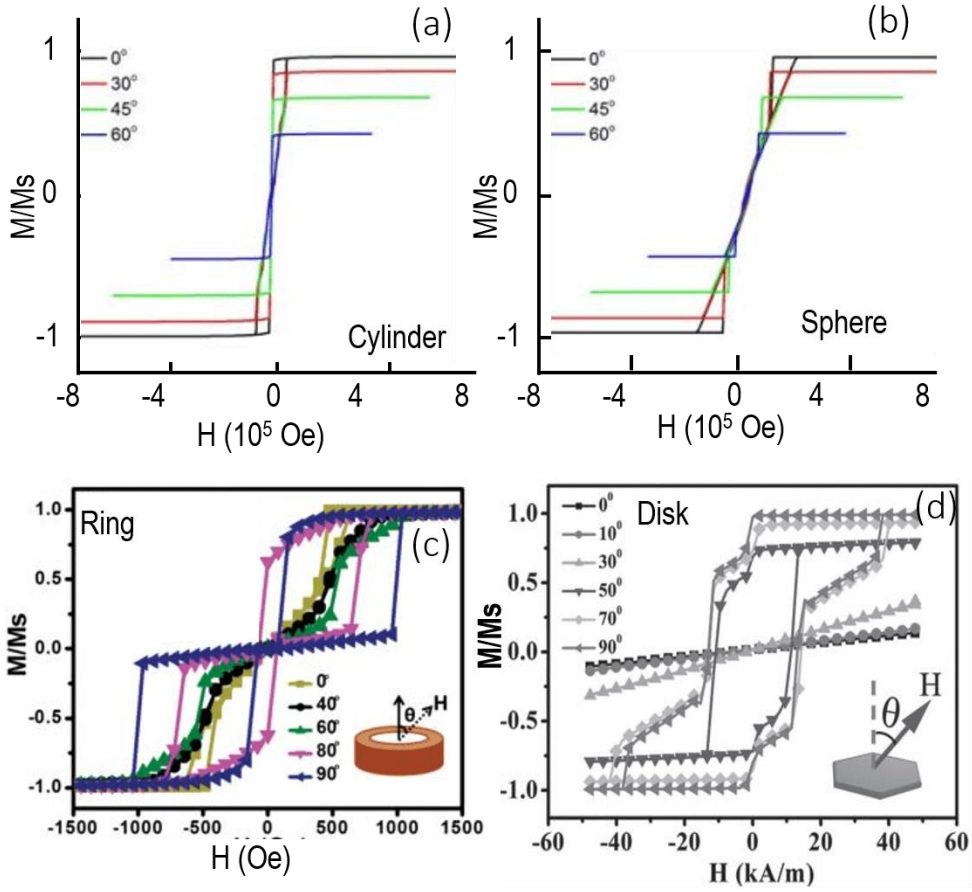

Figure 1.13: Simulated angle-dependent hysteresis loop in different shape NPs. (a-b) x-component hysteresis loops for different angles of the external applied field [128]; (c-d) net hysteresis loops along different angle [41,42].

The angle-mediated hysteresis loop in the application of magnetic field was first observed by Stoner and Wohlfarth (SW) model considering an impracticable constrain, i.e., the coherent motion of the particle magnetization during the reversal process [129]. When this SW model is applied to compute the MH hysteresis loop at different angles of the applied field, the hysteresis loop was evolved being narrowing with increase in angle between the direction of applied field and the easy-axis which completely disappears at 90^0. However, the non-coherent mechanisms of

magnetization reversal are considered, the different scenario of hysteresis loop are observed with lower coercive fields, several jumps or multiple loops. Figure 1.13(a-b) show the MH behavior of the x (easy-axis) component of the magnetization at angle 0^0, 30^0, 45^0 and 60^0 for cylindrical and spherical permalloy NPs in the application of magnetic fields. Similarly, Liu et al. and Yang et al. have studied the same angle dependent hysteresis loop in magnetite rings and disks, as shown in Figure 1.13(c-d) where it is clearly seen that the significant effect of orientation of the NPs on hysteresis loop and its obvious impact on desire hysteresis based application, for instances data storage and magnetic hyperthermia etc. In addition, these all the magnetic reversal loops shown in Figures clearly provide the effect of shape, size, and orientation on switching field of NPs along with magnetization dynamics.

1.14 Aim of the Present Work and Thesis Outline

Iron oxides NPs specifically magnetite (Fe_3O_4) and maghemite (γ-Fe_2O_3) are widely accepted as a most biocompatible magnetic materials in biomedical applications over other free metallic iron and ferrites such as nickel or cobalt analogues. As discussed before, the advantages of magnetic vortex configuration in NPs over superparamagnetic ones, this thesis is primarily devoted to the control synthesis of iron oxide NPs maintaining the vortex-spin-configuration. Secondly, it provides in-depth knowledge and analysis of characterization and possibility of potential use in magnetic fluid hyperthermia and magneto-transducers properties in cancer treatments. Overall, this thesis deals with iron oxide vortex NPs of diverse morphology viz., nanorods (NRs), nanospheres (NSs), ellipsoid, and hollow NTs and investigates their in-depth physio-chemical properties to utilize them in thermal therapeutic applications. The main objective of the thesis is summarized below:

- Control synthesis of iron oxide nanodisks, nanorods, nanospheres, and nanotubes via microwave-assisted hydrothermal route.
- To investigate the effect of precursors, volume of solvent (water), formation mechanism of different shapes of α-Fe_2O_3 and their controlled transformation into corresponding Fe/Fe_3O_4, Fe_3O_4, and Fe_3O_4-γ-Fe_2O_3 NPs
- Role of shape/size, temperature, time, rate of flow of gas (H_2 + Ar in the present work) on the reduction mechanism of α-Fe_2O_3 onto iron oxide (Fe/Fe_3O_4, Fe_3O_4, and Fe_3O_4-γ-Fe_2O_3) NPs.
- To envisage the magnetic vortex-spin-configuration in the synthesized NPs of diverse shape.

- To explore the shape-and size-dependent magnetic properties and their corresponding their utilization in thermal therapeutics applications.
- To scrutinize the effect of stoichiometry, orientation, and anisotropy of NPs on enhancement of magnetic fluid hyperthermia properties.
- In-vitro and in-vivo biological test in different cell lines to investigate the cell viability and the inflammation response.

Keeping the above objectives in mind, several morphologies based iron oxide NPs were synthesized and their in-depth physio-chemical properties and magnetic fluid hyperthermia and magneto-transducers properties were explored for thermal therapeutics applications.

- **Chapter 2** provides the synthesis protocols including the necessary experimental and theoretical background for the characterization of the iron oxide NPs.
- **Chapter 3** studies the mechanistic insight of PO_4^{3-} anions in shape-controlled synthesis of iron oxide from micro-scale to nanoscale particles, their phase composition and the origin of Verwey transition.
- **Chapter 4** investigates the vortex-spin-configuration in non-stoichiometric Fe_3O_4 nanospheres by means of theoretical, experimental and micromagnetic simulations.
- **Chapter 5** presents the enhancement of magnetic fluid hyperthermia properties caused by stoichiometry, orientation and switching field of Fe_3O_4 iron oxide vortex nanodisks.
- **Chapter 6** discusses the design of iron oxide hollow NPs and the role of shape anisotropy contribution in the enhancement of magnetic fluid hyperthermia response and in vitro cell viability and in-vivo inflammation test.
- **Chapter 7** depicts the theoretical analysis on evolution of magnetic energy, ground state stabilization, and mechanotransduction properties of Fe_3O_4 vortex nanorings and nanodiscs.
- **Chapter 8** summarizes the overall conclusions of the thesis and the future research directions.
- **Chapters 9** includes bibliography

Chapter 2

Microwave-Assisted Hydrothermal Synthesis and Experimental/Theoretical Background

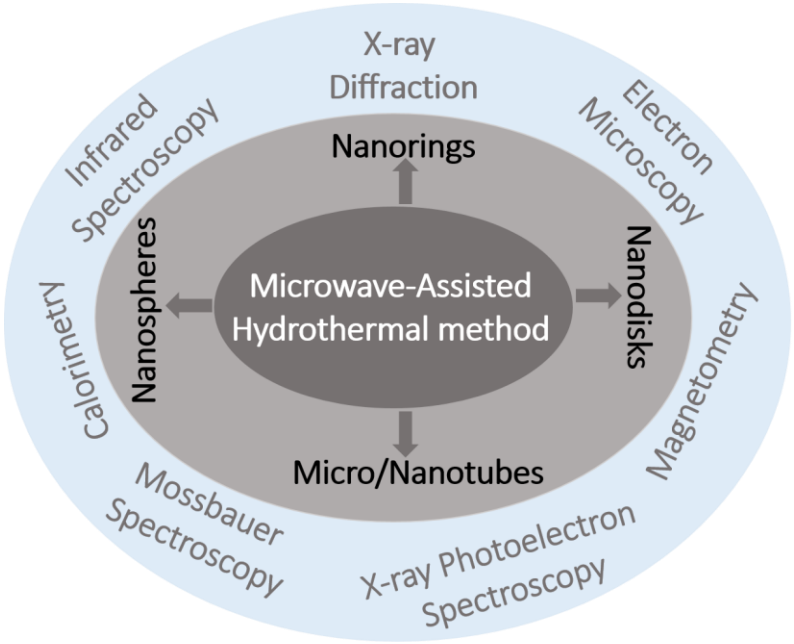

The understanding of the synthesis route, the formation mechanism and characterizations of as-obtained materials is essential prior to any application. This chapter first provides a complete overview of a microwave-assisted hydrothermal route and importance of surface modifications of the NPs for biological applications. In the second part, the working principle and all the necessary background of all the characterization techniques such as X-ray diffraction (XRD), electron microscopy, Fourier Transform Infrared Spectroscopy (FTIR), X-ray photoelectron spectroscopy (XPS), Magnetometry, Mössbauer Spectroscopy, and calorimetry method for magnetic fluid hyperthermia are discussed.

2.1 Microwave Assisted Hydrothermal Synthesis

Over two decades, large number of breakthrough are reported following the emergence of NPs in physical/natural sciences and engineering; specially their magnetic, electronic, optical and mechanical properties depending upon the shape and size. The optimization of size of NPs from microscale to nanoscale lead to reproduce NPs with great changes attaining new perspectives in their physio-chemical properties and allows them to test in different applications from industrial to biomedical nanotechnology [130,131]. The design of such NPs with diverse shape and size for the particular application is rather complex which needs a proper understanding prior to their engineering. Usually, bottom-up approach, also referred liquid phase synthesis (LPS hereafter) is utilized to synthesize diverse NPs rather than top-down approach. LPS methods have several advantages over other gas-phase and solid-phase synthesis methods, for instance, LPS helps to controlled size and shape of NMs at low temperature within a short time from minutes to hours, reasonably low-cost particularly compared to solid-phase synthesis methods, simple with high mass yield, and surface modifications with functionalization can be achieved in situ, even post-synthesis with respect to the application field. [132–134] Figure 2.1 shows different ways of preparing NPs and prepared [135]. The NPs obtained by LPS methods can be stored for a long time in their original form (either liquid or powder) for further/future use.

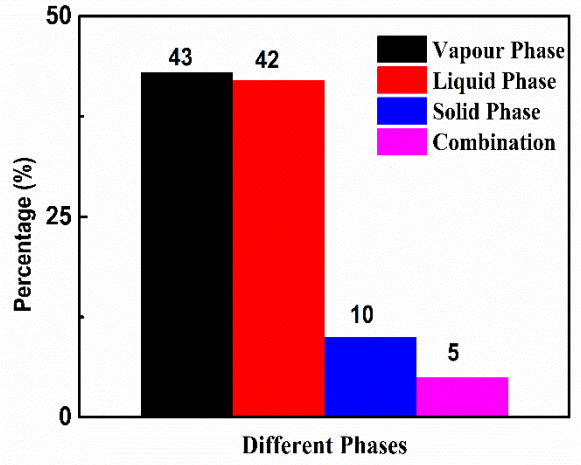

Figure 2.1: Different methods to prepare nanomaterials. (Reprinted with permission from ref. [135]. Copyright 2014 Manufacturing).

In the recent years, researchers/scientists have attracted towards microwave assisted synthesis method (Figure 2.2) and applied it in various laboratory of nanomaterial synthesis [136,137], solid-state chemistry, nanotechnology [138] and organic synthesis [139] etc. for diverse applications. Recent

time has witnessed that the microwave heating technology is emerging as an alternative heat source for rapid volumetric heating with shorter reaction time and higher reaction rate, selectivity, and yield as compared to the conventional heating methods, providing fast chemical reactions and quick materials preparation in a very short span of time, usually in minutes/seconds, instead of hours or even days usually required by the conventional heating methods, leading to relatively low cost, energy saving, and high efficiency for materials production [140–142].

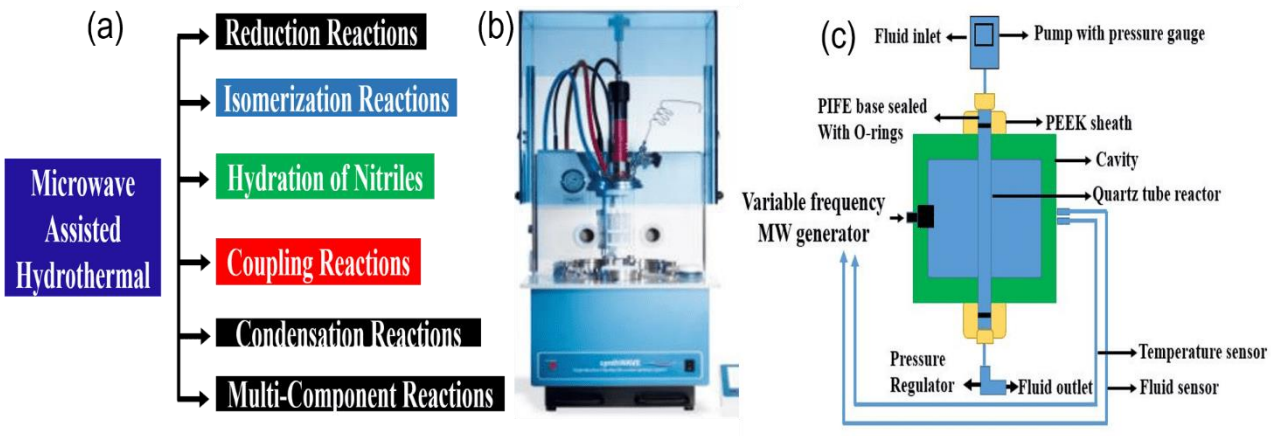

Figure 2.2: a) Application of Microwave-Assisted Method, and (b-c) Experimental setup of the MW-assisted flow reactor system with MW cavity part (Source: Figures (a, c) are self-made; Figure (b) is taken from the instrument available at UFMA).

Beside, having large numbers of advantages of microwave assisted synthesis, the limitation of microwave-assisted synthesis is rapid heating requires a reaction component with a large loss tangent, denoted by tan δ, (such as water, ethylene glycol) than their corresponding reaction media/solvent, phenomena is called selective heating [143]. So it is always beneficial to use those solvent having high microwave absorbing capacity to get high heating rates, water and alcohol for example. Also the poor solubility of organic reactants in aqueous media is another limitation for organic synthesis in water, which usually results in immiscible or biphasic reaction mixtures. However, there were several attempts to overcome this problem by using surfactants, mixing with co-solvents, heating of the reaction mixture, or grinding of reactants. Thus, in spite of those limitations, it has great promise in microwave-assisted organic synthesis (MAOS) and in MW-assisted nanomaterial synthesis [141,144]. Microwave-assisted chemical reactions depend on the ability of the reaction mixture to efficiently absorb MW energy, which often depends on choice of solvents for the reaction. The ability of a specific solvent or material to convert MW energy into

heat is determined by the so-called loss tangent (δ). The concept of dielectric loss tangent was introduced to compare heating efficiencies of microwave in materials with similar characteristics using, which is given by, $\tan \delta = \frac{\varepsilon''}{\varepsilon'}$, where ε'' is the imaginary component of the dielectric and represent the microwave radiation absorption and conversion to heat and ε' is the real component, which signifies the ability of the material to reflect or store an electric field [143,145]. The solvents used in microwave heating can be classified on the basis of their loss tangent (tan δ): high (tan $\delta >$ 0.5), medium (tan $\delta \approx$ 0.1-0.5), and low (tan $\delta <$ 0.1) [142]. The value of the loss tangent (tan δ) according to solvent is different and is given in Table 2.1.

Table 2.1: Loss Tangent (tan δ) Values at 2.45 GHz and 20 °C and Boiling Points of Different Solvents [144]:

Solvent	Boiling Point	Tan δ
Ethylene Glycol	198	1.350
Ethanol	78	0.941
2 - propanol	82	0.799
Methanol	65	0.659
1,2 dichlorobenzene	180.5	0.280
N- methyl 2 pyrrolidone	202	0.275
Acetic acid	118	0.174
N,N-dimethylformamide	153	0.161
1,2-dichloroethane	84	0.127
Water	100	0.123
Chlorobenzene	131	0.101
Acetone	57	0.054
Tetrahydrofuran	66	0.047
Toluene	111	0.040
Hexane	68 – 69	0.020

2.1.1 Microwave Heat Generation and Mechanism

Simply, microwave heating is process of transferring of electromagnetic energy to thermal energy rather than transfer of heat. The basic principles of microwave chemistry have been discussed in several review papers [140,143,145–148]. As an example, Gabriel et al. [148] has provided the theory of the microwave dielectric heating, which consists of two main mechanisms namely dipolar polarization and ionic conduction. Microwaves generally heat any material containing mobile electric charges such as polar molecules or conducting ions in a solvent or in a solid. During the microwave heating, polar molecules such as water molecules strive to orient with the rapidly changing alternating

electric field; thus heat is induced by the rotation, friction, and collision of molecules (known as dipolar polarization mechanism). Ions also move with the oscillating field, colliding and generating heat. These collisions of ions with other species in solution generate much more heat than dipolar polarization. The studies on the mechanisms of microwave heating are even complicated by the fact that the rate enhancements of chemical reactions are dependent on many complex factors. Gedye et al. [149] found the effects of several factors, such as sample volume, solvent, homogeneous and heterogeneous reactions, size of reaction vessel, and power level, on rate enhancements in microwave-assisted organic synthesis. In addition, higher pressure and temperature attained rapidly in MW-assisted processes may help increasing the rate of reactions via enhanced homogeneous mixing of the reactants (in-water) and decreasing the hydrophobic effects (on-water). They proposed that the rate enhancements were caused predominantly by the rapid superheating of the solvent by microwaves. Moreover, they found that the microwave heating rate increased due to presence of ions in the reaction mixture. In addition of these thermal heating effects, de la Hoz et al. [150] added the role of 'non-thermal microwave effects' also called 'specific microwave effects' which arise due to interaction of microwaves with materials in the reaction medium and hence conclude that irradiation on microwave is due to both thermal and non-thermal effects. So it is convoluted to separate discussion in regard of mechanism of heating factor in microwave. The reported "non-thermal microwave effects" include varied activation energy, increased collision efficiency by mutual orientation of polar molecules, and possible excitement of rotational or vibrational transitions [140,150–152]. Single mode microwave reactors, also referred as monomode reactors, having only one reactor vessel can be irradiated, a highly homogenous energy field of high-power intensity is provided, resulting in fast heating rates. [153] . In monomode cavities, only one mode is present, and the electromagnetic radiation is directed into the reaction vessel and creates a standing wave as shown in Figure 2.2 (b). Such microwave reactor was used for continuous flow reactions wherein the power was controlled by a temperature feedback module and resonance frequency auto-tracking function [154,155]. The continuous flow reactor is capable of operating in a genuine high-temperature/high pressure process window (310°C/60 bar) under MW irradiation conditions. The faster heating rate, small reactor volumes, and rapid change in reaction temperature in real time are some of the salient features of this continuous flow MW-assisted organic synthesis (CF-MAOS) system, which aims to be a unique laboratory tool for safe and fast

optimization of reaction conditions. Thus, the fusion of MW and a flow reactor system does offer unique features that can be adapted to organic and inorganic materials syntheses [156].

2.2 Surface Modifications

The surface modifications of MNPs is a crucial in biomedical applications and helps to stabilize and uniform dispersion the NPs onto solution. There are several strategies for the surface modification of NPs. The surface of MNPs can be functionalized by different bioactive substances such as DNA, protein, or antibody to widen their application in biomedical field [157]. Such surface modification of MNPs allows us to improve their stability and dispersion capability in solution and biocompatibility inside the body. The modifying the surface of NPs can be during synthesis (i.e. in-situ modification) and after synthesis (post-synthetic modification). The two routes end-grafting and surface encapsulation are convenient for the proper attachment of biological organic/inorganic ligands/molecules to the surface of MNPs. In end-grafting method, the biological ligands/molecules are attached on the surface of MNPs taking an advantage of capping agents at their one end, whereas surface encapsulation method often polymers having multiple active-agents are clamped on the surface of MNPs leading towards the stable modification. Thus, modifying the surface of NPs lead towards the direct changes to their physical, chemical and biological properties making them very suitable candidates in several interest of bio-applications.

2.3 Experimental /Theoretical Backgrounds

2.3.1 X-ray Diffraction

X-ray Diffraction (XRD) is a non-destructive characterization technique which allows to investigate all the basic information of the materials such as crystal phases, crystal size, phase composition, unit cell lattice parameter, micro-strain, crystallinity, orientation, and defect by performing the experiment at different temperatures. The technique based on Bragg's law in which the crystal diffracted X-rays represents the constructive interference in between the scattered rays come out by the electrons in several atoms from the set of parallel planes inside the crystals (Figure 2.3b). In principle, these constructive interference appears in the diffracted beam once a monochromatic X-ray beam strikes on the sample. According to Bragg's law, this is possible when the X-rays path difference is an integral multiple of wavelength ($n\lambda$) which must be equal to the $2d_{hkl}\sin\theta_{hkl}$, i.e.,

$$n\lambda = 2d_{hkl}\sin\theta_{hkl} \quad (2.1)$$

where n is an integer, λ is the wavelength, d_{hkl} is the inter-planer spacing in between two consecutive planes where hkl represents the Miller indices, and θ_{hkl} is the Bragg's angle of incidence [158]. Basically, the experimental setup of an X-ray diffractometer consists of an X-ray source, a goniometer to measure the angle, sample holder and an X-ray detector, for examples photographic film. The X-ray tubes are usually employed to generate X-rays by bombarding a metal target with high energy (approximately 10-100 keV) electrons which release the core electrons. There are two common targets such as Mo and Cu which have strong K_α X-ray emissions at 0.71073 and 1.5418 Å, respectively.

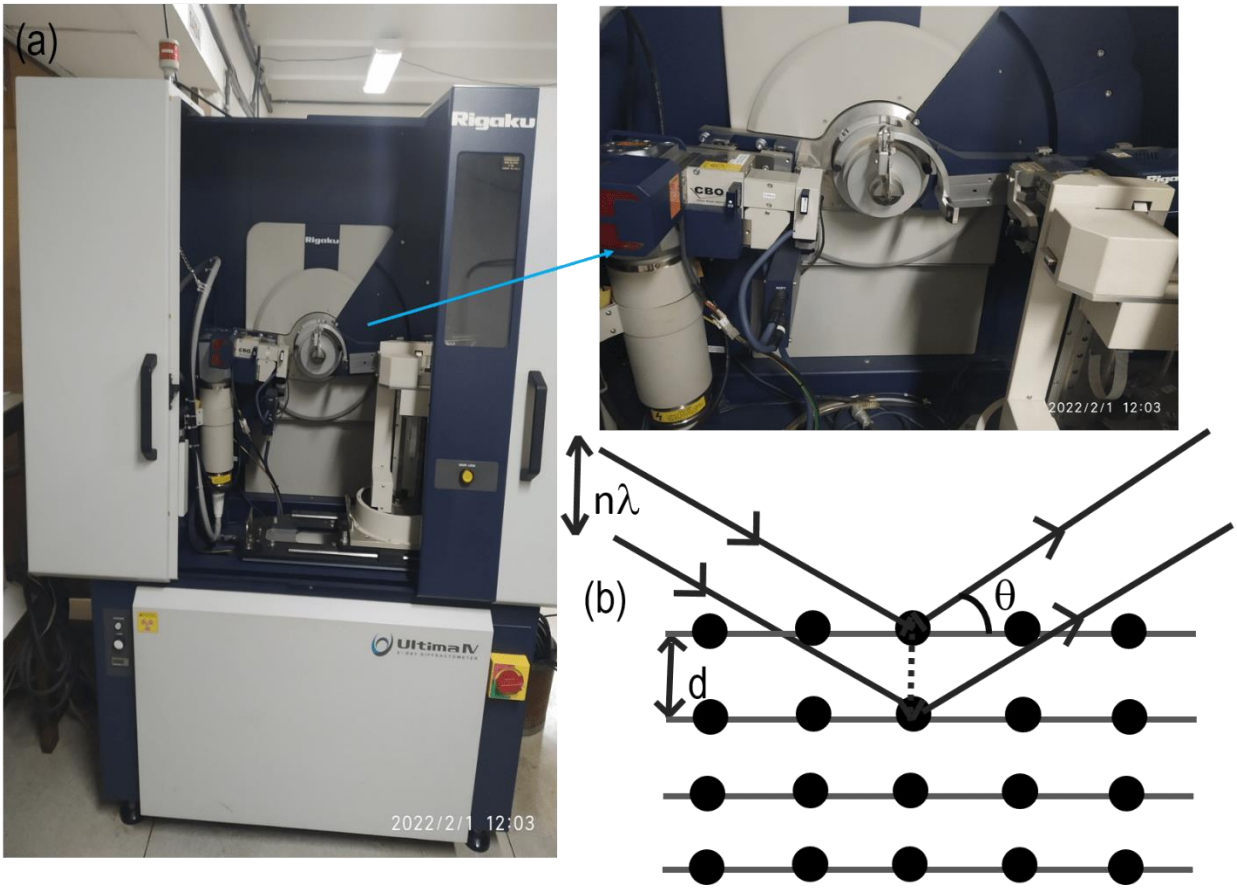

Figure 2.3: (a) Rigaku Ultima IV X-ray Diffractometer; magnification image shows the Goniometer and (b) Schematic diagram of X-ray diffraction from atoms in the crystal. Source: Figure (b) is self-made).

In the present work, we used X-ray diffractometer (XRD) (Bruker, model D8 Advance) equipped with Cu K_α radiation (λ = 1.5418 Å) to assess the crystal structure and phases, in the 2θ range of

15^{o}-85^{o} with an angular step of 0.05^{0} per second. Once the experimental patterns of the sample were recorded, we compared as-recorded patterns with a Joint Committee on Powder Diffraction Spectra (JCPDS) from international center for Diffraction Data (ICDD) to detect crystalline phases based on the relative intensities of the diffraction peaks. In addition, the XRD patterns were analyzed by Rietveld refinement method using GSAS (General Structure Analysis System) software within the EXPGUI Interface and TOPAS [159,160].

2.3.2 Microscopy Imaging

2.3.2.1 Electron Microscopy (Scanning & Transmission)

Scanning electron microscopy (SEM) is a robust imaging technique which mainly scans the material surface through electron beam and provides the images containing various information such as shape/morphology including grain size, their shape distribution, structural defects, surface textures, porosity and secondary phases of particles in the samples from nanometer to micrometer scale. When an extremely fine electron beams with an energy range between eV to 30 KeV strikes on the sample inside the vacuum of SEM, three types of electronic signals such as primary backscattered electrons (possess energy nearly equal to the incident electron beam), secondary emission electrons (possess energy less than 50 eV via inelastic collision between sample and incident beam), and X-rays (Auger electron via de-excitation of atoms) are produced from the surface of samples. Among these three electronic signals, secondary electrons (SE) provides the most important imaging data mapping their emission as a function of spatial position allowing the display of sample topography. It is known that energy of electron beams is greater than the energy of sample electron which restricts the emission of all kinetic energy of beam into secondary electron; thus, small amount of kinetic energy transferred into the secondary electrons after their collision. The total number of such emitted secondary electrons depends on the angle of incidence between the sample surface and the electron beam. The emitted electrons are counted by a detector and immediately sends the signals to an amplifier. Likewise, Backscattered electrons (BSEs) maps their emission as a function of spatial position and the total number of emitted BSEs directly depends on the atomic number (Z) of the element contained by the sample. It means that, in principle, BSEs images helps to investigate the chemical composition of the sample. However, it is hardly possible to record the BSEs images and hence figure-out the elemental-composition of the sample. Thus, it is advocated to incorporate BSEs images with energy dispersive X-ray

spectroscopy (EDS) to identify the chemical composition and their distribution in the sample; whereas, the compositional fraction also depends on the thickness of the NPs. Precisely, X-rays induced by the SEM is just to characterize the elemental composition rather than anything else for example topography. In EDS technique, the distribution of the X-ray energies measured by the detector is a main tool for the identification and quantification of elemental composition. The distribution of the elements contained by the sample can be recorded once the X-rays data are mapped as a function of spatial position. Similar to every instrument, EDS has its own detection limit as it is on the order of 0.5% by weight within the volume of X-ray generation [161–164]. The complete instrumentation and its schematic diagram is given is Figure 2.4.

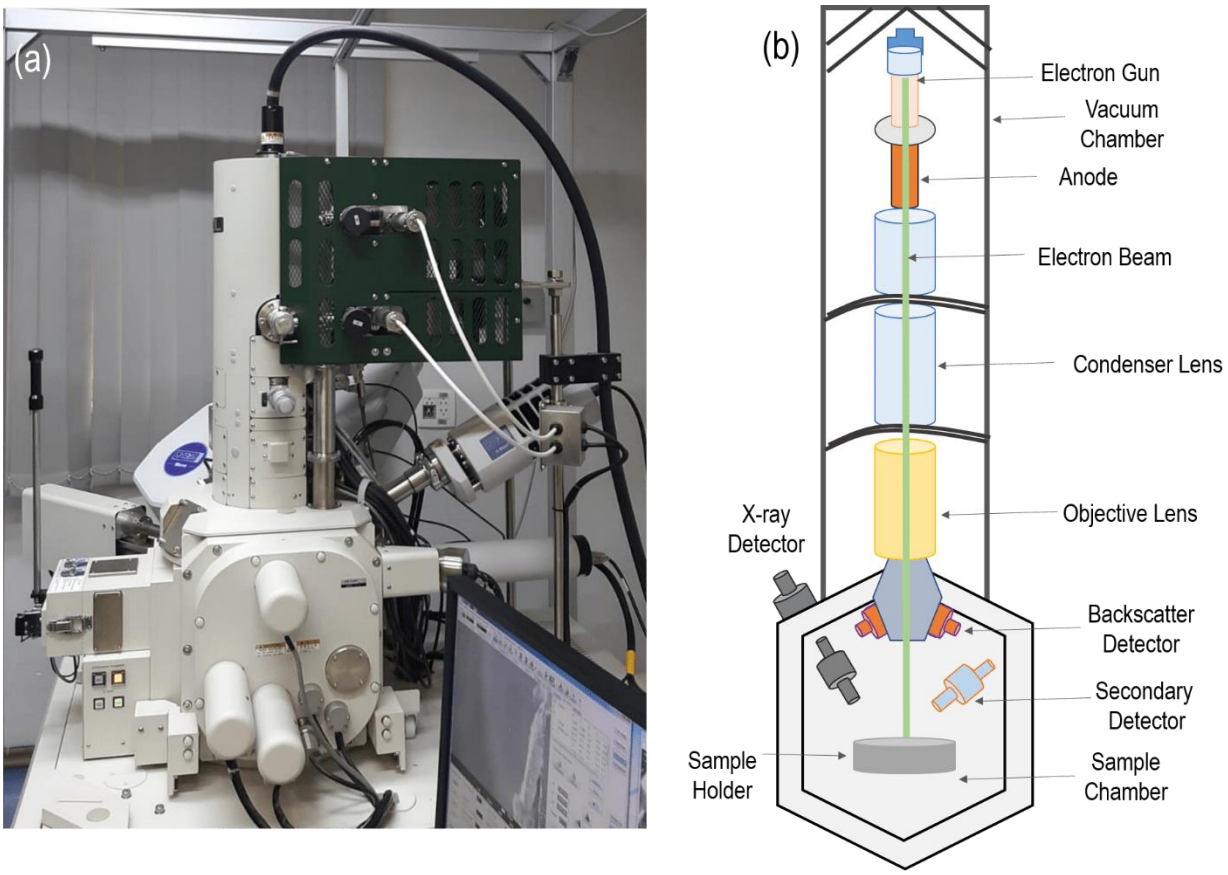

Figure 2.4: (a) JEOL 7100FT field emission scanning electron microscope and (b) schematic diagram of same instrument with internal setup and their name. Figure (b) is self-made.

Transmission Electron Microscopy (TEM) is a strong imaging technique which allows to accumulate the structural, physical and chemical information of materials such as shape/morphology, size distribution, crystal structure and growth direction, strain, different layer of the materials (for example core-shell), crystalline defects (dislocations/twining's), and

phases/chemical information etc. at very high spatial resolution down to an atomic level. All the information is recorded in the form image once the electrons are interacted with the samples; however, only specific technique allows you to corresponding information. For example, selected-area electron diffraction (SAED) provides the information about crystal structures, growth direction, and the crystallinity whereas dark field transmission electron microscopy (DFTEM) helps to find out the size distribution and crystalline defects. There are three types of interaction of electron beam namely transmitted beam (unscattered electron), diffracted beam (elastically scattered beam; for example, high angle annually dark field (HAADF)), and inelastically scattered beam (for example, it occurs during electron energy loss spectroscopy (EELS)). It's worth to note that in some cases all the scattered electron won't be appeared in the beam due to the density of materials since the scattering of the electron depends on the materials density. The great advantage of this technique is to have an electromagnetic lens which permits the electron beam to be focused in capturing the real-space images of materials at high resolution, and simultaneously record the diffraction information selecting the target area in the images. The sample size (thickness/diameter/width etc.) should be thin enough as possible in order to make sure the transmittance of electron beam through the sample because of the inverse relation of transmitted electron with the thickness of the sample. Fewer the transmission of electron occurs at larger thickness of the sample; poor the imaging brightness will be appeared. The complete imaging process follow a three stages of lenses namely the condenser, the objective, and the projector lenses. At first, the electron beams are emerged by the condenser lenses and the objective lenses are responsible for the focus of these beam on and/or through the sample. Further, the focus beams are amplified to the phosphor screen by the projector lenses and records the images; the amplification of the beams depends on the distance between the sample and the plane of the objective lenses. Following these three lenses, there are three typical parts: (i) gun, (ii) vertical column, and (iii) screen. In brief, gun is placed at the top of microscope that induces the electron beam which subsequently travel through the vacuum inside the vertical column and interacts with the sample and records the first images and finally amplified version display on the screen as a final image. The complete instrumentation and its schematic diagram is given is Figure 2.5.

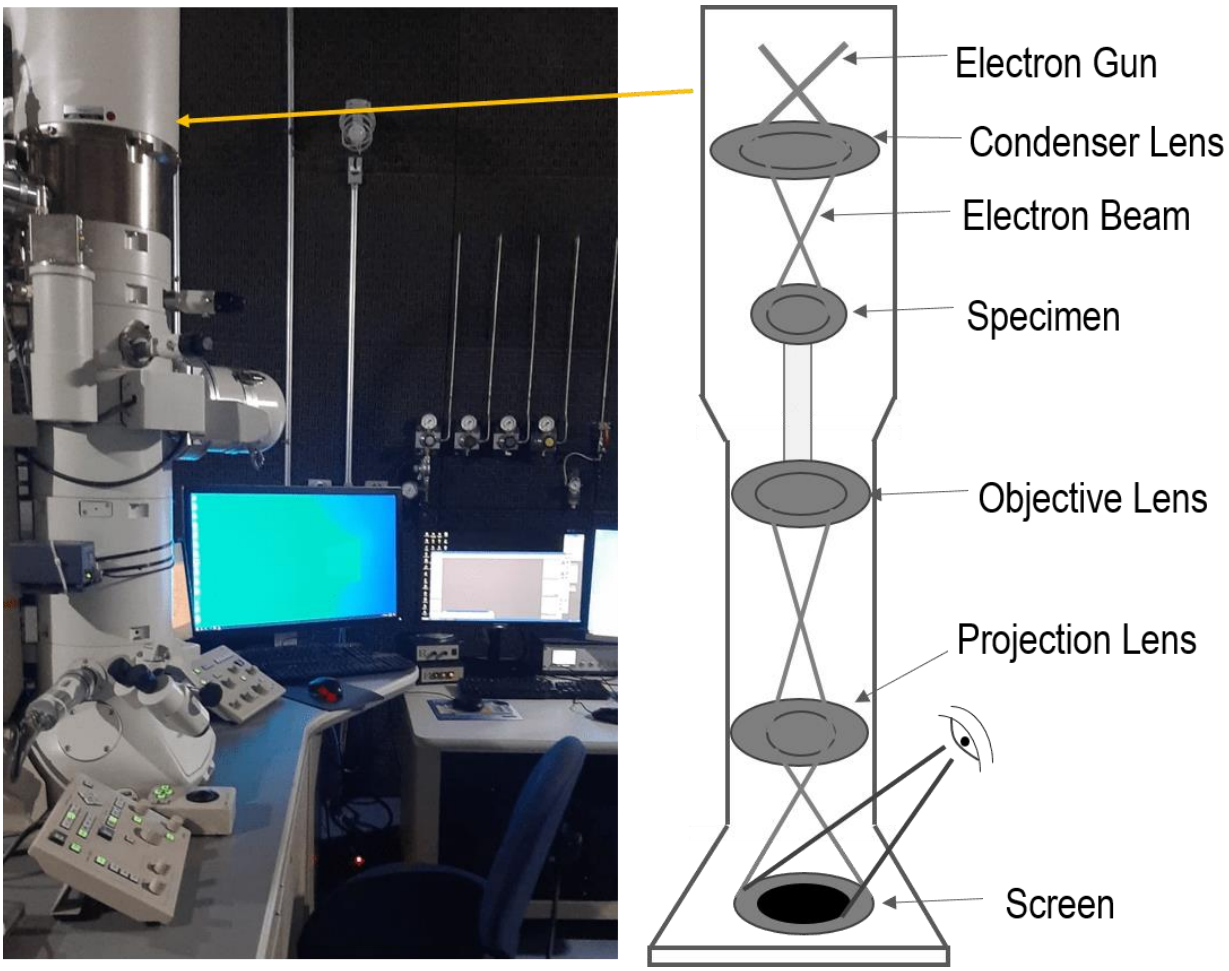

Figure 2.5: (a) JEOL 7100FT transmission electron microscope and (b) schematic diagram of same instrument with internal setup and their name. Figure (b) is self-made.

Electron Holography (EH) in TEM resolves the limitations in the spatial resolution of owing to aberrations of the primary imaging lens of the microscope. In magnetism, the magnetic states of ferro/ferrimagnetic materials are often complex and highly non-uniform and thus are ideally suited to characterization by using EH. Although several variations of electron holography have been developed, the TEM mode of off-axis electron holography (O-EH) for electromagnetic field mapping with high spatial resolution is the most effective and versatile. This off-axis electron holography is capable of providing real-space quantitative measurements of magnetic fields inside and around nanoscale materials with sub-5-nm spatial resolution, both in projection and, when combined with electron tomography, in three dimensions. Off-axis EH is a strong technique for imaging magnetic induction within three-dimensional (3D) nanoscale materials. The technique allows to gather the information's about both the amplitude and the phase of an electron wave to be recorded. When two electron waves, one is the wave that passes through a targeted region on

the sample and another is a reference wave, are overlapped, the O-EH forms an interference pattern or hologram. The phase shift can be retrieved digitally from a recorded off-axis electron hologram and interpreted to provide quantitative information about local variations in the electrostatic potential and magnetic vector potential. It allows to separate out the electrostatic and magnetic contribution to the phase shift in number of ways: (i) by recording the electron holograms before and after turning the sample, (ii) by recording the electron holograms below and above the Curie temperature of the sample, and (iii) by recording the electron holograms at different accelerating voltages. Once the magnetic phase images and induction maps are recorded, the data interpretation becomes a quite complex because of the two-dimensional projections of three-dimensional (3D) magnetic vector fields, insensitive to out-of-plane magnetizations, and integrated results of both inside and outside of the sample [165,166].

In the present study, the samples were investigated by using a JEOL 7100FT field emission scanning electron microscope (FESEM, 1.2 nm resolution, operated at 10–30 kV) available at LABNANO/CBPF. The high-resolution transmission electron microscopy (HRTEM) was performed on a JEOL 2100F instrument using an accelerating voltage of 200 kV.

2.3.3 Fourier Transform Infrared Spectroscopy

Fourier transform infrared spectrometry (FTIR) is a crucial technique to detect the absorption band (measure the radiation intensity as a function of wavenumber/frequency) of organic and inorganic compounds based on their functional group since each functional group has their specific absorption band. The nature of the absorption band provides various chemical information about the samples such as confirmation about the different phases and compositions, number of molecules, and unknown phases, if any, emerged from the mixture along with morphology. when the electron beam of infrared (IR) radiation hits on the samples, so-called irradiation process, the process of IR absorption by the samples and the transmittance through the samples take place simultaneously leading towards the absorption and transmission IR spectra generating own molecular fingerprint of the samples. All wavenumber/frequencies below 1500 cm^{-1} are referred as a characteristic of the ‘fingerprint’ region which extract the information of all the molecule or at least majority of the molecule in the samples considering the vibration modes. The word ‘fingerprint’ widely used in this technique because the resulting IR spectrum is uniquely associated

with the only one molecule likewise the fingerprint is associated with a specific person. Thus, it is rather easy to identify the molecules quickly based on the IR spectrum band. In addition, this technique is very sensitive with a higher precision which allow us to record the more accurate information of the samples [158,167]. The complete instrumentation and its schematic diagram is given is Figure 2.6.

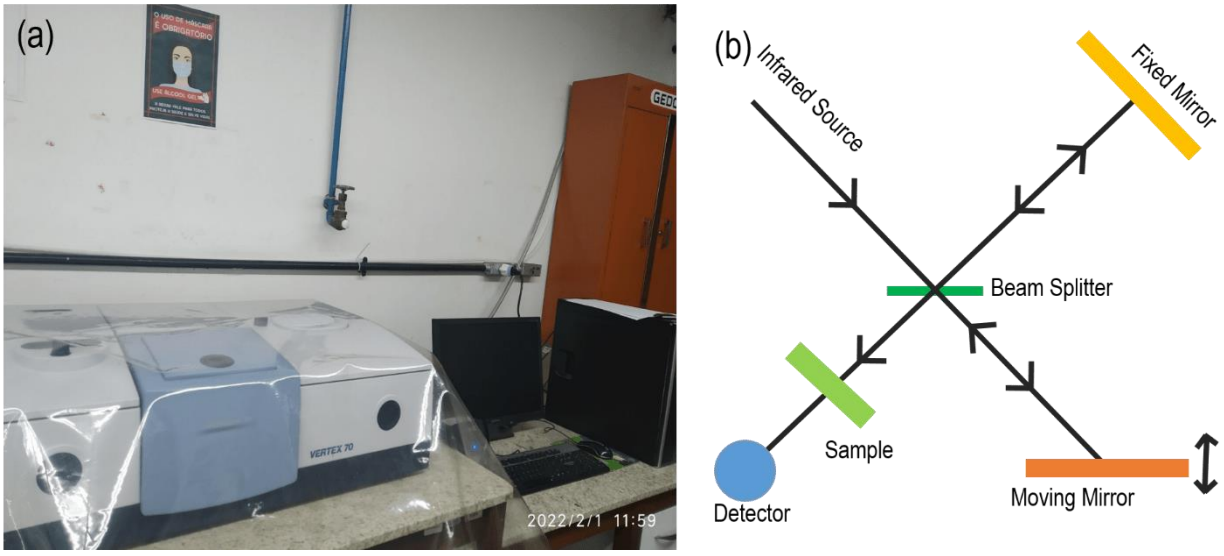

Figure 2.6: (a) Bruker VERTEX 70 FTIR Spectrometer and (b) Schematic diagram of FTIR spectrometer. Figure (b) is self-made.

In the present work, Fourier transform infrared (FTIR) spectrometer (Bruker, model Tensor 27), equipped with attenuated total reflectance (ATR) accessory, was used to identify functional groups present in the NPs within wave number range of 400-4000 cm^{-1}.

2.3.4 X-ray Photoelectron Spectroscopy

X-ray photoelectron spectroscopy (XPS), also called "Electron spectroscopy for Chemical Analysis", is a surface analysis technique which allows to identify the chemical composition of the NPs. For instance, while other experimental techniques are not feasible to detect the magnetite and maghemite phases of iron oxide, XPS can easily identify them based on the additional satellite peaks. It provides the quantitative elemental composition, stoichiometry, electronic/chemical states and examine surface impurities/mixtures of the materials/samples. The sensitivity of this technique is increases with increase in elements atomic number (Z). All the information's are assembled based upon the energy profile of emitted electrons (it measures the intensity as a

function of binding energy) once the X-rays are bombarded on the sample. Usually, two X-rays sources Mg-K_α with energy 1253.6 eV and Al-K_α with energy 1486.6 eV are available and these incident photon energy are sufficient to release the electrons from inner shell to the vacuum. This technique needs ultra-high vacuum environment because of the distance (~1 meter) between electron detector and the materials to be irradiated since the XPS detects only those electrons ejected from the surface of the sample, without losing the energy, to the vacuum. Although the X-rays can penetrate the sample deep inside, it records the information approximately up to 10 nm (let's assume the thickness) from the surface; electrons emitted from the deep inside probably lose the energy [168,169] .

It is well known that the photons are electromagnetic radiation with energy $h\nu$. When the X-ray photon hit the sample, the surface of the sample emits the electrons due to photoelectric effects with kinetic energy E_K. Once the photon energy and the kinetic energy of the emitted electrons are known then binding energy (B.E.) of the electrons can be determined by,

$$E_K = h\nu - B.E. - \phi_S \tag{2.2}$$

where ϕ_S is spectrometer work function which is usually very small as compare to the photon energy, thus can be neglected. Great care has to be taken such as cleanliness of the sample and its storage in glass or in Fluroware containers instead of plastic bags. The limitation is that sample should be in powder and vacuum compatible. In case of liquid sample, it should be dried on substrate used, for example silicon substrate. The complete instrumentation and its schematic diagram is given is Figure 2.7.

In the present study, the surface of powder sample was characterized by using X-ray photoelectron spectroscopy with electron analyzer model PHOIBOS 100/150 manufactured by SPECS co. and was employed X-ray dual gun with energy of 1486.6 eV(Al-Kα radiation) at fixed voltage and current (10 kV and 10.04 mA). The energy step of 0.5 eV binding energy resolution were used for survey and 0.02 eV for high-resolution spectra. Data processing and quantitative analysis of elements were performed using CASA-XPS software. All spectra were calibrated against C1s peak (284.6 eV).

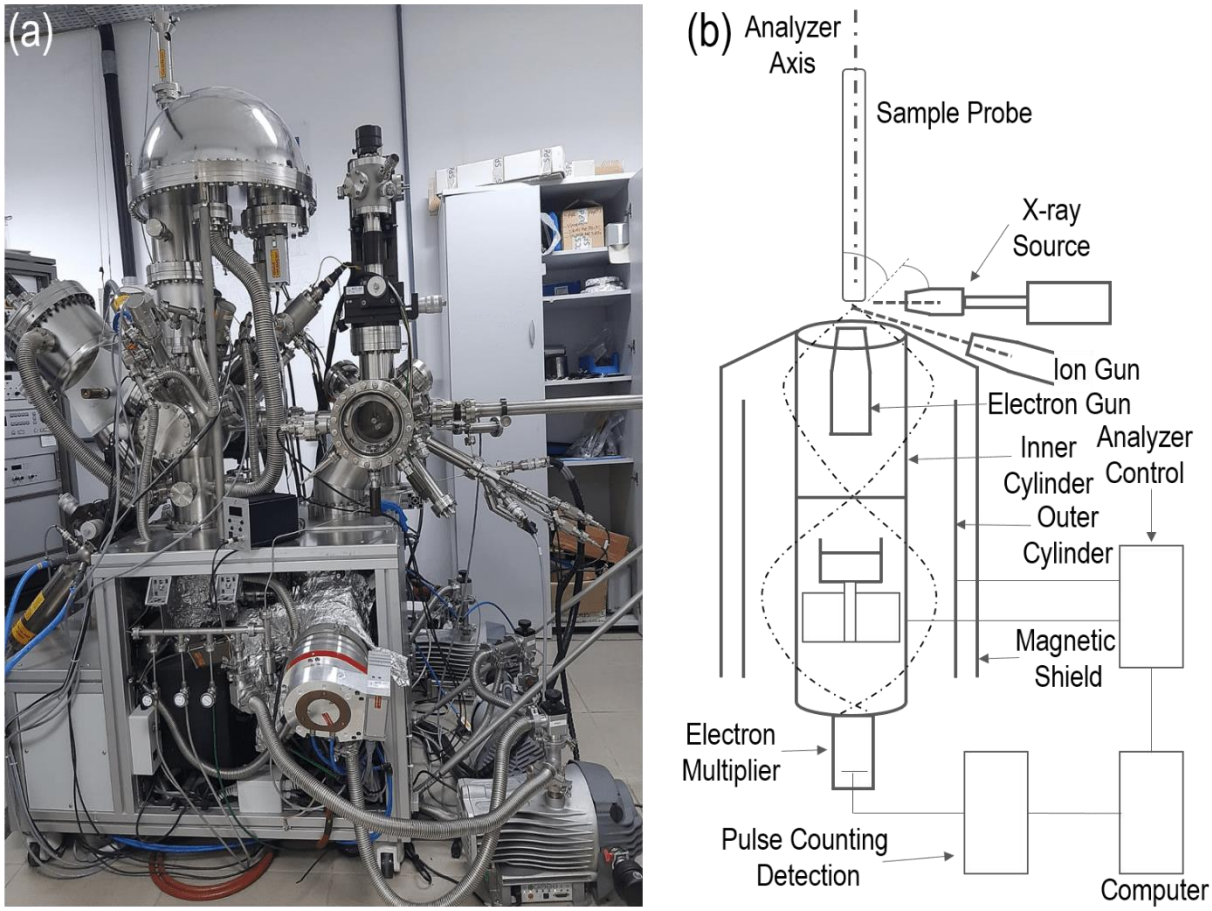

Figure 2.7: (a) X-ray photoelectron spectroscopy with electron analyzer model PHOIBOS 100/150 and (b) schematic diagram with internal setup and their name. Figure (b) is self-made.

2.3.5 Mössbauer Spectroscopy

Mössbauer spectroscopy (MS) is a great analytical technique for the characterization of elements having a Mössbauer-active isotope, for example iron, gold, and etc. It allows to envisage the magnetic and oxidation state along with crystal chemistry of such elements. The Mössbauer spectrum is recorded with only one radiation source (for example, ^{57}Co), at a time for the measurement of one particular type of Mössbauer-active nuclide (i.e., ^{57}Fe); it means radiation source ^{57}Co can be used to record the spectrum of iron (^{57}Fe) containing materials. The recoil-free resonance absorptions and fluorescence of γ-rays based MS records the nuclear energy with a high accuracy at different level allowing to perceive even a very small difference of nuclear energy levels arise due to interactions between the electrons and the nucleus. These physio-chemical

interactions directly affect the electronic, magnetic, geometric, or defect structure as well as in the lattice vibrational properties [170,171]. When a nucleus in an excited state with energy E_e and mean lifetime τ gets transition to the ground state with energy E_g, it emits the $\gamma-$ quantum with energy, $E_\gamma = E_e - E_g$. The emitted $\gamma-$ quantum is expected to be absorbed by a nucleus of same kind in its ground state (low energy state) so that transition to the excited state takes place, called resonance absorption. Subsequently, the nucleus at excited state undergoes transition to the ground state emitting a γ-quantum again, called resonance fluorescence. The resonance width (Γ) is very important, which is calculated by $\tau.\Gamma = h/2\pi$; where h is Planck's constant, and responsible for the resonance absorption since it can be observed only if the emission and absorption lines are properly overlapped. The Mössbauer effect of resonance cannot be observed for freely moving atoms or molecules in gaseous or liquid state due to witness of a recoil effect with energy $E_R = E_\gamma^2/2mc^2$. In the solid state, on the other hand, recoil-free emission and absorption of γ-quanta can be recorded that gives rise to the resonance absorption because of the overlapping unshifted transition lines.

Mössbauer spectra provide quantitative information on 'hyperfine interactions' that are originate by interacting the nucleus with its neighboring electrons. During the hyperfine interaction, the electrons around a nucleus perturb the small energies of nuclear states in the order of 10^{-9} to 10^{-7} eV as compare to the energies of γ-rays (10^5 eV). There are mainly three hyperfine interactions originate from (i) the electron density at the nucleus called 'isomer shift', (ii) the gradient of the electric field, called the nuclear quadrupole splitting, and (iii) the unpaired electron density at the nucleus known as hyperfine magnetic field. With the help of these three hyperfine parameters, MS is able to determine the valence and spin state, to identify the local chemical environments, quantitative phase analyses of the resonant atom, and the concentrations of resonant element in different phases. Figure 2.8 shows a complete overview of instrumentation and different energy level on isomer shift, quadrupole splitting and magnetic splitting.

Isomer Shift: The shifting of peak in Mössbauer spectra is called isomer shift which is a resultant (addition) of two shifting terms, i.e., chemical isomer shift (δ_C) and second-order Doppler shift (δ_{SOD}). The δ_C occurs by shifting of nuclear energy, without splitting of degenerate sublevels of different magnetic spin quantum numbers, caused by the electric monopole interaction between the nucleus and the electrons (s-electron) having nonzero density at the site of the nucleus; this

happens only in case of source and absorber materials are different because of different s-electron densities. As already mentioned above, such peak shift due to difference of source energy and absorber energy at nuclear level can be calculated from overlapped emission and absorption lines since the source and the absorber are moved relative to each other at variable velocities.

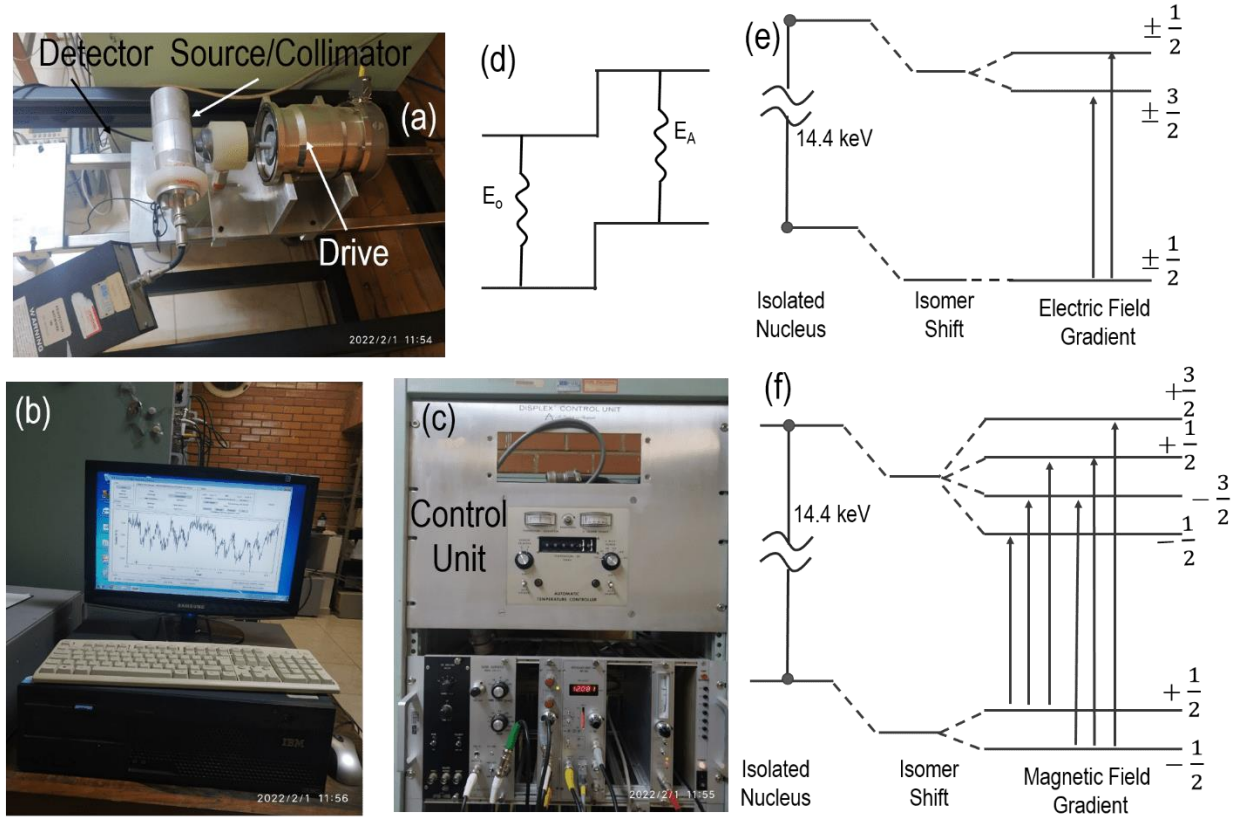

Figure 2.8: A complete overview of Mössbauer spectroscopy. (a) shows the arrangement of source/collimator, detector and Mössbauer drive, (b) computer, (c) control unit for the voltage, noise and signal control, (d-f) schematic images show the energy levels for Isomer Shift (IS), Quadrupole Splitting (QS), and Magnetic Splitting (Δm). In Figure (c) E_o and E_A represent the kinetic energy and absorption energy. Figures (d-f) are self-made.

The temperature-independent δ_C is strongly influenced by the oxidation state and the occupation numbers of electronic orbitals and largely depends on these two factors. On the other hand, the temperature-dependent δ_{SOD} (δ_{SOD} decreases with increase in temperature) depends on the mean square speed of lattice vibrations. Although δ_C is independent to the temperature, the overall isomer shift ($\delta = \delta_C + \delta_{SOD}$) is temperature dependent.

Quadrupole Splitting: The quadrupole splitting (QS) rises from the splitting of nuclear energy level owing to the interaction between the nuclear quadrupole moment (Q) of the ground and/or excited state and an inhomogeneous electric field gradient (EFG) of valance electrons, ligands charge and coordination at the nucleus. Since the Mössbauer atom is itself distorted by the ligand, it's worth to note that the contribution of the ligand field in an enhancement of EFG, the enhanced effect is called "Sternheimer antishielding," by a factor of about 7 for ^{57}Fe. The electric quadrupole moment in the nucleus originates with its asymmetrical shape, where the asymmetry of the nucleus depends on its different spin of a ground state and an excited state. Thus, the QS provides an information regarding the oxidation state, spin state and site symmetry based on electronic structure and lattice surroundings.

Let us take an example of isotope ^{57}Fe which has an excited state with nuclear spin quantum number $I = \frac{3}{2}$; and $I = \frac{1}{2}$ for a ground state. In the presence of EFG, the energy of excited state splits into two levels whereas a ground state energy remains same as a single level since EFG cannot affects the ground state. Then, QS energy level can be determined by,

$$\Delta E_Q = \frac{\pm 1}{4} eQV_{zz}\left(1 + \frac{\eta^2}{3}\right)^{0.5} \quad (2.3)$$

Where, e is charge, $\eta = \frac{V_{xx} - V_{yy}}{V_{zz}} < 1$ is asymmetrical parameter; $V_{xx}, V_{yy}, \text{and } V_{zz}$ are second derivative of electric potential in respective directions.

Magnetic Splitting: The magnetic splitting (Δm) [172] originates from the Zeeman splitting of energy at nuclear state levels with the existence of a nonzero magnetic field (B), the effect is called "nuclear Zeeman effect". The spins of nuclear state are projected at different angle along the magnetic field that induces the magnetic dipole moment (M). These Zeeman splitting occurs when the nuclear magnetic dipole moment (M) interacts with a magnetic field which provides the information about the magnetic properties of the material. For example in the case of iron isotope ^{57}Fe, such interaction between M and B to four substates of the excited state ($I = \pm\frac{3}{2}$) and two of the ground nuclear state ($I = \pm\frac{1}{2}$). Based on the selection rules ($\Delta I = \pm 1, \Delta m_I = 0, \pm 1$), six transition lines are allowed which provide six corresponding magnetically splitted sextet in the Mössbauer at the equidistant between dipole interaction. However, the presence of six peaks are

no longer equidistant because of distortion induces by electric quadrupole interaction in the presence of a relatively strong magnetic field.

The magnetic splitting of energy levels can be obtained by,

$$\Delta E_M = -g_I \mu_N B \Delta m_I \quad (2.4)$$

Where, ΔE_M is magnetic splitting energy (energy shift), g_I is a nuclear factor depends on nuclear spin I, μ_N is nuclear magneton, and m_I is magnetic quantum number.

In the present work, ^{57}Fe Mössbauer spectra were performed in the transmission geometry using a constant acceleration-type spectrometer with a ^{57}Co in Rh source kept at room temperature. The spectrums were fitted by Normos [173] and MosWin 4.0 [174].

2.3.6 Magnetometry

The direct current Superconducting Quantum Interference Device (dc-SQUID) based magnetometry measurement, widely recognized as a dc-measurement, is an indispensable technique to scrutinize the magnetic properties of the materials such as the magnetization, the coercivity and the magnetic remanance, blocking temperature (T_B), Curie temperature (T_B), Morin temperature (T_B) and nature of the materials (SPM/ferromagnetic/paramagnetic etc.). The fundamental working principle of the SQUID is the Josephson junction (JJ), Figure 2.9(a), which can be defined as a couple of semiconductor parted by a very thin insulator from which electrons (and hence the current) could pass through it. The JJ operating system makes SQUID (Figure 2.9 (b-c)) more sensitive measurement where current generation depends on the magnetic flux. SQUID is consisting of two such JJ connected in a parallel mode where each JJ creates a small superconductors loop to attain the superposition thus it allows electron to move simultaneously in more than one direction. The two bias current is need to be applied between superconducting and resistive behaviors with an operational point on the current-voltage curve in which a shunt resistor is responsible to prevent hysteretic behavior [175]. When the bias current is higher than critical current and the external magnetic flux gets coupled into the Josephson loop, voltage drop across the JJ changes in a periodic of the flux quantum (Φ=2h/e; h is Planck's constant and e is electron). This changing voltage is employed to receive a feedback current. Once the application of an external magnetic flux change, the resulting wave function phase also changes enhancing the current through one JJ if a total current is greater than a critical current while reducing the current through the other JJ if total current is smaller than a critical current. This relation in between the

voltage, current and magnetic flux conclusively called current-to-voltage converter and/or flux-to-voltage transducer.

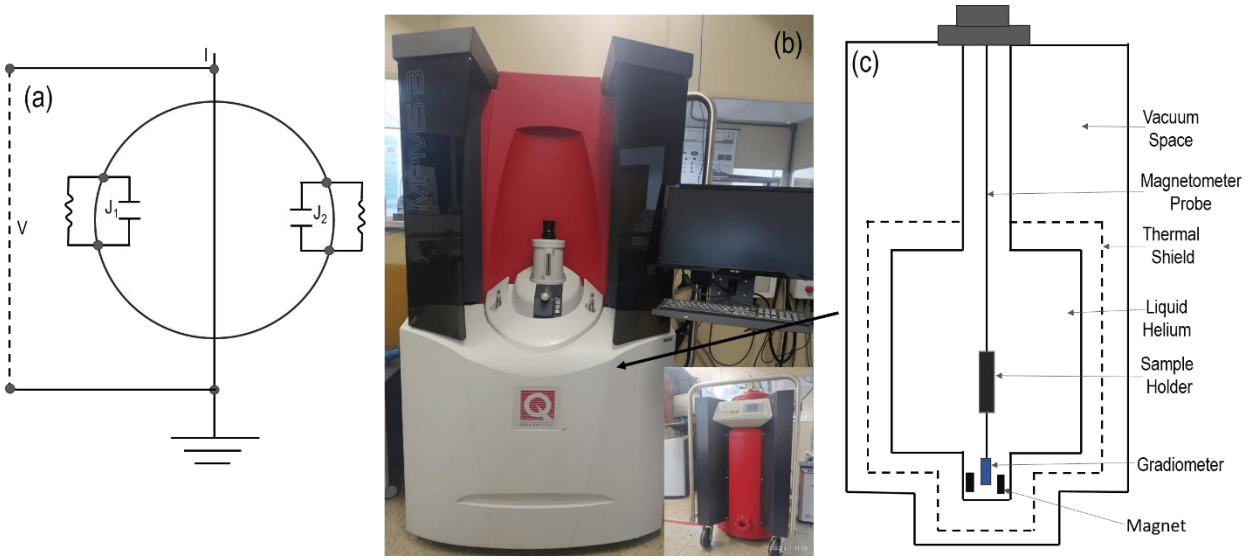

Figure 2.9: (a) Schematic diagram of a dc SQUID superconducting coil with two Josephson junctions, (b) MPMS3 SQUID magnetometer; inset shows the advanced technology liquefier (ATL 160) which used to liquefy the helium gas, and (c) schematic diagram inside the Dewar of magnetometry. Figures (a, c) are self-made.

Thus, the change in a current results the corresponding change in the output voltage which is proportional to the magnetization of the sample. The SQUID need to be set at very low temperatures prior to start the measurement, thus liquid helium and nitrogen seems compulsory to cool the system. The main advantage of the dc SQUID is having a very low noise level in comparison to radio frequency (RF) SQUID.

DC magnetization (hysteresis) measurements were carried out on a vibrating sample magnetometer SQUID (VSM-SQUID) (MPMS Quantum Design) equipped with a superconducting coil that produces magnetic fields up to ±7T at temperatures from 5-300 K and zero-field-cooled (ZFC)/field-cooled (FC) measurements were performed in the temperature range of 5-350 K under an applied field of 50 Oe. The ac hysteresis loops were measured using a homemade AC magnetometer setup at required magnetic field frequency.

2.3.7 Resistivity Measurement

In 1958 L. J. van der Pauw demonstrated that the four probe technique allows to measure the resistivity of NPs/thin films if the samples are thin with uniform thickness without any holes and

contacts are small and on the circumference [176]. Generally, the contacts are very small as compared to the sample size and they occur at the circumference of the material. Particularly, if the sample size is less than about 0.5mm in its largest dimension, some issue on contact size may arises. The pellets of iron oxide NPs are prepared and placed them in oxygen environment at temperature 60 ^{o}C for 24 hours inside the furnace. Once the sample are removed from furnace, copper wire is used to make the contact between NPs and the insulator attached in sample holder as shown in Figure 2.10 (a). In this four probe method, the two contacts are made to pass the current across the NPs and the rest two contacts are made to measure the voltage drop across them. The sample is fixed in the cryostat; the cryostat is joined to a rotary pump to achieve a pressure of 10^{-6} mbar inside the cryostat, and to a sensor of digital thermometer (resistance to temperature detection RTD) near the sample position. A current is applied to the sample by a current source D.C power supply type (Keithley model 6220 precision current source); the voltage drop is measured by a Keithley model 2182A nanovoltmeter. In addition, temperature is recorded by temperature controller (LakeShore DRC-91CA). Further, the voltmeter and ammeter connected to the cryostat through several connection boxes where the instruments are controlled through a LabView program.

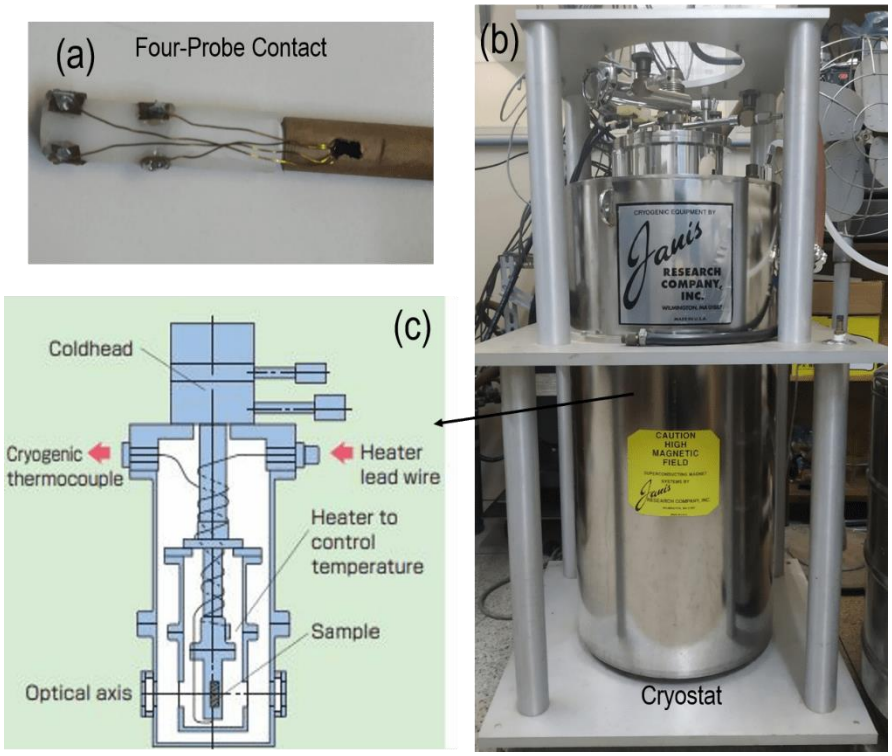

Figure 2.10: (a) Four-Probe contact of NPs, (b) cryostat, and (c) schematic diagram of internal setup and their names. Figures (a, c) are self-made.

A cryostat (Figure 2.10 (b)) is a device which provides an environment of the cryogenic temperature to the samples resided inside it allowing the potential temperature reach up to 77 K. When the sample holder gets mounted and plugged in, the cryostat is sealed and evacuated to pressures on the order of 10^{-6} mbar. The heat radiation shielding is maintained by filling the liquid nitrogen inside shield vessel. Figure 2.10(c) is schematic diagram of internal setup of cryostat.

2.3.8 Calorimetry

Calorimetry is a basic science that measures the amount of heat in the system where the heat generation is directly proportional to the change in temperature, i.e., heat induced by the sample can be quantified theoretically as well as experimentally by means of analyzing the temperature evolution under the specified condition. Here, the specified condition refers the several factors such as nature of the power source, sample geometry, their thermal properties, and accuracy/familiarity of an experimental set-up etc. An adequate experimental set-up is needed for the description of physical system that provides a clear understanding on thermal mechanism letting us to record the temperature. In physics, any resulting phenomena is a consequence of the equilibrium between the physical system and its environment. Likewise, in calorimetry, the change in temperature can be considered as a consequence of the balance between the induced heat and its interchanged with system environment; environment often signifies the entropy, space and time of the system. Based upon such temperature evolution in the physical system, the amount of heat can be determined and same heat in the form of specific absorption rate (SAR) is expected to utilize in killing of cancer tumor directly.

2.3.8.1 Specific Absorption Rate (SAR) and Intrinsic Loss Power (ILP)

The specific absorption rate (SAR), also called specific loss power (SLP), is the rate of power transformed into heat per unit of mass of magnetic NPs. This phenomenon exclusively depends not only on external factors such as the frequency and application of the applied ac magnetic field, but also on the internal parameters of the magnetic NPs, i.e., nature of the materials, size/shape, agglomeration/interaction, concentration and the viscosity of the dispersion medium [86,177,178]. In the clinical practice, the 'SAR' is used to define the transfer of thermal energy into the human body by radio frequency (RF) electromagnetic fields, such as that generated by MRI scanners and ultrasound. In particular, the SAR refers to the power dissipation per gram of living human tissue.

Generally, the amount of heat transfer into human tissue is small as compared to that delivered by the MNPs. As such, the SAR values reported do not reflect the situation one might expect to find in human tissue, where heat dissipation by physiological means, such as increased blood flow, is to be expected. Figure 2.11(a) shows the complete setup of calorimetry-based MFH instruments.
In a general thermal set up of calorimetry for SAR measurement, the sample is initially placed at the same temperature as its environment, usually room temperature, and wait some minutes for the complete temperature stabilization. Set the desire application of frequency and ac magnetic field (AMF). Once the temperature seems stable, the AMF is switch on at initial time; immediately optical Fibre response the magnetic field as temperature start to rise unless the AMF gets switch off. The complete setup and its expected result is shown in Figure 2.11. The SAR value of magnetic NPs in suspension is obtained experimentally using following equation [41,42,177,178],

$$\mathrm{SAR} = \mathrm{C}\frac{\mathrm{M_f}}{\mathrm{m_{mnp}}}\frac{\mathrm{dT}}{\mathrm{dt}}\ \mathrm{W/g} \tag{2.5}$$

where C is the specific heat capacity of the medium, $\mathrm{M_f}$ is the mass of the fluid, $\mathrm{m_{mnp}}$ is the mass of the NPs, and $\frac{\mathrm{dT}}{\mathrm{dt}}$ is the slope obtaining from recorded heating profile; optical Fibre thermometer measures the rise in temperature as a function of time, referred as a 'heating profile' (Figure 2.11 (b)).

The $\frac{\mathrm{dT}}{\mathrm{dt}}$ must be obtained by linear regression at the start of heating, i.e., initial time at which ac field is applied. The main considerable problem with the obtained SAR result is extrinsic one and every experimental has their own equipment specific limitation depending upon the application of magnetic field and frequency. To address this issue, normalization of resulted SAR is very important to compare the thermal efficiency among different samples and conditions. For this, the as-obtained SAR values can be normalized to the intrinsic loss power (ILP), as defining by the equation,

$$\mathrm{ILP} = \frac{\mathrm{SAR}}{\mathrm{fH^2}} \tag{2.6}$$

However, this normalization is valid only frequency up to several MHz and the amplitude of magnetic field below the saturation field of the MNPs [179]. The great advantage of this technique is the relative simplicity of the experimental arrangement. However, the fluctuation in temperature change at unknown degree of uncertainty is a major issue to tackle and still needs a further investigation.

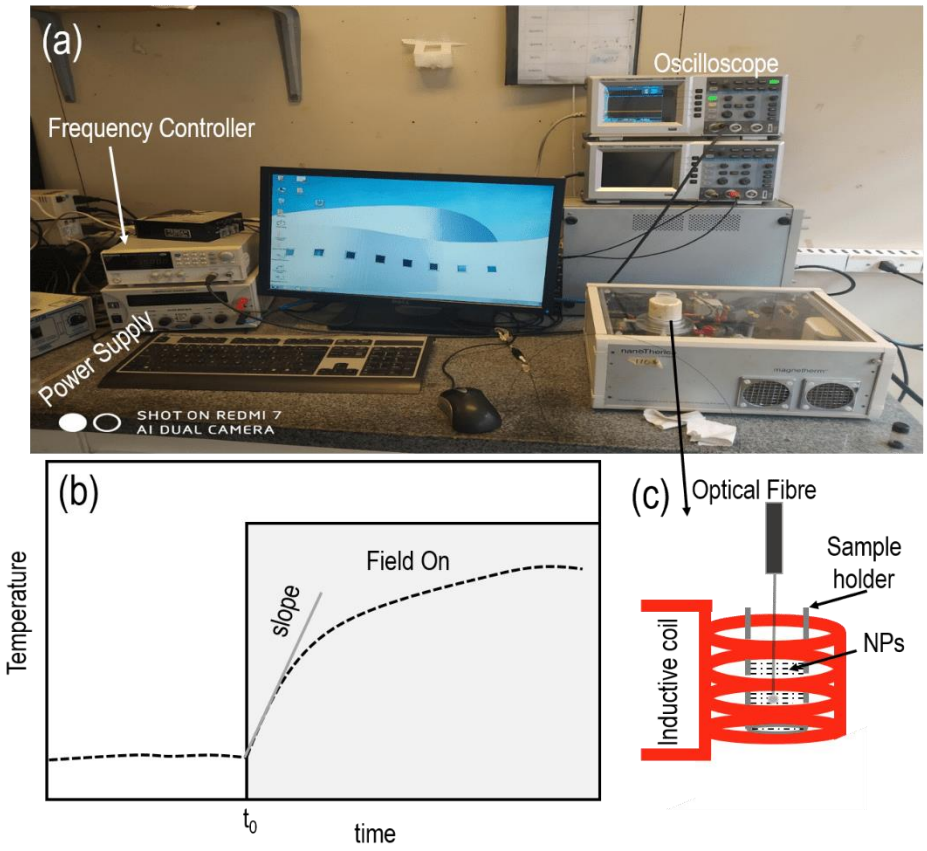

Figure 2.11: A complete experimental set-up of magnetic fluid hyperthermia. (a)Snap picture of MFH setup that we used for our experiment, (b) schematic that shows the nature of heating profile once the magnetic field is applied, (c) magnified view of induction coil where sample is inserted. Figures (b, c) are self-made.

In the present work, the nanotherics MagneTherm^{TM} setup is used measure the magnetic fluid hyperthermia properties of iron oxide NPs in collaboration with the Group of Thermal Nanomedicine, Institute of Physics, Federal University of Goias, Goiania, Brazil. The applied magnetic field range is from 100-450 Oe at a fixed frequency of 107 kHz. The concentration of the solution was used from 1-100 mg/ml; however, we have included the best heating profiles in the present thesis.

Chapter 3

Phosphate Anions-Mediated Shape, Size, Phase Composition, and Stoichiometry of Iron Oxide Nanoparticles

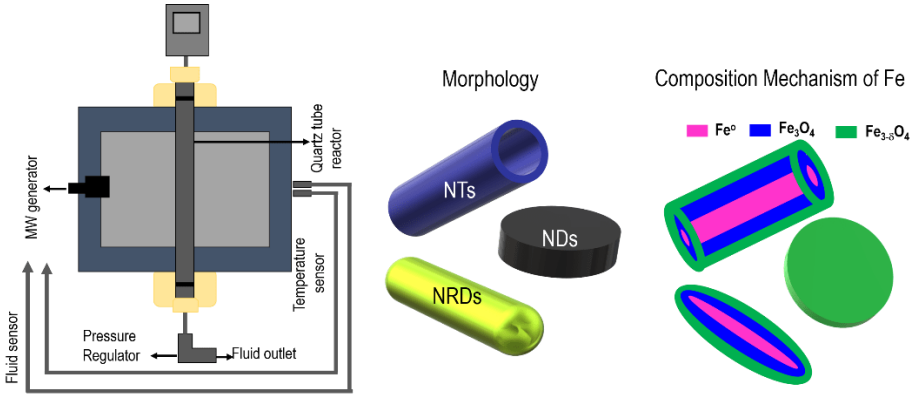

This chapter describes a microwave synthetic approach for the controlled assembly of α-Fe_2O_3 nanosystems with defined morphologies, such as hollow NTs, solid NRDs and NDs. The morphological control is aided during the crystallization processes by using phosphate anion (PO_4^{3-}) anions as key surfactants in solution. Furthermore, the thermal reduction under H_2 atmosphere of α-Fe_2O_3 NTs, NRDs and NDs to the correspondent Fe_3O_4 nanomaterials preserved their initial morphologies. It was observed that the concentration of PO_4^{3-} anions and volume of solvent had significant impact not only on controlling the shapes and sizes, but also phase composition and stoichiometry of the NTs, NRDs and NDs. X-ray Reitveld refinement analysis of the NTs, NRDs and NDs systems, after reduction in H_2, revealed the presence of zero-valent iron (Fe^0) in the final materials, with Fe^0 fractions that decreased gradually in % from NTs (~16 %), NRDs (~11%) to NDs (~ 0%) upon increasing amount of PO_4^{3-} anions. Bulk magnetic susceptibility measurements showed clear alterations of the Verwey transition temperatures (T_V) and the development of unusual magnetic phenomena, such as magnetic vortex states in NDs, which was subsequently verified by micro-magnetic simulations. From the combination of XRD analysis, bulk magnetic susceptibility and Mössbauer results, we provide herein a detailed mechanistic description of the chemical processes that gated the development of shape-controlled synthesis of NTs, NRDs and NDs and give a detailed correlation between specific morphology and magneto-electronic behaviors.

3.1 Introduction

The synthesis and shape-controlled assembly of iron oxide NPs, such as α-Fe_2O_3, Fe_3O_4, and γ-Fe_2O_3, that are arranged into 1-D, 2-D, and 3-D assemblies is an emerging field of research with potential applications that span from biomedicine, magnetic fluids, magnetic recording and spin-controlled electronics.[57,180,181] The nanoparticle's morphology, e.g. hollow NTs, NRDs and NDs, impact severely the magnetic/electronic behavior of these systems; the NPs shape-effect provides in fact a viable route for the generation of systems with well-defined spin-polarized currents, an effect that can be used in nano-electronics [42,56,57,97]. Spin polarized currents induce formation of magnetic vortexes, which are an in-plane circulation of magnetization around a nanometer-scale central core with out-of-plane magnetization pointing either up or down[36]. Magnetic vortex states have shown promising applications in spin based devices such as non-volatile memory[182], logic gates[183], vortex based transistor[184], in biomedicine and cancer treatments [42,43].

Several synthetic strategies have been tested in order to gain access to shape-controlled synthesis of iron oxide NPs. For example, co-precipitation, sol-gel, and the hydrothermal solution-based methods use phosphate and/or sulfate ions as additives during the metal oxide NPs assembly[97,185–187], providing a route to the fair access to 2-D and 3-D organized nanostructures, but at the cost of long reaction times needed for their effective synthesis. In contrast, the microwave assisted hydrothermal (MAH) route offers great advantages compared to conventional hydrothermal synthesis, because it is faster, simpler, and energy efficient due to very high rates of microwave heating.[141,188] To the best our knowledge, there is a very limited number of reports describing the shape/size-controlled synthesis of iron oxide NPs, following the MAH route.

In this chapter, we present the shape-controlled synthesis of α-Fe_2O_3 NTs, NRDs and NDs achieved by the MAH route, using cooperative action of sodium phosphate and sodium sulfate ions. Furthermore, we describe the conversion of these shape-controlled NPs into magnetite (Fe_3O_4) NPs by subsequent reduction processes that were capable to preserve the initial system's morphologies. The FESEM, XRD, FTIR, Mössbauer spectroscopy analysis complemented by bulk magnetic measurements and micro-magnetic simulations are given in detail, validating the potential of the MAH approach towards assembly of carefully engineered magnetic nanostructures with tailored electronic properties.

3.2 Experimental Section: Synthesis of α-Fe_2O_3 and Fe_3O_4 Nanoparticles

The α-Fe_2O_3 NTs, NRDs and NDs were prepared by a MAH reaction of iron chloride ($FeCl_3$) with addition of sodium phosphate (NaH_2PO_4) and sodium sulfate (Na_2SO_4) as additives to control shape and morphology. Briefly, 0.06 mol L^{-1}(~ 370 mg) of $FeCl_3$ with 35 mL of distilled water were stirred for 15-20 minutes. The additives NaH_2PO_4, and Na_2SO_4 mixed with 3 mL of distilled water separately and finally mixed with $FeCl_3$ solution to make mixture of final volume 38 ml; the concentration of NaH_2PO_4 ($2.7x10^{-4}$ mol L^{-1}, $5.4\ x10^{-4}$ mol L^{-1}, $1.94\ x10^{-3}$ mol $L^{-1}$and $4.32\ x10^{-3}$ mol L^{-1}), and Na_2SO_4 .$10H_2O$ ($1.65\ x10^{-3}$ mol L^{-1}). After a vigorous stirring for 10 minutes, the mixture was transferred into a reaction vessel in a Synth's microwave reactor, with an output power of 1000 W. The working cycle of the microwave reactor was set as (i) 20 ^{0}C/ minutes rapid heating until 200 ^{0}C from room temperature, and (ii) 60 minutes at 200 ^{0}C. The system was then allowed to cool down to room temperature, and the final material was centrifuged and washed with excess of distilled water and absolute ethanol and dried in a vacuum oven at 50 °C. In this way, we have obtained ~ 300 mg of α-Fe_2O_3 NPs. Fe_3O_4 NPs were obtained via a reduction process from the prepared α-Fe_2O_3. The dried α-Fe_2O_3 powders were annealed in a tube furnace at 550 °C for 6 hours under a continuous hydrogen/argon gas flow [H_2/ (H_2 + Ar) = 4/100]. The furnace was then cooled down to room temperature while kept under a continuous H_2 gas flow. As compared with the staring materials of α-Fe_2O_3, the size, shape and morphology of Fe_3O_4 nanostructures was well preserved after the reduction process. The samples were designated as FOXX where FO means iron oxide and XX symbolizes ratio of phosphate to sulfate ions. For instance, FO06 means iron oxide NPs with ratio $\frac{PO_4^{3-}}{SO_4^{2-}}$ = 0.06 (ratio was taken after conversion into 'gram' unit). In the present work, the samples were thus designated as FO06 (NTs), FO12 (NRDs), FO44 (mixture of NRDs/NDs) and FO97 (NDs).

3.3 Result and Discussion

3.3.1 Formation Mechanism of α-Fe_2O_3 Nanoparticles

Several studies have shown that concentration of phosphate ion has a significant impact to control the NPs shape, from NTs, NRDs to NDs, whereas the concentration of iron cations in solution is responsible for the final nanoparticle size. Higher the ferric cation concentration, larger becomes the size of the synthesized NPs.[57,189] In addition, sulfate anions allows to control the growth of α-

Fe_2O_3 nanocrystals.[189] Hydrolysis of the metal cation precursor ($FeCl_3$), which involves "coordination-assisted dissolution" and nucleation, is aided by the ligand phosphate and sulfate anions (NaH_2PO_4 and Na_2SO_4). The relative concentration of NaH_2PO_4 and Na_2SO_4 directly influences shape and morphologies of the final NPs, due to the superheating and non-thermal effects induced by the MAH process.[188] Figure 3.1 shows the synthetic steps involved in the formation of α-Fe_2O_3 NTs/NRDs/NDs and their reduction into Fe_3O_4 nanosystem. We suggest that the growth mechanism of NPs is primarily induced by local superheating of the aqueous solution, which leads to the generation of numerous "hot spots" that favor nucleation and larger seeds formation throughout the solution, with rates that depend upon the mutual reactant concentrations [188,190]. For example, by increasing the concentration of phosphate anions, can be obtained NTs, NRDs and NDs of α-Fe_2O_3.

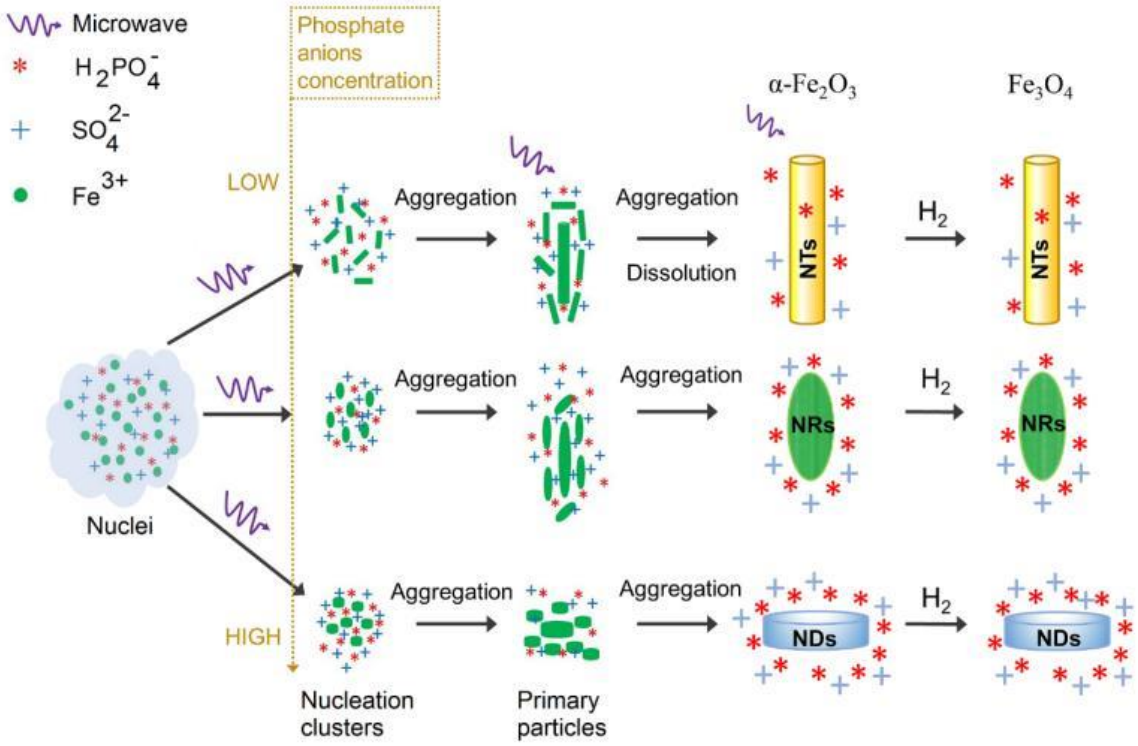

Figure 3.1: The growth process of the diverse iron oxide NPs exhibiting nanotubes, nanorods, nanodisks morphologies (NTs, NRDs, NDs) aided by phosphate and sulfate anions.

The phosphate anions act, mostly, as adsorbent/stabilizers of the α-Fe_2O_3 NPs surfaces. Sulfate anions are responsible for the fast dissolution process of the initial growth seeds and hence, the combined contribution of phosphate and sulfate molecules gate the formation of hollow NPs.[189,191].

At low concentration of phosphate ions, small NPs (β-FeOOH) aggregate into spindle-shaped with phosphate and sulfate ion at the surface (i.e., mostly at the face end of ellipsoidal/spindle-shaped NPs) due to strong interaction between these NPs. These spindle-shaped β-FeOOH phase shifts into the α-Fe_2O_3 NPs phase, preserving the initial morphology, then such α-Fe_2O_3 NPs tend to aggregate but the process is compensated by Ostwald ripening.[192,193] This process can be understood by recollecting that iron oxide NPs have an excellent microwave absorption property that lead to 'hot surfaces' at the two end of spindle α-Fe_2O_3, speeding up the crystal growth and subsequent dissolution. Furthermore, high conductivity and polarization of phosphate ions create localized ionic currents on the "hot surfaces" of hematite nanospindles, giving an additional driving force for the mass transport process.[188,190,191] Lastly, an available phosphate and sulfate ions at the center of end facets start to etch the α-Fe_2O_3 spindle along the [001] direction, leading to formation of the α-Fe_2O_3 NTs, the final product. The etching process was found to be in space non-uniform, from tubes to tubes and even within a single tube. This anisotropic etching process originate from the uncontrolled movement and cooperation between Fe^{3+} ions with phosphate/sulfate ions during microwave irradiation. The growth of α-Fe_2O_3 NPs as seen along different lattice planes indicates that (110) and (100) direction growth faster and preferential dissolution occurs along the (001) plane, because this is the least protected surface plane by phosphate ions, owing to the lack of singly coordinated hydroxyl groups.[191,194] On the other hand, the similar formation steps witnessed for NTs is followed during formation of NRDs and NDs, except for the presence of the etching process through dissolution. The etching process is mainly gated in NRDs and NDs by the increasing concentration of phosphate ion which enhance the negative charge at NPs surfaces, hence is gated by the presence of higher concentration of adsorbed PO_4^{3-}. Therefore, the electrostatic repulsion avoided aggregation of the β-FeOOH NPs and hence they grow separately. When higher concentration of phosphate anions is employed, the individual β-FeOOH NDs decomposed into randomly orientated α-Fe_2O_3 nanocrystallites and they selectively connected to each other on the plane to form nanoplates, which stacked layer-by-layer to form disk structures, as final product. The observed trend, decreasing size of the NPs with increasing concentration of phosphate ion, can be rationalized by the formation in solution of more stable monomers that produces NPs with smaller size. In contrast, lower phosphate concentration forms fewer stable monomers, with small number of nuclei in solution, so that to facilitate the growth of bigger particles. In the present work, the reaction process produced tube-like NPs with

length ~ 2515 nm and rod-like NPs with length of ~2230 nm at high $\frac{Fe^{3+}}{PO_4^{3-}}$ mass ratio whereas disk-shaped NPs with average diameter ~730 nm at a low $\frac{Fe^{3+}}{PO_4^{3-}}$ mass ratio. These morphological structures and reaction mechanism agree with previous literature results, as reported by Wu W. et al.[57] for iron oxide NTs synthesized through hydrothermal route and by Hu et. al.[188] which synthesized NRDs through MAH. However, our NPs are larger in size, which is mainly due to the use of higher concentration (0.126 M > 0.05 M [57]) of Fe^{3+} ion in almost similar volume of solvent.

The comparative study with existing literature, shows that the size of NPs is strongly dependent on the ratio of $\frac{Fe^{3+}}{PO_4^{3-}}$, i.e. higher the ratio, larger will be the size. Nevertheless, this is not the general scenario for every growth mechanism, because it should also depend upon concentration of precursors, amount of surfactant, synthesis temperature and more importantly amount of solvent used. In the present study, with low amount of solvent, the concentration of the growth species in the bulk solution is high, such that the concentrations of growth species at the interface of nuclei and in the bulk solution are kept nearly equal. Under these conditions, the diffusion distance becomes shorter, leading to a higher mass transfer and growth rates and therefore larger NPs are obtained.[195,196]

3.3.2 Structural/morphology Analysis

3.3.2.1 X-ray Diffraction and Microscopy Analysis

XRD and SEM images for α-Fe_2O_3 and its distribution are given in Figures 3.2-3.4. All the diffraction peaks are indexed for α-Fe_2O_3 (space group: R-3c, JCPDS No. 89-0597). Figure 3.5 (a-c) show the FESEM image of FO06(NTs), FO12(NRDs) and FO97(NDs) Fe_3O_4 and their size distribution are given in Figure 3.4. Figure 3.5 (d-e) show the HRTEM images taken for FO06 and FO97, respectively. For FO06, the fringes distance was found to be ~0.254 nm and ~0.212 nm that agree with the Bragg's diffraction (311) and (400) for Fe_3O_4, respectively. Similarly, for FO97, the obtained fringe distances were ~0.254 nm, ~0.251 nm and ~0.197 nm; the first two agrees well with the crystal direction (311) and last one with (400).

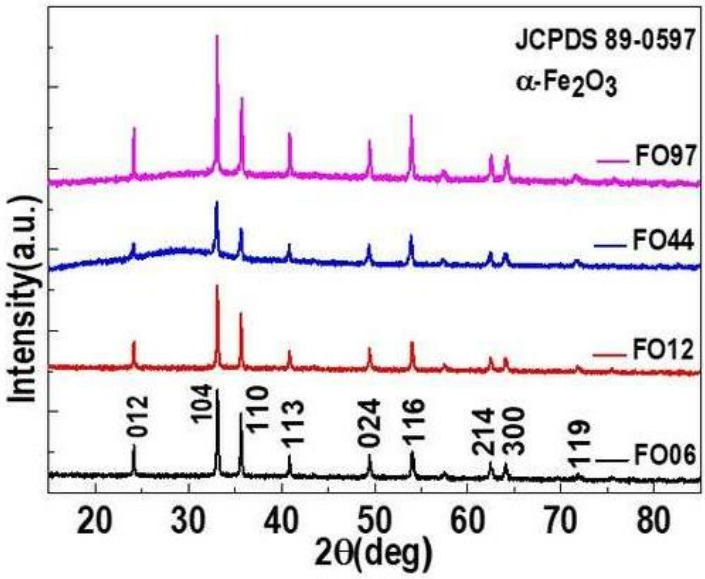

Figure 3.2: X-ray diffraction of α-Fe_2O_3 FO06(NTs), FO12(NRDs) FO44(NRDs/NDs) and FO97(NDs).

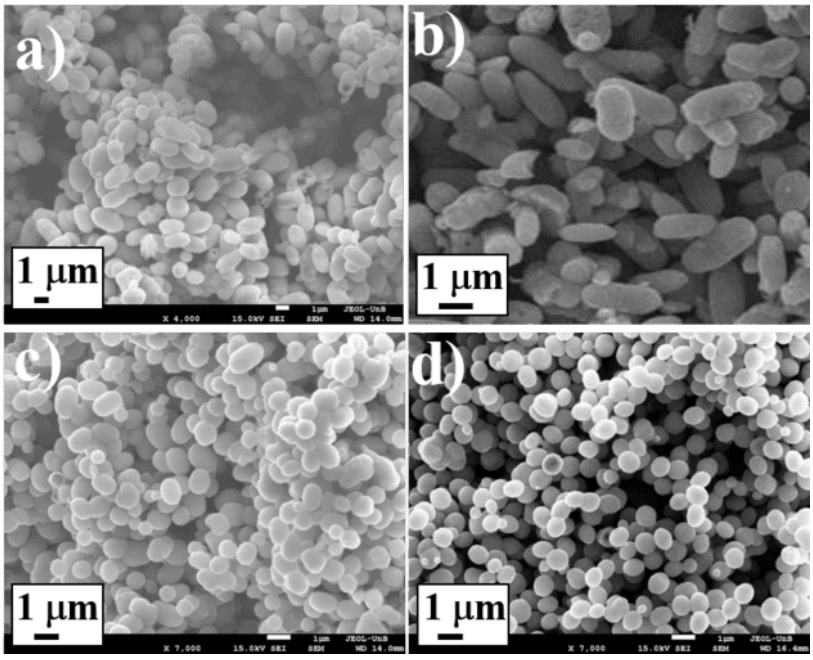

Figure 3.3: SEM images of α-Fe_2O_3 products prepared with different concentrations of phosphate's: a) [NaH_2PO_4] = 2.70x10^{-4} mol L^{-1} (FO06); (b) NaH_2PO_4] = 5.40x10^{-4} mol L^{-1} (FO12); (c) [NaH_2PO_4] = 1.94x10^{-3} mol L^{-1} (FO44); (d) [NaH_2PO_4] = 4.32x10^{-3} mol L^{-1} (FO97). In each case, [$FeCl_3$] = 0.06 M and [$Na_2SO_4.10H_2O$] = 1.65x10^{-3} mol L^{-1}.

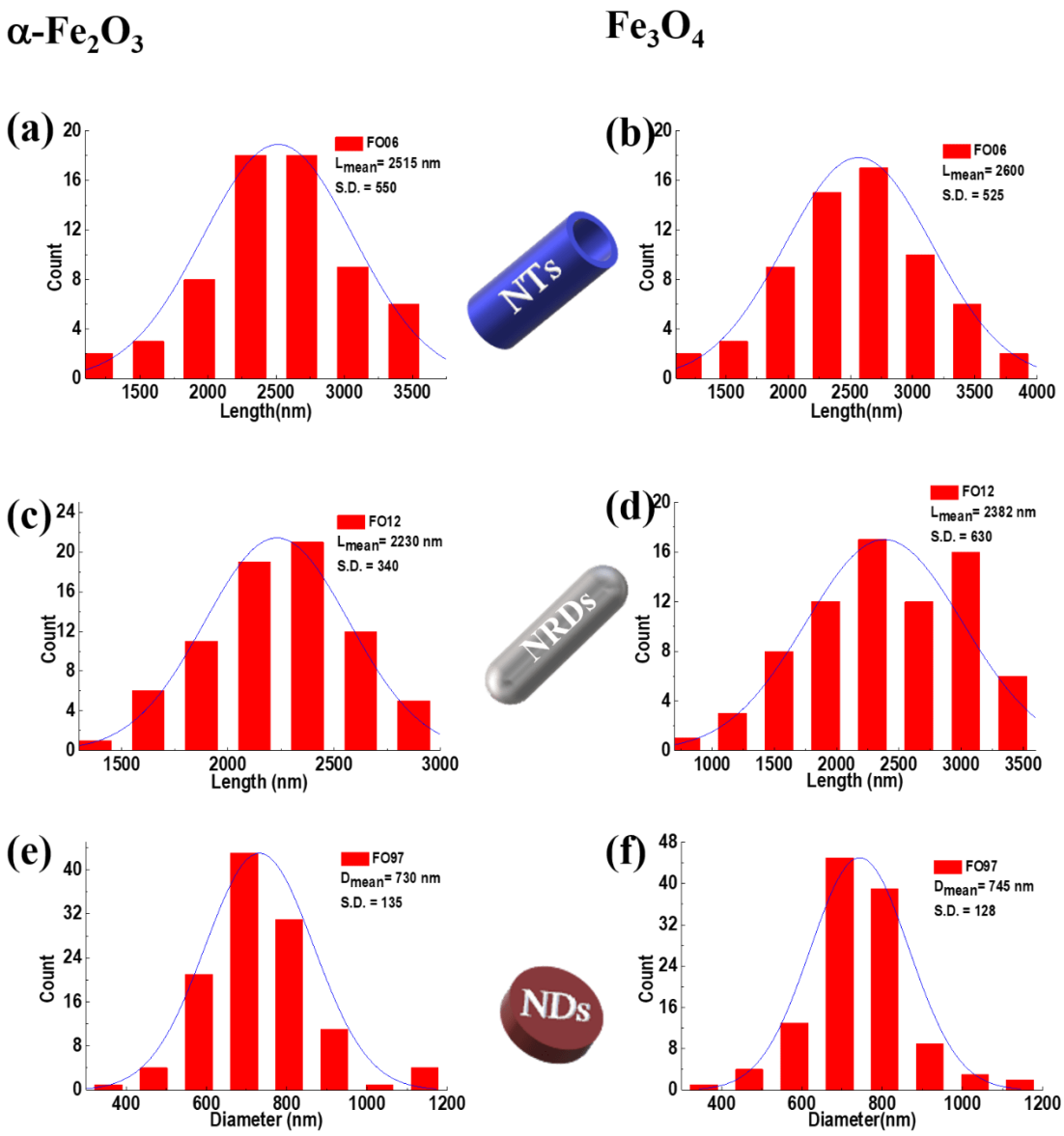

Figure 3.4: Size distribution of (a-b) FO06(NTs), (c-d) FO12(NRDs), and (e-f) FO97(NDs) before and after thermal annealing. Schematic images represent the respective morphology.

Figure 3.5(f) shows the XRD patterns and their Rietveld refinement for FO06, FO12, mixture of NRDs/NDs (FO44) and FO97. Interestingly, the XRD peaks from metallic iron (Fe^0) phase was also detected along with magnetite (Fe_3O_4) from FO06 to FO44 with the increasing concentration of phosphate ions. However, a clear identification of γ-Fe_2O_3 and Fe_3O_4 based on the XRD pattern is quite difficult, due to the similar crystal structure and close lattice parameter values (a = 8.346 Å for γ-Fe_2O_3 and a = 8.396 Å for Fe_3O_4). From Rietveld analysis, we observed that single cubic

phase of Fe_3O_4 in FO97 is formed at higher concentration of phosphate ions, whereas at lower phosphate ion concentrations it promotes the growth of mixed phase. Thus, FO06, FO12 and FO44 have mixed phase consisting of Fe^0 and Fe_3O_4 whereas FO97 has pure Fe_3O_4 phase. During the reduction process, we found that the phosphate anions concentration is key for the efficient conversion of α-Fe_2O_3 into Fe_3O_4. The reduction mechanism of α-Fe_2O_3 to Fe_3O_4 is well dissected in literature.[197] However, we proposed an updated reaction mechanism that involve the phosphate anion concentration as reported below:

For higher concentration of phosphate anions:

$$3Fe_2O_3 + H_2 \longrightarrow 2Fe_3O_4 + H_2O \quad \text{for complete reaction} \qquad (3.1)$$

For lower concentration of phosphate anions:

$$3xFe_2O_3 + yH_2 \longrightarrow 2Fe_3O_4 + H_2O \quad \text{intermediate product} \qquad (3.2)$$

$$zFe_3O_4 + 4(1-y)H_2 \longrightarrow 3aFe^0 + 4H_2O \quad \text{complete reaction} \qquad (3.3)$$

Where x, y, z and a are the concentration of adsorbed $H_3PO_4^0/H_2PO_4^-$ onto α-Fe_2O_3, the concentration of H_2 used to complete the reaction (3.2), concentration of Fe_3O_4 that must react with the remaining concentration of H_2 in (3.3) and concentration of metallic iron obtained after complete reaction. From equation (3.2) and (3.3), we found that when the concentration of phosphate ion is lower, higher will be the concentration of metallic iron (Fe^0) phase.

The XRD pattern for FO97 is nicely described by the reaction occurring through equation (3.1), whereas the XRD for the other samples (FO44, FO12, FO06) results from reactions following equations (3.2) and (3.3). The observed single phase structure of Fe_3O_4 is probably due to fact that the higher concentration phosphate ion creates a barrier that restricts the direct contact between H_2 gas and α-Fe_2O_3 at the surface of NPs, leading to the slowdown of the reaction with utilization of all H_2 gas in FO97. During the reduction of α-Fe_2O_3, the phosphate on the surface could not be reduced, but it started reducing from the inner core to the shell of the NPs. These adsorbed phosphates would be very stable in the reduction process, and act as a framework or a protection shell for the formation of NPs.[198]

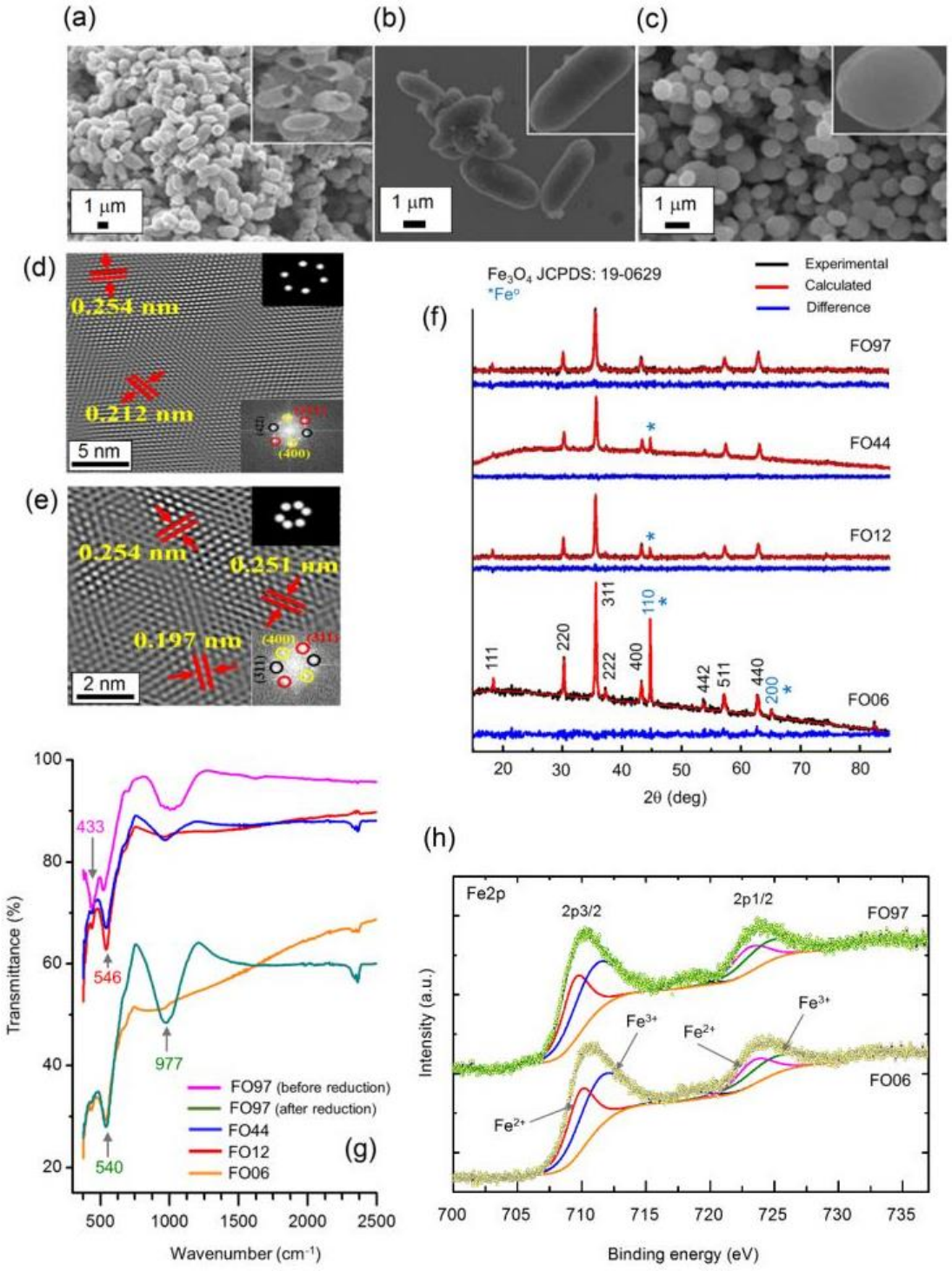

Figure 3.5: (a-c) FESEM image for FO06(NTs), FO12(NRDs) and FO97(NDs) after annealing, (d- e) HRTEM images of FO06(NTs) and FO97(NDs). Upper inset of figure (a – c) are magnified images with the same scale and the insets in panels (d) and (e) are IFFT and FFT images. (f) XRD patterns along with their Rietveld analysis, (g) FTIR spectra, and (h) XPS spectrum in the Fe2p core-level transition of FO06 and FO97.

3.3.2.2 Fourier Transform Infrared Spectroscopy

Figure 3.5 (g) shows the FTIR spectra of Fe_3O_4 NPs in the range of 400–3000 cm^{-1} which identifies the chemical bonds as well as functional groups in the compound. The characteristic peaks of iron oxide (i.e., especially α-Fe_2O_3 and Fe_3O_4) NPs is appeared between 600 cm^{-1} and 400 cm^{-1}. The absorption band at 546 cm^{-1} is assigned to the vibrations of Fe-O functional group. These broad low-intensity bands can be associated with the stretching and torsional vibration modes of magnetite whereas absorption band at 433 cm^{-1} and 518 cm^{-1} is assigned to α- Fe_2O_3 [199]. The characteristic peak of phosphate anions usually appears in the wavenumber range 950-1200 cm^{-1}.[200] No clear peak in this region was detected for FO06, whereas clear signatures can be seen for FO12 and FO44. A very sharp peak emerges in the FO97 sample; thus higher concentration of phosphate groups is trapped on the NPs surfaces. To have a better understanding of the reduction mechanism, we performed FTIR measurement for FO97(NDs) before and after H_2 reduction. The sensitivity of infrared radiation (IR) can help to dissect the protonation of phosphate residues, as illustrated by the differences witnessed among the IR spectra of PO_4^{3-}, HPO_4^{2-}, $H_2PO_4^-$, and $H_3PO_4^o$[200]. The spectral changes are interpreted in terms of acid-base reaction equilibrium[201]:

$$H_3PO_4^o \xrightarrow{K_1} H_2PO_4^- \xrightarrow{K_2} HPO_4^{2-} \xrightarrow{K_3} PO_4^{3-} \qquad (3.4)$$

where $pK_1 = 2.2$, $pK_2 = 7.2$, and $pK_3 = 12.3$

FTIR spectroscopy is a sensitive probe for the two vibration modes of phosphate: the non-degenerate symmetric stretching ν_1, and the triply degenerate symmetric stretching ν_3. The formation of protonated $H_3PO_4^o$, peak with α-Fe_2O_3, belongs to the symmetry $C_3\nu$, and as a result, three ν_3 bands (at 1062, 1038 and 1002 cm^{-1}) and one ν_1 band (at 967 cm^{-1}) are seen for this phosphate complex.[200,201] The formation of $H_2PO_4^-$ (belongs to $C_2\nu$ symmetry) and HPO_4^{2-} (belongs to $C_3\nu$ symmetry) complex could be obtained after removing the hydrogen atom in each step, which leads to symmetry oxidation from $C_3\nu$ to tetrahedral (T_d), as shown by the reaction (3.4). Following complete reduction, the non-protonated PO_4^{3-} anion, peak with Fe_3O_4 is observed with tetrahedral symmetry which belongs to the point group T_d. The non-protonated PO_4^{3-} anion has one active ν_3 band, centered at 977 cm^{-1}, whereas the ν_1 vibration becomes inactive, as shown

in Figure 3.5(g). Based upon these observations, we propose the following reduction process (Eq. 3.5):

$$3xFe_2O_3 + H_2\uparrow \longrightarrow 2yFe_3O_4 + H_2O \quad (3.5)$$

Here, x and y are the concentration of $H_3PO_4^o/H_2PO_4^-$ and PO_4^{3-} respectively. Higher the concentration ratios of $H_3PO_4^o/H_2PO_4^-$ stronger is the bonding between hydrogen phosphate groups that might prevent the reduction of α-Fe_2O_3 during thermal annealing under H_2 gas. From XRD and Mössbauer spectroscopy (discussed in later section), we found that FO06, FO12 and FO44 include some % of metallic iron that decreases in the following order FO06 > FO12 > FO44, whereas pure Fe_3O_4 phase is obtained for FO97. These evidences clearly indicate that the concentration of H_2 gas is effectively used in FO97(NDs), breaking the bonds between phosphoric acid groups ($H_3PO_4^o$), and hence achieved a complete transformation from α-Fe_2O_3 to Fe_3O_4. In contrast, when the amount of $H_3PO_4^o$ is limited, likewise in the synthesis of FO06, the excess of H_2 gas is left (i.e. not used in the reaction with phosphate groups) and reduces further some Fe^{2+} centers of Fe_3O_4 to Fe^0. Similar process occurs in FO12 and FO44. Lowering the concentration of phosphate anions, higher is the percentage of Fe^0 present in the final material. The difference between the XRD patterns of α-Fe_2O_3 (Figure 3.2) and Fe_3O_4 NPs (Figure 3.5f) show the presence of such phase conversion, from corundum to spinel. However, Fe_3O_4 exhibit crystal structure quite similar to that of γ-Fe_2O_3 and makes it difficult to distinguish between these two forms, simply based upon XRD analysis.

3.3.3 X-ray Photoelectron Spectroscopy

It allows to gain further details of the surface contribution of either Fe_3O_4 and/or Fe^0 phases. The results are given in Figure 3.5(h), where peaks are shown the electronic envelopes for the core-level of FO06 and FO97, recorded in the Fe2p regions. The two major components, at binding energies of 710.4 eV and 724.5 eV, are attributed to $2p_{3/2}$ and $2p_{1/2}$ core levels. However, in the XPS pattern of FO06(NTs), the broad Fe2p signals are arising from the coexistence of Fe^{3+} and Fe^{2+} states. In addition, no satellite peaks are observed, factor that confirms the absence of γ-Fe_2O_3 in the Fe_3O_4 samples. The ratio of Fe^{2+}: Fe^{3+} should ideally be 1:2, or 0.33:0.67, in stoichiometric Fe_3O_4. The obtained results of the convoluted peaks give the values Fe^{2+}: Fe^{3+} = 0.42:0.58, which clearly indicates a non-stoichiometric Fe_3O_4 present in the surface regions of the NPs. On the other

hand, small satellite peak (area = 5%) corresponding to the $2p_{3/2}$ transition is observed at 718.8 eV in FO97; this signature is assigned to the presence of higher concentration of Fe^{3+} ion. In addition, possibility of minor contribution from γ-Fe_2O_3 is always open for such satellite. The calculated ratio of Fe^{2+}: Fe^{3+} is 0.41:0.54 reflects more non-stoichiometric Fe_3O_4 compared to FO06. However, no evidence of Fe^0 is detected on the surface of FO06 and FO97 samples.

3.3.4 Mössbauer Spectroscopy

We have performed Mössbauer spectroscopy for the investigated samples at 300 K as shown in Figure 3.6 (a-d), and their hyperfine fitting parameters are given in Table 3.1. The spectra for all the samples were well fitted considering sextet patterns (magnetic sub-spectra). No evidence of SPM relaxation components was observed, which is a good agreement with the large size of the particles. The spectrum for FO06 (Figure 3.6(a)) is well resolved by five sextets (four sextets for Fe_3O_4 and one for Fe^0). Values of hyperfine parameters for all the samples are consistent with the two crystallographic sites of iron ions in the cubic spinel (Fd-3m) structure of Fe_3O_4.[202] However, the spectral area ratio on A- and B-site was found different from bulk magnetite (i.e., 1:2 for free-defect crystals). Such ratio of population indicates that the samples are not in stoichiometric proportion. Increase amount of population in the reverse order than bulk indicates the presence of vacancies/defects in octahedral B-site in an increased order. The results can be understood considering possible core/shell structure model assuming that some sample region in the core follows the bulk Fe_3O_4 composition i.e., stoichiometric (blue color) while the rest portion are non-stoichiometric with vacancies/defects (olive color), as shown in the Figure 3.6(e). In addition, the presence of metallic iron (Fe^0) is also observed, represented by pink color in the drawings shown in Figure 3.6(e). Two sextets, blue and pink, were used for the fitting of Fe in the core region, resulting in 14% and 28% of iron cations residing in A- and B- sites. Thus, 42% of the Fe population is represented by stoichiometric Fe_3O_4. Figure 3.6(b) and Figure 3.6(c) show the recorded spectra of samples FO12 and FO44. From spectra analysis, they both give well resolved sextets (four sextets for Fe_3O_4 and one for Fe^0). Two sextets (Figure 3.6b), given by blue and pink lines, correspond to the fitting for Fe in the core region, resulting in 10% and 21% of Fe in A- and B- sites. Thus, 31% of Fe population is associated to stoichiometric Fe_3O_4 for FO12; for FO44

(Figure 3.6c), 7% and 14% of Fe resides in the A- and B- site, thus 21% population is given by stoichiometric Fe_3O_4.

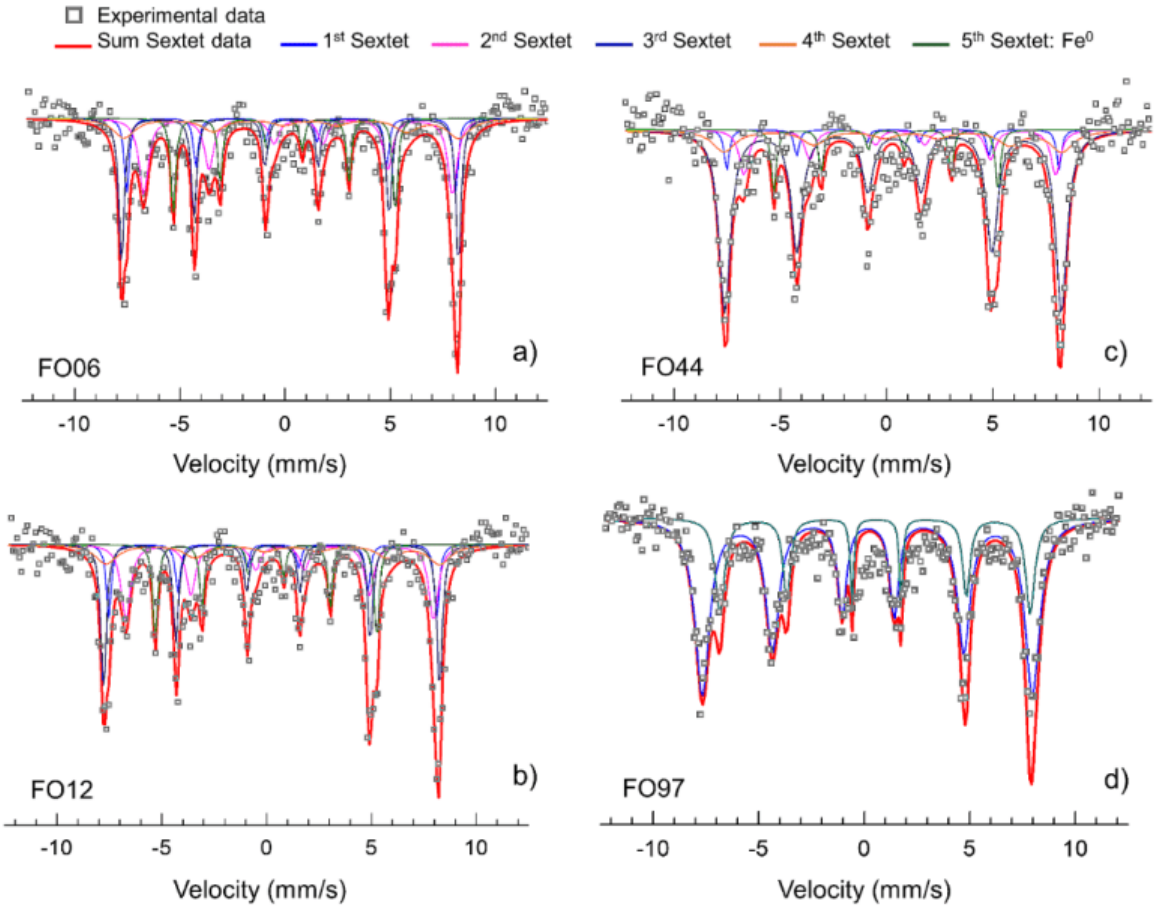

Figure 3.6: (a-d) Mössbauer spectra recorded at T = 300 K for FO06, FO12, FO44 and FO97.

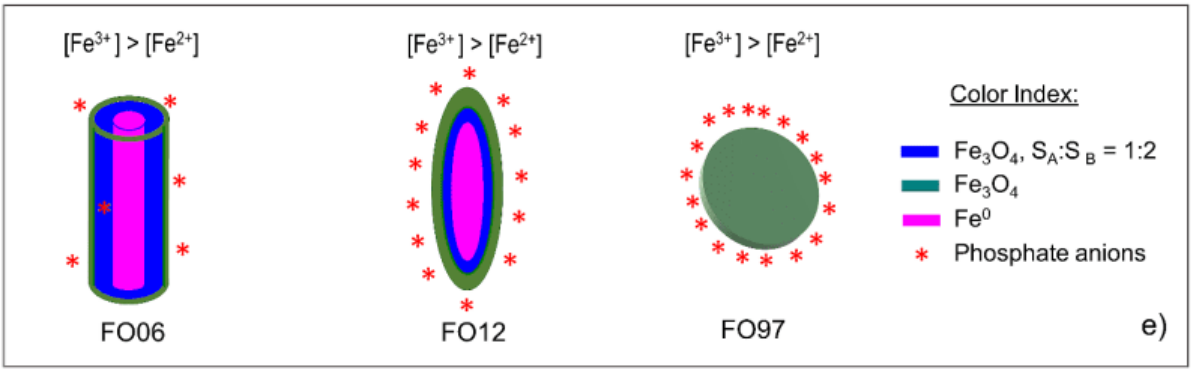

Figure 3.6: (e) The proposed Fe composition in the different samples.

The fitted sextet drawn in navy and violet colors represent the sites S1 and S2, because we were unable to distinguish either A- or B-sites, and show hyperfine parameters close to Fe^{3+} and Fe^{2+},

respectively. The observed Fe^{3+} population for S1-site is more than twice in comparison to the S2-site. This is probably due to the overlapping of two sextets of Fe^{3+}, also present in the S1- and S2-site, respectively.

Let us assume that Fe^{3+} population covered by S1 is collectively representing the Fe^{3+} population of S1- and S2-site in single sextet and thus the ratio of S1:S2 is 1:1.8 (for instance in FO06 (NTs) and for other components see equation below) indicating some cation vacancies and surface effects. In case of cation vacancies □ in S2-sites, the value S1/S2 for these samples would correspond to the non-stoichiometric Fe_3O_4 with chemical formula:

For FO06,

$$(Fe^{3+})_{S1}[Fe^{2.5+}_{1.80}\square_{0.2}]_{S2}O_4 \quad (3.6)$$

Similarly,

For FO12,

$$(Fe^{3+})_{S1}[Fe^{2.5+}_{1.71}\square_{0.29}]_{S2}O_4 \quad (3.7)$$

For FO44,

$$(Fe^{3+})_{S1}[Fe^{2.5+}_{1.56}\square_{0.46}]_{S2}O_4 \quad (3.8)$$

On the other hand, it is important to take into account the presence of surface effects. It is reported that the magnetic moments of some iron ions in the NPs are generally pinned at the surface layer owing to a high magnetic anisotropy.[203] Consequently, not all S2-site iron ions undergo electron hopping due to the surface effects. In this case, we can evaluate some of the iron ions participating in the electron $Fe^{2+} \rightleftarrows Fe^{3+}$ exchange in the stoichiometric Fe_3O_4. From the Mössbauer line intensities and hyperfine parameters, we have observed that charge distribution follows:

For FO06,

$$(Fe^{3+})_{S1}[\ [Fe^{2+}_{0.965} \rightleftarrows Fe^{3+}_{0.965}]_{S2}\ [Fe^{3+}_{0.07}]_{S2}O_4 \quad (3.9)$$

For FO12,

$$(Fe^{3+})_{S1}[\ [Fe^{2+}_{0.950} \rightleftarrows Fe^{3+}_{0.950}]_{S2}\ [Fe^{3+}_{0.10}]_{S2}O_4 \quad (3.10)$$

For FO44,

$$(Fe^{3+})_{S1}[\ [Fe^{2+}_{0.930} \rightleftarrows Fe^{3+}_{0.930}]_{S2}\ [Fe^{3+}_{0.14}]_{S2}O_4 \quad (3.11)$$

On the other hand, for FO97, it is clearly observed from Table 3.1 that the phase formed from oxidation of Fe^{2+} to Fe^{3+} has significantly more area in S1-site and area in S2-site. Such partially oxidized Fe_3O_4 can exist between the end-members of stoichiometric Fe_3O_4 and γ-Fe_2O_3 and can be referred to by their Fe^{2+} content (x), as calculated from $x = \frac{Fe^{2+}}{Fe^{3+}} = 0.33$. Such result is possibly due to the high concentrations of phosphate anions present in FO97(NDs). Let us take fitting idea of the recorded spectra similar to the non-stoichiometric region of previous three samples, 75% population in S1-site can be consider as population representation of Fe^{3+} of both S1-and S2-site in single sextet in S1-site (could be two sextets of same ion (Fe^{3+}) were overlapped), since we were unable to fit a separate sextet for Fe^{3+} in S2 -site. This consideration gives the ratio of S1:S2 ~ 1:1.68 indicating cation vacancies throughout the region indicated by green color, in Figure 3.6(b). Similar to the previous discussion cation vacancies in S2-sites, the value S1/S2 for FO97 would correspond to the non-stoichiometric Fe_3O_4 with the chemical formula,

$$(Fe^{3+})_{S1}[Fe^{3+}Fe^{2+}_{0.68}\,Fe^{3+}_{0.32}\,]_{S2}O_4. \qquad (3.12)$$

In a rough approximation of collinear magnetic ordering, the observed magnetic moment 'M' per formula unit of the stoichiometric magnetite is 'M' =4μ_B, which is the region indicated by the blue color in the Figure 3.6(e), whereas non-stoichiometric Fe_3O_4 has 'M' = 3.94μ_B with δ = 0.015 and thus can be well represented by the stoichiometric composition of $Fe_{2.985}O_4$ for FO06. For 'M' = 3.91μ_B with δ = 0.022 satisfy the formula $Fe_{2.978}O_4$ for FO12, for 'M' = 3.86μ_B with δ = 0.034 gives $Fe_{2.966}O_4$ for FO44 and 'M'= 3.16μ_B with δ = 0.21 gives $Fe_{2.791}O_4$ for FO97 sample. The increased presence of vacancies and surface effects from FO06 to FO97 is believed to be due to an increase in concentration of phosphate anions. In the NPs, except for FO97, besides the Fe_3O_4 sextets, an additional sextet was found. The extra pattern was associated to metallic iron Fe^0, which was confirmed by analysis of the hyperfine parameters (see Table 3.1) and agree with the results obtained from XRD data analysis as given in Table 3.2. Based on these experimental findings, from FTIR, Mössbauer spectroscopy, and XPS data, supported further by magnetic measurement (see section magnetic properties below), we propose that in these materials exist the presence of a core-shell structures, being composed of different layers formed by Fe^0, stoichiometric Fe_3O_4 and non-stoichiometric Fe_3O_4, which are shown as drawings in Figure 3.6(e).

Table 3.1: ^{57}Fe Hyperfine parameters, isomer shift (IS, δ_C), quadrupole splitting (QS, ΔQ), hyperfine field (B_{hf}) and spectral area (population distributions) for the diverse iron oxide nanoparticles.

Sample Code	Phase	Site	Mössbauer Fitted Data			
			IS, δ_C(mm/s) ±0.01	QS, ΔQ(mm/s) ±0.01	B_{hf} (T) ±0.1	Population (%) ±2
FO06(NTs)	Fe_3O_4	A	0.30	-0.042	48.60	14
		B	0.64	-0.018	45.65	28
		S1	0.28	0	49.80	30
		S2	0.75	0	49.40	12
	Fe		-0.03	0	32.88	16
FO12(NRDs)	Fe_3O_4	A	0.30	-0.016	48.64	10
		B	0.63	0.06	45.30	21
		S1	0.32	-0.002	49.70	42
		S2	0.77	0	48.6	14
	Fe		-0.02	-0.06	32.82	12
FO44(NRDs/NDs)	Fe_3O_4	A	0.29	-0.027	48.7	7
		B	0.63	-0.022	45.6	14
		S1	0.34	0.003	49.30	54
		S2	0.82	0	47	15
	Fe		0.004	0	32.99	9
FO97(NDs)	Fe_3O_4	S1	0.27	-0.03	48.63	74.69
		S2	0.68	-0.06	45.69	25.31

Table 3.2: Comparative study of phase analysis and magnetic saturation through XRD, Mössbauer and Magnetic data. The observed data from XRD and Mössbauer spectroscopy were very closed to each other. The phase of each sample was confirmed by analyzing these obtained data. Similarly, the magnetic saturation 'Ms' was analyzed comparing the result obtained from SQUID with 'Ms' obtained from Mössbauer spectrum. The obtained data is closed to each-other with maximum error ~8%. This error could be due to presence of defect on Fe^0, however we used 'M_S'= 221 emu/g as bulk Fe^0 during the calculation from Mössbauer data. In addition, instrumentation error should have to take in an account.

Sample	**Lattice parameter (nm) ±0.0005**	**Phase Analysis**				**Magnetic Saturation 'Ms' (emu/g)**	
		XRD(±1)		**Mössbauer(±2)**		**Mössbauer (emu/g)**	**SQUID (emu/g)**
		Fe_3O_4(%)	Fe^0(%)	Fe_3O_4(%)	Fe^0(%)		
FO06 (NTs)	Fe_3O_4 =0.8375 Fe^0= 0.286	85.5	14.5	84	16	112	115
FO12 (NRDs)	Fe_3O_4 =0.8375 Fe^0= 0.286	86	12.4	87	11	104	96

FO44 (NRDs/NDs)	Fe_3O_4 =0.8374 Fe^0= 0.286	87.3	10	89	9	98	92
FO97 (NDs)	Fe_3O_4 =0.837	100	-	100	-	73	80

3.3.5 Magnetic Properties

The dc magnetization hysteresis measurements, recorded at 300 K, allowed to unveil further the different magnetic behavior in the so-prepared materials. The samples FO06, FO12 and FO44 displayed ferrimagnetic trends with higher value of saturation magnetization (M_S) of 115, 96 and 92 emu/g, respectively. The FO97 material showed a lower value, of ~ 80 emu/g, which is about 87% of that of bulk Fe_3O_4, (see Figure 3.7a). The higher value of M_S in FO06, FO12 and FO44(NRDs/NDs) is mainly attributed to the presence of zero-valent-iron (Fe^0). The smaller value of M_S found in FO97 arised from the stoichiometry deviation for pure magnetite, cation distribution and absence of Fe^0 [204]. We observed that the coercive field H_C decreases with decreasing length or diameter of the NTs/NRDs/NDs. The observed values of H_C decrease from ~ 252 Oe (FO06), ~209 Oe (FO44) to ~182 Oe (FO97) whereas H_C for FO12 is ~ 297 Oe, which is larger than FO06. This property is due to the adsorption of phosphate anions on the surface of FO12. The experimental values of M_S and H_C are given in Table 3.3.

Table 3.3: Magnetic properties of all four sample are tabulated as below:

Sample	**Magnetic saturation (M_S) (emu/g)**	**Magnetic remanence M_R (emu/g)**	**M_R/M_S**	**Coercive field (H_C) (Oe)**
FO06	115	15	0.13	252
FO12	96	21	0.22	297
FO44	92	12	0.13	209
FO97	80	11	0.14	182

Although the morphology of FO06 and FO12 are similar, showing nearly identical size 'Length(L)' and volume 'V', the presence of phosphate anions on the surface of FO12 could generate local symmetry breakings, which are at the origin of the surface anisotropy due to structural defects, broken symmetry bonds and surface strain [205]. Therefore, higher Hc for FO12 may arise from enhanced surface anisotropy. To validate this hypothesis, we have calculated the surface anisotropy by using the law of approach to magnetic saturation[206],

$$M = Ms(1 - \frac{b}{H^2}) \tag{3.13}$$

where b is a factor correlated with the effect of the magneto-crystalline anisotropy. In case of uniaxial magnetic crystals, the fitting parameter b can be used to obtain an estimate of the anisotropy term K:

$$K = \mu_0 Ms(\frac{15b}{4})^{1/2} \tag{3.14}$$

In Equation (3.14) the term μ_0 represents the permeability in the free space and Ms the saturation value. Combining equations (3.13) and (3.14), we found that the anisotropy constant K_{FO12} = 6.6×10^5 J/m^3 for FO12(NRDs) whereas K_{FO06} = 5.15×10^5 J/m^3 for FO06(NTs), i.e. $K_{FO12} > K_{FO06}$. The existence of domain walls on the surface of iron oxide and their movement could easily be blocked by the adsorbed phosphate layers, resulting in domain walls-pinning, which contributes to enhance $'K'$ and higher the magnitude of H_C for FO12.

On the other hand, two samples FO44 and FO97 have comparatively lower Hc values than FO12, even with phosphate layer on their surface. Such low Hc values are due to finite size effects. Further, the ratio of M_R/M_S for all the sample is in the range 0.1-0.5, which indicates that all the samples are pseudo single-domain (PSD) NPs consist of multi-domain (MD) NPs [207]. The FO97 should have a vortex domain structure and possess an onion structure under a sufficiently high magnetic field. [42,47] Therefore, a drop in Hc from FO06 to FO97 is a clear indication of the formation of vortex states in FO97 while it is completely absent in FO06 due to its tubular morphology.[97] This effect has been further studied by micro-magnetic simulation through Mumax 3.9 software, as shown in Figure 3.7(b). The clear observation of vortex core in the center of FO97 at H =0 and its gyrotropic movement in the application of field, i.e. when H>0, are an evidence of a vortex configuration in FO97. In such magnetic vortex domain structure, the hysteresis loop is composed of a two-step magnetization reversal processes, which involved onion to vortex

transition and vice versa [42,47]. At large external magnetic field (H), FO97 is in a saturation state or single-domain state (Figure. 3.7b-iii) since, all spins are parallel to the field direction. The complete phenomena of hysteresis loop for FO97 is represented in Figure 3.7b-(i-v), where the green color indicates saturation magnetization in positive direction and navy indicates the saturation moment in negative direction. The negligible coercive field and remanence were observed in FO97. Such difference between experimental results and simulated envelope could be interpreted as an effect of the polydispersity of the sample, which was not take an account in the magnetic hysteresis simulation [208].

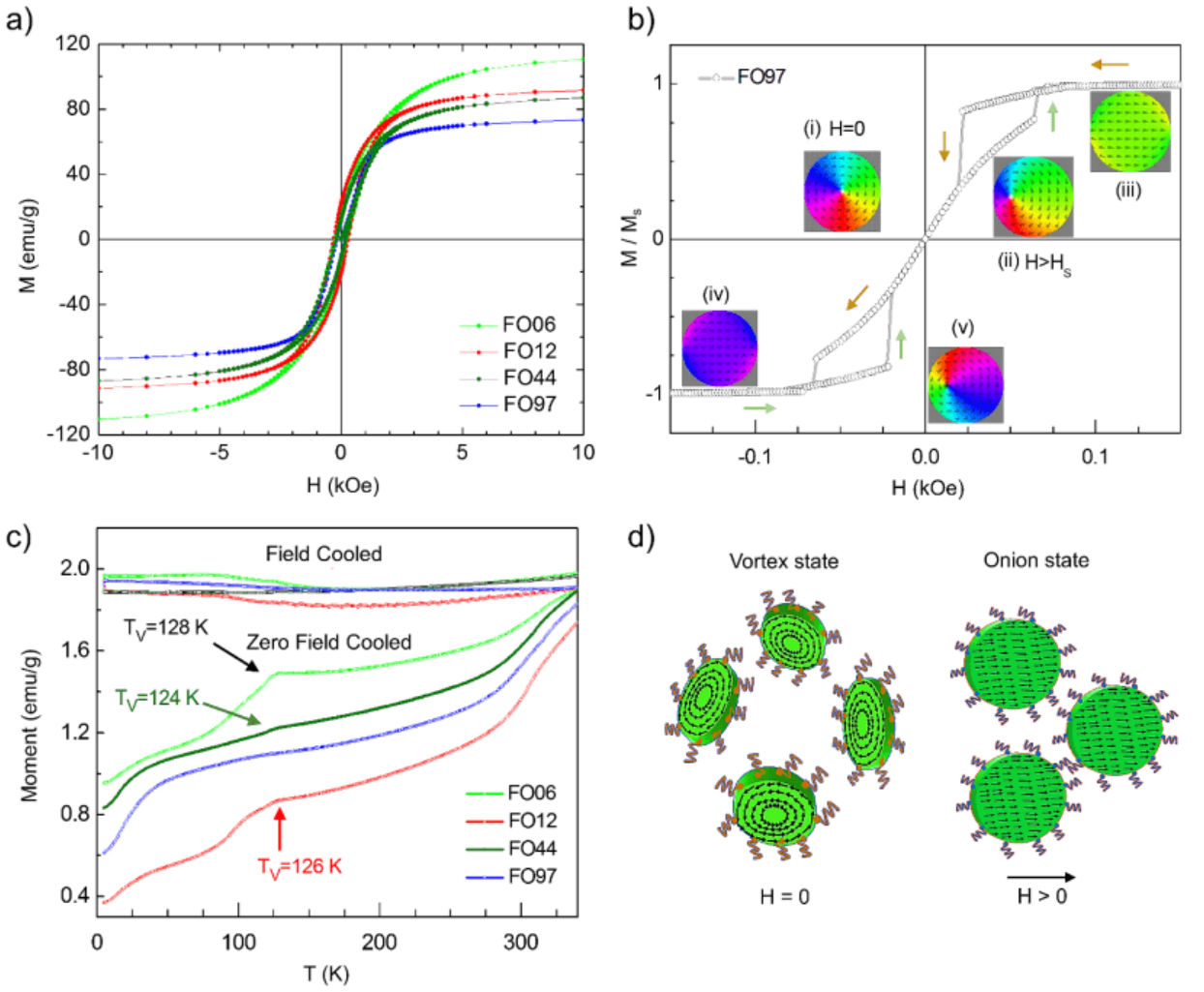

Figure 3.7: (a) Represent the hysteresis loops measured at T = 300 K, (b) Simulated hysteresis loop for the sample FO97(NDs), (c) ZFC-FC curves for all the investigated samples at T = 300 K and (d) Schematic illustration of vortex and onion states in FO97(NDs) in absence (H=0) and in the presence (H>0) of an external magnetic field H. Arrows indicate the spin's direction.

The zero field cooling-field cooling (ZFC-FC) curves in the Figure 3.7(c) exhibit a prominent Verwey transition (Tv) for the three samples i.e., FO06, FO12 and FO44 at about 128 K, 126 K and 124 K respectively, which is typically encountered in stoichiometric Fe_3O_4, whereas no such transition is detected in FO97. The Tv for bulk Fe_3O_4, $T_V \approx 119$ K, above which it occurs fast electron hopping between Fe^{2+} and Fe^{3+} ions on the octahedral sites.[209] In Fe_3O_4 NPs, the sharp transition observed is related to both the high crystallinity of the NPs, and to the presence of inter-particle interaction and electron hoping in between Fe^{2+} and Fe^{3+} sites.[210] There is another transition located at T ~50 K, implying the occurrence of spin reorientation and glass-like transition[211]. It is interesting to explore the trend of Tv from FO06 to FO97, with the structural transformation from cubic to monoclinic. We found that the observed transition is very sharp in FO06, more broadened for FO12 and FO44 and finally lost in FO97. The abrupt decrease in sharpness of such transition in FO12 and FO44 is ascribed to the decrease in the mobility of 3d electrons. The effect, simply called 'hopping', between the Fe^{3+} and Fe^{2+} cations at temperatures $T < T_V$ indicates significant loss of charge ordering between Fe^{3+} and Fe^{2+} located on octahedral sites at temperatures $T < T_V$. However, the same phenomenon does not appear to occur in FO97. This is explained by the following rationale; increasing the concentration of phosphate anions trapped on the surface, from FO06 to FO97, can promote easier oxidization of Fe^{2+} to Fe^{3+} cations (in high spin state configuration). This effect induces an unequal number of Fe^{3+} and Fe^{2+} ions on octahedral sites below T_V, which then lead to the disappearance of charge ordering [212].

The trend of Tv was analyzed further by comparing the population of stoichiometric Fe_3O_4, obtained from Mössbauer analysis, in all samples. The bulk composition of middle core (second layer i.e., blue color in the Figure 3.6e) NPs is the one mainly responsible for tuning Tv, while is expected to be minor the contribution on Tv coming from the surface layer (green color in Figure 3.6e).[213] The sharp transition in FO06 could then originate from the presence of higher population of stoichiometric Fe_3O_4, ~ 42%, whereas broadening, as observed in FO44, is induced by the estimated decrease in population of stoichiometric magnetite, ~ 21%. Moreover, minor contribution of electron hopping in the S2-sites comes from non-stoichiometric Fe_3O_4, as illustrated by green color in the structural drawings of Figure 3.6(e), is also responsible for the shift to lower temperatures in Tv, from high FO06, FO12 to low as in FO44. No transition was observed in FO97 due to the absence of significant electron hopping ($Fe^{2+} \rightleftarrows Fe^{3+}$) as well as due to the presence of more cation vacancies/defects. The obtained results can be rationalized as

"lowering the concentration of phosphate anions, induce a lowering in cation vacancies and in defects but it sharpens the Verwey transition". Moreover, higher the concentration of non-stoichiometric Fe_3O_4, broader becomes the Verwey transition and thus decreases in Tv is observed.[212,214,215] Thus, we can conclude that the absence of phosphate ion on the surface of FO06 facilitate emergence of sharp Tv transition and high concentration of such anion on the surface layer of FO97 hampers the Tv transition.

3.4 Conclusion

We have studied the impact of phosphate anions in impacting size, shape, phase composition and stoichiometry of Fe_3O_4 NPs. Analysis of the structural evolution and formation mechanism of the nanoparticle systems revealed that by using a controlled ratio of $\frac{Fe^{3+}}{PO_4^{3-}}$ and microwave irradiation we can effectively produce in water hollow NTs, NRDs and NDs, with tunable phase composition and stoichiometry. The magnetic properties of these morphologically different systems show that the coercive field for NRDs was higher than that of NTs, despite having similar shape and dimension. This phenomenon was ascribed to originate from surface anisotropy effects, which are induced by higher amounts of adsorbed PO_4^{3-} anions on the NPs surface. The obtained NDs were able to express a magnetic vortex state, as validated by micro-magnetic simulation. Therefore, selecting the concentration of phosphate ions, and the concentration of H_2 gas in the mixture during the synthesis allows to effectively prepare under mild conditions and without use of organic surfactants well defined systems with finely tuned shape, size, phase composition and stoichiometry.

Chapter 4

Magnetic Vortex Configuration in Submicrometer Fe_3O_4 Nanospheres

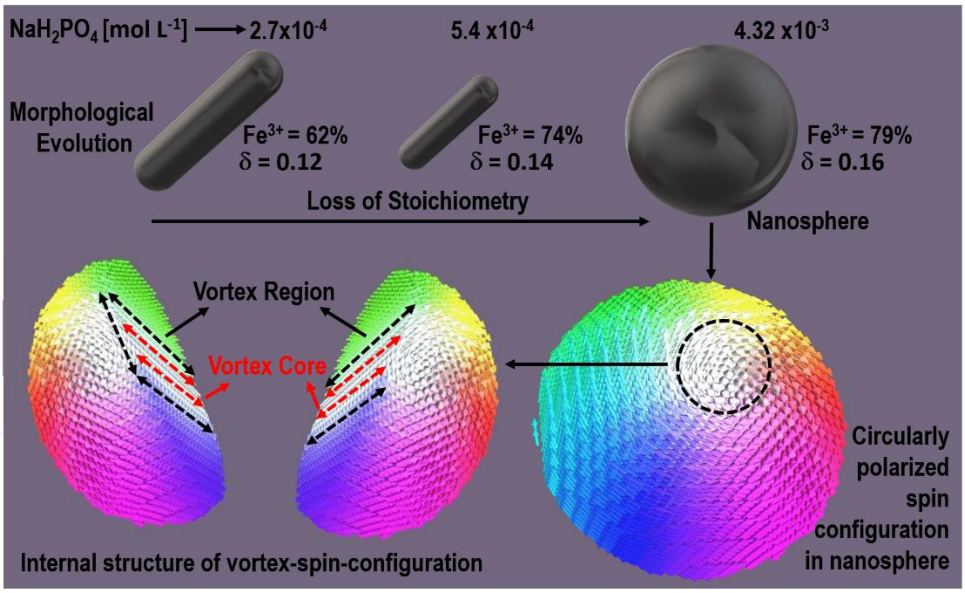

Recent theoretical and micromagnetic simulation studies on magnetic nanospheres (NSs) with novel vortex configuration reveal their possibility in several applications based on high-power-rate energy absorption and subsequent emission. In this chapter, we report a control microwave synthesis of Fe_3O_4 NSs and confirm the vortex-configuration via experiment, theoretical analysis, and micromagnetic simulation. Further, the stoichiometry of as-prepared vortex NSs is examined thoroughly. The zero-field/field cooling (ZFC-FC) magnetization, electrical measurements, and Mössbauer spectroscopy provide evidence of loss of stoichiometry in vortex-NSs due to the presence of surface oxide layer, defects, and higher cation vacancies. Although the stoichiometry is not preserved, the magnetite NSs exhibit a vortex configuration confirming that the geometry/size is a critical factor for the existence of vortex state rather than bulk properties. The results provide key information for the synthesis of magnetite NSs and open up possibilities for future technological applications based on three-dimensional magnetic vortex-structures.

4.1 Introduction

The existence of a magnetic vortex state, consisting of a non-collinear spin configuration and in-plane curling, enables negligible remanent magnetization at low fields with high magnetization at high fields in MNPs. The intrinsic stability, topology-driven dynamics, and more interestingly the switching field-dependent electrical and magnetic properties (widely known as "on/off" switching property) offers a great opportunity to practice in industrial technology, from quantum computing to biomedical applications [42,43,224,216–223]. Many works have reported these vortex nanostructures in magnetic-oxide NPs with controlled shape and size, in a variety of morphologies such as ellipsoids [44], cubes [225,226], disks/dots [37,42,43,220,227], and rings [56,58]. The vortex structure in MNPs with sizes of several hundred nanometers (i.e., above the single-domain size limit of most materials), allows manipulation of their electrical, magnetic, mechanical, and thermal properties. Recently, theoretical and simulation studies were reported for magnetic NSs where the vortex magnetic structure of the core exhibited a unique precession motion around the direction of an externally applied static field [117,228,229]. This unique vortex-core reversal behavior and its dependence on the frequency of the applied AC magnetic field allowed large power absorption values, making them appealing for potential application in bio-diagnostics and MFH, for example. While these studies have provided robust analytical and computational information on vortex NSs, there are not yet extensive reports on successful production of iron-oxide vortex NSs, which is the obvious step to validate experimentally the theoretical models. Hence the significant relevance of achieving the successful synthesis of such NSs with magnetic vortex configuration.

For the effective performance of these NPs in practical applications, it is essential to receive their properties in bulk. Often, the NPs exhibit a bulk property if they preserve their stoichiometry, which depends on several factors like shape, size, surface defects, charge ordering, cation vacancies, etc. Indeed, in magnetite, stoichiometry is strongly associated with a Verwey transition, which is essential for its potential applications in spintronics, sensors, energy conversion devices, and biomedical purposes [3]. The Verwey transition (T_V) near 120 K, also called metal-to-insulator transition, arises as a result of charge order-disorder of Fe^{2+} and Fe^{3+} that leads to sharp changes in the electric, magnetic, and structural properties [209,230]. Particularly, the change in unit cell structure from inverse-cubic-spinel to monoclinic, increase in resistance and sharp fall of magnetization below T_V directly affects the efficacy of NPs and limits prospective applications.

The absence of Verwey transition directly leads towards the loss of stoichiometry influenced by several external factors, such as, size, shape, growth during synthesis, defects, thermal treatment, etc.[231,232]. It is well known that the Verwey transition is size-/shape-dependent, usually appears in larger NPs in the range of blocked single domain/ferromagnetic particles and gets suppressed in SPM range (precisely for particles smaller than 20 nm) and completely disappears for particle sizes below 6 nm [3,233,234]. Despite the great experimental effort, however, the existence of ionic-charge ordering below Verwey transition, surface defects, cation vacancies, contribution of size/shape to the loss of stoichiometry in large-scale sphere magnetite still remains mysterious and under debate [235,236]. This chapter first reports the microwave assisted hydrothermal (MAH) synthesis route for Fe_3O_4 NSs and examines their vortex-spin-configuration by means of experiments, theoretical analysis, and micromagnetic simulation. Further, the role of surface defects and cation vacancies to the loss of stoichiometry in as-prepared vortex NSs is presented and discussed.

4.2 Experimental Section: Synthesis of Iron Oxide Vortex Nanospheres

Based on both recent reports and our own studies [56,237], we used phosphate anions for the shape controlled synthesis of NSs. The α-Fe_2O_3 long ellipsoidal rods (LERs), short ellipsoidal rods (SERs) and NSs were prepared by a MAH reaction of iron chloride ($FeCl_3$) with addition of sodium phosphate (NaH_2PO_4) and sodium sulfate (Na_2SO_4) as additives to control shape and morphology. Briefly, 0.06 mol L^{-1}(~ 370 mg) of $FeCl_3$ with 35 mL of distilled water were stirred for 15-20 minutes. The additives NaH_2PO_4, and Na_2SO_4 mixed with 3 mL of distilled water separately and finally mixed with $FeCl_3$ solution to make mixture of final volume 38 ml; the concentration of NaH_2PO_4 ($2.7x10^{-4}$ mol L^{-1}, $5.4\ x10^{-4}$ mol L^{-1}, mol $L^{-1}$and $4.32\ x10^{-3}$ mol L^{-1}), and $Na_2SO_4.10H_2O$ ($1.65\ x10^{-3}$ mol L^{-1}). After a vigorous stirring for 10 minutes, the mixture was transferred into a reaction vessel in a Synth's microwave reactor, with an output power of 1000 W. The working cycle of the microwave reactor was set as 20 ^{0}C/ minutes rapid heating to reach 220 ^{0}C from room temperature, and heat 60 minutes at same temperature. All other procedure is same as given in chapter 3 (section 3.2).

4.3 Result and Discussion

4.3.1 Structural/Morphological/Magnetic/Electrical Analysis

4.3.1.1 X-ray Diffraction and Microscopy Analysis

The complete synthesis process of defined α-Fe_2O_3 MNPs and their controlled conversion into Fe_3O_4 is given in the synthesis section (above and chapter 3, section 3.2). The morphological changes of as-prepared NPs, from long ellipsoidal rods (LERs), short ellipsoidal rods (SERs) to NSs with the decreasing in the ratio of iron (III) to phosphate anions is shown schematically in Figure 4.1(a) and their corresponding FESEM Figure 4.1(b-d).

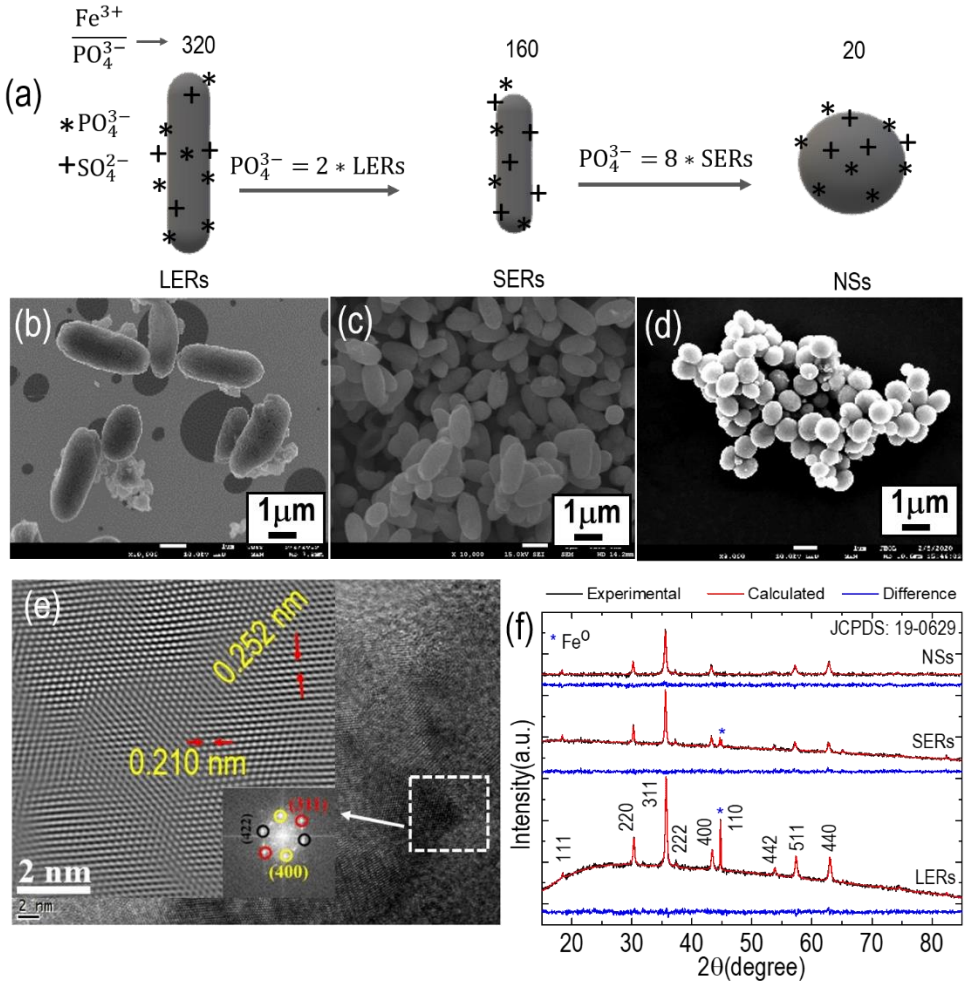

Figure 4.1: (a) Schematic of the formation process of NSs through reduction in PO_4^{3-} concentration compared to the LERs and SERs; (b-d) FESEM image of reduced LERs, SERs, and NSs respectively; (e) HRTEM images of NSs, and (f) XRD patterns with their Rietveld analysis.

It is observed that when the ratio of iron (III) to phosphate anions is reduced by one half; LERs shortened their length and results in SERs which are further converted into NSs because of the reduced ratio of iron (III) to phosphate anions by 20 times. The size distribution of the obtained NSs could be fitted with a Gaussian distribution yielding an average diameter <d> =701 ± 122 nm,

given in Figure 4.2. The HRTEM images of the NSs (Figure 4.1(e)) revealed lattice spacing of 0.251 nm and 0.210 nm, respectively, which corresponds to the lattice spacing of (311) and (400) planes of inverse spinel Fe_3O_4 [202].

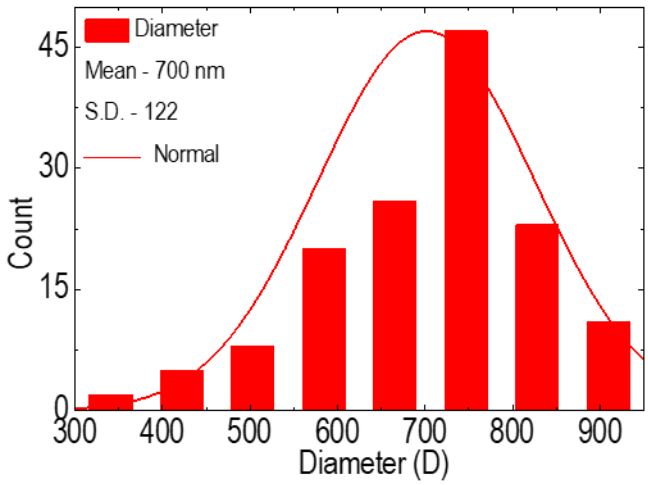

Figure 4.2: Size distribution of Fe_3O_4 NSs.

The fast Fourier transform (FFT) pattern reflects the polycrystalline nature of NSs. Figure 4.1(f) shows the XRD pattern of the Fe_3O_4 LERs, SERs, and NSs reaction products along with their Rietveld analysis. It is found that both LERs and SERs contains mixed phase of Fe_3O_4 and metallic iron (Fe^o) whereas NSs is pure Fe_3O_4. All the diffraction peaks are readily indexed to a cubic spinel phase (space group: Fd-3m with JCPDS No. 19- 0629, a = b=c= 8.37 Å) and the XRD Rietveld fitted data are given in the Table 4.1.

4.3.1.2 Fourier Transform Infrared Spectroscopy

The characteristic FTIR peaks between 600 cm^{-1} and 400 cm^{-1} observed in LERs, SERs and NSs samples correspond to the α-Fe_2O_3 and Fe_3O_4 phases, with the absorption band at 545 cm^{-1} assigned to vibrational modes of Fe_3O_4, clearly shown in Figure 4.3. A second characteristic peak detected at 976 cm^{-1} is consistent with phosphate (PO_4^{3-}) anions with typical wavenumbers within the 950-1200 cm^{-1} range [200]. A very sharp peak emerges in the NSs sample suggesting a high concentration of phosphate groups are trapped on the nanoparticle surfaces.

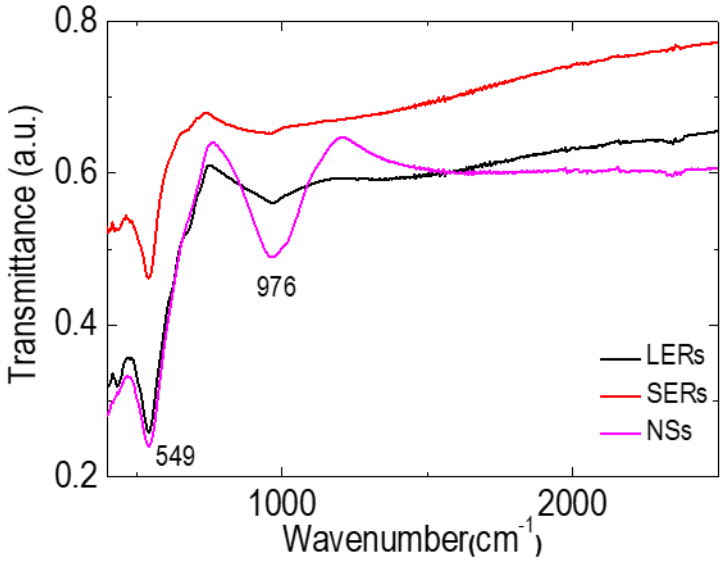

Figure 4.3: FT-IR of all the samples, i.e. LERs, SERs, and NSs. The detected peaks 549 cm^{-1} and 976 cm^{-1} represent iron oxide (Fe_3O_4 here) and phosphate anion, respectively.

Table 4.1: Study of lattice parameter and phase analysis.

Sample	Lattice parameter (nm) ±0.005	Phase Analysis				Magnetic measurement	
		XRD(±1)		Mössbauer(±2)		Verwey transition temp (Tv)	M_S (emu/g)
		Fe_3O_4(%);	Fe^0(%)	Fe_3O_4(%)	Fe^0(%)		
LERs	Fe_3O_4 =0.838 Fe^0= 0.286	85.5	14.5	84	16		132
SERs	Fe_3O_4 =0.838 Fe^0= 0.286	86	12.4	87	11	122 K	108
NSs	Fe_3O_4 =0.837	100	-	100	-		76

4.3.1.3 Theoretical and Micromagnetic Simulation

The theoretical analysis (see section 1.6) and micromagnetic simulation (see section 1.12) were exploited based on their magnetic energy. Figure 4.4(a) shows a schematic of the vortex structure

simulated for magnetic NSs with a cross sectioned drawing (Figure 4.4c) showing the internal vortex orientation, as inferred from the simulations of the spin configurations shown in Figure 42b and d. The size of the NSs is about 700 nm in diameter, which is above the single-domain region, i.e., belongs to a vortex region that avoids the singularity point of the exchange energy. Based on Figures 4.4 (b-c), we assumed that the NSs consist of two region curling-in-plane (x-y plane) and vortex-out-of-plane (z-axis). It is interesting to note in Figure 4.4 that vortex regions are formed in the shape of solid rods/cylindrical disks of radius R_V and height R. This vortex region stabilizes the core region with radius b, which exhibited the out-of-plane magnetization under the application of a magnetic field, i.e., magnetization has a non-zero component perpendicular to the plane of the vortex region (i.e., cylindrical disks). Within the vortex, core spins are aligned along the z-direction perpendicular to the in-plane circulating magnetizations. Furthermore, in principle, the spin configuration within vortex region should have to exhibit out-of-plane magnetization; from the simulated spin configuration (Figure 4.4d), however, the region in between R_v and b can be considered as a transition region from out-of-plane to in-plane. This transition region is important in terms of change-in-energy (energy transition) from vortex to single-domain which destroy the vortex state in NSs. Figure 4.5(a) shows the energy-diameter phase diagram, where the dependence of the geometry (diameter) of the NSs on the magnetic behavior, i.e., the transition from a single-domain (SD) state to a vortex configuration separated by their boundary line, is analyzed by means of a theoretical model and micromagnetic simulation. We observed that the phase diagram consists of three regions, namely, single-domain (in-plane), transition region (single-domain to vortex), and vortex region. The vortex state is a minimum energy state (i.e. the ground state) that occurs above the critical size 90-95 nm for Fe_3O_4 of the single-domain to multi-domain NPs [238]. Single-domain state is the most favorable configuration for particles below the critical size, and the full energies of the distinctive magnetization patterns decrease with increasing diameter D.

All phase transitions take place immediately as first order phase transitions. The constructed energy-diameter phase diagram by the theoretical model is in a complete agreement with the micromagnetic simulation. In any case, the small error at the boundary line is likely due to the impact of the cubic cell discretization within the micromagnetic recreation that contributes to the extra roughness energy and thus the full ground state energy of the framework. The discreteness of the method and the utilization of a cubic mesh is the source of systematic errors of nonrectangular systems, thus raising the imprecision of micromagnetic simulations reasoned by

discretization [239]. This is more applicable to NSs since the circular boundary is estimated by a staircase of straight-line segments. Such impacts are not observed in the theoretical phase diagram.

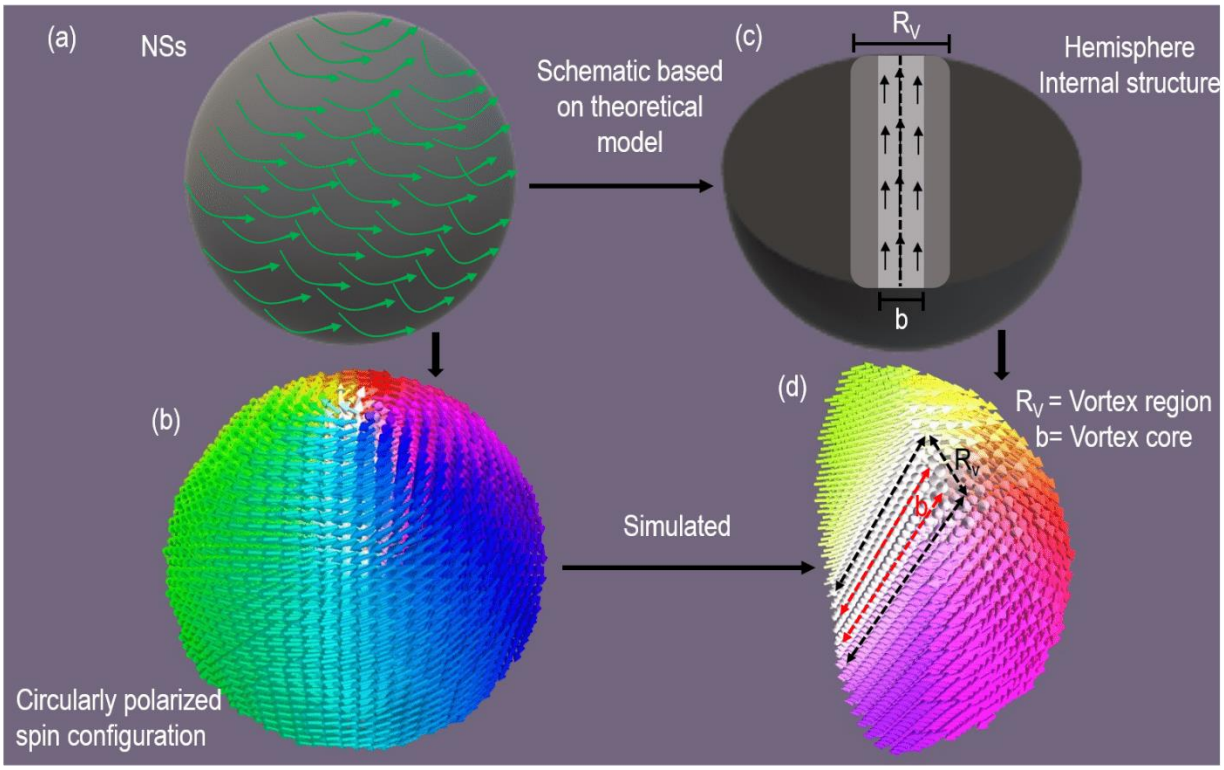

Figure 4.4. Schematic representation of the micromagnetic simulations for the spin configuration in NSs (a, b) and the corresponding cross sectioned hemisphere (c and d) showing the curling vortex internal state.

The vortex (flux-closure spin configuration) can occur in MNPs as a result of minimization of the total energy that includes magneto-crystalline anisotropy, exchange and magnetostatic energies. Although the formation of vortex state is a consequence of energy competition between exchange and magnetostatic energy, the total energy of the curling-vortex state is mainly dominated by the exchange energy; thus this interaction plays a key role in the formation of vortex states. The total energy, E_{tot}, of NSs as a function of diameter (Figure 4.5(a)) shows that E_{tot} decreases with increasing diameter within the vortex region. For diameter values above the single- to multi-domain limit (≈90-95 nm for Fe_3O_4) the NSs become a more energetically favorable state (lower energy state). The larger the diameter of NSs, the longer the displacement of the vortex core; which lowers the exchange energy and renders better stability of the vortex state reducing the remanent magnetization [38]. While the total energy is dominated by the exchange interaction through the formation of a vortex core within the vortex region, the single-domain state is dominated by the

demagnetization energy at the surface [239,240]. For large structures, the vortex state reduces the system energy by decreasing stray fields and thus lowering the magnetostatic energy. The central vortex core in NSs contributes to the out-of-plane magnetization (i.e., $m_z \neq 0$) at the origin, which is stabilized by the exchange interactions and therefore the dynamic magnetization has significant values just outside of the vortex core, i.e., in-plane magnetization [241]. Such out-of-plane magnetization leads to the observed magnetic remanence at H=0, with the actual remanence values depending on the sizes of both NSs and the vortex core.

From the energy-diameter diagram one can speculate that the NSs system should have a vortex domain structure and should possess an onion structure under application of sufficiently high magnetic field. Experimentally, evidence of vortex configuration in ferromagnetic NPs can be widely visualized via imaging techniques such as electron holography/tomography and magnetic force microscopy (MFM) techniques, but they have their own size, shape and dimension limitations. Both techniques are usually feasible for two-dimensional objects at maximum thickness/width of particles 200 nm[225,242–247]. This chapter reports chemically synthesized a three-dimensional sphere with a size 700 nm for which currently available imaging technique is not sufficient since the electron beam cannot penetrate end-to-end of the sphere, due to larger thickness, by which it is impossible to see any magnetic configuration with contrast/stray field. Even advanced technique combining electron holography with electron tomography is not feasible to detect the magnetic configuration and stray fields in 3-D materials of large-scale sphere[248,249]. Instead of imaging techniques, another way to verify the vortex configuration in NSs is through magnetometry technique which provides an unusual irreversible hysteresis loop for ferromagnetic NPs with negligible remanance and coercive field due switching behavior of loop[41,56,58].

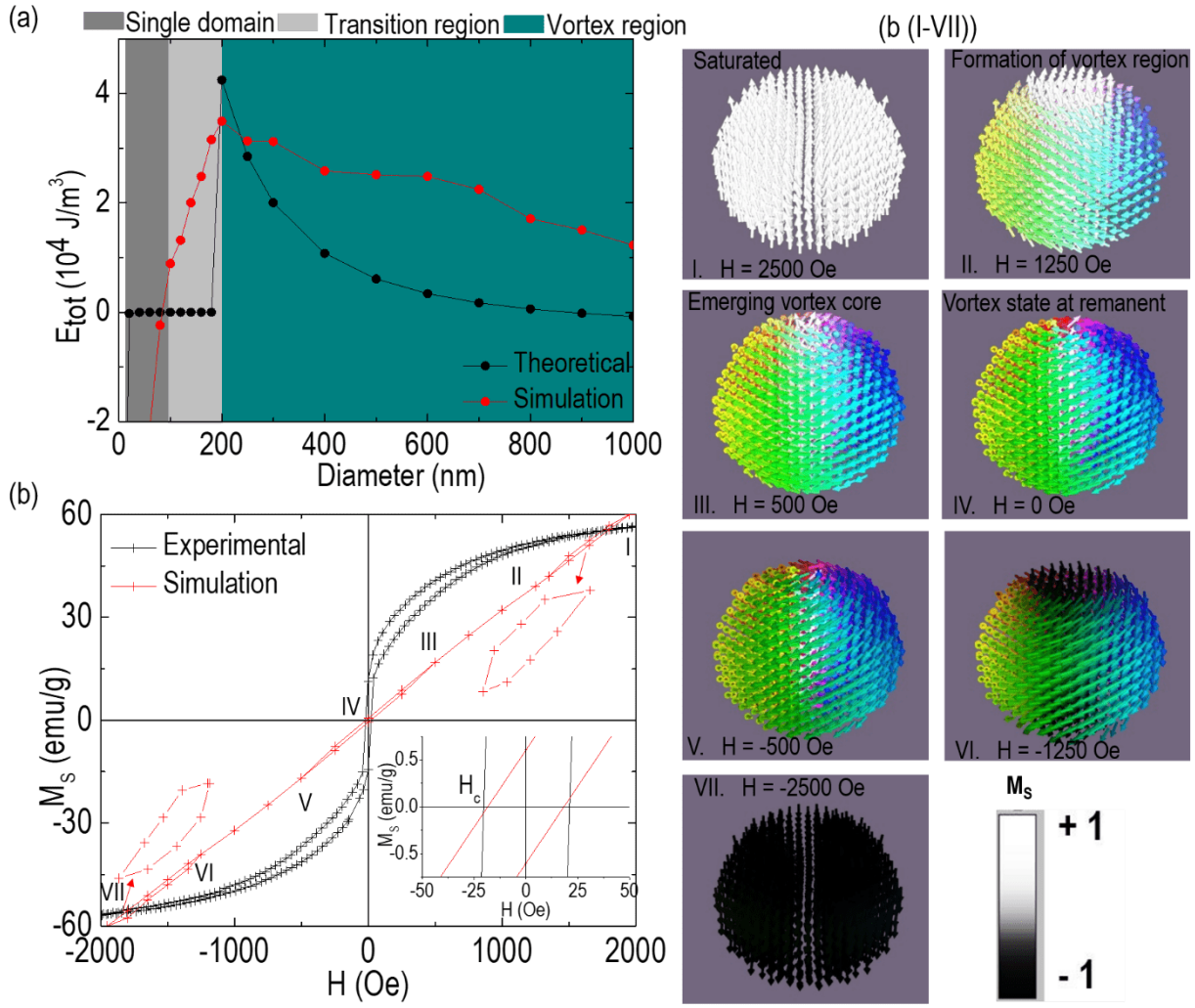

Figure 4.5: Magnetic Vortex configuration in NSs. (a) Energy-diameter phase diagram of NSs, (b) Experimental and simulated hysteresis of NSs, and (b(I-VI)) Field-dependent spin-configuration in NSs.

4.3.1.4 Magnetic Properties

Figure 4.5(a-b) shows the experimental and simulated hysteresis loops for NSs. The NSs are observed to exhibit a perfect irreversible magnetic behavior, as evidenced by the vortex-configuration having magnetic remanence and coercive field of approximately 10 emu/g and 21 Oe, respectively. The small magnetic remanence (10 emu/g) is expected from the vortex core of the NSs that induces an out-of-plane magnetization. Micromagnetic simulations consisting of moderate hysteresis loops with zero remanence and a coercive field of 21 Oe support these experimental results. The clear observation of a vortex core in the center of NSs at H = 0 and its

gyrotropic movement under the application of external field, H > 0, provides evidences of a vortex configuration in NSs. In such magnetic vortex domain structure, the hysteresis loop is composed of a two-step magnetization reversal process, which involves onion to vortex transition and vice versa [250,251]. At a large external magnetic field H values, NSs fall into a saturation state or a single domain state, as shown in Figure 4.5(b(III)) because all spins are parallel to the field direction. The complete phenomena of hysteresis loop (vortex, onion, annihilation and c-state) with respect to the magnetic field are represented in Figure 4.5(b(I-VI)), where the white color indicates saturation magnetization in positive direction and black color indicates the saturation moment in negative direction. Thus, taking all together i.e., from theoretical analysis, magnetometry experiment, and micromagnetic simulation, confirms the existence of vortex configuration in the NSs.

Figure 4.6(a) show zero field cooling and field cooling (ZFC-FC) magnetization versus temperature in the absence or presence of an external magnetic field. The data clearly indicate a prominent Verwey transition (T_v) for the two samples i.e., LERs and SERs, which is typically encountered in stoichiometric Fe_3O_4, whereas no such transition is found in NSs. The Verwey transition for bulk Fe_3O_4 occurs at a temperature T_V = 119 K, above which fast electron hopping between Fe^{2+} and Fe^{3+} ions occur among the octahedral sites. For our samples the Verwey transition was observed at T_V =122 K and 125 K for LERs and SERs, respectively. As mentioned, no jump of magnetization at T_V was observed for NSs, suggesting the absence the of this transition from monoclinic to cubic phase structure [212,215]. In Fe_3O_4 MNPs, the sharp transition is related with the high crystallinity of NPs and electron hoping in between Fe^{2+} and Fe^{3+} [210,252]. The slightly sharper transition in LERs as compared to SERs is attributed to the higher percentage of stoichiometric Fe_3O_4 (i.e., 55% in LERs > 50% in SERs). This induces the comparatively effective 'electron hopping' between the Fe^{3+} and Fe^{2+} cations in B-site of LERs at temperatures $T > T_V$. In addition, the sharper transition in LERs is supported by equations (4.1-4.3); significant cation vacancy was observed in SERs as compared to LERs and this fact should have hampered the regular Verwey transition. However, such transition phenomenon does not appear in NSs, indicating that a long-range order of Fe^{2+} and Fe^{3+} on the octahedral sites has been broken for $T < T_V$.

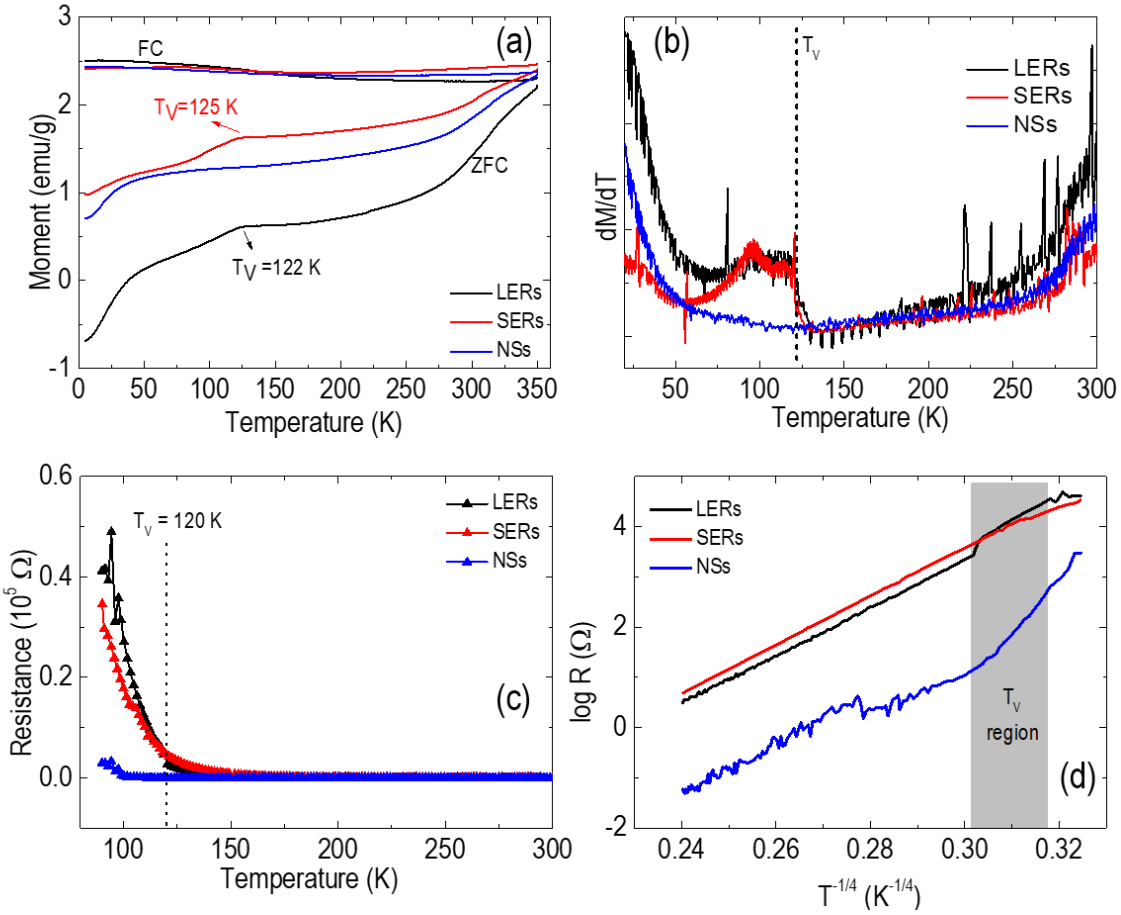

Figure 4.6: (a, b) ZFC-FC curves and their derivative at 300 K; (c) Temperature-dependent resistance variation measurements; and (d) Mott's variable range hopping law (log R vs. $T^{-1/4}$) for LERs, SERs and NSs.

4.3.1.5 Electrical Resistivity

Figure 4.6(c) shows the temperature dependent resistance that exhibits a metal-to-insulator transition, i.e., the Verwey transition, which increases exponentially with decreasing temperature below 120 K in LERs and SERs, and is indicative of stoichiometric Fe_3O_4. Here the temperature-dependent resistance curves are acquired as a function of increasing temperature, with the temperature stabilized for 20 minutes before a measurement is taken. This electrical transport measurement for all the samples were performed in a temperature range of 90-300 K. In the case of LERs and SERS, below 122 K and 125 K, a very sharp increase in resistance is observed, whereas no change in resistance is detected for NSs that almost remains constant until 100 K. Such increase of resistance with decreasing temperature below 120 K in LERs and SERs is a signature of stoichiometric Fe_3O_4. Also, we have tested the Mott's variable range hopping law [253]: Figure

4.6(d) shows the logarithmic of resistance as function of $T^{-1/4}$ in which LERs and SERs exhibit small kink around 122 K (shaded region) which is clear evidence of the Verwey transition. However, no such kink is found in case of NSs. Thus, both M_{ZFC-FC} versus temperature and electrical measurements provide a clear evidence of surface defect and oxygen vacancy in NSs that suppress the Verwey transition turning them into non-stoichiometric Fe_3O_4.

4.3.1.6 Mössbauer Spectroscopy

The Mössbauer spectra allow us to distinguish between the contributions of iron ions sitting either at A (tetrahedral) or B (octahedral) sites as well as surface defects and oxygen vacancy concentration. We have performed Mössbauer spectroscopy at 300 K as shown in Figure 4.7(a-c), and their hyperfine fitting parameters are given in Table 4.2. The spectra for all the samples were well fitted considering sextet patterns (magnetic sub-spectra). The spectrum for LERs and SERs (Figure 4.7 a, b) is well resolved by four sextets (three sextets for Fe_3O_4 and one for Fe^0) and exhibit almost similar behavior in light of compositions of Fe cation distributions. Values of hyperfine parameters for all the samples are consistent with the two crystallographic sites of iron ions in the cubic spinel (Fd-3m) structure of Fe_3O_4.[202] However, the spectral area ratio on A- and B-site was found different from bulk magnetite (i.e., 1:2 for free-defect crystals); such ratio of composition indicates that the samples have not perfectly preserved their stoichiometry. We observed that much more Fe^{3+} cations are present in the A-site than the bulk reference. Therefore, further deep analysis of Mössbauer fitting revealed that only ~ 55% of Fe_3O_4 preserved its bulk behavior i.e., stoichiometry in LERs; 18.86 % of Fe^{3+} in A-site and 35.74% of Fe^{3+} in B-site and ~ 50% of Fe_3O_4 preserved its bulk behavior i.e., stoichiometry in SERs; 16.43 % of Fe^{3+} in A-site and 33.64% of Fe^{3+} in B-site. The fitted sextet drawn in navy color represents A-site (represented by S_A) containing ~ 26% and ~ 41% of Fe^{3+} cation somewhere in the samples LERs and SERs, respectively. The results can be discussed considering possible core/shell structure model assuming that some sample region in the core follows the bulk Fe_3O_4 composition (i.e., stoichiometric) while the rest portion are non-stoichiometric with vacancies/defects probably in the shell/surface region, in agreement with previous results reported elsewhere [203,47]. The presence of stoichiometric Fe_3O_4 in these sample is the signature of the possible Verwey phase transition, which occurs near 120 K [209]. Below the Verwey temperature T_V, the valence states of all iron ions in A- and B-sites are stable, while above T_V an electron exchange between Fe^{2+} and Fe^{3+} ions in

octahedral B-sites appears and hence these valence states get unstable, giving rise to changes in many physical properties along with structural change from monoclinic to cubic, in agreement with the clear observation of Verwey phase transition in ZFC curve, shown in Figure 4.6(a).

When electron hopping occurs in B-sites of LERs and SERs, the valences of Fe^{2+} and Fe^{3+} ions are averaged to $Fe^{2.5+}$, and the charge distribution in the stoichiometric magnetite can be expected as,

$$(Fe^{3+})_A[Fe_2^{2.5+}]_BO_4 \quad (4.1)$$

It is well-established that stoichiometric magnetite has areal ratio of A-site to the B-site is $S_B/S_A = 2$; where S_B and S_A are area contain by Fe cations in each site. The overall ratio S_B/S_A is about 0.78 and 0.59 for the samples LERs and SERs, respectively. This could be explained either by the appearance of cation vacancies and/or by surface effects. In the case of cation vacancies (□) in B-sites , the LERs and SERs would correspond to the non-stoichiometric magnetite with the chemical formula

For LERs,

$$(Fe^{3+})_A[Fe_{0.78}^{2.5+}\square_{1.22}]_BO_4 \quad (4.2)$$

and,

For SERs,

$$(Fe^{3+})_A[Fe_{0.59}^{2.5+}\square_{1.41}]_BO_4 \quad (4.3)$$

The cation vacancies are in increase order can be seen in equations (4.1-4.3) as result of significant reduced of charge ordering between Fe^{3+} and Fe^{2+} at temperatures $T < T_V$ on the B-sites. In addition, one sextet of metallic iron (Fe^0) is also observed in both samples and represented by olive color in Figure 4.7(a, b) which is confirmed by analysis of the hyperfine parameters (see Table 4.2) and agree with the results obtained from XRD data analysis (Table 4.1).

For NSs, on the other hand, no evidence of stoichiometric Fe_3O_4 is found in terms of available composition of Fe^{3+} and Fe^{2+}. It is observed that three sextets containing one sextet of Fe cation in

A-site and two of Fe cations in B-site (i.e., each of Fe^{3+} and Fe^{2+} cation) as shown in Figure 4.7(c). The presence of two sextets in the B-site, each from Fe^{3+} and Fe^{2+} cation, indicates absence of electron hopping ($Fe^{2+} \rightleftarrows Fe^{3+}$) at $T > T_V$. The fitting hyperfine parameters as given in Table 4.2 show that the distribution of Fe^{3+} and Fe^{2+} in A- and B-sites are far away from the bulk (1:2) that concludes the large number of Fe^{3+} vacancies in B-sites. This result is further confirmed by ZFC and resistance measurements where no signal of Verwey phase transition is observed.

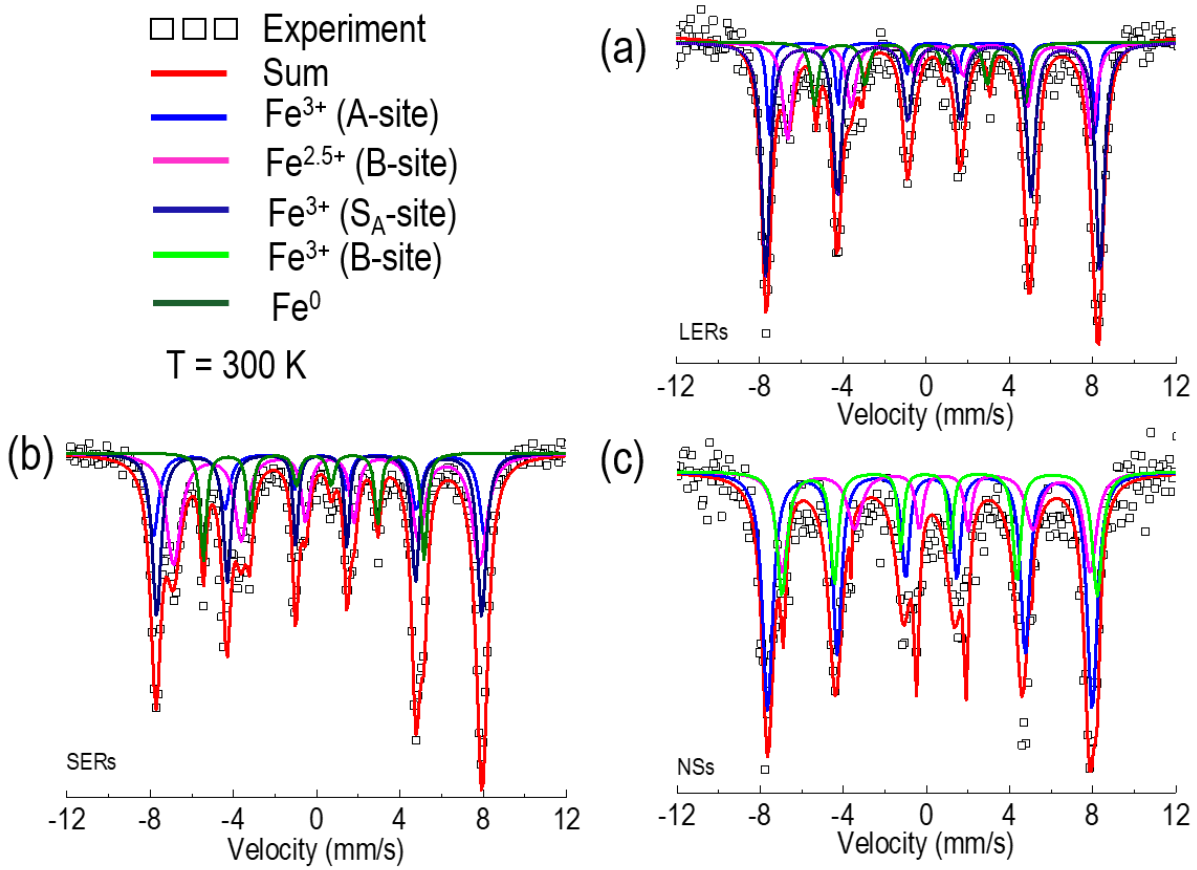

Figure 4.7: (a-c) Mössbauer spectra recorded at T = 300 K for LERs, SERs, and NSs.

The magnetic moment 'M' per formula unit of the stoichiometric Fe_3O_4 is 'M' $=4\mu_B$. In the present work, the part of non-stoichiometry in LERs, SERs, and NSs led to the magnetic moment 'M' = $3.76\mu_B$ with $\delta = 0.12$ and hence can be represented by non-stoichiometric formula $Fe_{2.88}O_4$, 'M' = $3.68\mu_B$ with $\delta = 0.14$ and represented by $Fe_{2.86}O_4$, and 'M' = $3.52\mu_B$ with $\delta = 0.16$ and represented by $Fe_{2.88}O_4$ for LERs, SERs, and NSs respectively. The increased presence of vacancies and

surface effects from LERs to NSs is believed to be due to an increase in concentration of phosphate anions during synthesis.

Table 4.2: ^{57}Fe Hyperfine parameters, isomer shift (IS, δ_C), quadrupole splitting (QS, ΔQ), and hyperfine field (B_{hf}) and spectral area (population distributions) for the diverse iron oxide NPs.

Sample	Phase	Site	Mössbauer Fitted Data			
			IS, δ_C(mm/s) ±0.01	QS, ΔQ(mm/s) ±0.01	B_{hf} (T) ±0.1	Population (%) ±2
LERs	Fe_3O_4	A(Fe^{3+})	0.29	-0.07	49.48	18.86
		B (Fe^{3+}, Fe^{2+})	0.69	-0.15	45.70	35.74
		A(Fe^{3+})	0.32	-0.002	49.70	26.54
	Fe		-0.02	0	33.00	18.85
SERs	Fe_3O_4	A(Fe^{3+})	0.32	-0.04	49.64	16.43
		B (Fe^{3+}, Fe^{2+})	0.63	0.07	45.33	33.64
		A(Fe^{3+})	0.32	-0.002	49.70	41.17
	Fe		-0.02	0	32.96	8.8
NSs	Fe_3O_4	A(Fe^{3+})	0.31	-0.064	48.83	55.58
		B(Fe^{2+})	0.79	-0.37	46.52	21.20
		B(Fe^{3+})	0.38	0	47.64	23.22

Let us recall the synthesis of the reaction products presented in this work; the LERs, SERs, and NSs were produced by simply increasing the concentration of phosphate anions. Increase concentration of phosphate anions, which consists particularly O_2, would easily oxidize Fe^{2+} to Fe^{3+} ions to possess higher spin states resulting the numbers of Fe^{3+} and Fe^{2+} ions on octahedral sites are unequal below T_V, leading to disappearance of charge ordering and hence no transition in NSs. Now, if we relook at Mössbauer and magnetic data which is consistent with synthetic process; higher percentage of oxidation state (Fe^{3+}) is expected in NSs. The reduced population of Fe^{2+} and increasing population of Fe^{3+}, raised cation vacancies, which are conversely supporting to each other. No transition was observed in NSs due to the absence or lacking of significant electron hopping($Fe^{2+} \rightleftarrows Fe^{3+}$) due to the presence of more cation vacancies/defects. Thus, the loss of stoichiometry in NSs was due to the presence of large number of Fe^{3+} cations, which is mainly due to increasing concentration of phosphate anions during synthesis.

4.4 Conclusion

In this work, we have successfully synthesized large magnetite NSs by simply controlling the concentration of phosphate anions in solution and presented the evidences of vortex spin configuration through experimental, theoretical, and micromagnetic simulations. Further, we showed the loss of stoichiometry in NSs due to the presence of defect and cation vacancies in the surface layer that impeded the electron hoping between Fe^{2+} and Fe^{3+} reinforcing the NSs into non-stoichiometry which need to be further addressed in future synthesis of such vortex NSs.

Chapter 5

Stoichiometry and Orientation- and Shape-mediated Switching Field Enhancement of the Heating Properties of Fe_3O_4 Circular Nanodisks

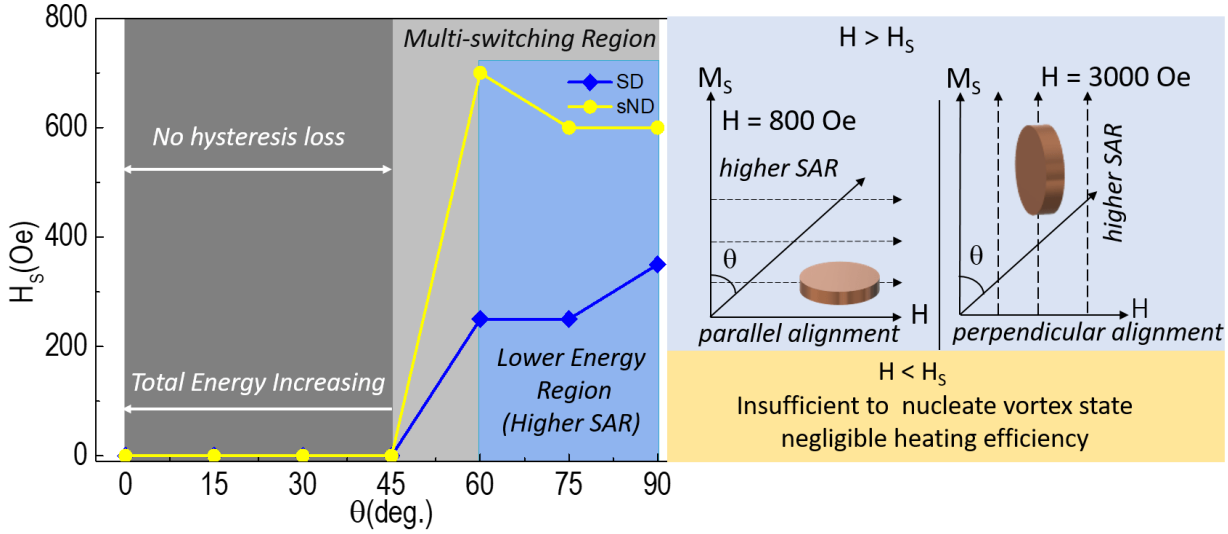

The generation of topological magnetic vortex-domain structures in iron oxide NPs has promising applications in biomedical scenarios, such as heat generators for hyperthermia treatments. In this chapter, we describe a new kind of magnetic-vortex NPs, circular Fe_3O_4 NDs, and dissect their heating properties by in-depth investigation of their shape/size, stoichiometry, orientations and switching field 'H_S' behaviors, through experiments and theoretical simulation. We found that the stoichiometric NDs show better heating performance than non-stoichiometric ones because of the significant electron hopping between Fe^{3+} and Fe^{2+} ions. The higher heating efficiency (in terms of specific absorption rate, SAR) was observed only for the higher switching field regime, effect that was associated with the parallel and perpendicular alignment of NDs with respect to low and high ac magnetic field, respectively. A higher SAR of ~ 270 W/g was observed at higher switching field (~700 Oe) for NDs of diameter 770 nm, which increased by a factor 4 at switching field of ~360 Oe for NDs of diameter 200 nm. The reported results suggest that the heating efficiency in these systems can be enhanced by controlling the switching field, which is, in turn, tuned by size, shape and orientation of circular magnetic vortex NDs.

5.1 Introduction

The technological applications of magnetic oxide based NPs, such as magnetite (Fe_3O_4) and maghemite (γ-Fe_2O_3) nanosystems, have been intensively researched and screened over the last three decades in biomedical domains, especially for their use in magnetic resonance imaging (MRI), as drug delivery systems and in magnetic fluid hyperthermia treatments (MFH)[42,57,97,254,255]. Fe_3O_4 and γ-Fe_2O_3 NPs express high biocompatibility under physiological conditions and are efficient magnetic nanoheaters. The heating efficiency of MNPs is therefore regarded by many researchers in the biomedical field as a promising therapeutic tool for enhancing selectivity in thermal therapies [256–258]. The technique involves the use of MNPs intravenously administered that are subsequentially subjected to an external ac magnetic field at a defined frequency; in this way, it can be generated local heat to those tissues in which NPs are mostly localized; in principle, this procedure allows to target specific tumor locations and to deliver heat only in the tumor area without affecting the healthy tissues [91,93]. Experimental work with SPM Fe_3O_4 NPs showed, however, that the induced heat diminishes due to low saturation magnetization (M_S) and coercivity (H_C), and hence a large quantities of NPs need to be injected to obtain therapeutic effect, which in turn might enhance the toxicity [95]. To tackle this issue, several work have been optimized; which include replacing iron oxide by other with higher M_S (Fe, FeCo etc.) [259,260]; tuning the size of the NPs; enhancing the H_C (or anisotropy) through exchange coupling/doping [259–262] or modifying the morphology (aspect ratio, shapes): cubes, octopods, octahedral, cube-octahedral of the MNPs [1,9,16 20], to tune their anisotropy and improve their overall heating efficiency. Ferro/ferrimagnetic(FM/FiM) iron oxide NPs with multi-domain structure exhibit better heating performance as compared to SPM Fe_3O_4. Nonetheless, proclivity to agglomeration of FM/FiM NPs remains a major challenge to overcome the preparation of stable colloidal suspension [42,89,96]. Recently, it has been shown that such limitations can be addressed by tailoring NPs geometry, such as NDs/NRs etc. [41–43,56,58,97,208]. The disks shaped MNPs have high M_S, large surface energy which increase their effective anisotropy, and at bigger sizes, they develop a vortex magnetic domain structure (with negligible H_C and M_R) that ensure null magnetization in the absence of magnetic field, hence reducing the long-range dipole-dipole interactions and avoid the unwanted particle agglomeration. The nucleation (H_n) and annihilation field (H_{an}), also called switching field (H_S), are responsible for the nucleation and annihilation of different state in the NPs.

An efficient magneto-hyperthermia property has been reported in the literature in the permalloy ($Fe_{20}Ni_{80}$) NDs/MDs[43,47]. Recently, another work describing orientation mediated heating performance of magnetic vortex in Fe_3O_4 NDs has also been investigated, which exhibited the highest specific absorption rate (SAR) reported so far in literature [42]. Nevertheless, there is still lack of critical understanding of the geometrical variables connected to the observed switching field distribution as function of different shape, size and orientation of NDs. Understanding the physical principles underneath such geometry-based switching field 'H_S' and their macroscopic effects on heating properties may lead to the desired generation of nanomagnetic systems in which the heating efficiency is achieved fully in a controlled way. In this chapter we describe a systematic study of MAH synthesis of Fe_3O_4 NDs (stoichiometric/non-stoichiometric) and analyzed the systems magnetic heating performances as a function of stoichiometry, geometrical factors and orientation/shape mediated switching fields. We employed the MAH route for material's assembly because it is fast and an energy efficient synthetic approach [136,141,267].

5.2 Experimental Section: Synthesis of Iron oxide Nanodisks

Two α-Fe_2O_3 NDs were prepared by a MAH reaction of iron chloride ($FeCl_3$) with addition of sodium phosphate (NaH_2PO_4) and sodium sulfate (Na_2SO_4) as additives at temperature 200 ^{0}C and 220 ^{0}C and give non-stoichiometric disc (NSD) and stoichiometric disk (SD), respectively. In brief, 0.06 mol L^{-1} of $FeCl_3$ with 35 mL of distilled water were stirred for 15-20 minutes. The additives NaH_2PO_4 ($4.32x10^{-3}$ mol L^{-1}), and $Na_2SO_4.10H_2O$ ($1.65x10^{-3}$ mol L^{-1}) mixed with 3 mL of distilled water separately and finally mixed with $FeCl_3$ solution to make mixture of final volume 38 ml. After vigorous stirring for 10 minutes, the mixture was transferred into a reaction vessel in a Synth's microwave reactor, with an output power of 1000 W. The working cycle of the microwave reactor was set as 20 ^{0}C/minutes rapid heating until 200 ^{0}C and 220 ^{0}C from RT and heat for 60 minutes at same temperature. The other procedure is same as given in section 3.2 of chapter 3.

5.3 Result and Discussion

5.3.1 Structural and Microscopy Analysis

5.3.1.1 X-ray Diffraction and Microscopy Studies

As shown schematically in Figure 5.1, the first step in the material synthesis involves assembly of the hematite (α-Fe_2O_3) NDs, which are later reduced to Fe_3O_4 in the presence of Ar and H_2.

Controlling the conversion of α-Fe_2O_3 NDs to Fe_3O_4 is a challenging task because it depends on several physio-chemical factors such as concentration of Fe^{3+}, annealing temperatures, time, gas-flow rate, concentration of H_2 gas, and amount of phosphate anions. Uncontrolled combination of H_2 and monobasic phosphate anions lead towards biphasic material; the high temperature and long duration for thermal reduction may provoke the shape coalescence [268,269].

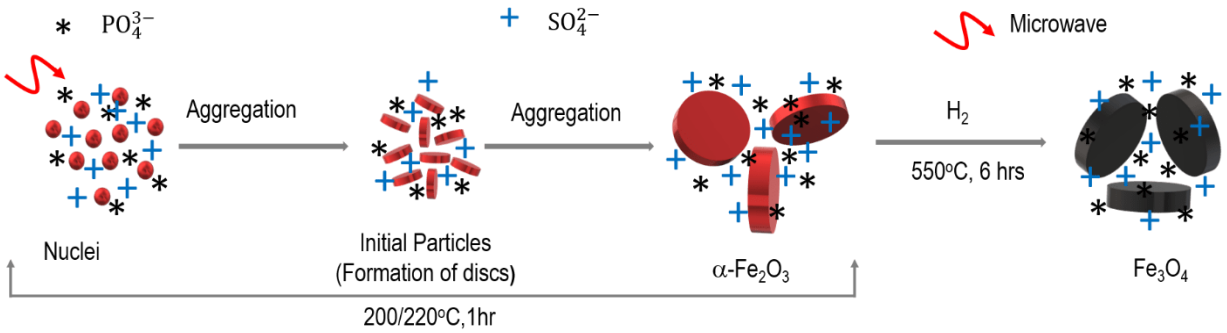

Figure 5.1: Schematic illustration of Fe_3O_4 NDs formation.

In the literature, some thermal reduction is performed using a mixture of trioctylamine (TOA) and oleic acid (OA) in order to avoid coalescence of bare NPs[19]. However, as described in detail in the synthesis, we could maintain the NDs size, phase and morphology without any addition of surfactants during the thermal reduction process. Figure 5.2(a) shows the XRD pattern of the so-formed Fe_3O_4 NDs along with their Rietveld analysis. All the diffraction peaks are readily indexed to a cubic spinel phase (space group: Fd-3m) with JCPDS No. 19- 0629, a = b=c= 8.375 Å). No other scattering signals are observed that are addressable to impurities, such as α-Fe_2O_3, and γ-Fe_2O_3, an indication for the presence of pure Fe_3O_4 phase in our NSD and SD samples.

Figure 5.2(b-c) show the FESEM images of Fe_3O_4 NSD and SD. These materials exhibit average thickness (t) ~100 nm and a mean diameter (d) ~745 for NSD and ~ 770 nm for SD (Figure 5.2(f, g) respectively) with aspect ratio (β=t/d) ~0.13. HRTEM images reveal a lattice spacing of 0.254 nm and 0.198 nm for NSD, which corresponds to the lattice spacing of (311) and (400), whereas 0.253 nm and 0.197 nm for SD agrees well with (311) and (400) planes of inverse spinel Fe_3O_4 [202] (see Figure 5.2(d-e). Polycrystalline structures are observed in both samples, NSD and SD, as analyzed through fast Fourier transform (FFT) pattern (inset of Figure 5.2(d-e)).

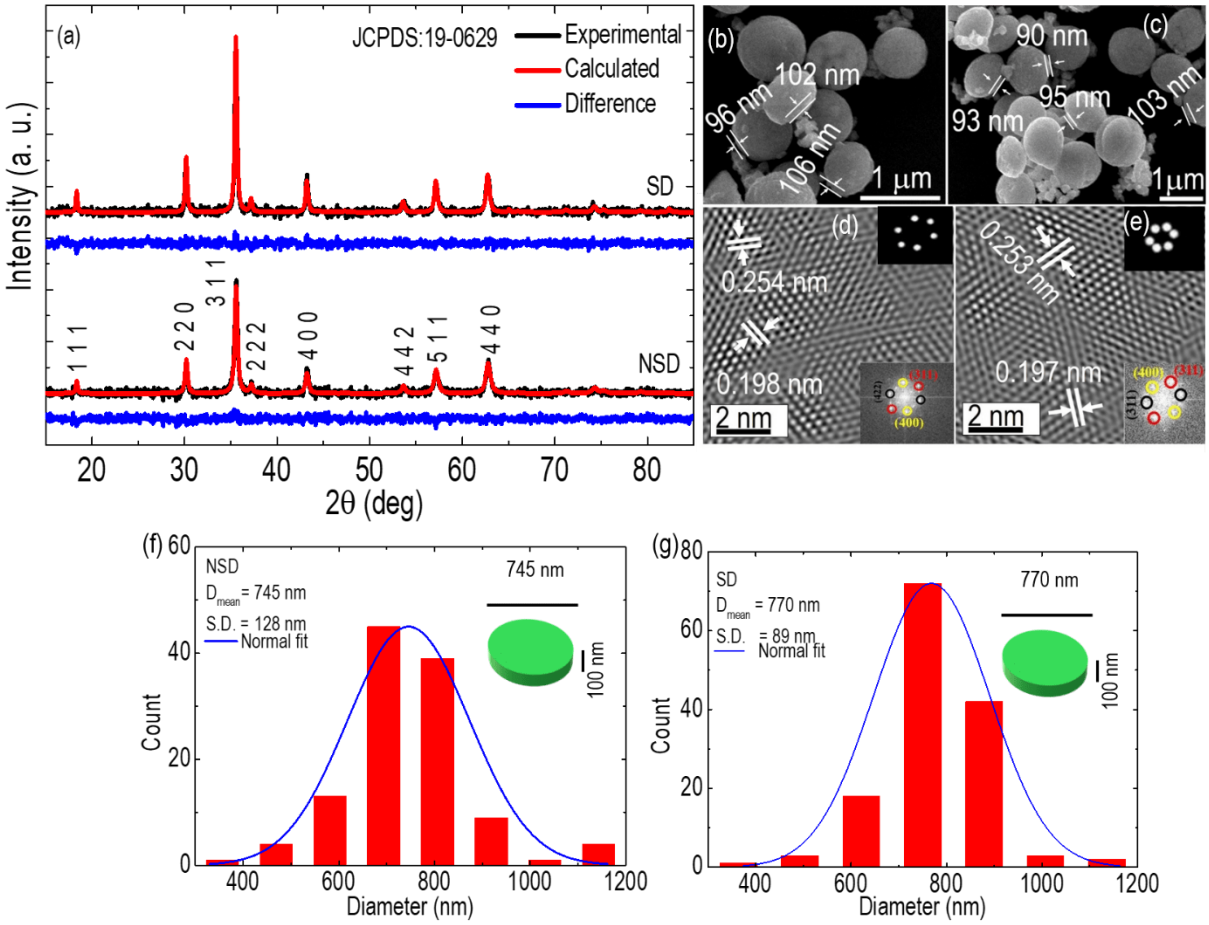

Figure 5.2: (a) XRD with Rietveld analysis, (b-c) are FESEM image after reduction, and (d-e) are HRTEM images of NSD and SD, respectively. Upper inset of figure (b, c) are magnified image with same scale. Upper and lower inset of figure (d) and (e) are IFFT and FFT images, and (f, g) are size distribution of NSD and SD respectively.

5.3.2 Magnetic Properties and Mössbauer Spectroscopy

The dc magnetization experiments, performed at 300 K, show saturation magnetization M_S for SD and NSD of ~ 83 emu/g and ~ 80 emu/g, respectively as shown in Figure 5.3(a). The higher 'M_S' of SD could be ascribed due its stoichiometry properties [204]. A small difference in 'M_S' in both samples as compared to the bulk magnetite is probably due to the presence of cation vacancies/defects, and stoichiometry deviation [204], which is subsequently discussed in Mössbauer spectroscopy section. Low value of coercive field (H_C) is observed in these materials, ~232 Oe and ~182 Oe for the SD and NSD, respectively. Although, the morphology of SD and NSD is somewhat similar, the higher 'Hc' value for SD may point towards the existence of enhanced

surface anisotropy, contribution to that may arise from structural defects, broken symmetry bonds and surface strain effects[205].

There is always an open space for defects namely point defects, dislocations, stacking faults, sub grain boundaries, inclusions and voids in the NPs generated during the synthesis [270–272]. Generally, these defects could affect magnetization in two ways: (i) they can act as centers for the nucleation of new domain walls and aid magnetization reversal. This occur at sites where the domain wall energy is locally changed by physical or chemical defects which would decrease magnetocrystalline anisotropy by creating a nucleation site and hence result in decrease of Hc, (ii) the existence of domain walls on the surface and their movement could easily be blocked by the adsorbed phosphate layers, resulting in domain walls-pinning, which contributes to effective anisotropy, which increase Hc in SD. It is worth to mention that, it is difficult to determine the type of defects and the way which affect the magnetization, but their influence on Hc is easily understood by analyzing the effective anisotropy (i.e., magnetocrystalline anisotropy, and surface anisotropy)[273]. In the present study, the surface anisotropy might have the contribution of defects; however, it is still hard to discern the exact mechanism. The observed surface anisotropy contribution is estimated as 3.02×10^6 erg/cc (for NSD) and as 3.35×10^6 erg/cc (for SD). These value are calculated using the law of approach to saturation [206], which is one order of magnitude larger than for bulk Fe_3O_4 (1.1×10^5 erg/cc) [91]. The zero field cooling-field cooling (ZFC-FC) curves exhibit a prominent Verwey transition ('T_V') for the SD at ~ 125 K, which is a typical characteristic of stoichiometric Fe_3O_4, whereas no such transition is observed for the NSD which is clearly seen in the Figure 5.3(b). The 'T_V' for bulk Fe_3O_4, is $T_V \approx 119$ K[209]. The term 'T_V' depends on the stoichiometry of Fe_3O_4 and is very sensitive to the composition of NPs as well as on the growth mechanism [212,232].

The room-temperature Mössbauer spectroscopy analysis for both NDs are well fitted considering sextet patterns (magnetic sub-spectra). From Figure 5.3(c), the spectrum for SD is well resolved by four sextets. The hyperfine parameters for both samples (Table 5.1) are consistent with the two crystallographic sites of iron cations in the cubic spinel (Fd-3m) structure of Fe_3O_4 [202]. However, the spectral area ratio on Fe cations residing on A- and B-sites diverge from those present in the bulk magnetite (i.e., 1:2 for free-defect crystals) and is 1:1.38. Such divergent A/B ratio of Fe population is evident for the samples that are not perfectly stoichiometric. These results can be

interpreted by considering the existence of a core@shell structure as model system, assuming that the core region follows the bulk Fe_3O_4 composition, i. e. stoichiometric, while the shell region is non-stoichiometric, due to vacancies/defects. In the Figure 5.3(c), two sextets, blue and pink line, were fitted using bulk parameters. These signatures belong to the Fe residing in the core region.

From the fitting analysis we obtained Fe cations with 12 % and 24 % residing in A- and B- sites, respectively, thus 36% population of Fe is stoichiometric Fe_3O_4. In this region of SD, charge ordering between Fe^{3+} and Fe^{2+} must occur, such as electron hopping ($Fe^{2+} \rightleftarrows Fe^{3+}$) at the octahedral sites, factor that has major contribution in tuning the transition temperature as observed in ZFC magnetization data. Similarly, the other two sextets considered for the shell region, drawn in Figure 5.3(c) with navy-line and green-line, represent the Fe residing in A-site and B-site, and their ratio is consistent with non-stoichiometric NPs. The population ratio in A-site and B-site is, in fact, 1:1.13 and such value indicates the presence of cation vacancy/defects.

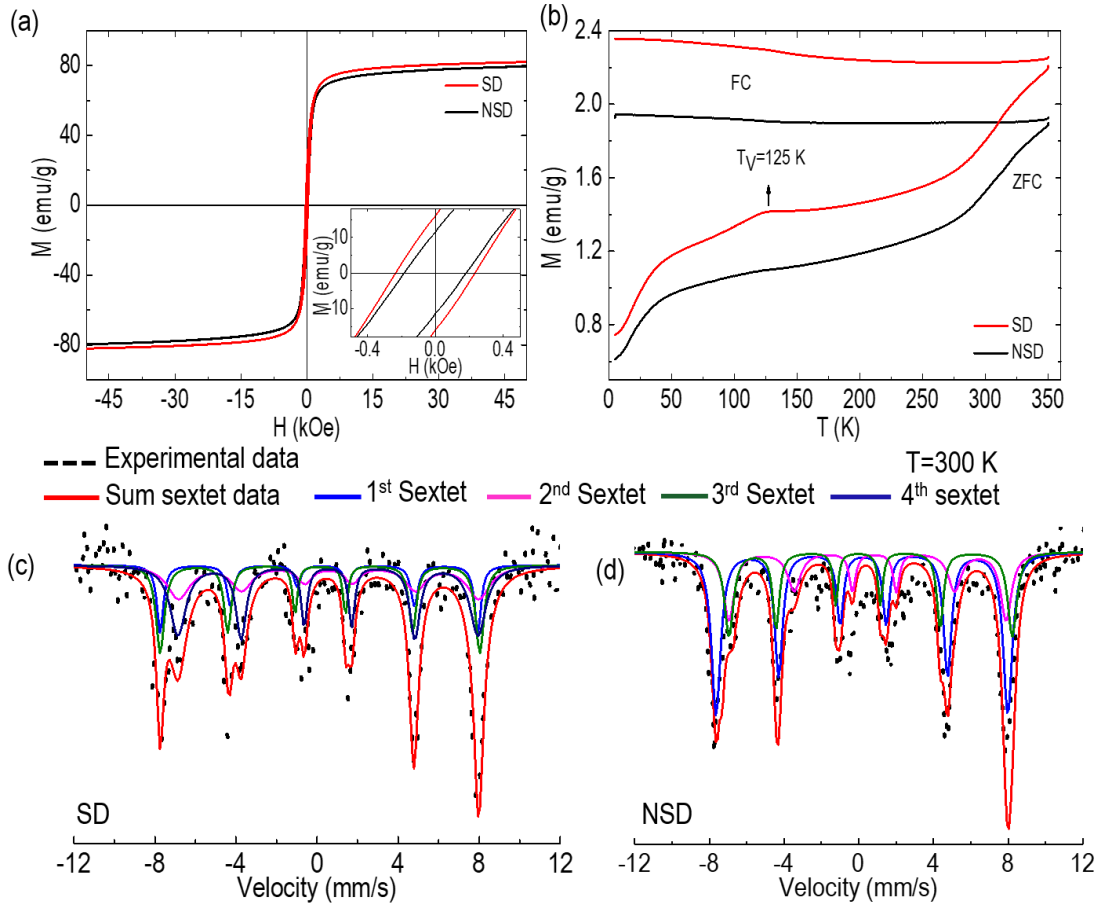

Figure 5.3: (a) represent the hysteresis loop recorded at 300 K, (b) ZFC-FC measurement, and (c, d) represent Mössbauer spectra of SD and NSD respectively at T = 300 K.

In case of cation vacancies □ in B-site, the value A/B would correspond to the non-stoichiometric magnetite with chemical formula:

$$(Fe^{3+})A[Fe^{2.5+}_{1.13}\square_{0.87}]_BO_4 \quad (5.1)$$

On the other hand, it is important to consider the surface effects. It has been reported that the magnetic moments of some iron cations in the NPs could be pinned when they belong to the surface layer, due to the presence of high magnetic anisotropy [203]. Consequently, not all B-site iron ions undergo electron hopping in response to the surface effects. In this case, we may try to evaluate some of the iron ions participating in the electron $Fe^{2+} \rightleftarrows Fe^{3+}$ exchange in the stoichiometric magnetite at $T>T_V$. From the Mössbauer line intensities and hyperfine parameters, we derive the charge distribution, as follows:

$$(Fe^{3+})_{S1}[\ [Fe^{2+}_{0.80} \rightleftarrows Fe^{3+}_{0.80}\ ]_{S2}\ [Fe^{3+}_{0.41}\ ]_{S2}O_4$$

$$(Fe^{3+})A[Fe^{2.5+}_{1.60}Fe^{3+}_{0.41}\ ]_BO_4 \quad (5.2)$$

From the above analysis of core@shell structure, we found that the core region is a stoichiometric and has a major contribution for Verwey transition 'T_V' in SD.

The quantitative size of core@shell structure of SD is analyzed using Mössbauer spectroscopy based on the distribution of Fe^{3+} and Fe^{2+} cations in A- and B-site and it is found to be ~ 277 @ 493 nm. Additionally, the observed magnetic moment 'M' per formula unit for the stoichiometric core region of Fe_3O_4 is ~ $4.0\mu_B$ with density, ρ ~ 5.1 g/cm^3, whereas the shell component (non-stoichiometric) has 'M' ~ $3.68\mu_B$ with δ = 0.074 (ρ ~ 4.66 g/cm^3) and hence represented as $Fe_{2.93}O_4$. The calculated value of M_S based upon the Mössbauer analysis is ~87 emu/g, which is very close to 83 emu/g, as obtained from dc magnetic measurements.

For NSD, it is clearly observed that the presence of three sextets: one for Fe^{3+} cations at A-site and two for Fe^{2+}, Fe^{3+} cations at B-site as shown in Fig. 5.3(d). Here, the presence of two sextets at the B-site, each from Fe^{3+} and Fe^{2+} cations, indicates clearly the absence of electron hopping ($Fe^{2+} \rightleftarrows Fe^{3+}$) above T_V. Based upon a comparative analysis of magnetization data of bulk and the NSD sample, the observed magnetic moment 'M' per formula unit for the non-stoichiometric disc is ~ $3.48\mu_B$ throughout the region and density 'ρ' ~ 4.43 g/cm^3 (as given in Table 5.2). It is anticipated that the NDs system should have a vortex domain structure and should possess an onion structure under application of sufficiently high magnetic field [42,47]. Such property has been further studied

by micro-magnetic simulation through Mumax3.9 software. The clear observation of core (vortex core) in the center of SD at H = 0 and its gyrotropic movement under the application of external field, H > 0, provides evidences of a vortex configuration in SD.

Table 5.1: **^{57}Fe Mössbauer fitted Parameters i.e. isomer shift (IS, δ_C), quadrupole splitting (QS, ΔQ), hyperfine field (B_{hf}) and obtained spectral area (population) for our different samples are tabulated as follows:**

Sample Code	Phase	Site	Mössbauer Fitted Data			
			IS, δ_C (mm/s) (±0.01)	QS, ΔQ (mm/s) (±0.01)	B_{hf} (T) (±0.1)	Population (%) (±2)
NSD	Fe_3O_4	A(Fe^{3+}) B(Fe^{2+}) B(Fe^{3+})	0.30 0.76 0.39	-0.064 -0.37 0	48.53 46.1 47.14	49.63 25 25.37
SD	Fe_3O_4	A (Fe^{3+}) B(Fe^{2+}+Fe^{3+}) A (Fe^{3+}) B(Fe^{2+}+Fe^{3+})	0.28 0.67 0.32 0.64	-0.016 0.06 -0.002 0	48.64 45.30 49.70 48.6	12 24 30 34

In such magnetic vortex domain structure, the hysteresis loop is composed of a two-step magnetization reversal process, which involves onion to vortex transition and vice versa [250,251]. At large external magnetic field (H), SD falls into a saturation state or a single domain state, as shown in Figure 5.4(a(ii)) because all spins are parallel to the field direction. The complete phenomena of hysteresis loop (vortex, onion, annihilation and c-state) in the SD nanomaterial is represented in Figure 5a(i-v), where the green color indicates saturation magnetization in positive direction and navy color indicates the saturation moment in negative direction.

Table 5.2: Quantitative analysis of physical, structural and magnetic composition of SD and NSD based upon the core@ shell model.

Sample code	Percentage (%) (±2 %)	Size (nm) (±15 nm)	Magnetization, M_S (emu/g)	Magnetic moment (μ_B)	Density, ρ (g/cm^3)
SD	Core - 36 Shell - 64	Core - 277 Shell - 493	Core - 92 Shell - 83	Core – 4.00 Shell – 3.68	Core – 5.11 Shell – 4.66
NSD	No core@shell	745	80	3.48	4.43

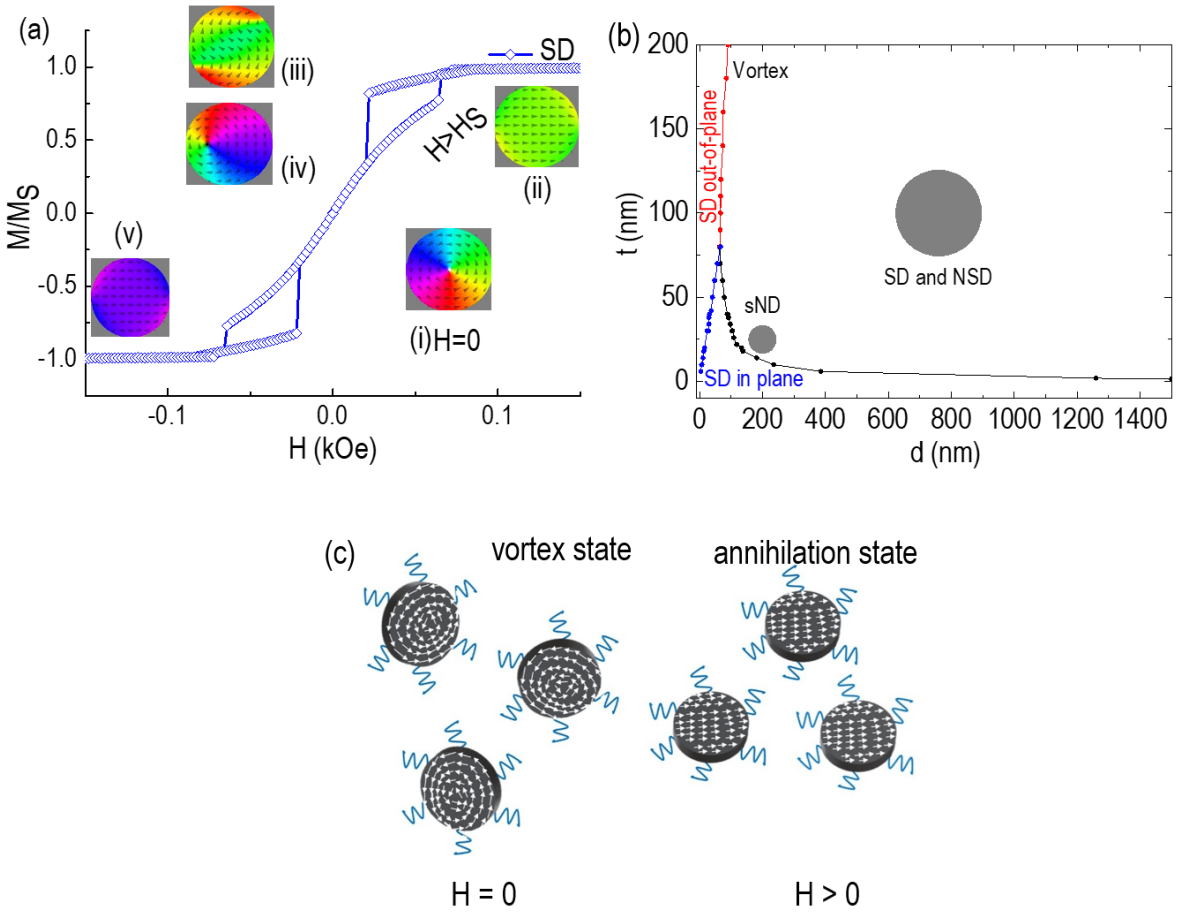

Figure 5.4: (a) Simulated hysteresis loop showing magnetic states during switching of SD, (c) Schematic illustration of vortex and onion state of SD in dispersion in absence and presence of external magnetic field 'H' respectively. Arrows indicate the spin direction.

The negligible coercive field and remanence are expected to emerge in SD through simulation. Such difference between experimental results and simulated envelope could be interpreted as an effect of the polydispersity of the sample, which was not taken into account in the magnetic hysteresis simulation. Several experimental studies of the magnetic vortex state in ferrimagnetic NDs/nanodots have been performed using magnetic force microscopy[37,274], Lorentz microscopy [127,274], and magneto-optical techniques[36,40,275] in agreement with numerical micromagnetic simulation; micromagnetic simulation is a robust numerical techniques to probe the existence of vortex configuration on experimental data. Therefore, in order to confirm the magnetic vortex configuration for nanodisc samples, a micromagnetic phase diagram is constructed based upon the lower energy state and the relative stability of magnetic phases as a function of diameter 'd' and thickness 't' (Figure 5.4(b)), based on a Landau-Lifshitz-Gilbert (LLG) equations approach. It is

clearly observed that the nanodisc samples are found in the vortex region and far from any limit of other possible ground state. We found the point at which the three ground states have the same energy, so called "triple point" ('t' ~ 80 nm and 'd' ~ 66 nm). This triple point clearly separates the three ground state region, i.e., in-plane single domain, out-of-plane single domain, and vortex region (multi-domain). From simulation, we found that critical diameter (Dc) ~ 66 nm; below which single domain region and above which multi-domain region occurs (single domain < Dc < vortex/multi-domain), which is very closed to theoretical critical size (Dc) ~ 64 nm for Fe_3O_4[276]. A detail analytical description to find the phase boundary between the in-plane, out-of-plane, and vortex magnetic phases is discussed in ref. [277,278]. In this way, we have constructed and analyzed the ground states in magnetic NDs providing explicit transition lines between vortex and in/out of plane single domain states, which is in a good agreement with ref.[278–281] and therefore provides explicitly the magnetic vortex configuration in the nanodisc samples.

5.3.3 Heating Efficiency: Experimental and Simulation

The contribution of stoichiometric NDs on the heating profile versus the non-stoichiometric one has been analyzed by using calorimetric experiments. The samples were first coated with biocompatible citric acid as a stabilizer [282] (see FITR spectra given in Figure 5.5).

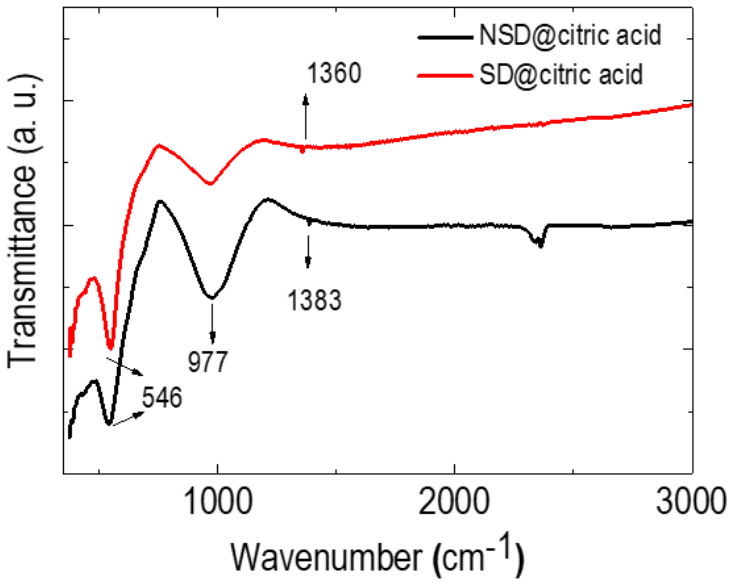

Figure 5.5: FTIR spectrum of Fe_3O_4 NSD and SD with citric-acid coating. The peak 1360 cm^{-1}, and 1383 cm^{-1} indicating the citrate molecules have been adsorbed on the surface of NSD and SD.

The SAR values were evaluated based on the temperature vs time curves. To analyze the heating efficiency, the samples were exposed to an ac magnetic field (H = 200 Oe, 300 Oe and 450 Oe, f = 107 kHz) under biologically safe conditions; the maximum product of our condition is H×f = 3.8×10^{9} $Am^{-1}s^{-1}$ which is a under Dutz conditions ($5.1\times10^{9}Am^{-1}s^{-1}$) [92]. It was observed that the heat generated after 5-6 minutes of application of magnetic field 'H' and frequency 'f' produced a small increase in temperature, ΔT, for the investigated samples (see heating profile in Figure 5.6), which is expected for large ferrimagnetic NPs. Generally, the heating performance displayed by large NPs depends on the hysteresis loss, due to its size-dependency along with applied field and frequency.

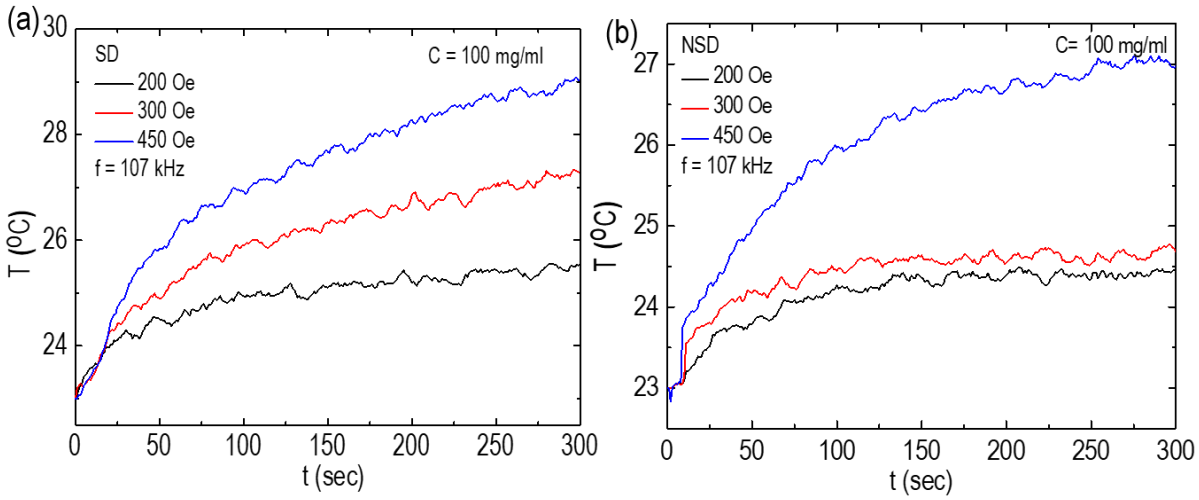

Figure 5.6: Heating profile of SD and NSD at f = 107 kHz.

Figure 5.7(a) shows the experimental and simulated SAR values for SD and NSD. The obtained SAR value are rather low, ~5 W/g for NSD, 6.5 W/g for SD and ~7 W/g for SD (obtained through simulation). The SAR value of SD is slightly higher than NSD, However, it is worth to remark that, quantitatively, the difference observed between experimental SAR values of SD and NSD were rather small, falling within the experimental errors. However, the heating profile as shown in ESI supports our assumption of the different contribution in the SAR development brought by stoichiometric over non-stoichiometric Fe.

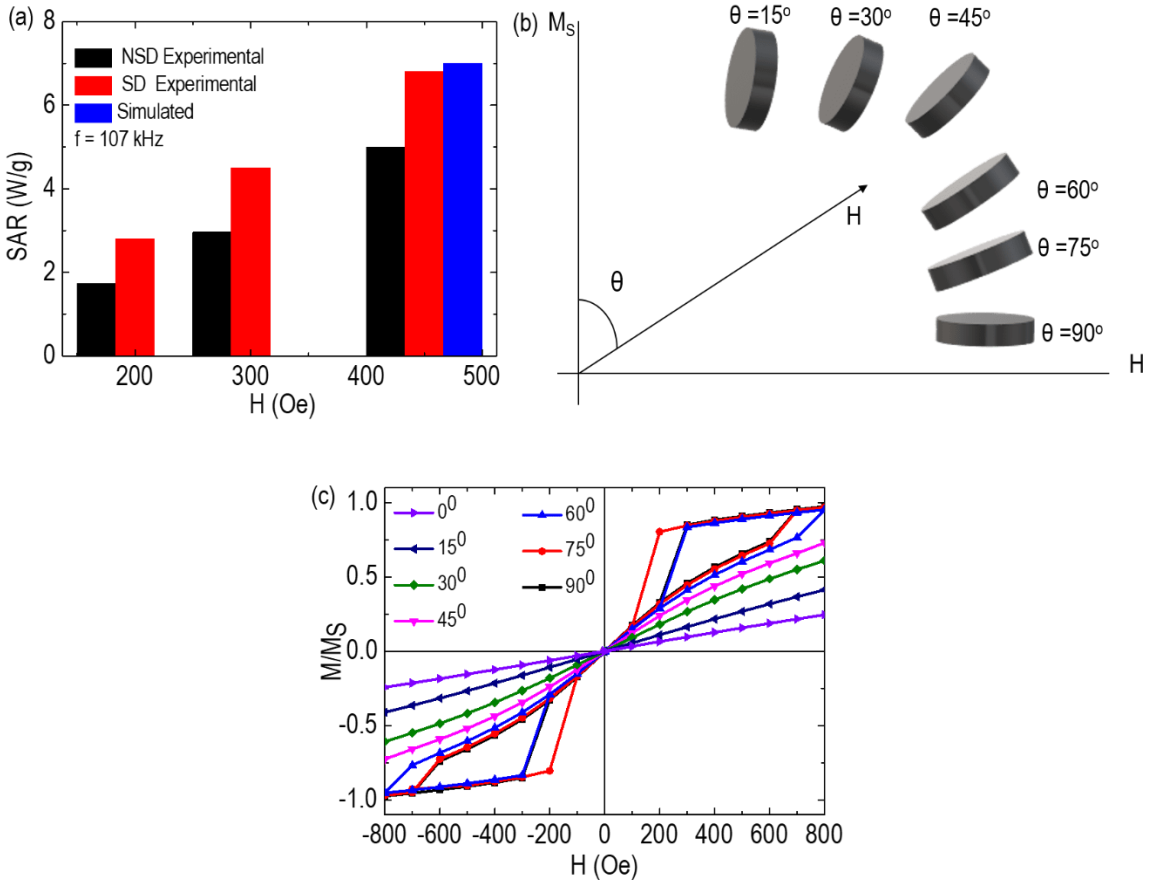

Figure 5.7: (a) represents experimental and simulated SAR value NSD and SD (Error bars indicate the standard error of the means of different SAR measurements), b) Orientation of NDs with the application of magnetic field at different angle (θ), and (c) represents the hysteresis loops of SD in different directions at 'H' = 800 Oe.

The discrepancy between experimental and simulated SAR values is probably due to the scattered alignment of NDs, in accordance with the previous published data [42,283]. The obtained SAR values for SD and NSD systems are much smaller than those reported by Yang et al.[42] and Ma et al.[284]. Nevertheless, it should be noted that even though the SAR values reported by Yang et al.[42] are among the highest reported so far in the literature, these materials remain difficult to be implemented in the real clinical trials, because the product of the field strength and frequency (H×f) range from 7.8×10^9 to 2.3×10^{10} A m^{-1} s^{-1} and exceed the upper safe limit of 5×10^9 A m^{-1} s^{-1}. Indeed, their SAR values would be lower under the application of magnetic fields that falls within the clinical relevant conditions".

The field (H = 400 Oe, 600 Oe) below switching field 'H_S', no appreciable hysteresis loss was observed, which clearly indicates that the field amplitude is not sufficient to promote the nucleation of the vortex state to onion, hence results in low SAR value. Due to the limitation of experimental setup, the maximum field and frequency (H = 450 Oe; f = 107 kHz), further, we have simulated the SAR values for SD obtained above the 'H_S'. The field dependence simulated hysteresis curves at 400-800 Oe is shown in Figure 5.9. A significant hysteresis loss was observed at 'H'= 800 Oe due to the switching phenomenon which take place around 600 Oe, thereafter vortex is nucleated to onion state. Theoretically, the area A of a particular hysteresis loop can be calculated in the variables (M/M_S, H). Hence the corresponding SAR value is then calculated by following equation [96,285]

$$\mathrm{SAR} = \frac{10^{-7} M_S f A}{\rho} \ \mathrm{W/g} \tag{5.3}$$

Where ρ is the nanoparticle density i.e., for magnetite, ρ =5.1 g/cm^3. The inset in Figure 5.9(a) represents the simulated SAR value at different field 'H' and frequency 'f'=100 kHz where increase in SAR with 'H' was observed at 'H'= 600 Oe. At low field, the observed SAR has a rather small value (< 50 W/g). When 'H' is more than 600 Oe, the SAR rises sharply and reached ~ 184 W/g ('f'=107 kHz; 'H'=800 Oe). In fact, the simulated value of SAR for 'H' in the range from 600-800 Oe, there is rapid increase in its value due to inset of switching field.

To receive an idea about SAR changes as a function applied field in these SD and NSD, we have performed ac magnetometry hyperthermia experiments which allows the direct observation on how the hysteresis loop area changes with increasing ac field and therefore their SAR evolution associating with the magnetic response (hysteresis loop area) of the NDs. For this experiment, well-stabilization of NDs in solution is necessary, and therefore we first prepared gelatin solution where 5.55 g of gelatin was dissolved in 50 mL of Milli-Q water and stirred at 80 ^oC until forming the uniform solution in light yellow color. Then, we dispersed the NDs in gelatin solution and prepared the final concentration of 6 mg/mL within volume of 0.5 mL and performed the ac hysteresis measurements. Once the hysteresis loop area is obtained, the SAR values can be calculated by using integral of the dynamic magnetization,

$$\mathrm{SAR} = \frac{f}{c} \oint_{-H}^{+H} M \, dH \ \mathrm{W/g} \tag{5.4}$$

where f is the frequency and c is the concentration of NDs, M is magnetic moment and H is ac field.

Figure 5.8 (a, b) show the ac hysteresis loops measured for SD and NSD samples in field range of 200-600 Oe at 107 kHz. Both SD and NSD exhibit similar hysteresis loop that resembles Rayleigh loops with small area; it is cleared that the hysteresis loops below 300 Oe is negligible with magnetic saturation ~ 6 emu/g and hence the observed corresponding SAR is low as shown in Figure 5.8(c). For both SD and NSD, the observed SAR at 200 Oe and 300 Oe are ~ 2 W/g and ~ 6 W/g, which quantitatively agreed with calorimetric and simulated hyperthermia results as reported in Figure 5.7. Once the ac field is increased above 300 Oe, the hysteresis loop becomes wider and subsequently the corresponding SAR increase rapidly. At 450 Oe, the magnetic saturation and coercive field in the hysteresis loop are ~ 13 emu/g and 100 Oe, respectively, which increases to ~ 20 emu/g and ~ 200 Oe at 600 Oe. The obtained corresponding SAR is ~ 22 W/g at 450 Oe and ~ 82 W/g at 600 Oe for both SD and NSD. The ac hysteresis SAR value obtained at 450 Oe (~ 22 W/g) is three times of that obtained from calorimetric method (5-7 W/g) at the same field. This discrepancy is probably due to the uniform stabilization and dispersion of NDs; we found that NDs were well dispersed in gelatin solution during the ac hysteresis measurement, as compared to citric acid coated SD and NSD measured in calorimetric method. Nevertheless, further in-depth study is necessary for complete understanding of this discrepancy.

The results obtained from ac hysteresis measurement can be explained based on the ratio of anisotropic field (H_A) to the applied ac field (H) [286,287]. From the obtained hysteresis loop, it seems that H_A of SD and NSD is higher than 450 Oe since below this no appreciably loss is obtained. We assumed that at low field (200 Oe and 300 Oe), $H < 0.5$, H_A in which heat generation is mainly caused by the viscous losses in the system exhibiting only a minor loop. Such minor loops changes to intermediate and finally to major loops with increase in ac field. On the other hand, when the field $H > 0.5$, H_A (450 Oe and 600 Oe), the maximum heat power is transferred to the NDs, and the hysteresis loop area become more and hence the SAR values rapidly increase. However, the obtained hysteresis even higher field (600 Oe) is not enough to get its saturation which indicates that ac applied field is still smaller than H_A and higher fields would be required to saturate the ac loops. This ac hysteresis measurement allowed us to observed the low-field heating response hysteresis loop of the NDs which is not possible from calorimetric method.

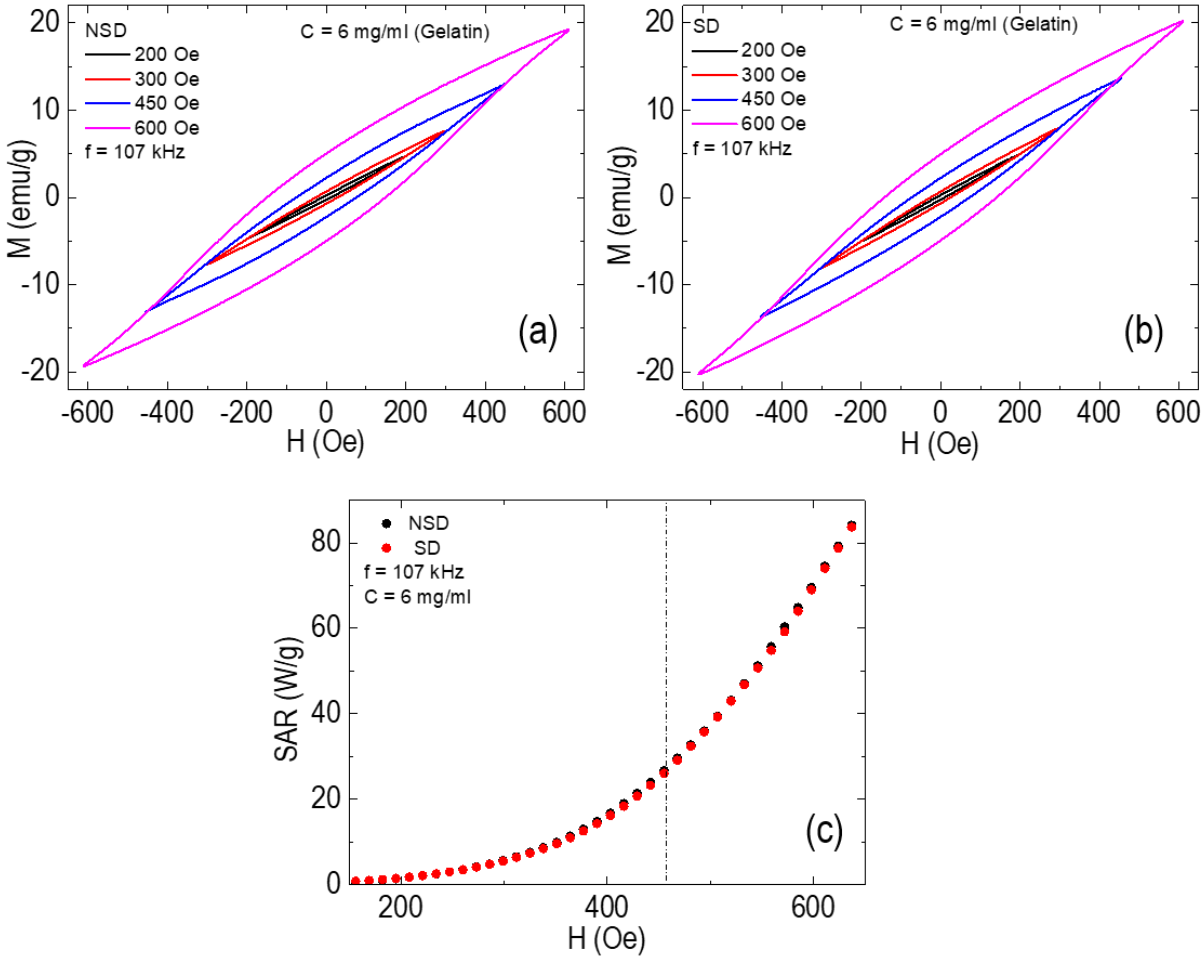

Figure 5.8: (a, b) AC hysteresis measurement at room temperature and (c) corresponding SAR values for NSD and SD.

Recently, it is reported that orientations dependent hysteresis loop of NDs with respect to ac magnetic field has significant impact in the enhancement of SAR value [41–43]. The inclination of each SD in the application of field 'H' is shown schematically in Figure 5.7(b), where symbol 'θ' represents the angle between the magnetic field 'H' and the normal direction of the SD. The hysteresis loops of SD along these incline directions are obtained through simulation, as shown in Figure 5.7(c), which disclose the possible anisotropic magnetization reversal behaviors of circular SD [44]. For θ = 0°- 45°, no hysteresis loss was observed. In the vicinity of the NDs center, the angle between adjacent spins becomes increasingly large when the spin directions remain confined in-plane. Consequently, at the core of the vortex structure, the magnetization within a small spot will turn out-of-plane and parallel to the plane normal. Although, the concept of such magnetic vortex

with a turned-up magnetization core has been introduced, still direct experimental evidence for this phenomenon is lacking.

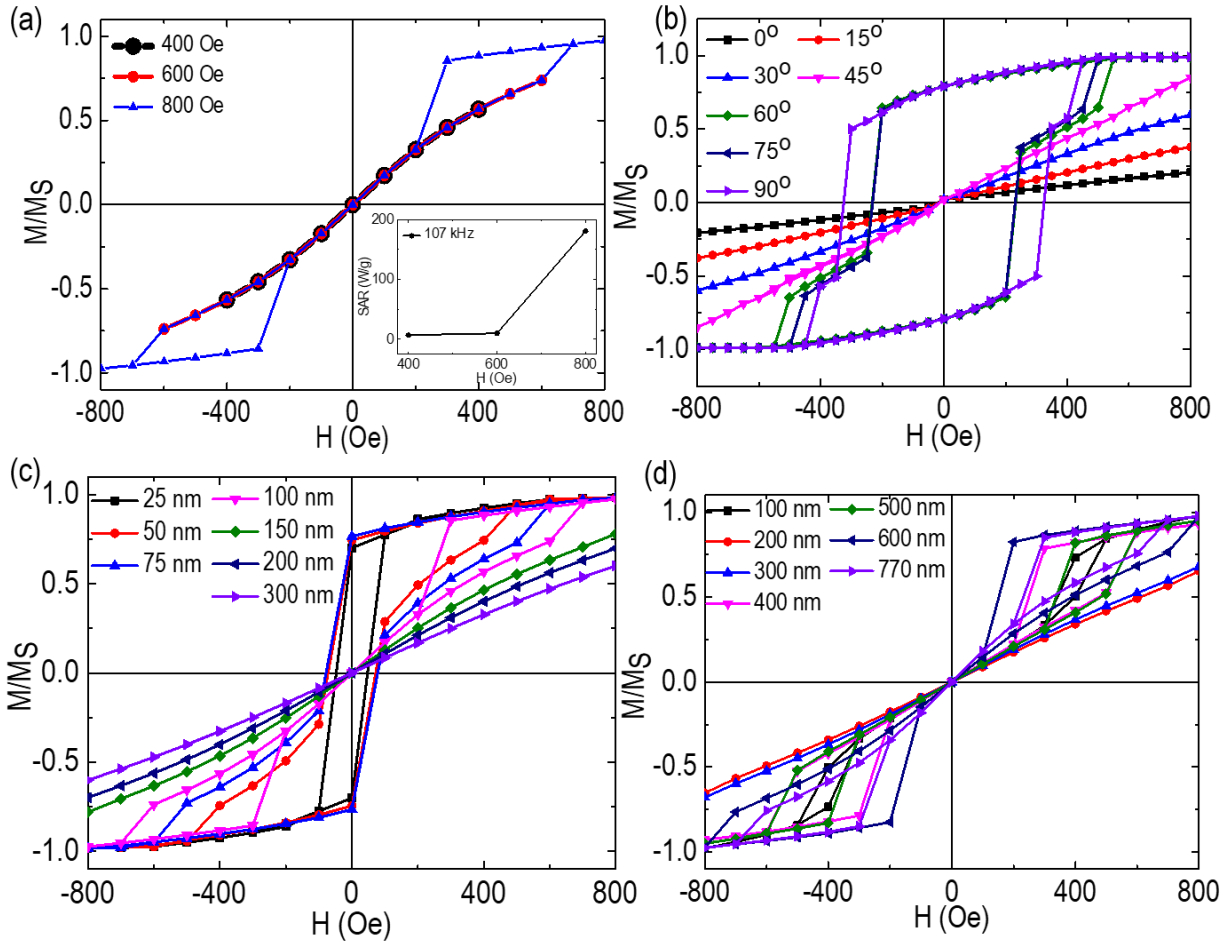

Figure 5.9: (a) Field dependent hysteresis loop at different field H=400-800 Oe, (b) direction dependent hysteresis of sND at H=800 Oe, (c) thickness(t) dependent hysteresis loss at diameter d=770 nm, (d) diameter dependent hysteresis loss at thickness, t=100 nm.

In the present work, the SD clearly shows vortex core whose spin configuration will be out of plane under the application of field in perpendicular direction ($\theta=0^o$), and hence contribute non-zero magnetization. This is in a good agreement with the study reported on the vortex state in magnetic nanodots/disks exhibiting a core region in which the magnetization has a non-zero component in the z-axis, i.e., perpendicular direction [37,239,288]. From the Figure 5.7 (c), no significant hysteresis loss is observed in out-of-plane magnetization ($\theta=0^o$). The heating properties of NDs depend on the area of hysteresis loss. Therefore, we believe that the present SD shows no significant heating efficiency in the perpendicular direction even at higher magnetic field.

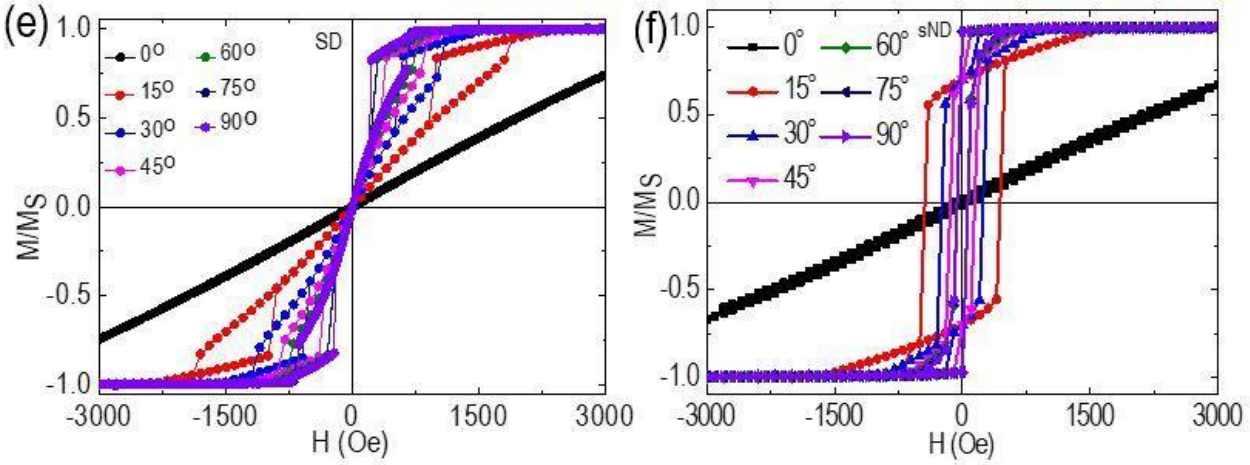

Figure 5.9: (e, f) direction dependent hysteresis loss of SD and sND respectively at H = 3000 Oe.

The multi-switching in hysteresis loop are observed when θ lies between 60°- 90°. Figure 5.10(a) shows a simulated direction-dependent SAR values of SD and it is clearly seen that the SAR changes efficiently with orientation. When θ = 60°, the SAR rises quickly and reaches a maximum value of ~ 270 W/g. The rapid increase in SAR at θ = 60° could ascribed to the occurrence of multi-switching hysteresis behavior at 'H_S'~700 Oe, clearly observed in inset of Figure 5.10(a). When θ > 60°, the SAR value is started to decrease until θ = 90° which indicates the stability of vortex state for longer time at θ = 60°, whereas the vortex state just undergoes a brief stay and is then swiftly annihilated at θ = 75° and 90° [44]. Thus, higher SAR has been observed in the parallel alignment of SD at 'θ'= 60° to 90°. The orientation of SDs for θ = 60° to 90° at 'H'= 800 Oe could consider as a vortex region owing to their lowest total energy as shown in Figure 5.11(a). It is generally believed that nanostructures with vortex domain structure should enhance the hysteresis loss due to existence of different switching field H_S but it does not mean that only the existence of vortex state is sufficient to enhance the hysteresis loss and hence the SAR value [41,42,47]. For this, the first requirement is applied field 'H' should able to nucleate the vortex state to onion state and this is possible only when $H > H_S$, where 'H_S' depends on size and shape [39,99]. In order to further strengthen this point, we consider and simulate the small hypothetical NDs (as denoted here by sND) of diameter 'd'= 200 nm and thickness 't'= 25 nm with aspect ratio 'β' = t/d = 0.13 (same as for our SD) and exhibits the magnetic vortex configuration, shown in phase diagram Figure 5.4(b). We have performed direction dependent hysteresis loss at similar simulation condition as for SD.

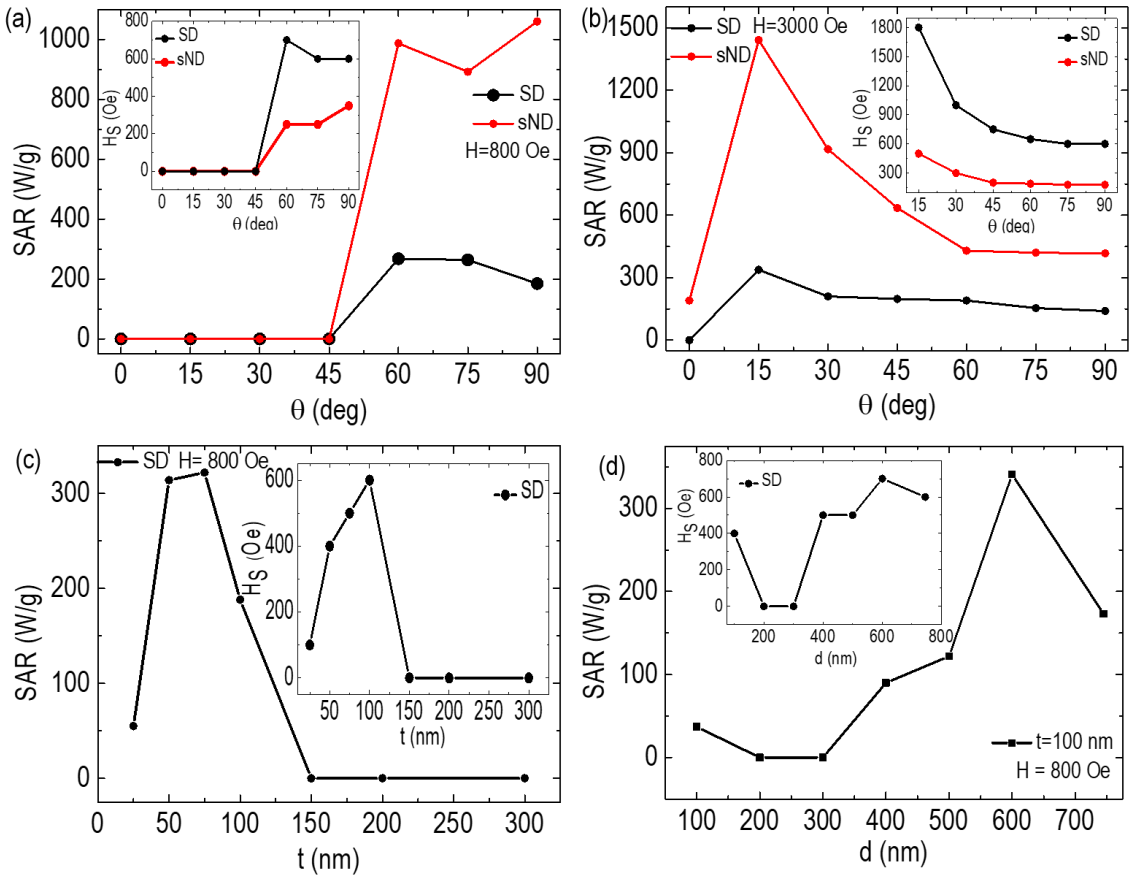

Figure 5.10: (a-b) direction dependent SAR value of SD and sND at f = 107 kHz and respective inset show an angle dependent switching field 'H_S' respectively, and (c-d) thickness 't' and diameter 'd' dependent SAR value of SD at f = 107 kHz and respective inset show thickness 't' and diameter 'd' dependent switching field 'H_S' respectively.

The observed hysteresis losses are given in Figure 5.9(b) consisting of switching field 'H_S' ~ 360 Oe (< for SD) and their respective SAR value is shown in Figure 5.10(a). In comparison, the simulated result for sND and SD, the SAR value of sND is ~ 4 times higher than that of SD i.e., 1028 W/g, which agrees well with the fact that the size is almost four times smaller than SD.

Furthermore, we have explored this correlation at higher field ('H'=3000 Oe) by analyzing similar angle dependent hysteresis loss as shown in Figure 5.9(e, f) and its corresponding SAR values is in Figure 5.10(b). At θ = 0° and 5°, no hysteresis loss was observed and the multi-switching in hysteresis loss take place at θ =10°-90°. When θ = 15°, the SAR rises quickly and reached to a maximum value ~ 340 W/g and ~ 1452 W/g for SD and sND, respectively. The direction dependent higher SAR is obtained at θ = 15°, which contradicted with direction dependent higher SAR at

'H'=800 Oe. This contradiction of angle dependent SAR at different field is probably due to the connection between the switching field (size), orientation and applied field during the formation of vortex in the SD and sND. In addition, there is always possibility of anisotropic magnetization reversal behaviors of NDs as mentioned above. However, the switching field 'H_S' is still well consistent with SAR value of SD and sND i.e., higher SAR at higher switching field 'H_S'. In both cases ('H'=800 Oe and 'H'= 3000 Oe), the angle dependent SAR is in complete agreement with 'H_S' and hence higher SAR are observed in higher 'H_S' regardless of orientation and applied field. Furthermore, to study the effect of geometrical parameters on switching field 'H_S', we have analyzed a thickness i.e., 't' (25-300 nm) and a diameter i.e. 'd' (100-770 nm) dependent hysteresis loss in reference of SD. The observed 'H_S' and SAR are shown in Figure 5.10(c-d). The obtained SAR values increases with diameter 'd' and reached to a maximum value ~ 348 W/g at 'd' = 600 nm (i.e., at higher 'H_S' as shown in inset Figure 5.10(d), but started to decrease to ~180 W/g at 'd'=770 nm at constant thickness 't' = 100 nm.

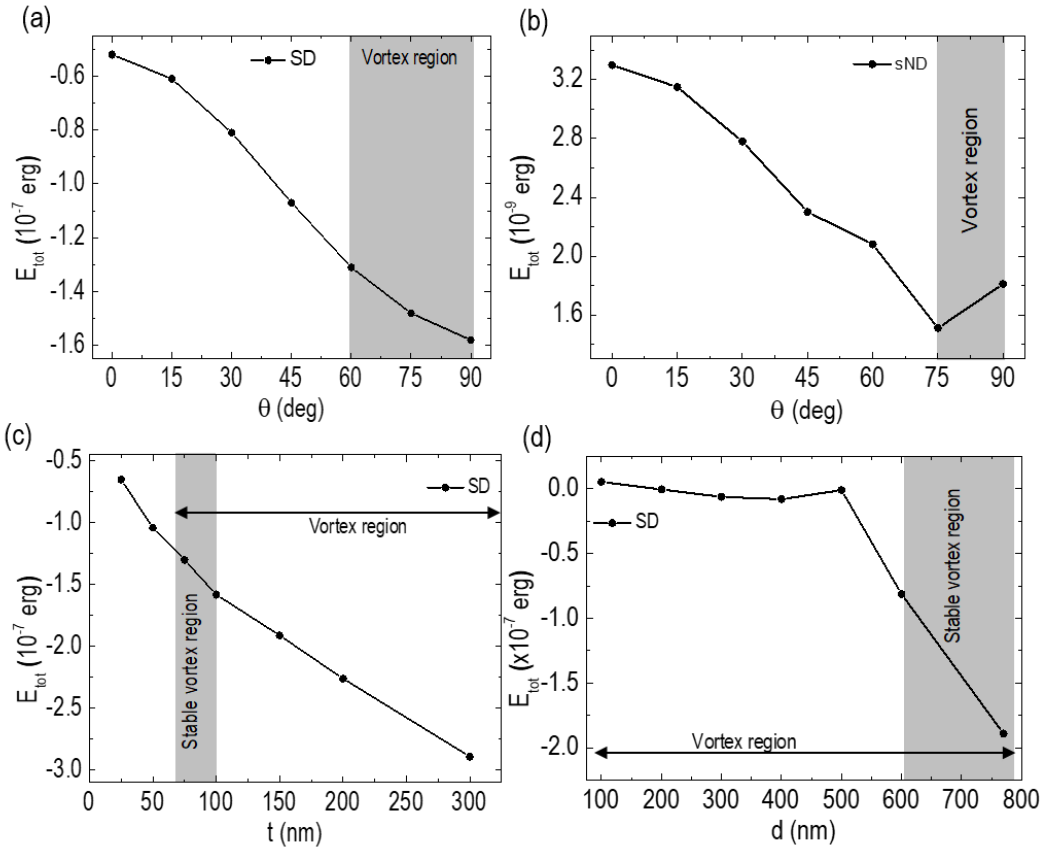

Figure 5.11: (a, b) Total energy (E_{tot}) of the SD and sND in application of field H=800 Oe and (c, d) total energy (E_{tot}) of the SD with respect to thickness 't' and diameter 'd' at H=800 Oe.

Furthermore, to study the effect of geometrical parameters on switching field 'H_S', we have analyzed a thickness i.e., 't' (25-300 nm) and a diameter i.e. 'd' (100-770 nm) dependent hysteresis loss in reference of SD. The observed 'H_S' and SAR are shown in Figure 5.10(c-d). The obtained SAR values increases with diameter 'd' and reached to a maximum value ~ 348 W/g at 'd' = 600 nm (i.e., at higher 'H_S' as shown in inset Figure 5.10(d), but started to decrease to ~180 W/g at 'd'=770 nm at constant thickness 't' = 100 nm.

The total energy (E_{tot}**)** decreases with increasing diameter 'd' and reaches a minimum at 'd' = 770 nm in our observation limit as clearly seen in Figure 5.11(d). Owing to lower energy at 'd' = 770 nm, one can expect higher SAR at 'd' = 770 nm instead of at 'd' = 600 nm. But this result is ascribed due to the stable vortex configuration at 'd' = 600 nm as compared to 'd' = 770 nm which can efficiently enhance the hysteresis loss. This result indicates that although the vortex configuration is observed in SD, perfect geometry for its stability is major factor to enhance the heating efficiency significantly which was observed at 'd' = 600 nm rather at 'd' = 770 nm in the present work. Thus, we anticipate the region of vortex configuration of SD is in the range of 'd'=600-770 nm at 't'=100 nm which is most energetically preferred region as shown in Figure 5.11(d) and lies within the vortex region given in the magnetic phase diagram Figure 5.4(b). Here whatever the vortex configuration, our concern is with diameter 'd' dependent switching field and its effect on the SAR. Thus the observed result of higher SAR at higher 'H_S' further confirm the relation between switching field and SAR as shown in Figure 5.10(d). Similarly, the hysteresis loops for SD with thickness ranging from 't'= 25-300 nm at constant diameter 770 nm, the observed highest SAR is ~ 322 W/g at t = 75 nm, as shown in Figure 4.9(c), and 188 W/g at t = 100 nm ('H'=800 Oe and 'f'=107 kHz). Here, the highest SAR is observed at second highest switching field 'H'=500 Oe which is quite different than our expectation. This is probably due to the absence of perfectness of geometry for vortex configuration as mentioned above. Thus, the anticipated region 't'=65-100 nm is vortex configuration region at 'd'= 770 nm suggesting SD with 't'=75 nm and 'd'= 770 nm has most stable vortex configuration due to which higher heating efficiency is observed at higher switching field 'H_S'. The corresponding total energy (E_{tot}) decreases with increasing thickness 't' and the corresponding vortex region as shown in Figure 5.11(c) and is well agreed with magnetic phase diagram Figure 5.4(b). It can be worth to mention that SD seems to be flat with increasing diameter (decreasing thickness) at constant 't' ('d') which means to grows towards thinner from thicker with small aspect ratio (β = t/d). For a thinner particle

('t'<< 'd'), the bending state tends to rotate as a whole with decrease in the applied magnetic field. Therefore, the lowest energy state i.e., the vortex configuration, is not accessible during evolution of the magnetization pattern in external magnetic field. At 't'= 25 nm, the vortex could not nucleate during magnetization reversal, probably due to the small thickness ('t'<< 'd') of the SD where the magnetization reversal resembles the process of quasi uniform rotation. When the thickness of SD is above 100 nm, the SAR abruptly falls to zero due to absence of hysteresis loss. Thus, the behavior of the particle resembles a single-domain one, although the actual particle size exceeds the effective single-domain regime. The shape of SD was grown towards tubular structure with the increase of thickness and one could expect the higher hysteresis loss owing to contribution of shape anisotropy. However, the size of these tubular structure is larger for which 'H' = 800 Oe is insufficient to generate the hysteresis and hence no efficient hysteresis loss is observed.

5.4 Conclusion

In summary, we have presented a circular magnetic vortex NDs of Fe_3O_4 and investigated their heating properties by both experimental as well as theoretical simulations. It is observed that the heating performance is better for stoichiometry Fe_3O_4 NDs as compared non-stoichiometry one due to charge ordering between Fe^{2+} and Fe^{3+} which is further tuned by controlling the switching field mediated shape, size and orientation of NDs in the direction of applied field in a controlled way. Larger the switching field, higher the observed SAR value. These finding could be an important insurgency in magnetic vortex NPs that the existence of vortex configuration is not only a factor to enhance heating capability but switching field mediated by shape, size and orientation are also important factors to be considered. Finally, this study sheds on light to effective design of vortex configuration Fe_3O_4 NDs and studied their heating performance by systematic adjusting their size, shape, orientation mediated switching field and stoichiometry.

Chapter 6

Engineering Shape Anisotropy of Fe_3O_4-γ-Fe_2O_3 Hollow Magnetic Hyperthermia

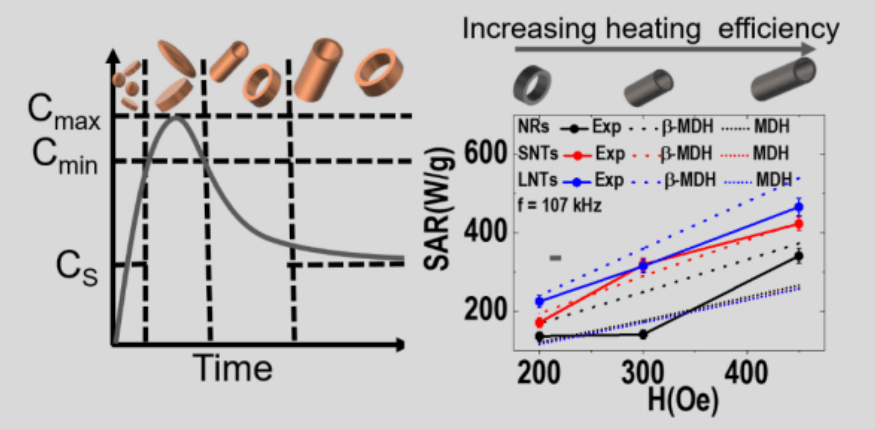

The use of MAH synthesis (in water) of α-Fe_2O_3 nanomaterials followed by their transformation onto iron oxide Fe_3O_4-γ-Fe_2O_3 hollow nanosystems encoding well-defined sizes and shapes (NRs and NTs) is henceforth described in this chapter. The impact of experimental variables such as concentration of reactants, volume of solvent employed, and reaction times/temperatures during the shape-controlled synthesis revealed that the key factor that gated generation of the morphologically diverse NPs was associated to the initial concentration of phosphate anions employed in the reactants mixture. The hollow NPs that expressed the most promising magnetic responses, NTs and NRs, were further tested in terms of efficiencies in controlling the hyperthermia phenomena, in view of their possible use for biomedical applications, possibility supported by their excellent viability as screened by in-vitro cytotoxicity tests. These systems NTs and NRs expressed very good magneto-hyperthermia properties, results that were further validated by micromagnetic simulations. The observed specific absorption rate (SAR) and intrinsic loss power (ILP) of the NRs and NTs peaked the values of 340 W/g and 2.45 nH m^2 kg^{-1} (NRs) and 465 W/g and 3.3 nH m^2 kg^{-1} (NTs) respectively, at maximum clinical field 450 Oe and under frequency of 107 kHz, and are the highest values among those reported so far in the hollow iron-oxide family. The higher SAR in NTs accounts the importance of magnetic shape anisotropy, which is well predicted by modified dynamic hysteresis (β-MDH) theoretical model.

6.1 Introduction

The application of MNPs based on various metal-oxides have been studied extensively in the last three decades within the research contexts of medical therapy and diagnostics [44,180,289–292]. Ferro/ferrimagnetic magnetite NPs (Fe_3O_4) exhibit low toxicity levels in vitro compared to other mixed-metal-oxide systems (e.g. Co/Fe, Mn/Fe, Ni/Fe) [43,293–295], but they all suffer from limited chemical stability in physiological solutions (pH values 6.6 – 7.5 and 9g/L NaCl), being accompanied with the proclivity to aggregate; those factors limit severely the range of safe-concentrations in which these magnetic nanosystems can be used in clinical application/treatments. Such limitations can be circumvented, on one hand, by functionalization of the particle surface, using for example organic/inorganic and biocompatible canopies, in order to protect the magnetic core from fast degradation (e.g. polyethylene glycol (PEG), polyvinylpyrrolidone (PVP), chitosan, SiO_2) [296–299]. On the other hand, the surface modification of the magnetic nanoparticle with organic/inorganic material often results in the decrement of the system magnetic properties expressed in terms of a reduced value in the saturation magnetization (M_s), i.e., the nonmagnetic part strongly reduces the overall magnetic property of the composite. The partial loss of the magnetic moment is expected to diminish the heating efficiency in magnetic fluid hyperthermia (MFH) application, limiting their potential use in hyperthermia treatments. To address such aggregation on ferromagnetic nanosystem, the synthesis of hollow nanosystems with magnetic flux-closure-configuration is a unique idea which avoids or at least reduces the dipole-dipole interaction [41,300]. Although, magnetism and crystal structures of magnetite (Fe_3O_4) and maghemite (γ-Fe_2O_3) are quite similar, the latter form is fully oxidized with all iron in a Fe^{3+} state and thus it is more stable against oxidation than Fe_3O_4 and more biocompatible. Also, the presence of Fe^{2+} contents of magnetite has deleterious effects in vitro due to the generation of Reactive Oxide Species (ROS) related to Fenton reaction during the cell cycle [301]; thus, it is significant for advancements in the theranostic fields to explore the potentiality of combining shape and phase controlled synthesis of Fe_3O_4 NPs interfaced with γ-Fe_2O_3. Such organization not only should translate into a better heating efficiency of the system, but also provide a fully stable and biocompatible in suspension during the MFH process. In the MFH phenomenon, the heating efficiency of the magnetic nanosystem can be enhanced upon altering the effective system anisotropy (K_{eff}), property that is related to the coercive field (H_C) [302]. The effective anisotropy can be interpreted in terms of directional dependence of the magnetic moment (μ), with anisotropic

contributions that reflects the material's magneto-crystallinity, shape, nanoparticle's surface disorder and/or surface corrugation [202]. Structural organization encoding well defined anisotropy components, such as nanosystems that adopt a hollow NPs (HNPs), are seen by many as particularly attractive for achieving better control of the MFH effect [42,264,298]. Therefore, upon altering the phase composition and the form factor (shape), one can, in principle, fully manipulate the effective anisotropy barrier in the system, which is one direct way to increase the overall heating efficiency during hyperthermia treatments. In the present chapter, we report results from our studies on the size, i.e. from microscale to the nanoscale, and shape-controlled synthesis of hollow α-Fe_2O_3 NRs and NTs using the MAH route since it is faster, simpler, and energy-efficient, due to the very high rates of microwave heating. We tested several experimental variables such as the reactant concentration, solvent (type and volume) and reaction conditions (time and temperature). After assessed the best synthetic conditions leading to hollow systems, we assembled α-Fe_2O_3 NRs and NTs that were further transformed into Fe_3O_4-γ-Fe_2O_3 materials by reduction-oxidation processes that retained the NPs initial hollow morphology. The presented Fe_3O_4-γ-Fe_2O_3 NTs and NRs systems were characterized by X-ray diffraction, scanning electron microscopy, Fourier transform infrared spectroscopy (FT-IR), Mössbauer spectroscopy, and SQUID magnetometry. The heating efficiency of these systems have been thoroughly analyzed, both experimentally and theoretically, by micromagnetic simulations and modified dynamic hysteresis model (β-MDH), which is a model applicable in the case of multidomain ferrimagnetic NPs. We found that the most promising system for theranostic applications was the long NTs (LNTs) system, which exhibited the highest SAR and ILP values of 465 W/g and 3.3 nH m^2 kg^{-1}, respectively, under clinical conditions, $\leq 5.1\times10^9 Am^{-1}s^{-1}$. Cytotoxicity tests run against three different cell lines, showed promising biocompatibility of LNTs (up to 100 μg/mL for 4T1 cells, murine mammary adenocarcinoma cell line and CT26, murine colorectal carcinoma cell line), even though a much lower viability value (2 μg/mL) was found against the J774A.1, murine monocyte/macrophage cell line. Taken together all the system properties, we believe that for further advancement in the biomedical-nanotechnology field and, in particular, in the case of iron oxide systems tailored for hyperthermia treatments, is key to develop synthetic protocols where the phase composition and anisotropic shape factor becomes the research key.

6.2 Experimental Section

6.2.1 Synthesis of Fe_3O_4-γ-Fe_2O_3 Nanorings and Nanotubes

The α-Fe_2O_3 NRs and NTs were prepared by a microwave-assisted hydrothermal reaction of iron chloride ($FeCl_3$) with the addition of sodium phosphate (NaH_2PO_4) and sodium sulphate ($Na_2SO_4 \times 10\ H_2O$) as additives to control the shape and morphology. The additives, NaH_2PO_4, and $Na_2SO_4 \times 10\ H_2O$, were mixed with 3 mL of distilled water separately and mixed with solution of $FeCl_3$ (73 mL) to obtain a mixture of final volume 76 ml which was then stirred for 15-20 minutes; the reactants concentrations used for the nanomaterials assembly were $FeCl_3$ (0.06 mol L^{-1}), NaH_2PO_4 (1.8×10^{-4} mol L^{-1}, 3.6×10^{-4} mol L^{-1}, and 7.2×10^{-4} mol L^{-1}), and $Na_2SO_4 \times 10H_2O$ (1.65×10^{-3} mol L^{-1}). After vigorous stirring for 10 minutes, the mixtures were transferred into a reaction vessel in a Synth's microwave reactor with an output power of 1000 W. The working cycle of the microwave reactor was set to (i) first step: 20 ^{0}C/minutes rapid heating until two different temperatures were reached 220 ^{0}C and 240 ^{0}C starting from RT, and second step (ii): kept for different time (30 and 60 minutes) at those temperatures. The systems were then allowed to cool down to room temperature and the final materials were obtained by centrifugation and were washed with an excess of distilled water and absolute ethanol. Finally, the solids were dried in a vacuum oven at 50 °C. These as-obtained, dried α-Fe_2O_3 NRs and NTs were subsequently reduced by annealing in a furnace at 420°C for 5 hours under a continuous hydrogen/argon gas flow [H_2/ (H_2 + Ar)) = 4/100]. Then the system was cooled down to room temperature under a continuous gas flow to obtain the Fe_3O_4 phase. Finally, the Fe_3O_4 phase was transformed into Fe_3O_4-γ-Fe_2O_3 by oxidation under oxygen flow at 240 °C for 1 hour, keeping the desired Fe_3O_4-γ-Fe_2O_3 phase composition while preserving their initial NRs and NTs morphology.

6.2.2 Cells Culture Procedures

The murine mammary adenocarcinoma cell line (4T1); murine colorectal carcinoma (CT26); and murine monocyte/macrophage (J774A.1) used in this work were purchased from American Type Culture Collection (USA) and cultured in RPMI supplemented with 10% (v:v) faecal bovine serum (FBS), 100 units penicillin/ml and 100 mg streptomycin/ml (Gibco®, Carlsbad, CA).

Cells were maintained in an incubator under a humidified atmosphere with 5% CO_2 at 37 °C. The in vitro tests were performed using 96-well microplates, with initial cell density of 10^4 cells per well. We tested the cytotoxic potential of the two nanoparticle samples, NR and LNT, against three different cell lines: (i) J774A.1; (ii) CT26, and (iii) 4T1. Briefly,

cells were seeded in cell density of 10^4 cells/well in 96-well culture microplates and after 24 hours to cell attachment, culture media was replaced by new media containing the NPs (NR and LNT) in different concentrations (0-100 µg/mL). Cells were exposed to NPs for 24 hours, and after that media was removed, the cells were washed with PBS and the cell viability was then assessed by the MTT assay.

Table 6.1: Synthetic conditions employed for the assembly of the reported nanostructured materials (precursor's concentration, temperature employed, and solvent's volume), including the final shape and size distribution of the so-obtained nanomagnetic components. In all cases, the values for $FeCl_3$ and $Na_2SO_4.10H_2O$ were 0.06 mol/L and $1.65x10^{-3}$ mol/L, respectively.

#	NaH_2PO_4 [mol L^{-1}]	Solvent (ml)	time (minutes)	T (^0C)	Shape	Size (nm)
1.	2.7×10^{-4}	38	60	200	Capsule Shape microparticles (CSMPs)	l =2515; b = 1360 [303]
2.	5.4×10^{-4}				Ellipsoidal microrods (EMRs)	l =2230; b =1250 [303]
3.	4.32×10^{-3}				NDs	d =730; t = 100 [303]
4.	2.7×10^{-4}			220	Capsule Shape microparticles (CSMPs)	l =2723; b = 1482
5.	5.4×10^{-4}				Ellipsoidal microrods (EMRs)	l =1218; b = 670
6.	4.32×10^{-3}				NDs	d =741, t =100
7.	2.7×10^{-4}			240	Capsule Shape microparticles (CSMPs)	Similar to ESI S2
8.	5.4×10^{-4}				Ellipsoidal micro-rods (EMRs)	Similar to ESI S2
9.	4.32×10^{-3}				NDs	Similar to ESI S2
10.	1.8×10^{-4}	76	30	220	NRs	l = 275; d_{out} = 201; d_{in} = 125
11.	3.6×10^{-4}				Short NTs (SNTs)	l = 411; d_{out} = 251; d_{in} = 120
12.	7.2×10^{-4}				Long NTs (LNTs)	l = 515; d_{out} = 229; d_{in} = 124
13.	2.7×10^{-4}				Sample 'S'	l = 300; d_{out} = 207; d_{in} = ~125

6.2.3 Cell Viability Test

Cell viability was evaluated by the colorimetric assay method of 3- (4,5-dimethylthiazol-2-yl)-2,5-diphenyl-tetrazolium bromide (MTT, ThermoFisher) [304]. After the treatments, the culture medium was replaced by a culture medium with 10% (w:v) MTT. Next, cells were kept in standard culture conditions for 2.5 hours to allow the MTT reaction with the mitochondrial enzymes. Next, the MTT solution was replaced by 100 µl of dimethylsulfoxide (DMSO 99.5%, Sigma Aldrich) to dissolve cell membranes and extract the formazan crystals produced by the MTT reaction. The optical density formed by solution was measured with a spectrophotometer (λ=595 nm) and used as an index of cell viability.

6.3 Results and Discussion

6.3.1 Formation Mechanism of α-Fe_2O_3 and Fe_3O_4-γ-Fe_2O_3 Nanorings and Nanotubes

Here, we investigate comprehensively the role of phosphate anion in the formation of HNPs and show how the size, shape and morphology of HNPs can be obtained by fine tuning the concentration of reactant, volume of solvent employed, time, and reaction temperatures. The experimental variables needed to obtain such shape/morphology defined systems are collected in Table 6.1. Figure 6.1(a-c) shows the so-obtained morphology-based NPs, from micro-scale to nanoscale, resulting from the analysis of the synthetic variables given in Table 6.1. The morphological evolution of the α-Fe_2O_3 particles, from capsule-shape microparticles (CSMPs), ellipsoidal micro-rods (EMRs) to mixture of circular/spherical NDs (NDs/NSs), depended directly on the increasing concentration of phosphate anion present in the reactants mixture; the respective concentration of phosphate anion used for obtaining CSMPs, EMRs, and NDs/NSs were 2.70×10^{-4} mol L^{-1}, 5.40×10^{-4} mol L^{-1}, and 4.32×10^{-3} mol L^{-1}, respectively. When the concentration of phosphate anion was decreased by one-third (i.e., from 2.7×10^{-4} mol L^{-1} for CSPMs to 1.8×10^{-4} mol L^{-1} for NRs) and the volume of solvent was increased two fold (~76 mL from the initial ~38 mL at T=220°C), a set of NRs with length reduced by almost one order of magnitude as observed in the FESEM images (Figure 6.1d).

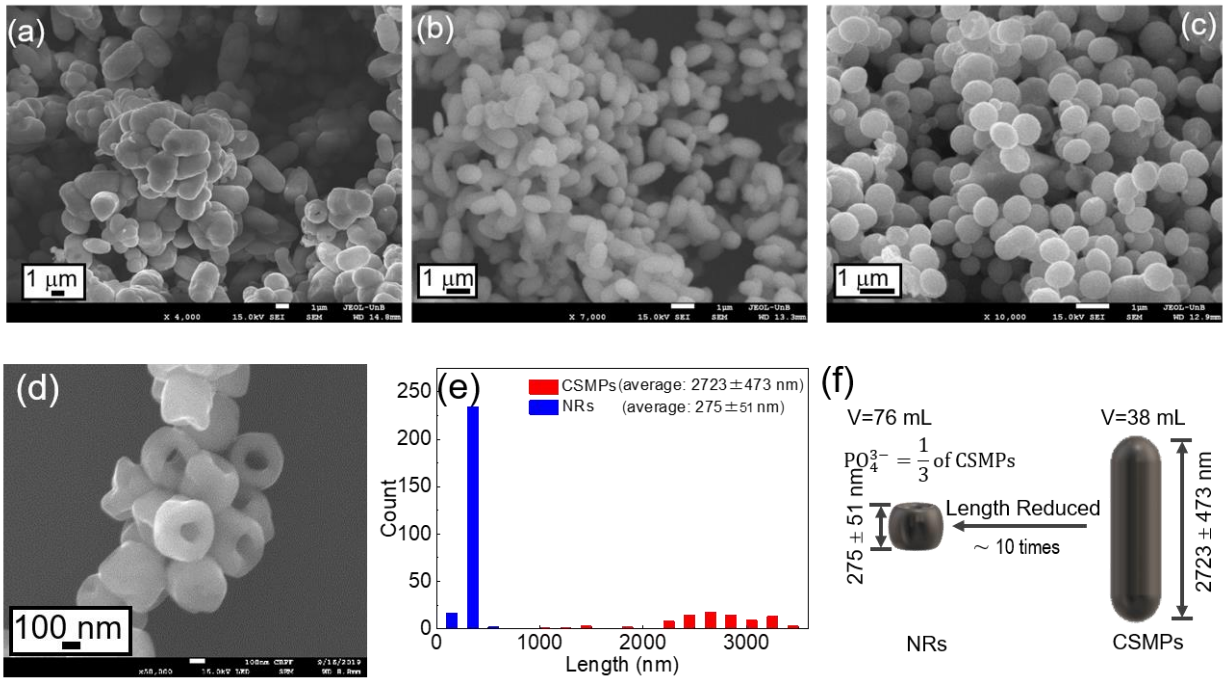

Figure 6.1: SEM images of α-Fe_2O_3 products prepared with different concentrations of phosphate anions. (a-d) represents α-Fe_2O_3 samples including CSMPs, EMRs, NDs and NRs, respectively: (a) [NaH_2PO_4] = 2.70×10^{-4} mol L^{-1}, (b) [NaH_2PO_4] = 5.40×10^{-4} mol L^{-1}, (c) [NaH_2PO_4] = 4.32×10^{-3} mol L^{-1}, (d) NaH_2PO_4 :1.8×10^{-4} mol L^{-1} (t = 30 minutes and volume of solvent V = 76 mL), (e) comparative distribution of CSMPs (a) and NRs (d), and (f) schematic illustration showing the effect of solvent volume and phosphate anion impacting the morphological parameters (length). For each case (a-d), [$FeCl_3$] = 0.06 M, [$Na_2SO_4.10H_2O$] = 1.65×10^{-3} mol L^{-1}. The temperature employed in the synthesis (T) = 220°C, time (t) = 60 minutes, and volume of solvent of 38 mL for (a-c) while time and volume solvent are different for (d) as per defined.

The size distributions (Figures 6.1e and 6.1f) showed that the length distribution of CSMPs and NRs are easily distinguishable with average length 2723 ± 473 nm and 275 ± 51 nm, respectively. The XRD patterns of α-Fe_2O_3 CSMPs, EMRs, NDs/NSs, and NRs are given in Figure 6.2 which were refined using the Rietveld method to obtain their structural parameters. These results were consistent with the α-Fe_2O_3 phase which consists of two different components, that is, grain and crystallite, in a two- crystallite size distribution, and are given in Table 6.2, with the α-Fe_2O_3 phase with bigger crystallite size being ~75-95% and the smaller crystallites ranging from ~5 to 25%. It is further noticed that the amount of minority phase is similar (i.e. ~26-29%) for CMPs, EMRs, and NDs/NSs, whereas for NRs, it is only 5%.

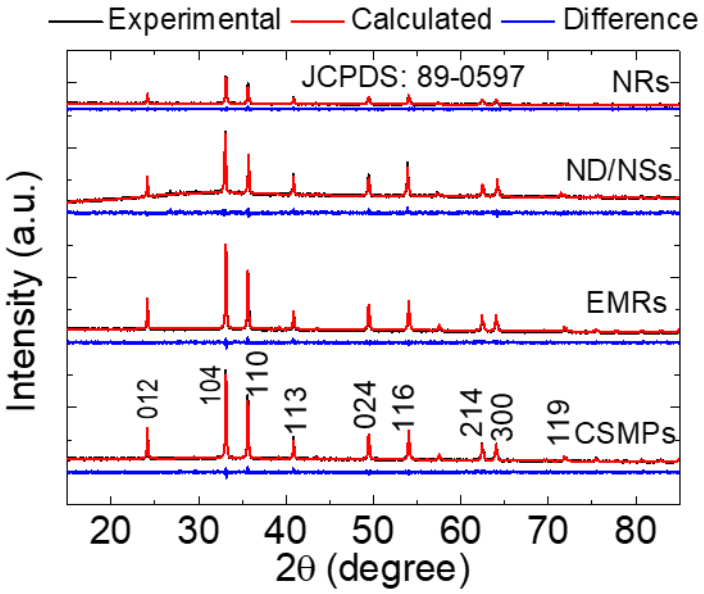

Figure 6.2: XRD pattern of α-Fe_2O_3 CSMPs, EMRs, ND/NSs, and NRs.

Interestingly, the NRs structures grown into SNTs and LNTs upon further increase of the concentration of phosphate anions. The FESEM pictures and size distribution analysis of NRs, SNTs and LNTs are shown in Figure 6.3(a-c). Scheme 1 illustrate the synthetic steps (nucleation, aggregation, dissolutions and reductions) involved in the formation of α-Fe_2O_3 NRs and NTs (SNTs, and LNTs) and their reduction into Fe_3O_4 NRs (l = 275 ± 51 nm; d_{out} =201 ± 55 nm), SNTs (l = 411 ± 92 nm; d_{out} = 251 ± 45 nm), and LNTs (l = 515 ± 98 nm; d_{out} = 229 ± 42 nm). The role of phosphate and sulphate anions in the formation of NRs to NTs is relatively different. It is reported that the sulphate anions are considered as growth controller and dissolute agent and has practically no role on shape modification at any concentration [189], thus for whole synthesis conditions, the concentration of sulphate anions were fixed. The α-Fe_2O_3 hollow NRs were obtained using low concentration of phosphate anions; further increase in the concentration of phosphate anions lead to the growth of SNTs and then long LNTs.

Table 6.2: Structural analysis of α-Fe_2O_3 CSMPs, EMRs, ND/NSs, and NRs through XRD.

Sample	Lattice parameter (nm) ±0.005		α-Fe_2O_3 (%) (±1)		α-Fe_2O_3 (Size) (±1)	
	Crystallite	Grain	Crystallite (%)	Grain (%)	Crystallite Size (nm)	Grain (nm)
CSMPs	a= 0.504 c=1.377	a= 0.504 c=1.379	74.1	25.9	190	33
EMRs	a= 0.504 c=1.378	a= 0.504 c=1.379	70.7	29.3	164	32
ND/NSs	a= 0.502 c=1.385	a= 0.504 c=1.390	72	28	220	43
NRs	a= 0.504 c=1.378	a= 0.505 c=1.381	95	5	85	33

The schematic growth of NRs towards SNTs and LNTs with increased phosphate anion is shown in Figure 6.3. The suggested growth mechanism of HNPs (Figure 6.3) was based on local superheating of the aqueous solution that produces numerous "hot spots", boosting the nucleation process. [188,190] Simply, superheating is the meta-stable state, induced by external or internal effects, in which a liquid is heated to a temperature higher than its boiling point (> 100^oC), but without boiling. It can be achieved by heating a homogeneous particles in a clean container and free of nucleation sites on microwave. Further, 'hot spot' formation is due to the localized excessive heat flux on the surface of nanoparticle during microwave irradiation. The localized overheating and resultant growth of non-protective α-Fe_2O_3 scale were considered the primary factors in the initiation of 'hot spots'. During irradiation, these 'hot spot' starts to etch due to localize ionic current generated by high conductivity and polarization of phosphate anion [305–308]. The formation of such 'hot spots' on the surface of NPs drives the assembly process of hollow NPs in a very short span of time. This effect would induce the formation of larger seeds throughout the solution, with rates that depend on the mutual reactant concentrations. The rapid formation of these "hot spots" on the surface of α-Fe_2O_3 disk/spindle-shaped NPs via irradiation is therefore a unique advantage brought by the microwave synthesis route, which cannot be achieved from any conventional heating methods.

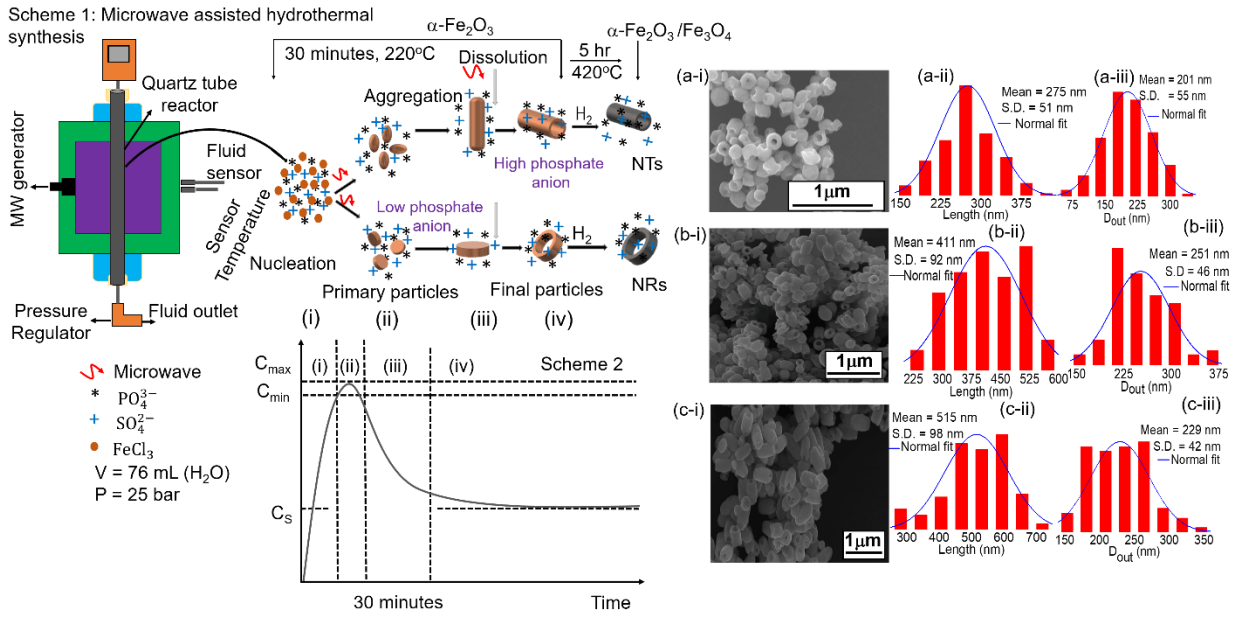

Figure 6.3: Scheme 1 illustrates the growth process of the diverse iron oxide NPs adopting NTs and NRs morphologies. Scheme 2 is the LaMer's configuration of NPs growth vs. time. Panels (a-c) give the SEM images of NRs (Panel a-i), SNTs (Panel b-i), LNTs (Panel c-i), and their respective size distribution analysis. NRs (NaH_2PO_4 :1.8×10^{-4} mol L^{-1}), SNTs (NaH_2PO_4 :3.6×10^{-4} mol L^{-1}) and LNTs (NaH_2PO_4 :7.2×10^{-4} mol L^{-1}), $FeCl_3$:0.06 mol L^{-1}, and $Na_2SO_4.10H_2O$: 1.65×10^{-3} mol L^{-1}, synthesis temperature (T) = 220°C, time (t) = 30 minutes, and volume of solvent V = 76 mL.

Localized ionic current is generated on these "hot surfaces" of α-Fe_2O_3 disc/spindle-shaped NPs, due to high conductivity and polarization of phosphate anions during the continuous irradiation process. This localized current in the α-Fe_2O_3 disc/spindle-shaped NPs drives the preferential dissolution along the crystallographic c-axis (i.e. [001] direction), and favours the formation of hollow structure in α-Fe_2O_3 NRs/NTs [57,191]. Finally, the obtained hollow NPs underwent Ostwald ripening, which leads to the final growth of NRs, SNTs, and LNTs upon increasing concentration of phosphate anion [192,193]. In the whole synthetic process, sulfate anions thus acted in two steps, i) during the dissolution process and ii) during the Ostwald ripening process, while the phosphate anions acted as shape controller only. The sulfate anions in fact are responsible for the fast dissolution process in the initial seeds growth and then they control the further growth of the system by modulating the Ostwald ripening [189,191]. Overall, the results reveal clearly that the phosphate anions act as a shape controller to induce anisotropic growth and play a crucial role in the formation of HNPs. During the anisotropic growth, the phosphate anions are attributed to the selective adsorption on surfaces parallel to the c-axis, while sulphate anions favors only the

dissolution effect due to their coordination with Fe^{3+} cations. The suggested NPs formation and their sequential growth mechanism through steps (i-iv) can be visualized with the model pathway proposed by 'Extended LaMer's Mechanism (ELM)' [309] ,shown in Scheme 2, which analyse the growth of NPs with time. Here, C_s is the super-saturation concentration, where monomers are produced and accumulates in solution, but without any formation of NPs; C_{min} and C_{max} are minimum and maximum level of supersaturation (also called as critical level of supersaturation) between which the nucleation is energetically favorable.

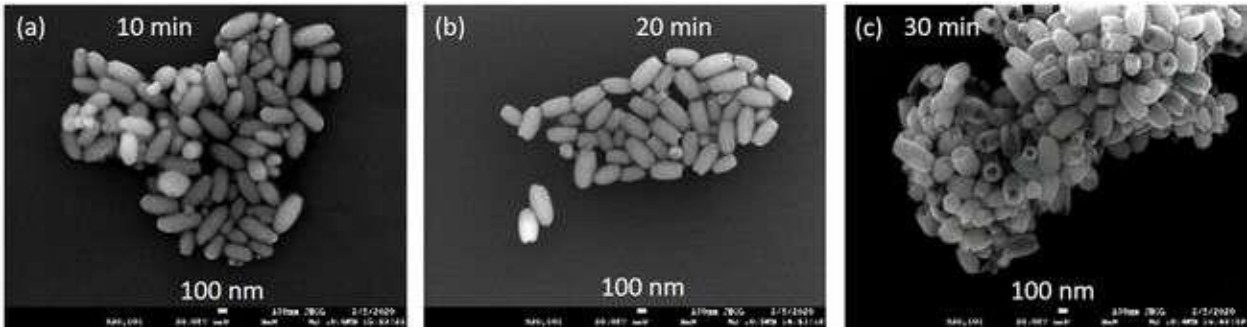

Figure 6.4: (a-c) Time varying growth of α-Fe_2O_3 LNTs at 10, 20, and 30 minutes, respectively. NaH_2PO_4 :7.2×10^{-4} mol L^{-1}, $FeCl_3$:0.06 mol L^{-1}, and $Na_2SO_4.10H_2O$: 1.65×10^{-3} mol L^{-1}, synthesis temperature, (T) = 220°C, and volume of solvent, V = 76 mL.

To understand the time dependent growth mechanism of our hollow nanosystem, we have synthesized LNTs at different time, shown in Figure 6.4, which is analogous to the proposed mechanism Figure 6.3. We believe that NRs and SNTs follow a similar mechanism w.r.t. to time. The Fe_3O_4 NPs were finally obtained by direct thermal reduction of these α-Fe_2O_3 NRs, SNTs and LNTs (see Experimental) by preserving their novel morphology. We found that the phosphate anions concentration during the reduction process was the key factor that gated conversion of α-Fe_2O_3 into Fe_3O_4. The crystallographic orientation [001] of α-Fe_2O_3 NRs/NTs transform into [111] orientation in Fe_3O_4 NRs/NTs during thermal reduction process, and this effect is a well-established topotactic transformation [97]. In addition to the topotactic transformation, Becker et al. [310] proposed another scenario potentially responsible for transforming the crystallographic orientation of α-Fe_2O_3 NTs -[001] into Fe_3O_4 NTs-[112] and Fe_3O_4 -[113], which is the one driven by formation of twining dislocation [311]. Once Fe_3O_4 NRs and NTs are obtained, they are partially oxidized in a furnace in the presence of oxygen. Although the reduction process of α-Fe_2O_3 to

Fe_3O_4 has been well investigated in literature [197], the proposed reduction-oxidation pathway, driven by phosphate anions as key factor, represent a novelty. The reduction process depends on the annealing temperature, time, mass of sample used for reduction and concentration of precursor used during synthesis. In the present work, we found that phase composition after reduction-oxidation process were varying with the concentration of phosphate anions. Thus, based upon the phase composition obtained from XRD Rietveld analysis, Mössbauer spectroscopy, and literature[303], we proposed the mechanism with following reduction-oxidation process at constant time, temperature and hydrogen gas flow:

$$3x\alpha - Fe_2O_3 + H_2 \longrightarrow 2y\,Fe_3O_4 + H_2O(gas) \quad \text{reduction process} \quad (6.1)$$

$$Fe_3O_4 + O_2 \longrightarrow z\gamma - Fe_2O_3 + 4H_2O\,(gas) \quad \text{oxidation process} \quad (6.3)$$

Where x, y, and z are concentration of adsorbed phosphate anion with α-Fe_2O_3, concentration of remaining α-Fe_2O_3 on Fe_3O_4 after reduction, and concentration of remaining Fe_3O_4 on γ-Fe_2O_3 after oxidation. Lower the concentration of phosphate anion, higher the percentage of Fe_3O_4 is obtained after reduction. This is probably due to fact that the higher concentration phosphate ion creates a barrier that restricts the direct contact between H_2 gas and α-Fe_2O_3 at the surface of NPs, leading to the slowdown of the reaction by which some percentage of α-Fe_2O_3 couldn't be transformed into Fe_3O_4 within the given frame of time.

6.3.2 Structural and Microscopy Analysis

6.3.2.1 X-ray Diffraction, Electron Microscopy, and Fourier Transform Infrared Spectroscopy

After thermal reduction and oxidation process, we found that the NRs, SNTs, and LNTs consisted of a mixture of Fe_3O_4 phase along with γ-Fe_2O_3 and α-Fe_2O_3. Figure 6.5(a) presents the XRD patterns and their Rietveld refinements for NRs, SNTs, and LNTs. The lattice parameters and phase analysis are given in Table 6.3. The % of α-Fe_2O_3 was found to be increased with the concentration of phosphate anion i.e., 3 ± 1 % (NRs), 6 ± 1 % (SNTs) and 8 ± 1 % (LNTs) along with majority phase of Fe_3O_4 with minority of γ-Fe_2O_3 ($\sim 22 \pm 1$ % of γ-Fe_2O_3 is present in all samples, i.e. NRs, SNTs and LNTs. The intense

peaks at 2θ = 24° and 33° (marked with ∗ in Figure 6.5(a)) matched those tabulated for the standard spectra of α-Fe_2O_3 (JCPDS No. 72-00469), and the broad ones at 2θ = 27.3° corresponded to the diffraction peak (116) of γ-Fe_2O_3.

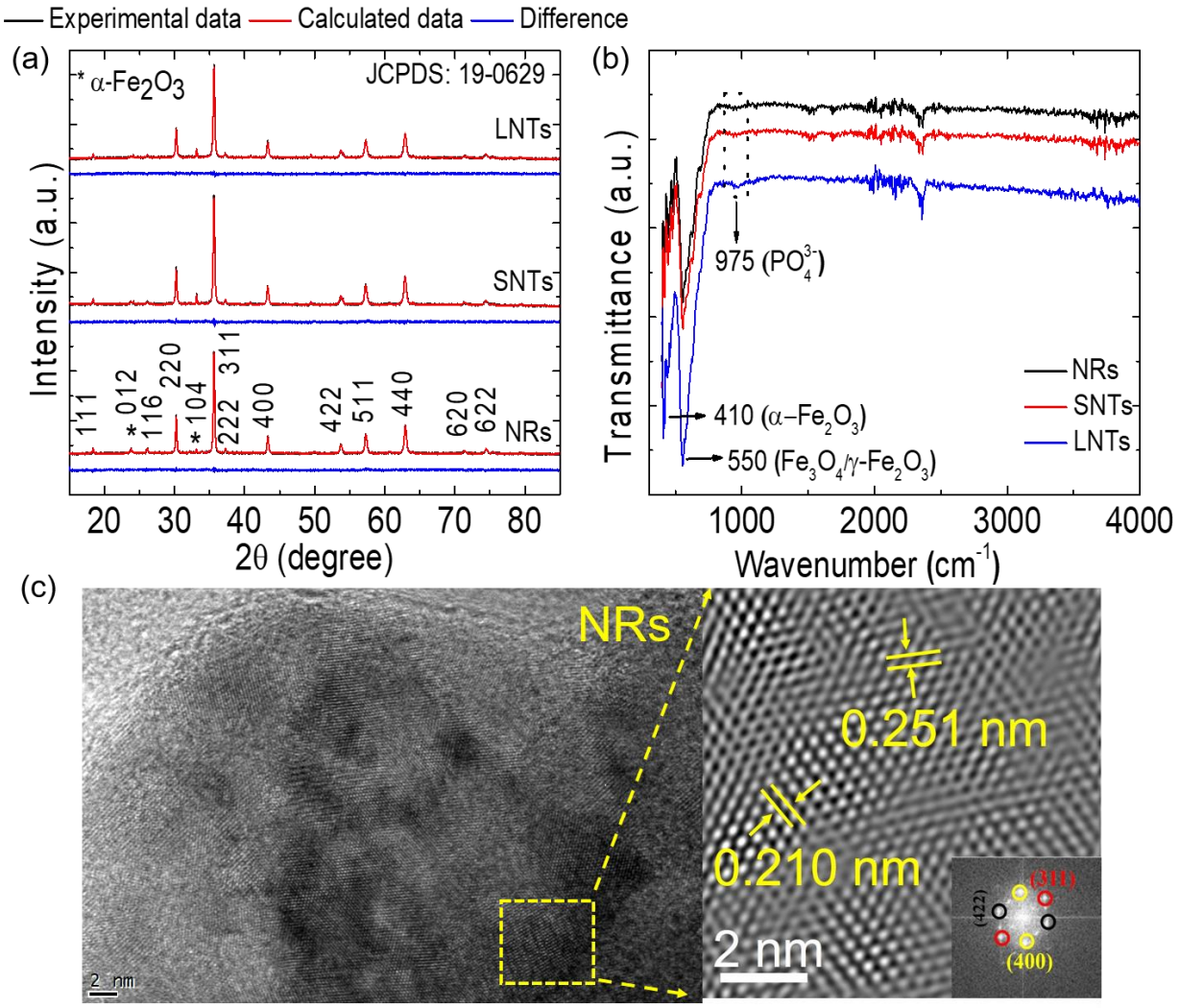

Figure 6.5: (a) Rietveld refining analysis of XRD data and (b) FTIR spectra of α-Fe_2O_3/Fe_3O_4 -γ-Fe_2O_3 NRs, SNTs and LNTs, (c) HRTEM image of Fe_3O_4 -γ-Fe_2O_3 NRs showing the lattice spacing from indexation. Lower inset of (c) is Fast Fourier Transform (FFT) image.

The experimental FTIR spectra of α-Fe_2O_3/Fe_3O_4 /γ-Fe_2O_3 NRs, SNTs, and LNTs (Figure 6.5(b)) obtained in the range of 400-4000 cm^{-1} showed the characteristic vibrational bands from iron oxide (α-Fe_2O_3/ Fe_3O_4 /γ-Fe_2O_3) NPs between 600 cm^{-1} and 400 cm^{-1}. The absorption band at 550 cm^{-1} is assigned to the vibrations of the Fe-O functional group. This band is associated to the stretching and torsional vibration modes of Fe_3O_4 /γ-Fe_2O_3,

whereas the absorption band at 410 cm^{-1} is assigned to the α- Fe_2O_3 system [199]. The characteristic peak of phosphate/sulphate anions is also detected at 975 cm^{-1}, value that agrees with the fingerprint known for these functional groups that usually appears in the wavenumber range 950-1200 cm^{-1} [200]. The HRTEM image reveals a lattice spacing of 0.251 nm and 0.210 nm at the surface Fe_3O_4 -γ-Fe_2O_3 NRs agrees well with (311) and (400) planes of inverse cubic spinel structure [312] as shown in Figure 6.5(c).

Table 6.3: Comparative study of phase analysis from XRD and Mössbauer analysis for α-Fe_2O_3/Fe_3O_4 -γ-Fe_2O_3 NRs, SNTs, LNTs, and sample 'S'.

Sample	Lattice parameter (nm) ±0.005	Phase Analysis					
		XRD(±1)			Mössbauer(±2)		
		Fe_3O_4(%)	γ-Fe_2O_3 (%)	α-Fe_2O_3 (%)	Fe_3O_4(%)	γ-Fe_2O_3 (%)	α-Fe_2O_3
NRs	Fe_3O_4 a=b=c=0.836 γ-Fe_2O_3 a=b=c=0.835 α-Fe_2O_3 a= 0.503 c=1.376	76.5	21.0	2.6	78.07	21.93	-
SNTs	Fe_3O_4 a=b=c=0.836 γ-Fe_2O_3 a=b=c=0.835 α-Fe_2O_3 a= 0.504 c=1.376	71.8	22.7	5.4	71.94	21.46	6.6
LNTs	Fe_3O_4 a=b=c=0.836 γ-Fe_2O_3 a=b=c=0.835 α – Fe2O3 a= 0.504 c=1.376	71.7	21.9	7	70.34	22.32	7.34
S	γ-Fe_2O_3 a=b=c=0.835 α-Fe_2O_3 a= 0.504 c=1.376		84.8	15.2		85.96	14.02

6.3.3 Mössbauer Spectroscopy

To better identify the phase composition of the as-prepared iron oxide NPs, room temperature Mössbauer spectroscopy was performed on α-Fe_2O_3/Fe_3O_4 /γ-Fe_2O_3 NRs, SNTs, and LNTs samples. The obtained spectra (Figure 6.6a-c) could be fitted with five magnetic sites except in the case of NRs, which required only four sextets (see the hyperfine parameters in Table 6.4. The magnetic sextet having hyperfine field B_{hf}= 51.40 and 51.70 T observed in SNTs and LNTs corresponds to the α-Fe_2O_3 phase (violet solid line in Figure 6.6(b-c), with an estimated population of 7 (± 2) % (SNTs) and 8 (±2) % (LNTs), consistent with the XRD analysis. However, this signal was not detected in NRs (Figure 6.6a), suggesting that the amount of α-Fe_2O_3 in NRs is below the detection limit of our experimental set-up (i.e., less than ~2 wt%). The spectrum analysis, indicated by navy and purple lines, show the A- (tetrahedral) and B-site (octahedral) sites of Fe^{3+} cations in γ-Fe_2O_3. After several fitting attempts with the use of standard parameters [313] of γ-Fe_2O_3, we found that ~ 22 % of γ-Fe_2O_3 is present in all preparations, NRs, SNTs and LNTs in agreement with XRD data, and the population ratio of A:B equals to 1:1.67 which well agreed with bulk γ-Fe_2O_3. The result translate into the estimated chemical composition $(Fe^{3+})_A[Fe^{3+}_{1.67}\,\square_{0.33}]_BO_4$ [313].

A similar percentage (~ 22%) of γ-Fe_2O_3 in all sample was expected after oxidation of Fe_3O_4 of 1 hour at 240°C. The fitting analysis, indicated by blue and olive lines in Figure 6.6(a-c), represent the tetrahedral (A-) and octahedral (B-) site of Fe_3O_4, respectively. The total population of Fe_3O_4 phase contained in A- and B- sites of NRs, SNTs and LNTs were found to be ~78 (± 2) %, ~72 (± 2) %, and ~70 (±2) %, respectively. The observed population of Fe^{3+} cations residing on A-sites is about 3-4 times larger than those occupying the B-site (Table 6.4) and, as such, indicates the presence of a large number of cation vacancies (expressed by the symbol □) and defective region on B-site.

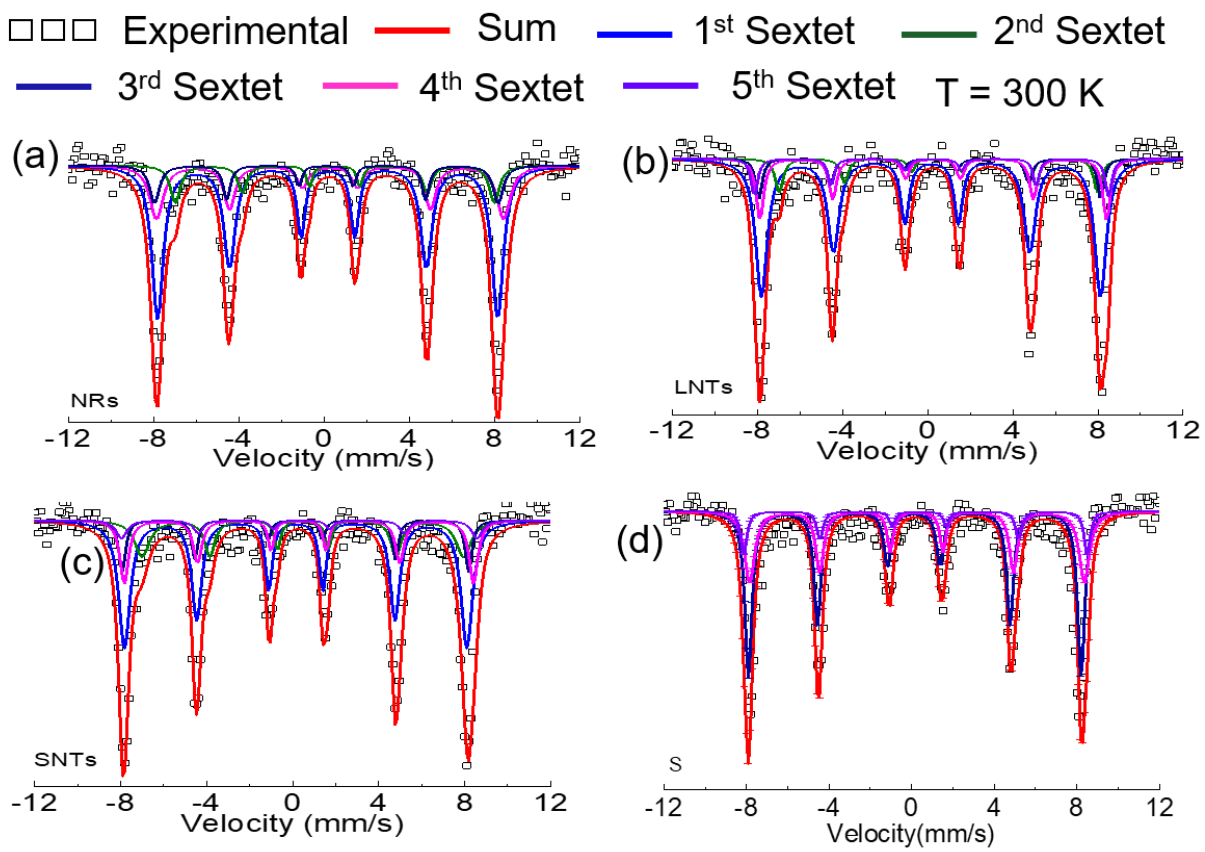

Figure 6.6: (a-d) Mössbauer spectra of α-Fe_2O_3/Fe_3O_4 -γ-Fe_2O_3 NRs, SNTs, LNTs, and 'S' sample respectively at 300 K.

The result is a clear signature for formation of non-stoichiometric Fe_3O_4, which can be represented by the chemical formula $Fe_{3-\delta}O_4$, where the factor δ varies continuously from zero in the case of stoichiometric Fe_3O_4 up to one third, for stoichiometric γ-Fe_2O_3 [313]. The higher fraction of Fe^{3+} in A-site arises from oxidation of Fe^{2+} cations, a process that is enhanced upon increasing the concentration of phosphate anion, from NRs to LNTs, used during the shape- controlled synthesis. Furthermore, the oxidation process favours the creation of cation vacancies in the B-site and thus drives the Fe_3O_4 NPs towards the adoption of non-stoichiometric composition. The observed relative composition of Fe_3O_4 and γ-Fe_2O_3 from Mössbauer spectroscopy analysis allow to calculate the approximate value of magnetic saturation, which is ~ 92 emu/g for NRs, ~ 88 emu/g for SNTs, and ~ 87 emu/g for LNTs. Based upon the phase composition analysis, the speculated diameter of Fe_3O_4 -γ-Fe_2O_3 NRs, SNTs, and LNTs are estimated as 156 nm-45 nm, 196 nm-55 nm, and

179 nm-50 nm, respectively. The calculated magnetization values in the so-prepared NPs have been then assessed by bulk dc magnetization experiments.

Table 6.4. ^{57}Fe Hyperfine parameters, isomer shift (IS, δ_C), quadrupole splitting (QS, ΔQ), hyperfine field (B_{hf}) and spectral area (population distributions) for Fe_2O_3/Fe_3O_4 -γ-Fe_2O_3 NRs, SNTs, LNTs, and sample 'S'.

Sample Code	Phase	Site	Mössbauer Fitted Data			
			IS, δ_C (mm/s) ±0.01	QS, ΔQ (mm/s) ±0.01	B_{hf} (T) ±0.1	Population (%) ±2
NRs	Fe_3O_4	A	0.31	-0.015	49.57	62.63
		B	0.64	0.010	46.60	15.44
	γ-Fe_2O_3	A	0.23	0.010	50.10	7.61
		B	0.41	0	50.60	14.32
SNTs	Fe_3O_4	A	0.28	-0.010	49.50	53.51
		B	0.61	0.000	46.50	18.43
	γ-Fe_2O_3	A	0.26	0.010	50.10	8.14
		B	0.42	0.010	50.50	13.32
	α-Fe_2O_3		0.35	-0.100	51.40	6.60
LNTs	Fe_3O_4	A	0.31	-0.032	49.21	56.78
		B	0.62	0.080	46.45	14.34
	γ-Fe_2O_3	A	0.24	0.010	50.20	8.22
		B	0.40	0.010	50.60	14.10
	α-Fe_2O_3		0.36	-0.100	51.70	7.34
S	γ-Fe_2O_3	A	0.23	0.05	50.1	52.32
		B	0.35	0.02	50.4	33.64
	α-Fe_2O_3		0.38	-0.18	51.7	14.04

6.3.4 Bulk Magnetic Properties

The dc magnetic data of all samples reflected their ferromagnetic behaviour, with saturation magnetization (M_S) of ~ 88 emu/g for NRs, ~ 84 emu/g for SNTs, and ~ 84 emu/g for LNTs. The magnetization trends shown in Figure 6.7(a) evidenced that the values from magnetic saturation were slightly lower (about 3-5%) than those predicted by Mössbauer analysis. The observed discrepancy of M_S is due to the presence of non-stoichiometric Fe_3O_4 phase, which should be slightly larger than those estimated from Mössbauer analysis. We note that the M_S decreases from NRs to LNTs, due to an increased % of oxidized Fe_3O_4 (i.e., increase in % of $Fe_{3-\delta}O_4$) owing to higher concentration of phosphate anion. Therefore, the obtained M_S values were greater than those found in literature of Fe_3O_4 NRs [41,56], ellipsoidal magnetic particles (EMPs) [44], and NTs [292].

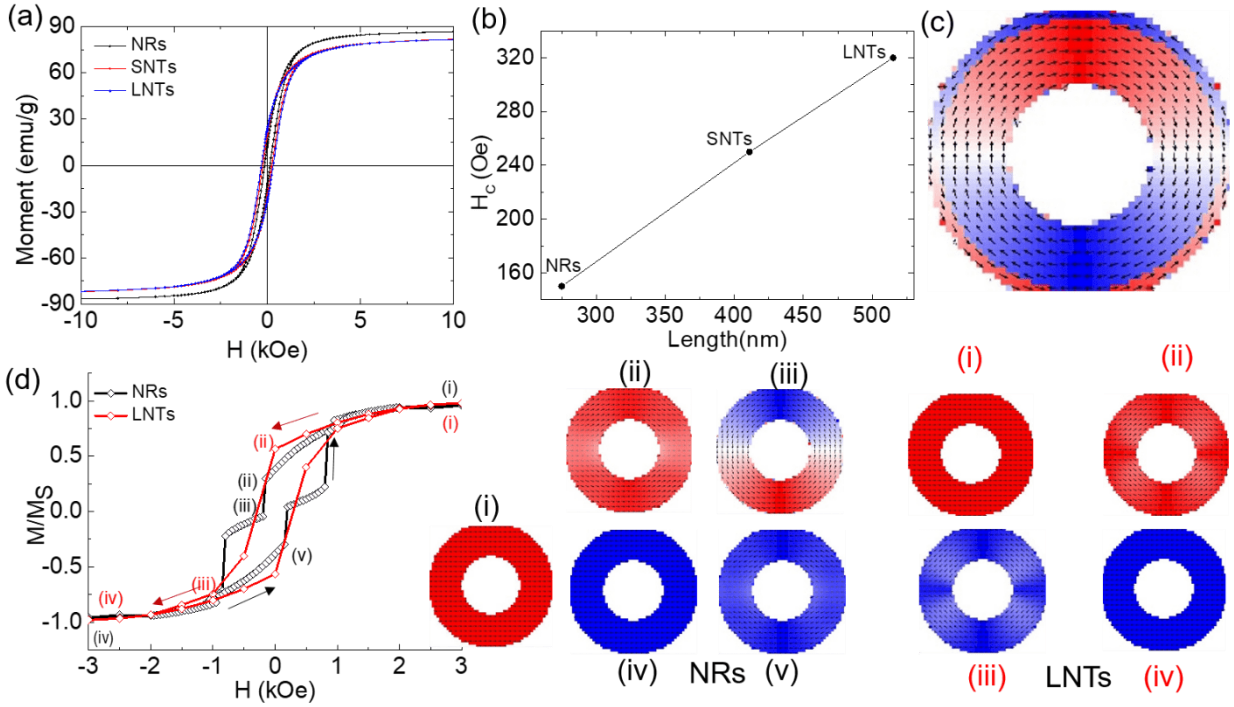

Figure 6.7: (a) represents the hysteresis loop at 300 K, (b) The coercive field (Hc) dependences on the length of α-Fe_2O_3/Fe_3O_4 /γ-Fe_2O_3 NRs, SNTs, and LNTs at 300 K, (c) Simulated magnetic ground state of NRs/NTs (upper view), and (d) simulated hysteresis loop of α-Fe_2O_3/Fe_3O_4 /γ-Fe_2O_3 NRs and LNTs and their magnetic moment evolution with an applied field.

Figure 6.7(b) shows the coercive field Hc that increases with the increasing thickness (or length) of NRs (or NTs), factor that is ascribed to the shape anisotropy contribution of NTs.

The shape anisotropy contribution of these NPs can be calculated by using the following Equation 6.4 [312],

$$K_{eff} = K_u + K_s \quad (6.4)$$

where K_{eff} represents the effective anisotropy constant and K_u and K_s are the magnetocrystalline and shape anisotropy, respectively. Equation 6.5 gives the anisotropy constant estimation,

$$K_S = (\pi - \frac{3}{4}N_C)M_S^2 \quad (6.5)$$

with

$$N_C = \frac{4\pi}{(\rho^2-1)}[\frac{\rho}{\sqrt{\rho^2-1}}\ln(\rho + \sqrt{\rho^2-1}) - 1] \quad (6.6)$$

where $\rho = c/a$, being a and c the lengths of the shorter and longer axes of the NPs, respectively. From these expressions we calculated K_S = 2.3×10^3 erg/cm^3, 3.9×10^3 erg/cm^3, and 6.0×10^3 erg/cm^3 for NRs, SNTs, and LNTs, respectively, consistent with the micromagnetic simulations (see below) . The simulated Hc values give ~190 Oe in NRs and ~ 295 Oe in NTs. Moreover, Figure 6.7(c) depicts the spin configuration, upper view, at ground state (i.e. H=0) simulated by adjusting the standard parameter of Fe_3O_4 and γ-Fe_2O_3.The opposite spin direction (only to identify the core and shell region since has no physical significance here) on the surface indicates the presence of γ-Fe_2O_3 in the surface region. The magnetization reversal process involved in NRs and LNTs is shown in Figure 6.7(d), with the coded red and blue colour that indicate M_S in the positive and negative direction, respectively. The drop of H_C from LNTs to NRs and the presence of vortex states (Figure 6.7(d-iii)) in NRs and found in a good agreement with results on similar systems reported by Yang Y. and co-authors in Fe_3O_4 nano disks [42] and Liu et al. [41] whereas it is completely absent in LNTs, probably due to its tubular morphology [97]. Owing to their higher effective (shape) anisotropy, the LNTs are expected to express larger specific adsorption rate values (SAR) once compared to the NRs system. However, the presence of a vortex configuration in NRs should translate into a better heating efficiency, as highlighted in one literature work [41]. Therefore, MFH experiments were performed in these nanosystems (NRs, SNTs and LNTs), and the results are presented and discussed in the following section.

6.3.5 Heating Efficiency

Since hollow NPs with well-defined shapes such as the NRs, SNTs and LNTs studied here are appealing for biomedical applications due to their flux-closure vortex (e.g. in NRs) and curling (LNTs) configurations that minimize aggregation by dipole-dipole interactions, we studied their heating efficiency for potential MFH applications. Moreover, we added further functional flexibility for MFH applications by coating these NPs with citric acid as a stabilizing agent (Figure 6.8), as described elsewhere [282]. We observed that all the coated samples were stable in water for 5 minutes, but then start precipitating/sedimentation. The SAR measurement were carried out on the water-based colloids with standard concentration of 1 mg/mL. The applied magnetic field parameters were fixed frequency $f = 107$ kHz and amplitudes up to $H = 35.9\ kA/m$ (450 Gauss), i.e., with a product $H \times f \leq 3.8 \times 10^9\ Am^{-1}s^{-1}$ in such a way to operate below the limit $H \times f \leq 5.1 \times 10^9\ Am^{-1}s^{-1}$ proposed by Dutz [92]. The SAR values of NRs, SNTs and LNTs, extracted from the T vs. t curves (see Figure 6.9) were measured at increasing field amplitudes H and given in Figure 6.10. The data showed the expected increase of SAR with increasing H but no obvious functional dependence of H.

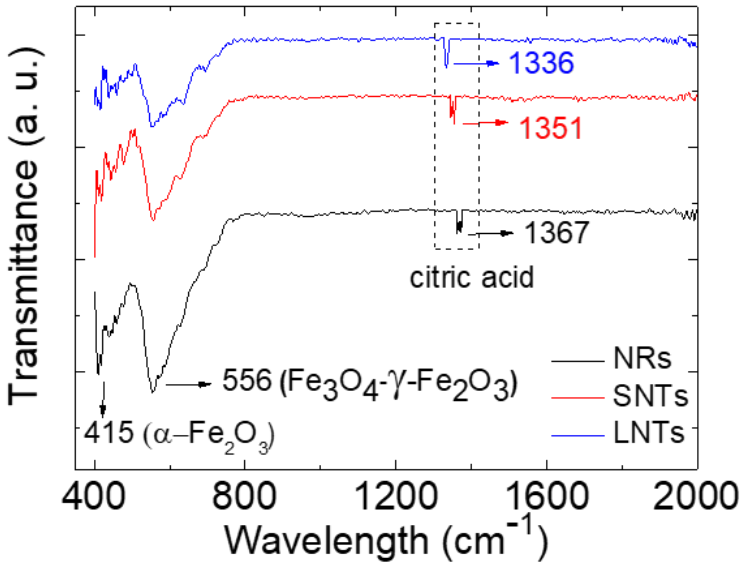

Figure 6.8: FTIR spectrum of α-Fe_2O_3/Fe_3O_4 -γ-Fe_2O_3 NRs, SNTs, and LNTs coated by citric acid. The peak inside the box indicate the citrate molecules on the surface of respective NPs.

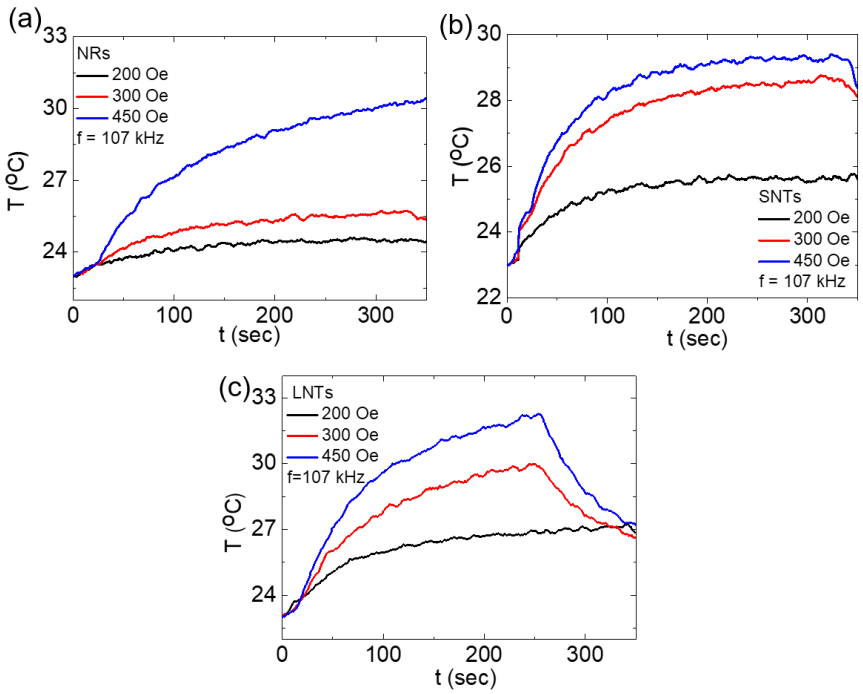

Figure 6.9: (a-c) Heating profile of α-Fe_2O_3/Fe_3O_4-γ-Fe_2O_3 NRs, SNTs, and LNTs at the concentration of 1 mg/ml in water.

The highest SAR and ILP values obtained in our samples corresponded to the LNTs, with SAR= 465 W/g and ILP=3.3 nH m^2 kg^{-1}, these values are among the largest reported for the iron-oxide phases in any nanostructured form under similar f and H conditions. On the other hand, the lowest SAR and ILP values were those from the NRs system (SAR= 340 W/g and ILP=2.45 nH m^2 kg^{-1}). Although the magnetic saturation M_S of NRs was larger than that of LNTs, the heating efficiency appears to be clearly dominated by the shape anisotropy factor. We therefore unveiled, in more details, the role of shape anisotropy on the heating efficiency of hollow NTs in comparison to NRs. For the purpose, we have synthesized a specific sample consisting of size distribution (l = 300 nm; d_{out} = 207 nm; d_{in}=125 nm) labelled sample 'S', having a $H_C \approx 155$ Oe value very close to the $H_C \approx 150$ Oe of the NRs.

We have performed several characterizations as well for this 'S' sample. The Mössbauer spectra is shown in Figure 6.6(d). The XRD, FESEM image, size distribution, magnetic properties and heating profile are given in Figure 6.11. The lattice parameter and Mössbauer data are given in Table 6.3 and Table 6.4, respectively. After careful analysis, it is confirmed that sample 'S' contains α-Fe_2O_3/γ-Fe_2O_3. The SAR values for 'S' sample

reached 409 W/g at maximum field amplitude of 35.9 kA/m (450 Oe), which is higher than NRs (SAR=340 W/g). Although sample 'S' has lower M_S and similar H_C, the SAR value of sample 'S' is higher than that expressed by NRs, a clear indication that the better anisotropic properties of 'S' (K_S = 2.4×10^3 erg/cm^3) are translated into better heating profile. The observed results suggest that the contribution of the shape anisotropy is a key factor to enhance the heating efficiency of hollow NPs.

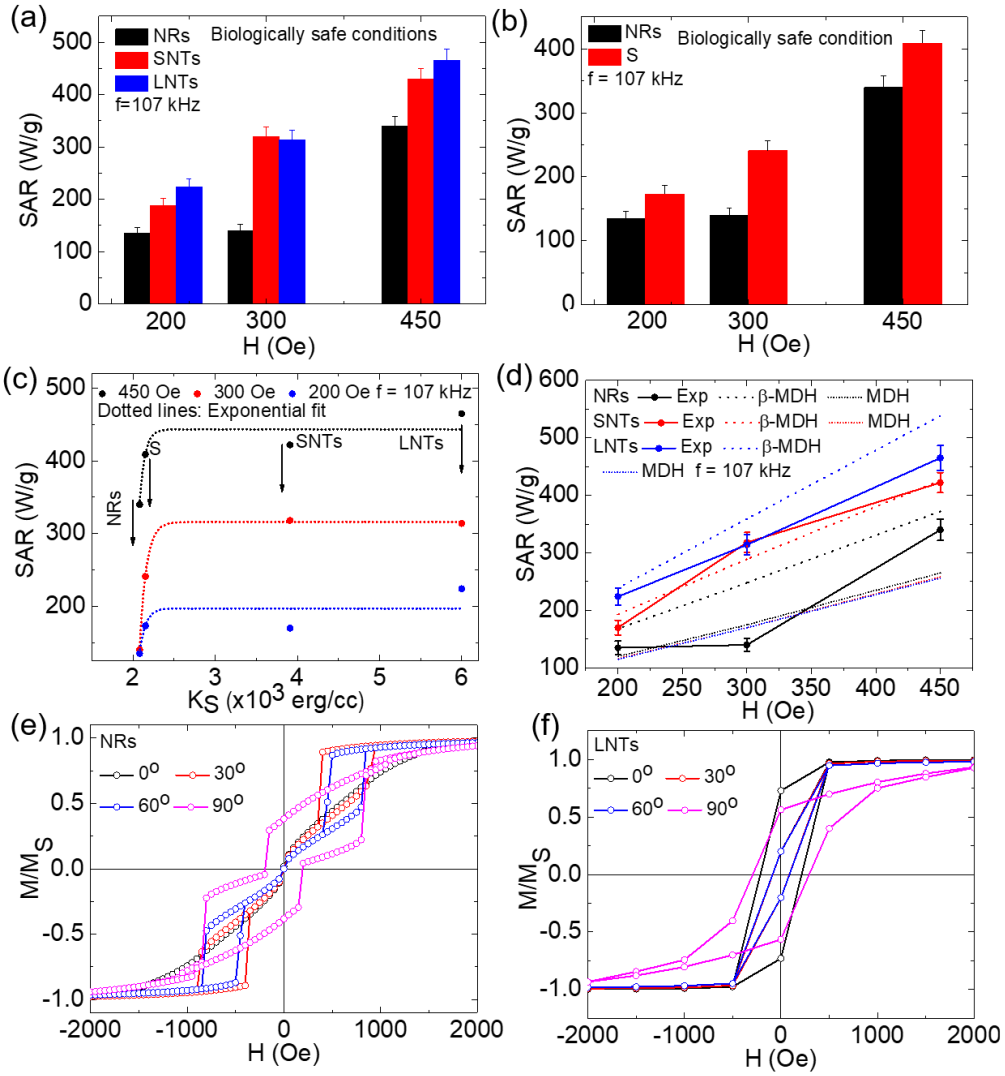

Figure 6.10: a) SAR values for α-Fe_2O_3/Fe_3O_4 -γ-Fe_2O_3 NRs, SNTs, and LNTs; b) SAR values for NRs and sample 'S'; c) SAR values for increasing values of shape anisotropies K_S, (d) Comparison of experimental value of SAR with theoretical prediction based on β-MDH model, and (e-f) Simulated direction dependent hysteresis loop of Fe_3O_4 -γ-Fe_2O_3 NRs and LNTs.

Interestingly, Figure 6.10(c) shows that the heating efficiency is enhanced exponentially as a function of shape anisotropy, from NRs to LNTs at each field. The exponential fit (dotted lines in Figure 6.10c) well agreed with the experimental trend. Recently, Tong et al. [314] proposed the use of a modified dynamic hysteresis model (MDH) to obtain SAR values of ferromagnetic iron oxide NPs at the clinically relevant condition, the area of hysteresis loss, A is given by,

$$A = 3.53\mu_0 M_S H_{max} (1 - 0.7\kappa) \quad (6.7)$$

where μ_0 is the magnetic permeability of vacuum, κ is a non-dimensional constant and is negligible for ferrimagnetic materials, M_S is the saturation magnetization, H_{max} is the maximum applied field.

However, we observed that the theoretical SAR values obtained through the proposed MDH model does not satisfactorily reproduce the observed trend for the nanosystems reported in the present study (see MDH SAR in Figure 6.10(d). Tong et al.[314] has in fact neglected to include the shape anisotropy factors in their work, thus, we have modified the MDH model by considering the nanoparticle's aspect ratio (β= major axis/minor axis), termed here as β-MDH model, with mathematical expression given by Equation 6.8,

$$A = 3.53\ \mu_0\ M_S\ H_{max}\ (1 - 0.7\kappa)\ \beta \quad (6.8)$$

Where, β = 1.37, 1.67, 2.23, and 1.44 for NRs, SNTs, LNTs, and sample 'S', respectively. Theoretically, the value of 'A' (M/M_S, H) obtained using Equation (6.8) allows to calculate the SAR value from Equation 6.9 [96,285] as

$$SAR = \frac{M_S\, f\, A}{\rho} \times 10^{-7}\ \ W/g \quad (6.9)$$

where ρ is the density of the NPs and f is experimental frequency of the applied field. The calculated SAR values using the modified β-MDH model gives, overall, better adjustment to the trends seen in the experimental data of NRs, SNTs, and LNTs as clearly observed in Figure 6.10(d). However, the β-MDH model still does not account for variables such as the NPs size distribution [315,316], coercive field [89], and alignment [42,96,263]. Several studies have demonstrated that the magnetic field gradient usually present in the experimental coils of the magnetic field applicators can induce partial alignment of the free MNPs in the colloid, increasing the absorption power of the colloids up to 2-4 times respect to the non-oriented

NPs.[41,42,263] To assess the impact of this effect on our samples, we performed micromagnetic simulations for the hysteresis losses along different directions of the applied field (Figure 6.10(e-f)) for NRs and LNTs to show the possible anisotropic magnetization reversal behaviour of NRs and LNTs along different directions [44].

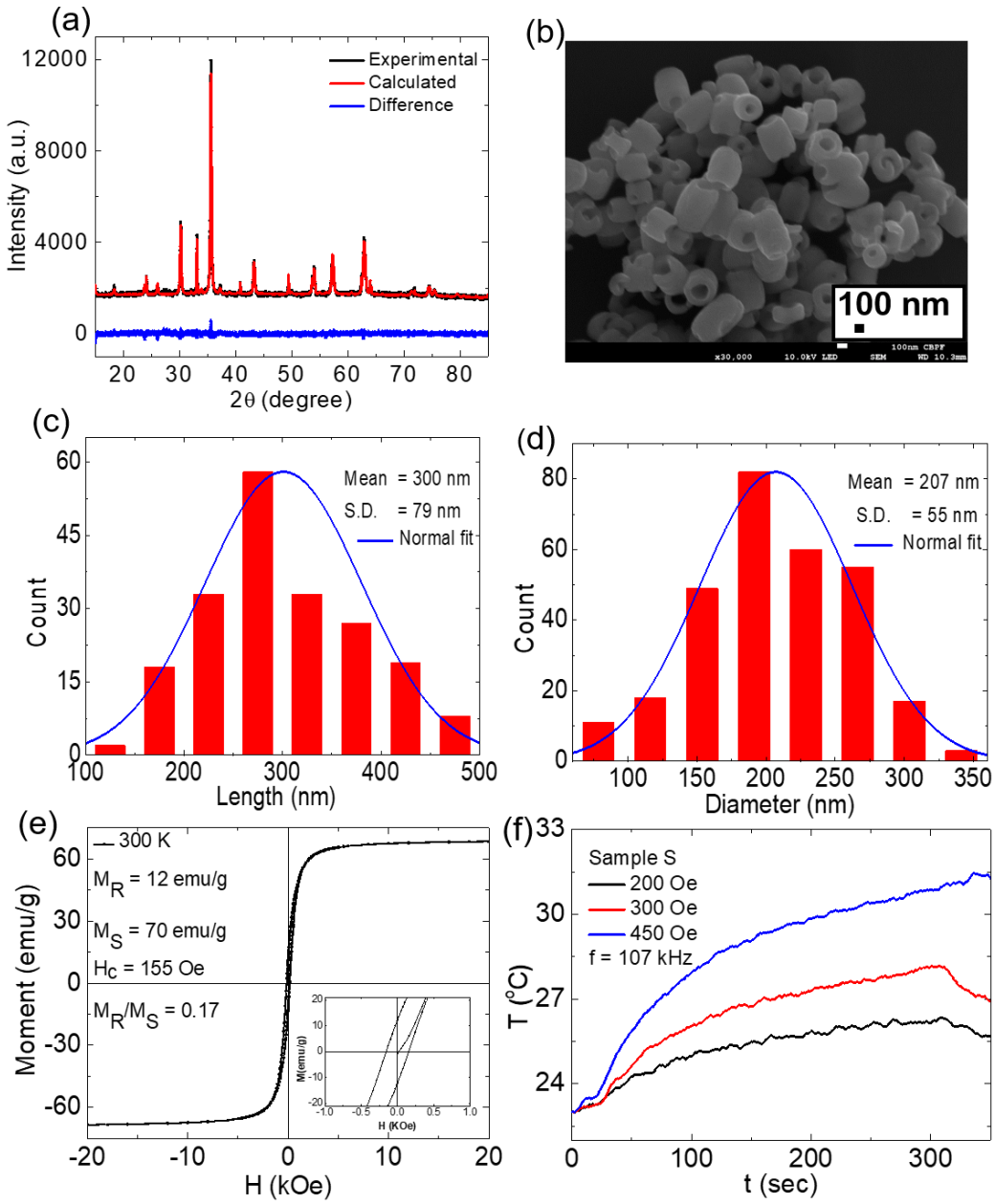

Figure 6.11: Sample 'S' prepared at [NaH_2PO_4] = 2.70x10^{-4} mol L^{-1}, [$FeCl_3$] = 0.06 M and [$Na_2SO_4.10H_2O$] = 1.65x10^{-3} mol L^{-1}, synthesis temperature (T) = 220 °C, time (t) = 30 minutes, and volume of solvent = 76 mL; (a) XRD pattern, (b) FESEM image, (c-d) represent its length and diameter distribution respectively, (e) hysteresis loop at 300 K, and (f) heating profile at concentration (c) = 1 mg/mL.

In agreement with previously reported data, a large hysteresis loss was found in the parallel alignment ($\theta = 90°$) for NRs and LNTs, resulting in a higher SAR value [41,42,263]. However, there is no significant difference in the hysteresis loss for both parallel and perpendicular direction of LNTs, as shown in Figure 6.10(f).

Recently, Liu et al. [41] reported the highest SAR (~ 3050 W/g Fe at 400 kHz and 740 Oe) for magnetic vortex iron oxide NPs, which turned into a much lower value when analysed at biological relevant conditions. In another work in iron oxide NTs by Das et al. [292], the reported SAR values was found to fall at ~ 360 W/g at 800 Oe. Chen X. et al. [298] reported a significant loss of SAR for γ-Fe_2O_3@SiO_2 NTs (65 W/g) when compared to neat γ-Fe_2O_3 NTs (~ 230 W/g) at H= 840 Oe and f= 120 kHz; in the present work, the SAR value of LNTs (465 W/g) shows excellent heating efficiency at low field H = 450 Oe and f ~ 107 kHz, thus LNTs is the magnetic nanosystem with the highest promises for further studies in living organism.

6.3.6 Cytotoxicity Test

The *in vitro* cytotoxicity of two of our systems, namely NRs and LNTs, were assessed through standard MTT viability tests against three different cell lines: 4T1 cells, murine mammary adenocarcinoma cell line; CT26, murine colorectal carcinoma cell line; and J774A.1, a murine monocyte/macrophage cell line. It is important to highlight here that these tests provided evidence of the cytotoxicity of the nanosystems in different cells lines, therefore providing an ample environment for potential applications in biomedicine.

The results are presented in Figure 6.12(a-b) and demonstrated that NR and LNT samples did not produce any significant ($p<0.01$) cytotoxicity effects for 4T1 and J774A.1 cells in the range of concentration examined. However, the CT26 cells were found more sensitive than the earlier types when treated with both NRs and LNTs samples. Conversely, a significant cytotoxic factor was expressed above 2 μg/mL concentration. The viability reduction observed in CT26 cells followed a dose-dependent pattern, indicating the maximum concentration that should be used in this cell type during magneto-hyperthermia applications. Thus, taken together, from these in vitro cytotoxicity experiments reinforce the possibility to implement LNTs in thermal therapy-based applications.

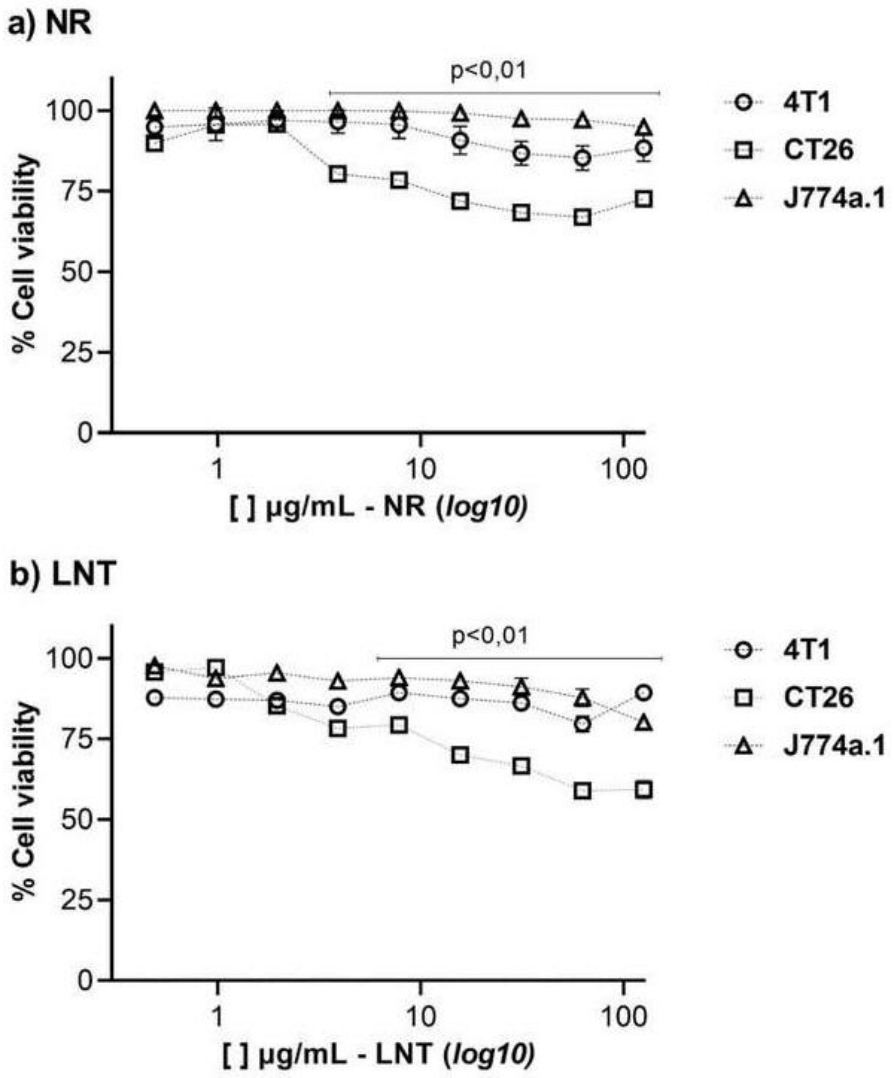

Figure 6.12: (a) Cell viability tests of NRs and LNTs on 4T1, CT26 and J774 cell lines as a function of increasing a) NRs concentration, and b) LNTs concentration. Difference p <0.01 between strains 4T1, J774a.1 and CT26. y-axis refers to untreated cell control and x-axis different sample concentrations in µg/mL. Data presented with standard error in quintuplicates.

6.4 Conclusion

In this work, we have shown the MAH synthesis of hollow Fe_3O_4-γ-Fe_2O_3 nanosystems encoding well-defined sizes and shapes (NTs and NRs). The obtained iron-oxide samples showed different well-defined geometries (i.e., NDs, NRs or nanocylinders) depending on the synthesis conditions. The shape-controlled synthesis route was largely influenced by the synthesis parameters such as concentration of reactants, volume of solvent, or reaction time were and temperature during the growth process that generated the hollow/capsule tubes, micro-rods and NDs, and this was

associated to the initial concentration of phosphate anions in the reactants mixture. Indeed, reducing the concentration of phosphate anion by one-third (and duplicating the solvent volume) in the reactant mixture the length of the obtained capsule-shaped microparticles (CSMPs) decreased by about one order of magnitude (from ~2723 nm to ~275 nm). Conversely, when the concentration of phosphate anions was increased 4 times the length of NRDs duplicated its value, leading to the formation of long NTs (LNTs, length of ~511). The α-Fe_2O_3 NTs and NRs were then selected as the key NPs to be transformed into hollow nanosystems, Fe_3O_4-γ-Fe_2O_3, by using reduction-oxidation processes that preserved their initial morphologies. We have assessed the heating efficiency of these morphologically different hollow nanosystems for MFH applications, finding that the LNTs were the best suited for heating, with SAR values up to ≈465 W/g for the largest applied fields. These hollow nanosystems were found biocompatible and chemically stable. These values are the highest among those reported so far in the hollow ferrimagnetic iron oxide family. Although the magnetic saturation M_S of NRs was found larger than that of LNTs, the heating efficiency appeared to be clearly dominated by the shape anisotropy factor, which was larger in LNTs. Therefore, our work emphasizes the relevance of the nanosystems anisotropy factor, the importance to achieve its control during the bench-synthesis, in a way to optimize formation of nanomaterials for thermal therapy-based applications.

Chapter 7

Energy evolution, Stabilization, and Mechanotransducer Properties of Fe_3O_4 Nanorings and Nanodisks

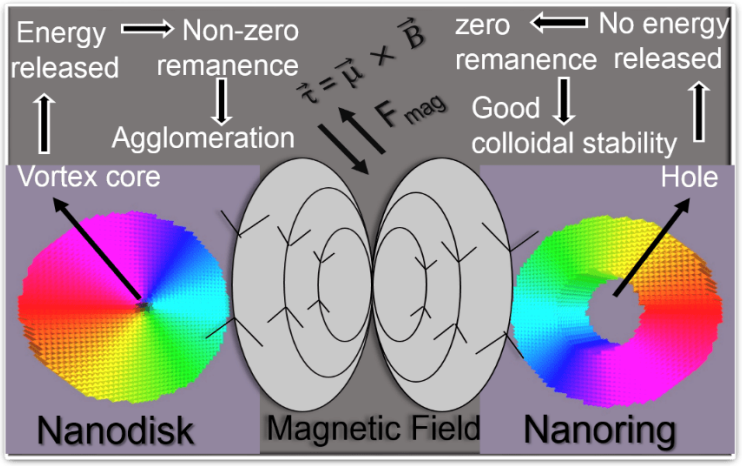

Recent reports on novel spin structures produced in nanomaterials due to confinement of spins imposed by geometrical restrictions are at the centre of rising scientific interest. Topological curling magnetic structures (vortices) exhibit unique properties regarding the energy profile, colloidal stability in suspension, manipulation under a low-frequency magnetic field, and torque exertion. The latter property provides the potential to mechanically eradicate cancer cells via magneto-mechanical actuation using remote ac magnetic fields. In this chapter, we study, theoretically and by micromagnetic simulations, the magnetic energy evolutions for vortex nanosystems, i.e., Fe_3O_4 NDs and NRs. The obtained results on magnetic energy, magnetic susceptibility, and magnetization reversal confirm that the vortex-domain structure in NRs exhibits better stability and avoids agglomeration in solution owing to the presence of a central hole, whereas the presence of a vortex core in NDs induces magnetic remanence. Although NDs are found to exert slightly higher torques than NRs, this weakness can be compensated by a small increase (i.e., ≈20%) in the amplitude of the applied field. Our results provide evidence on the magnetic stability of the curling ground states in NRs and opens the possibility of applying these systems to magneto-mechanical actuation on single cells for therapeutics in biomedicine, such as cancer cell destruction by low-frequency torque transduction.

7.1 Introduction

The capability of a magnetic field to safely permeate the human organs and interact with MNPs provides promising new routes for therapies and diagnostics in biomedicine [220,317–321]. Among these routes, transduction of the magnetic interaction of an external ac field and magnetic nanosystems into magneto-mechanical actuation makes it possible to mechanically destroy previously targeted cells, bacteria, or other unicellular organisms. The physical mechanisms involved are based on the torque induced by NPs under the rotation effect of a low-frequency (i.e., few Hz frequency) ac magnetic field, which mechanically actuates on cells [322–324]. This torque can be exploited in several ways to trigger receptors connected with cell death, open ion channels, or transfer direct physical spoilage to cells and has been shown to reason cell death both in vitro and in vivo. For instance, it has been reported that the oscillation of MNPs can induce calcium influx out of membrane ionic channels or calcium cast from internal cell origins, which outcomes in perturbation of cellular calcium homeostasis and stimulate of the apoptosis process [43,223,325].

The MNPs with vortex structures provide a stable configuration that can rotate with the application of an external field. The magnetic field suffices to produce the magnetization process that generates a large magnetic moment in these systems due to the high intrinsic magnetization, allowing their manipulation even by a weak external magnetic field. One advantage of the vortex configuration over the simple single-domain magnetic structure is that it can show negligible dipole-dipole interactions and thus negligible magnetic remanence, allowing the magnetic nanosystems to remain well dispersed in colloidal formulations in the absence of an exterior magnetic field. Recently, the possible use of magnetic vortex MDs and NDs for in vitro experiments with glioma cancer cells and mechanosensory cells has been studied under weak and slow magnetic fields, suggesting that vortex disks are excellent mechanotransducers compared to SPM NPs for eradicating cancer cells [43,223]. An important result relates to the significant remanent magnetization (M_R) in these systems due to the presence of a central vortex core that gives out-of-plane magnetization in NDs; such M_R significantly contributes to agglomeration of NDs in suspensions [42]. The M_R distribution is a complex phenomenon that rely on the size and shape of the particle as well as on the balance of different energy contributions to the magnetic energy. The zero-field vortex configuration is specified by the balance among the exchange and magnetostatic energies, which can be controlled by the defined geometry, i.e., the thickness and diameter of the

vortex nanosystem; in the vortex state, the total energy is almost dominated by the exchange energy because of the formation of a central vortex in NDs [74]. Upon decreasing the disk diameter at a constant thickness, the comparative contribution of the exchange energy of the central vortex surges and renders the vortex state less stable lower than the critical diameter. It is worth noting that the M_R of NDs is higher near the critical size (closer to the single-domain region). Such M_R can be reduced to zero by increasing the diameter of NDs to within 0.5-1 μm, but this size limits the use of NDs in biomedicine [278,326]. On the other hand, the absence of a central vortex core substantially reduces the exchange energy in NRs, making their vortex state energetically favorable, i.e., the lowest energy state (ground state), without out-of-plane magnetization (M_R = 0), which avoids possible agglomeration in suspensions [41,74]. In addition, vortex NRs have lower energy than NDs and do not produce surface magnetostatic charges, thus becoming more stable. It is clear that the understanding of the energy evolution in defined magnetic vortex nanosystems and its stabilization is a crucial factor to examine the possibility of using such systems in biomedicine. One great advantage of NRs over NDs is that the vortex state is always an energetically lower state in NRs, whereas it is an energetically lower state only above a critical size in NDs [74]. Thus, in this scenario a novel strategy can be envisaged, in which vortex NRs are used as magneto-mechanical transducers for cancer cell destruction.

In this chapter, we report a numerical study on the vortex states in NRs and NDs using a theoretical model and micromagnetic simulations of the exchange and magnetostatic energies and their contribution to the total magnetic energy of the system. We also analyze how such magnetic energy evolves from the ND topology to the NR topology. From our results on the energy and magnetic susceptibility of these configurations, the dispersion and agglomeration effects in the colloidal state are discussed. Finally, the magneto-mechanical properties of NRs and NDs under a very low field (<250 Oe) are compared. Our results show that the vortex NR magnetic configuration might potentially be used to perform mechanical actuation at the nanoscale, particularly as a nanotransducer to produce mechanical damage on targeted cells in biomedical therapeutics.

7.2 Conceptualization

7.2.1 Micromagnetic Modelling

The micromagnetic simulation was performed by the Mumax 3.9 package. Within this package, the time evolution of the magnetization allocation is obtained by solving the Landau-Lifshitz-Gilbert-Langevin equation:

$$\frac{\partial \vec{M}(r,t)}{\partial t} = \frac{-\gamma}{1+\alpha^2}\vec{M}(r,t) \times \overrightarrow{H_{eff}} - \frac{\gamma\alpha}{(1+\alpha^2)M_S}\vec{M}(r,t) \times (\vec{M}(r,t) \times \overrightarrow{H_{eff}}) \quad (7.1)$$

where $\overrightarrow{H_{eff}} = \frac{\partial E_{tot}}{\partial M_S}$ (7.2)

Here, $\vec{M}(r,t)$ is the magnetization distribution, $\overrightarrow{H_{eff}}$ is the effective field, M_S is the saturation magnetization, and γ is the gyromagnetic percentage (= 1.78×10^{11} s^{-1} T^{-1}). The total energy (E_{tot}) is the addition of five energy terms: the exchange, self-magnetostatic, magnetocrystalline anisotropy, surface anisotropy, as well as Zeeman, where the exchange and magnetostatic energies are crucial in vortex systems.

The magnetic parameters of Fe_3O_4 used in the micromagnetic simulation were the maximum saturation magnetization M_S = 480 kA/m, exchange stiffness constant A = 1.2×10^{-11} J/m, and magneto-crystalline anisotropy constants K_1= -1.35×10^4 J/m^3 and K_2 =-0.44×10^4 J/m^3. The lateral cell size was 5×5×5 nm^3; this lateral size (5 nm) is less than the exchange length, l_{ex} (≈10.7 nm), as expressed by $l_{ex} = (\frac{2A}{\mu_o M_S^2})^{0.5}$ to ensure the high accuracy of the simulation, and the Gilbert damping coefficient was set to α = 0.5 [76,327].

7.2.1.1 Construction of Phase Diagram

We investigated the low energy configurations as a function of thickness, t, and diameter, d, of NDs and as a function of thickness, t, and internal diameter, d_{in}, at constant external diameter, d_{out}, of NRs. The system was relaxed to a local energy minimum, and the final spin arrangement and the lower energy states in both types of system, i.e., NDs and NRs, were studied. Thereafter, we compared the relative energy of each final configuration and selected as a ground state the state with a low energy value. This process was repeated for many diameter and thickness collections, and the phase diagram was structured as a function of the dimension. In the case of NDs, three idealized main characteristic configurations are found: (i) in-plane single domain (planar), (ii) out-of-plane single domain (perpendicular), and (iii) vortex state in that most of the magnetic moments are parallel to the plane of NDs. In contrast, in NRs, four idealized characteristic configurations

are found: (i) in-plane single domain, (ii) in-plane flower state, (iii) vortex state, and (iv) helix state.

7.2.2 Theoretical Model

7.2.2.1 Construction of Phase Diagram for Nanodisks

We used two different expressions proposed by Altbir Drullinsky D.R. et al. [328] to construct the complete phase diagram separating the in-plane single-domain (SD), out-of-plane SD and vortex as the ground state in NDs: (i) the transition between in-plane and vortex phases was obtained by applying the expression $R = 9.82\left(\frac{l_{ex}^2}{t}\right) + 2.37l_{ex}$, and (ii) the transition between out-of-plane and vortex phases was obtained by the expression $R = l_{ex}\left(\frac{t}{0.082l_{ex}}\right)^{0.3}$, where R, l_{ex}, and t are the radius, exchange length, and thickness, respectively. We have theoretically described the ground states in magnetic nanodots, providing explicit expressions to calculate the transition lines among vortex and single-domain (SD) states.

7.2.2.2 Construction of Phase Diagram for Nanorings

Furthermore, we used the expression $R = 9.82\left(\frac{l_{ex}^2\, t}{\alpha(\beta)}\right)^{0.33}$, as collectively proposed by Landeros P. et al [329] and Escrig J. et al [330], to construct a phase diagram for NRs, where l_{ex} and t are the exchange length and thickness, respectively, and $\alpha(\beta)$ is a transition function that separates the uniform state and vortex state; where $\beta = \frac{d_{out}}{d_{in}}$ is the aspect ratio for NRs only.

7.3 Result and Discussion

7.3.1 Magnetic Phase Diagram

Figure 7.1(a, b) shows a schematic illustration of NRs and NDs indicating the surface and side charge regions essential for analyzing the energy terms in the magnetic vortex system. The circular region indicated by the black spin in NDs, Figure 7.1(b), is the vortex core, and spins perpendicular to the plane are responsible for out-of-plane magnetization. Figure 7.1(c) shows the phase diagram, where the dependence of the magnetic behavior on the geometry (thickness, t, and diameter, d) of the NDs, i.e., the transition from a single-domain (SD) state to a vortex configuration separated by their boundary line, is analyzed through the theoretical model and micromagnetic simulation. In NDs, three possible ground states of the magnetization are found at remanence: in-plane SD,

vortex, and out-of-plane SD; the point at which the three ground states have the same energy (thickness t ~ 80 nm and diameter d ~ 66 nm) is called a 'triple point'. If the NDs are very thin, then all the magnetic moments are arranged in-plane; if the diameter is small and the thickness is large, then the magnetization is perpendicular to the plane of the NDs (out-of-plane); and another ground state is a vortex state observed above a certain thickness and diameter, referred to as the critical size. The phase diagram constructed through the theoretical model is in very good agreement with the micromagnetic simulation result. However, the small discrepancy at the boundary line is probably due to the effect of the cubic cell discretization in the micromagnetic simulation that contributes to the additional roughness energy and hence the total ground state energy of the system. Such effects are not observed when constructing a phase diagram through the theoretical model. The nature of the phase diagram constructed for NDs, which provides explicit transition lines among vortex and in- and out-of-plane SD, agrees well with the theoretical and simulated results found elsewhere [331,332].

Figure 7.1(d, e) shows the theoretical and simulated phase diagrams of NRs as a function of thickness, t, and internal diameter, d_{in}, at constant outer diameter, d_{out}. The presence of the hole in a ring considerably modifies the vortex state, avoiding the possible out-of-plane SD state. Theoretically, we find only two possible ground states, i.e., the uniform state (SD state) and vortex state. Here, we have analyzed the minimum to maximum region, below ($< \alpha(\beta) = 0.1$) and above ($> \alpha(\beta) = 0.3$), where the possibility of the ground state vortex configuration is disregarded. In addition, it is worth mentioning that an intermediate mixed vortex phase could be possible for $0.1 < \alpha(\beta) < 0.3$ [329]; this phase depends on the inner radius of the NRs and occurs if the inner radius is sufficiently small compared to the outer diameter. Furthermore, within the reported range of t, d_{in}, and d_{out} here, four ground states, namely, in-plane SD, in-plane flower (also called onion), vortex and helix states, are observed through the micromagnetic simulation and agree well with the literature [58,333], and most of the region is found to correspond to the vortex state at intermediate values of thickness, t, and internal diameter, d_{in}, at fixed $d_{out.}$ We found that the triple point, i.e., the boundary point of in-plane SD, in-plane flower and vortex in NRs, is close to thickness t ~ 30 nm and internal diameter d_{in} ~ 37 nm.

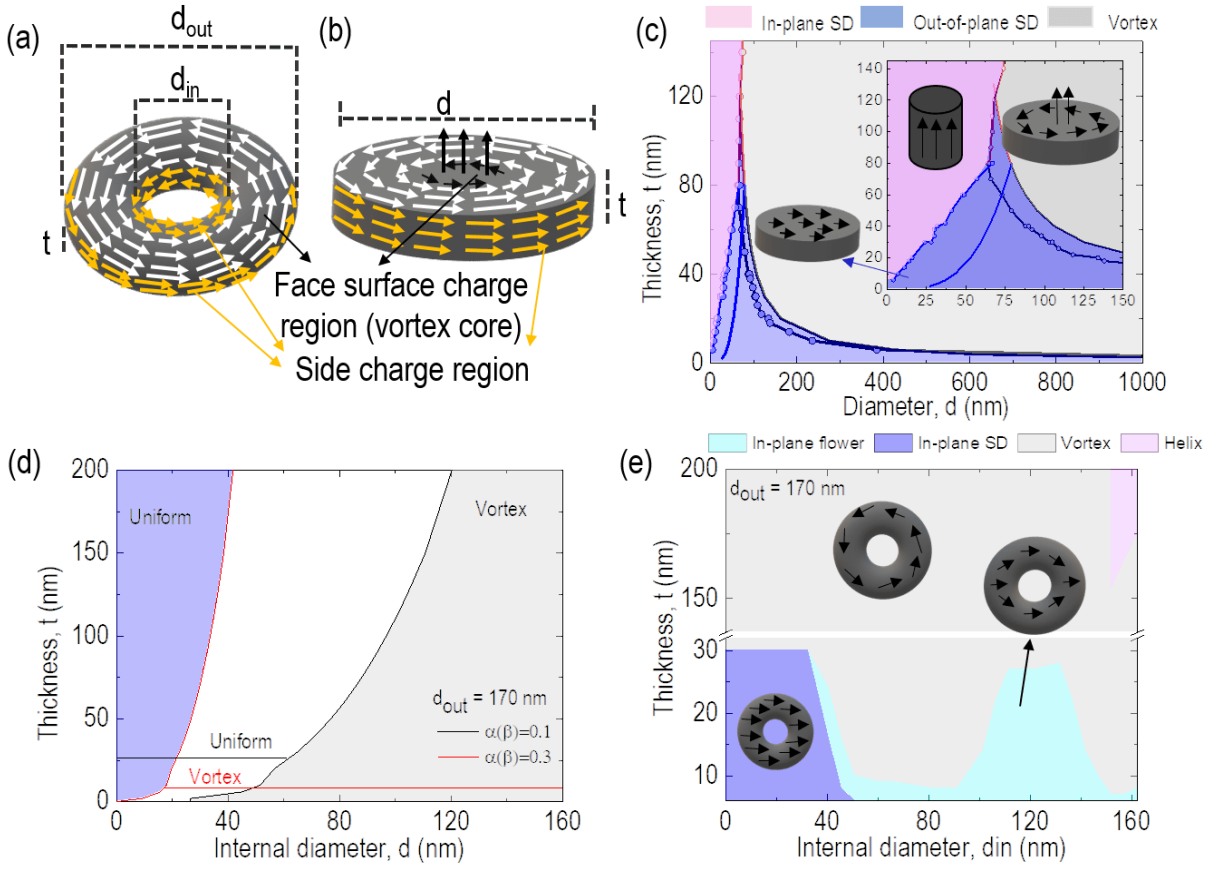

Figure 7.1: (a, b) Schematic pictures of NRs and NDs, (c) phase diagram of NDs obtained by the theoretical model (solid line) and micromagnetic simulation (solid line with point circles), and (d) and (e) phase diagrams of NRs obtained by the theoretical model and micromagnetic simulation, respectively.

Furthermore, when the thickness t approaches a larger value, the demagnetization energy increases proportionally [76], and when $t > d_{in}$, the strong out-of-plane demagnetizing field compels the top and bottom in-plane spin to point out and ultimately form a helix state. The helix state is a combinatorial result of the vortex and out-of-plane configurations in which the spins in the top and bottom planes of NRs exhibit a counterclockwise vortex configuration to reduce the fringe field, while in the middle planes, the spin is indicated to be out-of-plane along the z-axis [334]. These in-plane flower and helix states are considered metastable states that exhibit a nonzero net magnetization, although they have NRs structures, leading to considerable magnetostatic interactions in suspensions and aggregation[335,336]; therefore, these dimensional NRs are usually not recommended for biomedical applications.

7.3.2 Exchange energy

Figure 7.2(a) shows the exchange energy, E_{ex}, of NDs as a function of diameter, in which E_{ex} is decreasing with increasing diameter (from diameter d=200 to 1000 nm), where the full line and point circles indicate the energy obtained by the theoretical model and micromagnetic simulation, respectively.

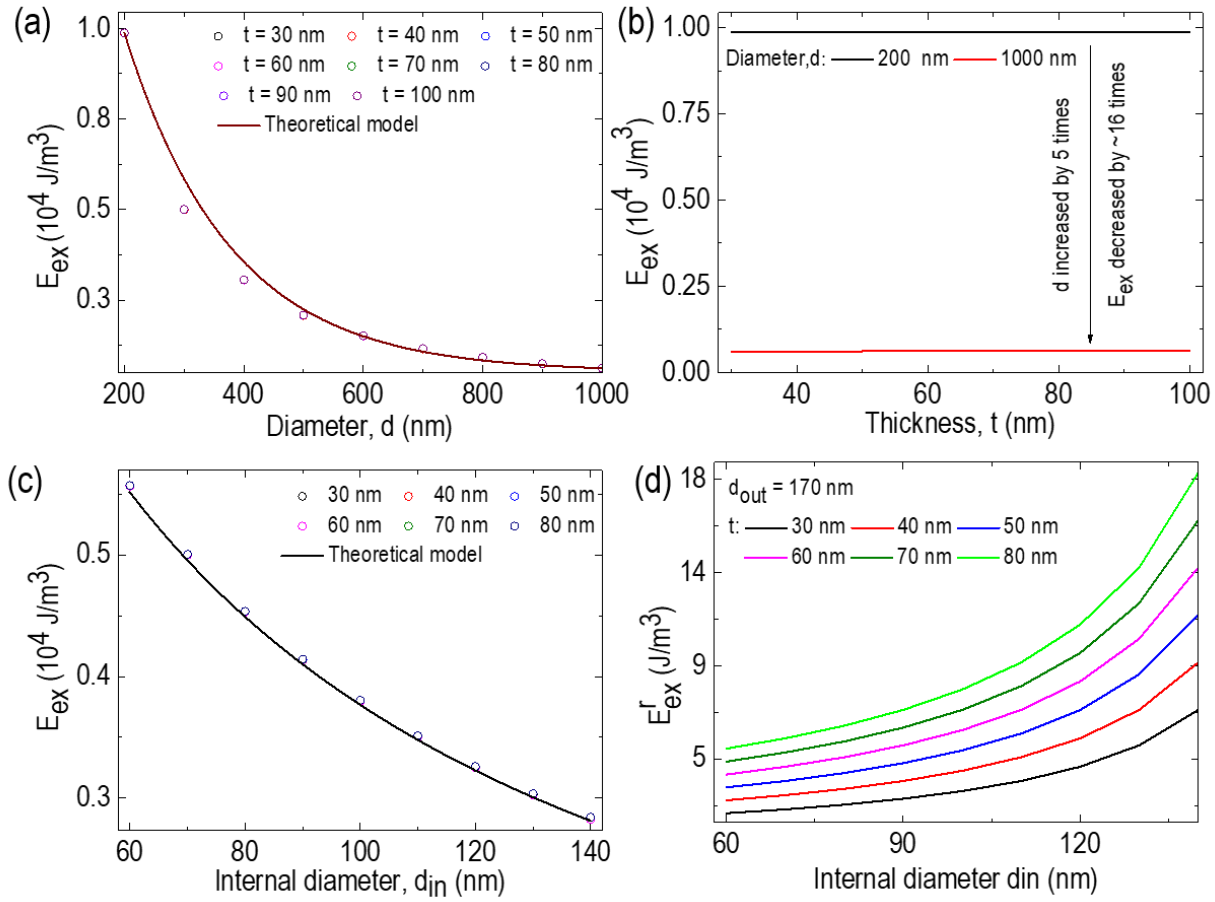

Figure 7.2: (a) Exchange energy, E_{ex}, evolution of NDs as a function of diameter, d, (b) comparison of E_{ex} loss with increasing diameter of NDs, and (c) and (d) exchange energy, E_{ex}, evolution and roughness contribution to E_{ex} in NRs as a function of internal diameter, d_{in}, respectively.

Quantitatively, when the diameter is increased by ~5 times, E_{ex} is decreased by ~16 times; NDs become a more energetically favorable state (lower energy state) for values much larger than the critical diameter (≈92 nm for Fe_3O_4), as observed in Figure 7.2 (a). Furthermore, from Figure 7.2 (b), it is observed that E_{ex} in the vortex region is independent of the thickness of the NDs. It is well reported that the total energy is almost dominated by the exchange energy because of the formation of a central vortex within the vortex state of NDs, whereas the single-domain state is dominated

mainly by the demagnetization energy generated by the surface charges on top of the lateral surfaces [239,240]. For large structures, the vortex state lowers the system energy by decreasing stray fields and thus reducing the magnetostatic energy. The central vortex of NDs has a vortex core of a certain radius, the so-called vortex core radius r_{vc}, which is much smaller than the radius of the NDs R ($r_{vc} << R$), and the magnetization in the region is out-of-plane, $m_z \neq 0$; however very smaller as compared to in-plane magnetization, whereas in the outer regions of the vortex, the magnetization lies completely in-plane. In principle, the vortex core is a stable formation, that is greatly coupled by exchange forces, and it could be assumed that the dynamic magnetization has significant values just outside of the vortex core, i.e., in-plane magnetization [241].

The value of the vortex core radius (r_{vc}) can be obtained by minimizing the total magnetic energy (details are given in refs. [39,337]); r_{vc} proportionally depends on the radius of NDs (at constant thickness), which favours a large reduction in exchange energy for a larger structure of the disk centre at the expense of a low dipolar energy increase. For biomedical applications, it is essential to have a large vortex core in NDs to reduce their magnetic remanence to a negligible value, and therefore to avoid agglomeration of NDs in suspension. With decreasing disk diameter at a constant thickness, as shown in Figure 7.2 (a), the relative contribution of the exchange energy for the central vortex increases, which thus increases the overall energy and renders the vortex state as a single-domain state under a critical diameter, d_c (sizes larger than 92 nm are not shown here); the largest exchange energy is observed for 200 nm NDs since this is close to the single-domain region (single-domain<d_c<vortex). The larger the diameter of NDs is, the longer the displacement of the vortex core, which lowers the exchange energy and renders better stability of the vortex state, reducing the remanent magnetization. Additionally, it is worth mentioning that by applying a field (H), the exchange energy decreases with increasing displacement of the vortex(s) [38]. On the other hand, the micromagnetic simulations precisely identify the equilibrium configuration, that is not a perfect vortex state. Nevertheless, the discreteness of the method and the utilization of a cubic mesh a the source of systematic errors of nonrectangular systems, thus limiting the precision of micromagnetic simulations reasoned by discretization [239]. This is more applicable to NDs and NRs since the circular boundary is estimated by a staircase of straight-line segments. Such edge roughness causes surface charges that rise the demagnetization energy. To investigate such roughness energy analytically, a simple analytical method was derived taking into account the ratio of the perimeter to the volume of the NPs; the roughness energy contribution generated from the

edge of dimension-based NPs. An increase in thickness contributes to the additional energy, the so-called 'exchange roughness energy', from the edge surface of each disk, which acts to make the edge spins point in directions far from the azimuthal direction. Although exchange roughness energy (E_{ex}^{r}) is negligible as compared to E_{ex}, its effect is accountable within the intermediate region (200-500 nm) due to some significant energy discrepancies between the theoretical model and micromagnetic simulations. We should note that E_{ex}^{r} is significant close to the single domain but is dominated when NDs are far from the SD region, even though the small exchange roughness energy of the particles examined could contribute significantly to the magnetic behavior of a disk-shaped particle in the pre-vortex stadium [326]. With the edge roughness being taken into account analytically, the total exchange energy led to good agreement between the theoretical model and simulations, as shown in Figure 7.2(a).

We note that the geometry of a ring is a disk when considering the internal diameter to be $d_{in}=0$, and it has already been mentioned that in such cases, $m_z \neq 0$. The maximum vortex core magnetization amplitude is 1 (for a disk), and the minimum is zero (for a narrow ring, $d_{in}/d_{out} > 0.9$). This means that the amplitude of the vortex core m_z varies from 1 to 0 in rings depending on the width, w ($w=d_{out}-d_{in}$, d_{out} is the external diameter); a wider ring has greater m_z. Figure 7.2 (c) shows the E_{ex} in NRs as a function of internal diameter d_{in} at a constant thickness, t, and reveals a similar energy trend to that exhibited by NDs. E_{ex} decreases with increasing d_{in}, where the full line and point circles indicate the energy obtained by the theoretical model and micromagnetic simulation, respectively, and are consistent with each other. The formation of the vortex core at a wider ring (closer to a disk) is expected; however, m_z is <1 and is responsible for the generation of exchange energy. When the width of the ring decreases, formation of the core has a lower probability and cannot be expected at narrow rings ($d_{in}/d_{out} > 0.9$), and the contribution to the exchange energy decreases with increasing internal diameter d_{in}. Likewise, for NDs, Figure 7.2 (d) shows the additional roughness energy, E_{ex}^{r}, contribution to E_{ex} as a function of d_{in}. The increase in E_{ex}^{r} with increasing d_{in} is due to the increased perimeter of the inner side of the ring, which contributes to making the inner edge spins point in directions away from the azimuthal direction. Furthermore, E_{ex}^{r} is linearly dependent on the thickness of the NRs. The E_{ex}^{r} contribution to the E_{ex} in NRs as a function of thickness is one order of magnitude greater than that in NDs within approximately similar dimensions (NDs: d = 200 nm, t = 40 nm; NRs: d_{out} = 170 nm, d_{in} = 140 nm and t = 40 nm). This larger contribution arises from the inner edge of NRs.

7.3.3 Magnetostatic energy

The magnetostatic energy of the system is considered an effect of the roughness of the surface. This roughness sources the presence of distributed magnetostatic charges on top of the interfaces. In practice, edge roughness arises due to the different steps involved during the synthesis process, for instance, NPs fabricated by different deposition techniques and thermal treatments [338] and with different substrates [339], growth conditions [340], growth rates [341], and nanoparticle thicknesses [342,343]. This edge roughness makes a significant contribution to the nucleation field for magnetization reversal [344–346] and, more importantly, to the stabilization of metastable equilibrium states [55]. Unlike the small roughness energy contribution to the exchange energy as discussed above, the edge roughness causes rise to a great magnetostatic energy contribution depending on the geometry of the NPs. The magnetostatic energy consists of significant surface (on the faces and sides) and negligible volume (for small thickness) contributions [240]. In the case of disk-shaped particles, two active inhomogeneous terms appear: (a) a face surface charge term (easy-plane anisotropy of thin disks and easy-axis anisotropy of thick disks, which can change sign near the edge, and (b) an edge side charge term, which causes the tangential magnetization distribution producing in clockwise or counter clockwise vortex chirality [347,348]. The vortex core generates non- vanishing surface magnetostatic charges with different signs on top of the different face surfaces. Their minimization causes complicated vortex results both in the plane as well as in the axial direction [349].

An inhomogeneous magnetization arrangement in magnetically soft NPs is due to the stray field produced by surface magnetostatic charges. The core magnetostatic energy is only produced by the surface magnetic charges along the perimeter of the particle since volume charges are absent (div m=0) and thickness t remains unchanged with the vortex displacement. The vortex core magnetostatic energy in disks arises from the out-of-plane magnetization ($m_z \neq 0$); surface magnetic charges on top of the faces of the disk localize near the vortex centre, which is a topological singularity. On the top and bottom surfaces, the surface charges are proportional to m_z, and the net side surface charges is zero on the circumference of the disk [350]. Thus, $E_{ms}^{vc} = \left(\frac{l_{ex}}{R_O}\right)^2$, where the vortex core radius approximately equal to l_{ex} is used, in agreement with micromagnetic simulations [76,351].

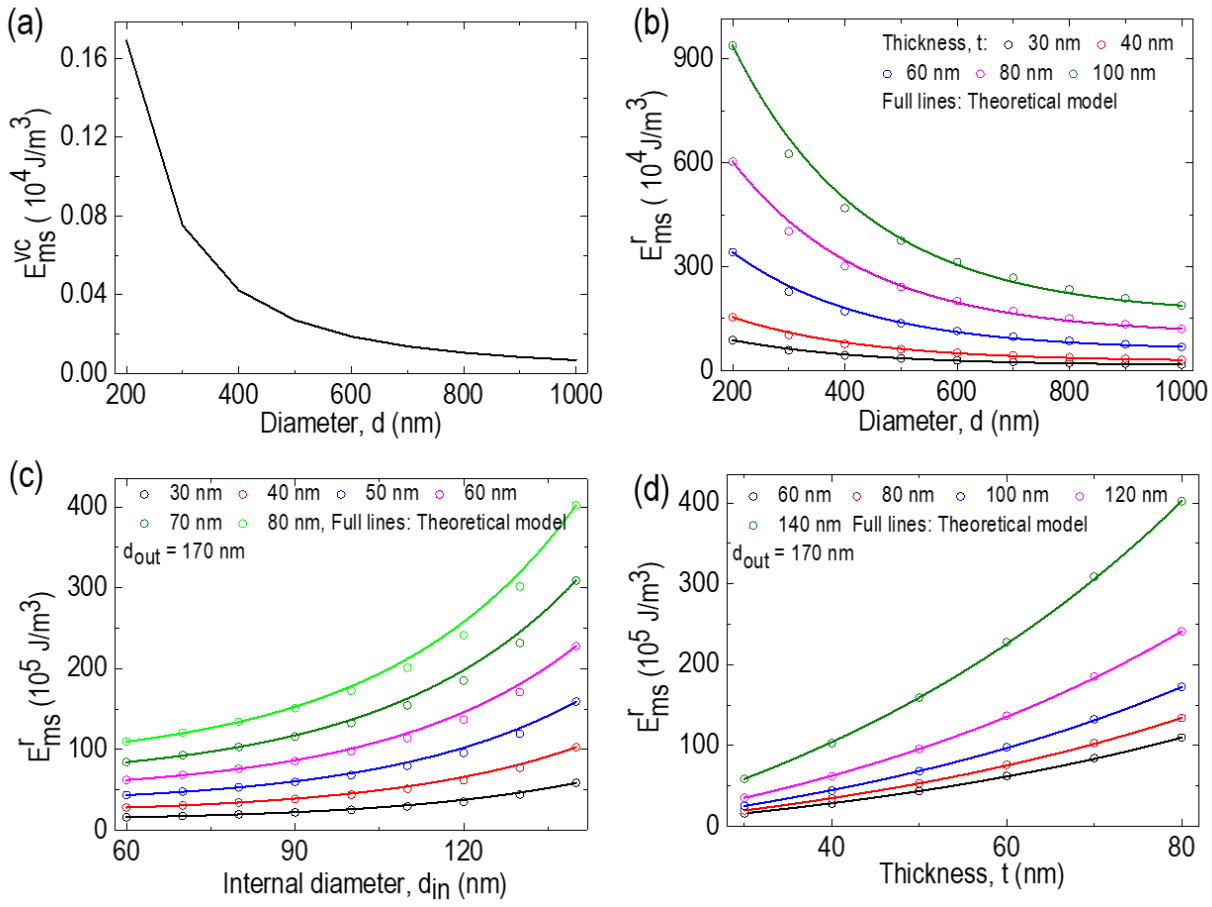

Figure 7.3: (a) Vortex core magnetostatic energy density, E^{vc}_{ms}, evolution of NDs as a function of diameter, d, (b) magnetostatic energy, E^{r}_{ms}, evolution as a function of diameter, d, in NDs, and (c) and (d) magnetostatic energy, E^{r}_{ms}, evolution as a function of internal diameter, d_{in}, and thickness, t, in NRs, respectively.

Figure 7.3 (a, b) shows the vortex core and roughness magnetostatic energy profiles as a function of diameter d in disks; the E^{vc}_{ms} contribution to the total magnetostatic energy is almost zero (approximately 10^5 times lower); thus, the total magnetostatic energy is dominated by E^{r}_{ms}. Mathematically, the magnetostatic energy is inversely proportional to the square of the disk diameter, d, and directly proportional to the thickness, t; however, the physics of the magnetic vortex system and the interpretation are quite different. At remanence (zero applied field, H=0), the centers of the vortices are at the centre of the NDs. In this state, the magnetic charges are practically absent, and the magnetostatic interaction between the individual NDs is small. Once an external magnetic field is generated and applied to the system, the centers of vortices are shifted, and few magnetic charges arise at the boundaries of the NDs, which leads to an rise in the self-

magnetostatic energy of the poles distributed on both faces of the disks with surface density $\sigma(\rho)$ [39]. The total displacement of the vortex core from the centre to the edge boundary is an important determining factor in reducing the core magnetostatic energy, depending on the diameter of the NDs. When the vortex core accessions the circumference of NDs, the elliptically distorted vortex shape effectively reduces the core magnetostatic energy because of the reduction in surface charge. The influence of vortex distortion is then crucially important for NDs with a smaller diameter (near the critical diameter discussed above) since the vortex core occupies approximately all the disk volume. When the applied field is sufficient to annihilate the vortex state, the minimum of the total energy reaches a maximum, making the vortex state unstable; as the vortex core is close to the edge, the surface charge density induced by the magnetic charges on the top and bottom faces increases on the circumference. Accordingly, the systems proceed towards the next energy minimum, that can be found for the state with a homogeneous magnetization distribution. On the other hand, the vortex state can be stabilized by the dominant energy engendered by magnetic charges on the side (thickness) of the NDs, i.e., the roughness magnetostatic energy. The rate of the decrease in this energy decreases with increased diameter, d, at a fixed thickness, t. This decreased rate is related to the decrease in the possible amount of side magnetic charges forming at $t< d$ with increasing d at fixed thickness t [240].

Similarly, Figure 7.3 (c, d) shows the magnetostatic energy profile of NRs as a function of thickness, t, and internal diameter, d_{in}, at constant external diameter, d_{out}. An increase in the internal diameter increases the perimeter of the inner side of NRs, and thus, more side charge can contribute to the magnetostatic energy, E^{r}_{ms}. Likewise, side charges are increased with an increase in thickness, contributing more to E^{r}_{ms}. The absence of the core region is a great advantage of NRs over the disks that avoids possible remanent magnetization, i.e., no out-of-plane magnetization ($m_z = 0$), and hence enhances the stability of NRs. Therefore, the total roughness magnetostatic energy induced by side charges is considered the total magnetostatic energy in NRs.

In the above section, we comprehensively studied the roles of the shape, size, vortex core, magnetic surface and side charges, hole and cell discretization/additional roughness contribution in the evolution of the exchange and magnetostatic energies of NDs and NRs through a theoretical model and micromagnetic simulations. Taking all these physical factors together, we have an idea of how they affect the stabilization and agglomeration of vortex NDs and NRs and the advantage of NRs

over NDs. Considering the potential to be used in cancer cell destruction, we further take NDs and NRs with different d_{in} at fixed t = 50 nm and d_{out} = 170 nm (diameter, d, considering d_{out} for NDs to obtain a common diameter with NRs). The main reasons to take this size range for further study were: (a) their feasibility to be chemically synthesized through a hydrothermal synthesis route and (b) biological consideration regarding their safety for potential in vivo applications (e.g. lack of remanence, compatible size for injection, cell uptake mechanisms) [41,42,223].

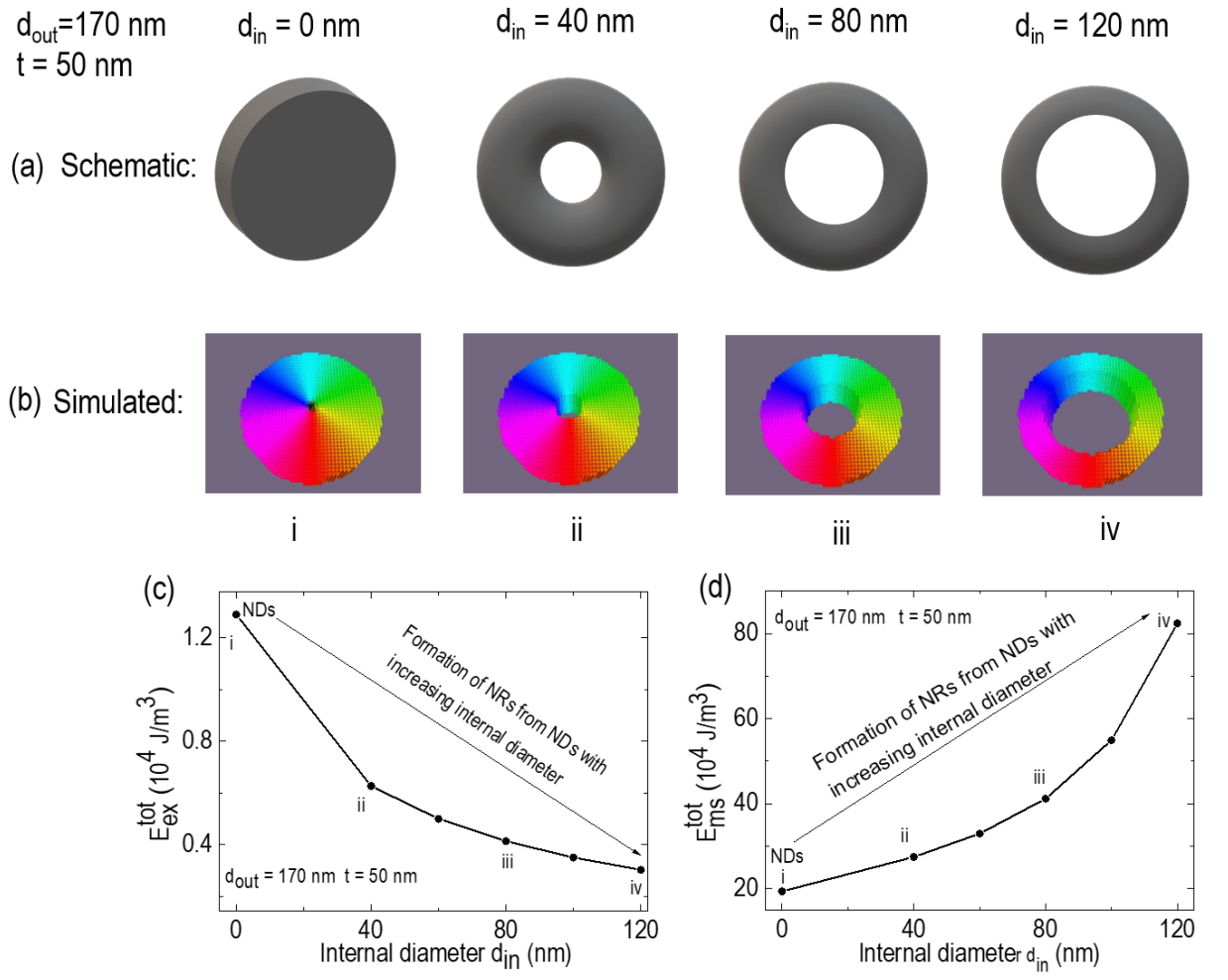

Figure 7.4: (a) Schematic geometrical formation of NRs from NDs, (b) simulated spin configuration for each geometry in the vortex state (H=0), and (c, d) total exchange energy, E_{ex}^{tot}, and total magnetostatic energy, E_{ms}^{tot}, evolution from NDs to NRs as a function of d_{in} at fixed t = 50 nm and d_{out} = 170 nm. We assumed d_{in} = 0 nm for NDs.

Figure 7.4 (a, b) shows schematics and vortex state spin configurations of NDs and NRs with increasing d_{in}. The exchange and magnetostatic energies of the respective geometries (NDs and NRs) are shown in Figure 7.4 (c, d). We have already discussed above how the energy evolves on

NDs and NRs separately. The energy evolution from the starting NDs into NRs shown in Figure 7.4 (c) demonstrates that the total exchange energy, E_{ex}^{tot}, is reduced by more than half along the corresponding steps i-iv (Figure 7.4(c)). This loss of energy is due to loss of the vortex core since the vortex core is responsible for the overall exchange energy in the vortex state of NDs. This means that the vortex state in NRs definitely exists in a much lower energetically favourable state than that in NDs and hence becomes more stable. Similarly, Figure 7.4(d) shows the increase in total magnetostatic energy, E_{ms}^{tot}, with increasing d_{in} is due to the inner edge perimeter (depending on the hole formation) contribution in the single-domain state. Here, E_{ex}^{tot} and E_{ms}^{tot} represent the total exchange energy (exchange energy, E_{ex}, plus additional roughness energy, E_{ex}^{r}) and total magnetostatic energy (vortex core magnetostatic energy, E_{ms}^{vc}, plus roughness energy, E_{ms}^{r}).

7.3.4 Dispersion and Agglomeration Capability

For most biomedical uses of MNPs, the samples are in colloidal form, and thus, obtaining stable particle dispersions and avoiding subsequent agglomeration is a primary concern. The magnetic vortex configurations for NDs and NRs discussed above show negligible remanence values in the absence of an applied field, favoring stable dispersions without agglomeration in a liquid medium, provided that their reversible magnetic behavior at low fields is preserved, as demonstrated in previous experimental work reported elsewhere [41–43,223]. The physical parameters that determine reversible magnetic behavior can be optimized through the numerical analysis presented here by reducing the susceptibility of the nanosystems. In recent work, Leulmi et al. [352] proposed two kinds of theoretical concepts for magnetic susceptibilities, the actual susceptibility of particles, $\chi(0)$, and the critical susceptibility ($\chi_{critical}$), also called the threshold susceptibility, below which self-polarization of particles can be avoided. Such magnetic susceptibilities are given as:

$$\chi(0) = \frac{4\pi}{2\pi\left(ln(\frac{8}{\beta})-\frac{1}{2}\right)} \tag{7.3}$$

$$\chi_{critical} = \frac{\partial M}{\partial H} = \frac{16K}{\left(\sum_{k=1}^{N}\frac{1}{k^3}\right)\beta} \tag{7.4}$$

The sum, in which N refers to the number of particles, converges quickly to 1.202, so a larger value of N has minimal importance. The numerical constant K, on the order of 1 to 4, refers to the stray field generated on a particle. In the present case, we assume $\beta = t/(R_{out} - R_{in})$ as the aspect ratio.

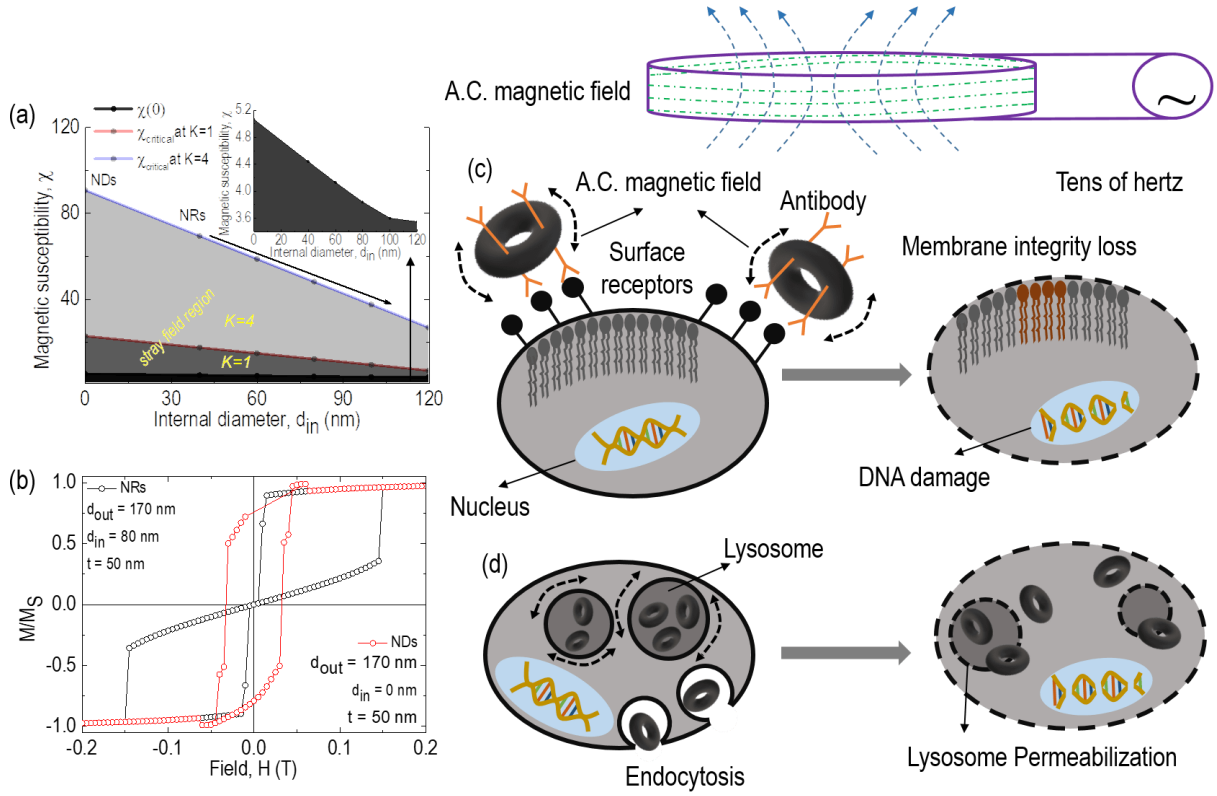

Figure 7.5: (a) Actual susceptibility, $\chi(0)$, and critical susceptibility, $\chi_{critical}$, from NDs to NRs as a function of internal diameter d_{in}, (b) micromagnetic simulation of NDs and NRs at a defined size, and (c) and (d) illustration of extracellular and intracellular magneto-mechanical actuation of vortex NRs on cancer cells, respectively; these schematic figures were made by ourselves but motivated by ref. [43].

Figure 7.5(a) shows the actual susceptibility, $\chi(0)$, and critical susceptibility, $\chi_{critical}$, of NDs and NRs as a function of internal diameter. Here, $d_{in} = 0$ refers to NDs. The magnetic susceptibility decreases with increasing d_{in} (hole) from NDs to NRs at constant $d_{out} = 170$ nm and t=50 nm. The value of $\chi(0)$ is lower than the critical self-polarization value ($\chi_{critical}$) even at K = 1, which indicates that the size of NDs and NRs we have taken here is free from the generation of a stray field. In addition, the obtained result of $\chi(0) < \chi_{critical}$ adds strong evidence for vortex NPs that avoid agglomeration or at least always reduce agglomeration [352]. Compared to NDs, NRs have a lower $\chi(0)$, which suggests better dispersion and stabilization in a suspension. The lower value of $\chi(0)$ in NRs is due to the absence of a vortex core, which has significant out-of-plane magnetization and contribution to the exchange energy in the case of NDs; details about the vortex core and hole contribution to the energy evolution in NDs and NRs have already been discussed above. Furthermore, our concern is how the vortex core and hole can affect the remanent magnetization

of these systems. Figure 7.5(b) shows the micromagnetic simulated hysteresis loop for NRs and NDs at some specific size. It is observed that ~ 75% of the saturation magnetization remains as remanence in NDs, although a flux-closure vortex configuration is observed; whereas zero remanence is observed in NRs. The results from the simulations agree well with the reported experimental values on nearly similar NDs [42,223] and NRs [41,56]. Thus, Figure 7.5(a, b) collectively confirms the roles of the vortex core and hole in the magnetic susceptibility and remanence properties in a vortex nanosystem. The hollow nature of the NRs changes the topological properties of the vortex solution, making it unnecessary for the vortex amplitude to attain a unity value at the centre of the ring. The NR does not exhibit an out-of-plane magnetization component at all if the inner hole is large enough; the amplitude of the vortex decays faster when the inner hole becomes larger, rendering better stabilization/dispersion in suspensions. Figure 7.5(c) illustrates the extracellular actuation of NRs on cancer cells in which the oscillation of NRs, attached by antibody-receptor bonding, influences the membrane integrity during exposure to ac magnetic field, triggering apoptosis within the cancer cell. Similarly, Figure 7.5(d) shows the intracellular actuation of NRs endocytosed within the cancer cell and accumulated in lysosomes, that are permeabilized due to oscillation of the NRs under the influence of ac magnetic field, generating cell self-destruction by apoptosis.

7.3.5 Magneto-mechanical Properties

The biomedical application aimed at targeted cancer cell destruction and the magneto-mechanical vibration efficiency of these NDs and NRs, activated by an alternating field, are thoroughly studied. For the potential case of triggering cancer cell apoptosis [43], generally, a larger torque applied on the cell membrane is a more efficient treatment. The magnetic torque (τ) effecting on a magnetic nanoparticle can be approximated by $\tau = |\mu|.|B|$, where μ is the magnetic moment and $B = \mu_o H$ represents the magnetic field. The detailed calculations are given in the Supplementary Information. In principle, the initial torque of the nanosystem will be similar regardless of if the applied magnetic field is rotational. However, further increase of the field varies the response of the system. In the vortex nanosystem, once the in-plane magnetization of the particles aligns with the plane of the rotating field, the magnetization shall rotate regardless of the exerting further torque on the particles [324]. When the applied field (H) is sufficient to saturate NPs, the magnetization will align with the field direction; however, as the field approaches to zero, NPs

will demagnetize and relax in the fluid, returning back to an arbitrary orientation. Similarly, when the magnetic field approaches a maximum, net magnetization is induced in NPs, that tend to align along the field direction. The repetition of this process would cause to a continuous oscillation of the NPs.

Figure 7.6 (a) shows the torque exerted for the investigated vortex NDs and NRs. The torque exerted by NDs is higher than that exerted by NRs, as expected because it depends on the volume; the presence of a hole in the NRs obviously lowers the net volume. An increase in the internal diameter decreases the volume and thus decreases the torque. Figure 7.6 (b) shows the upper limit of the force applied to a cell at the edge of NDs and NRs that can be achieved in the quasi-static regime using material and field parameters during an experiment. The increase in the upper force with increasing internal diameter is due to the additional increase in the inner edge perimeter along with the external edge. Here, we found that the magnetic-vortex-induced forces are in the range of > 100s of pN. While physically rupturing a cell within a membrane usually requires minimum of hundreds of pN, it has been demonstrated that even 0.5 pN activates ion channels that could accelerate cell apoptosis [353–355]. Therefore, the investigated NDs and NRs could potentially be used for magneto-mechanical cell destruction. The resulting force to oppose the magnetic torque (τ) is almost three orders of magnitude greater than the force required to activate an ion channel in the cell membrane. Although NDs can exert a torque (τ) of up to an order of magnitude greater than that of the studied NRs, the NDs have great susceptibility and remanence, as shown in Figure 7.6 (b), which might induce potential agglomeration in suspensions.

On the other hand, vortex NRs have lower susceptibility and negligible remanence compared to NDs, which suggests that NRs could be a better candidate from biological perspectives. Recently, the effectiveness of cell death/damage in different systems, (a) perpendicular synthetic antiferromagnetic state (P-SAF system) and (b) vortex state, has been studied accounting the importance of symmetry of magnetic anisotropy in P-SAF system Permalloy³²⁴ ($Ni_{20}Fe_{80}$). However, the present study deals with Fe_3O_4 NPs in two different geometries i.e., NRs and NDs with the same vortex configurations.

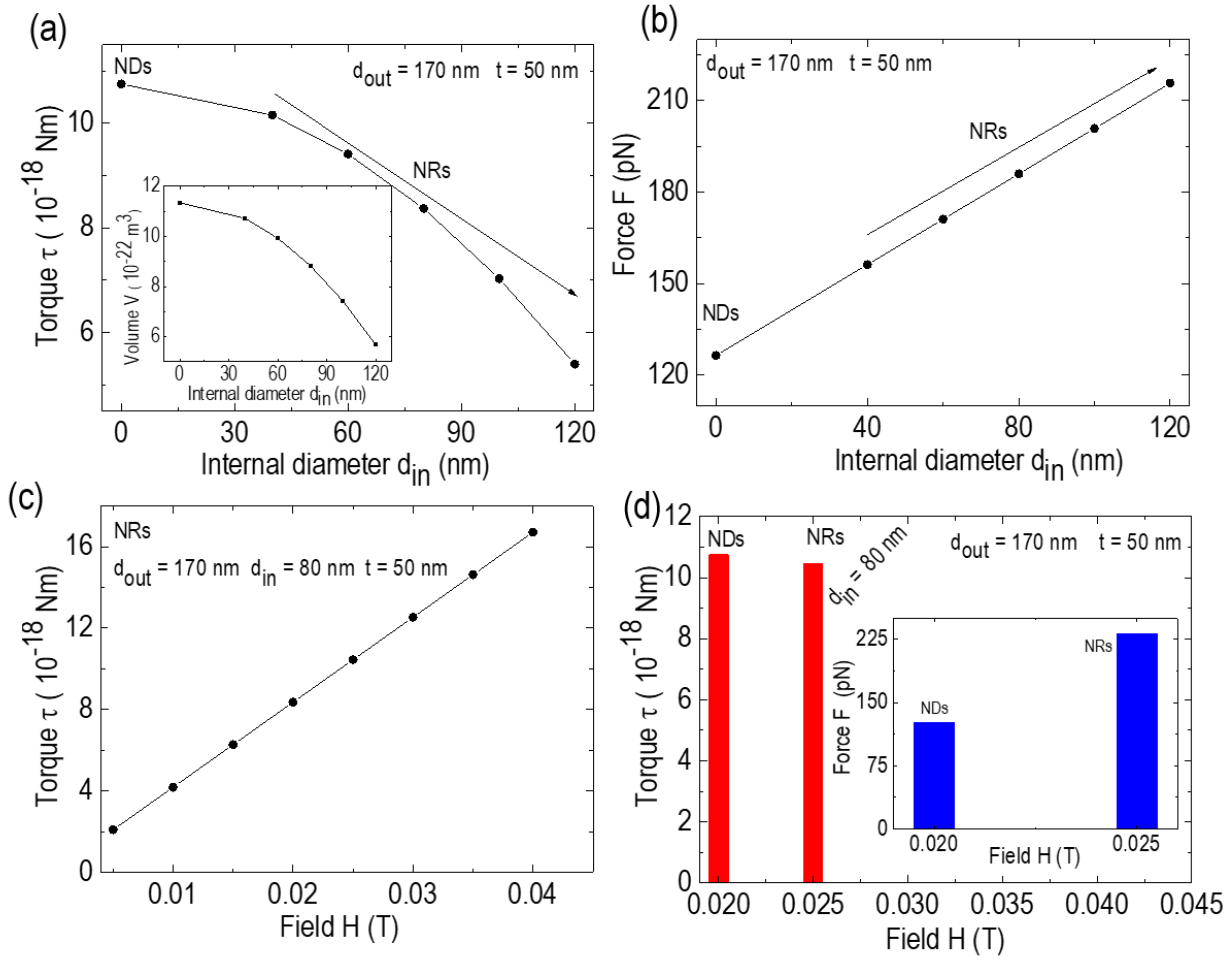

Figure 7.6: Torque exerted by NDs and NRs at a defined size, (b) force to be applied to rupture a cell membrane at the edge of NDs and NRs, (c) torque exerted by NRs as a function of an applied field, H, and (d) comparative study of torque (τ) and required force (F) at the edge of NDs and NRs at different fields.

The relevance of this comparative approach is that the effectiveness of cell death through magneto-mechanical action depends upon the magnitude of torque and their translation into force rather than symmetric anisotropy. The torque (τ) of NRs can be enhanced by increasing the thickness, diameter, and applied field (H) since the torque does not rely on the material magnetic properties, such as exchange stiffness constant. Figure 7.6 (c) clearly shows the linear field-dependent torque exerted by NRs. The idea is to compare the applied field H required for NRs to exert a torque (τ) equivalent to that exerted by NDs. Figure 7.6 (d) shows a comparative study of the torque (τ) and required force (F) at the edges of NDs and NRs. In the present case, it is clear that the same torque (τ) as NDs is exerted by NRs with an increase in the applied field of 20%. Similar to Figure 7.6

(b), the inset of Figure 7.6(d) shows the comparative force to be applied to rupture a cell membrane at the edge of NDs and NRs.

Experimentally, the state-of-art concept of magnetic-vortex-driven triggering of cancer cell apoptosis and further death via a magneto-mechanical approach was proposed by Kim D. G. et al. [43] for gold-coated permalloy ($Ni_{20}Fe_{80}$) MDs with a diameter of 1 μm and a thickness of 60 nm. Later, some works expanded this concept using a magnetic vortex disk as a magneto-mechanical transducer to eradicate cancer cells [324,331,352,356]; however, to the best of our knowledge, no further theoretical study has been performed taking vortex rings as a transducer. Recently, Gregurec D. et al. [223] studied Fe_3O_4 vortex NDs (diameter range: 98-226 nm and thickness range: 24-37 nm) as magneto-mechanical transducers of signals to remotely control mechanosensory cells under low and slow magnetic fields (H= 0.026 T, f=5 Hz). The torque (τ) generated by 226 nm NDs is approximately 1.6×10^{-17} Nm (slightly larger than that of our NDs), and the force to be applied to rupture a cell membrane is approximately 140 pN (larger than that of our NDs but smaller than that of our NRs). Furthermore, they observed that in dorsal root ganglia explants (DRGs), DRGs contain sensory neurons stating an extensive range of mechanoreceptors, and cultures adorned with 226 nm MNDs under 0.026 T, 5 Hz magnetic fields (MFs) did not cause significant and measurable variations in cell viability, indicating that the modest reactions to MFs of hippocampal neurons adorned with 226 nm MNDs were likely interceded by the influences of torque anion channel gating greater than on membrane permeability. Although excellent biological results were obtained by their study with 226 nm NDs, we propose better results for NRs, taking advantage of their negligible remanence and better stability in suspensions. It is necessary to functionalize the NPs with biocompatible materials, so it is suggested to bio-functionalize these vortex NRs before starting to work on cells and inserting them into targeted tumor's. Thus, based on the theoretical overview of the energy profile, dispersion/agglomeration capability, torque (τ) exerted and force applied to oppose the exerted magnetic torque (τ) of vortex NDs and NRs with tuning of the shape, size, and applied field reported in the present work, we motivate and inspire researchers to carry out in vitro and in vivo experiments using NRs as a cancer cell transducer to make progress in this emerging research field.

7.4 Conclusion

We studied the energy evolution, magnetic susceptibility, and magneto-mechanical properties of Fe_3O_4 NRs and NDs through theoretical and micromagnetic simulations. The presence of holes in NRs in comparison to NDs significantly reduced the exchange energy and magnetic susceptibility and hence minimized possible agglomeration effects in colloidal dispersions. Our numerical results show that for constant values of outer diameter, thickness, and applied field amplitude, the vortex magnetic configuration within ND topologies should be more efficient than the corresponding NR topology in transducing the magnetic coupling into mechanical actuation (i.e., physical oscillation of the NDs affecting the membrane integrity). Although vortex NDs could generate larger torque (τ) than vortex NRs, it is important to note that the remanence found from the out-of-plane magnetization in the ND vortex core would promote some degree of agglomeration, limiting the use of NDs in actual biological treatments. Possible alternatives to improve the torque of NRs and therefore their mechanical effects on biological systems could be to increase either the NR radius (since the magnetic torque depends on the volume) or to work under larger magnetic field amplitudes.

Chapter 8

Summary and Future Directions

8.1 Summary

The main objective of this thesis was to synthesize iron oxide vortex NPs and investigate their targeted therapeutic properties. The iron oxide NPs synthesis was optimized by fast and inexpensive MAH route. The structural, magnetic, magneto-hyperthermia and magneto-transducers properties of iron oxide vortex NPs were explored in detail. The main findings of the thesis are summarized below:

- The structural evolution and formation mechanism of the α-Fe_2O_3 HNPs, NRDs, NRs, NSs, and NDs and their transformation onto Fe/Fe_3O_4, Fe_3O_4, and Fe_3O_4-γ-Fe_2O_3 phase composition and stoichiometry were tuned by controlling the ratio of $\frac{Fe^{3+}}{PO_4^{3-}}$, chemical reagents, volume of solvent, synthesis temperature, reduction temperatures, and flow of the gas (H_2 + Ar).
- It was found that the loss of stoichiometry in Fe_3O_4 NPs was associated with the disappearance of the Verwey transitions due to the presence of defect and cation vacancies in the surface layer that impeded the electron hoping between Fe^{2+} and Fe^{3+} reinforcing the NPs into non-stoichiometry.
- The magnetic vortex configuration in iron oxide NRs, NDs, and NSs is examined and validated by means of theoretical, experimental and micromagnetic simulation. Taking all these together, it was found that the geometry of NPs is a key factor for the existence of vortex-configuration rather than their bulk properties.
- The magnetic properties of morphologically different nanosystems showed the coercive field for NRDs was higher than that of NTs, despite having similar shape and dimension. This phenomenon was ascribed to originate from surface anisotropy effects induced by higher amounts of adsorbed PO_4^{3-} anions on the NPs surface.
- The MFH properties of a circular Fe_3O_4 vortex NDs were investigated by experimental, theoretical, and simulations which revealed that the heating efficiency is better for

stoichiometry Fe_3O_4 NDs as compared to the non-stoichiometric one because of charge ordering between Fe^{2+} and Fe^{3+}.

- The role of switching field mediated shape, size and orientation of NDs in the direction of applied field was examined carefully. It was observed that larger the switching field, better the thermal efficiency.
- The existence of vortex-configuration is not only a factor to enhance the magnetic fluid hyperthermia properties but switching field mediated by shape, size and orientation were also important factors to be considered.
- The heating efficiency of different hollow nanosystems such as NRs and NTs for MFH applications was monitored. It was observed that the heating efficiency appeared to be clearly dominated by the shape anisotropy factor; NTs showed a better heat as compared to the NRs because of the larger shape anisotropy contribution in NTs.
- The energy evolution, magnetic susceptibility, and magneto-mechanical properties of Fe_3O_4 NRs and NDs were discussed thoroughly by theoretical analysis and micromagnetic simulations and suggested the presence of holes in NRs in comparison to NDs significantly reduced the exchange energy and magnetic susceptibility and hence minimized the possible agglomeration effects in colloidal dispersions.
- The rigorous theoretical analysis and simulated results showed the vortex magnetic configuration within NDs topologies should be more efficient than the corresponding NRs topology in transducing the magnetic coupling into mechanical actuation.
- The magnetic remanence (M_R) rises from out-of-plane magnetization in the NDs would promote a degree of agglomeration that limits the potential use of NDs in actual biological treatments, whereas NRs strongly avoid this issue owing to presence of holes. Thus, possible alternatives to improve the torque of NRs and therefore their mechanical effects on biological systems could increase either the NRs radius (since the magnetic torque depends on the volume) or applying larger magnetic field amplitudes. In overall, nanorings could be the best candidates as compared to nanodisks, nanospheres, and nanotubes in targeted therapeutic applications.

8.2 Future Directions

To date, most of the magnetic vortex NPs were synthesized through either beam lithography as a physical route or hydrothermal method as a chemical route. These both routes were very time consuming which take several days to a week. To tackle this issue, all the iron oxide NPs presented in this thesis were synthesized by fast and cost-effective microwave-assisted hydrothermal method which allow to prepare the same NPs within 30-60 minutes. Although, we were able to produce vortex NPs in several morphologies such as NRs, NDs, and NSs, the size of these NPs was not achieved as per our expectation within and/or below 100 nm. In addition, stoichiometry was another factor that was not finely attained. Even though this thesis has provided a profound understanding on the shape and size control synthesis of vortex/hollow NPs and their ground-work on thermal therapeutic applications, we would like to extend this work as per information given below:

- The microwave-assisted hydrothermal method was able to control the shape and size from micro-scale to nanoscale. Although the size of vortex NPs was quite large than expected, one can reproduce the same vortex configuration within and/or below 100 nm in size maintaining the stoichiometry of NPs by controlling the concentration of iron cations, phosphate anions, and volume of solvent.
- We found that the shape and size control vortex NPs can be produced through microwave-assisted hydrothermal route. However, while synthesizing the NPs, all the synthesis route have taken two-step process, i.e., first prepare α-Fe_2O_3 and transform onto their corresponding desire by means of thermal reduction. We also adopted same two-step process which seems a long way itself. In our opinion, it would be great if one can reproduce same magnetic vortex NPs directly in one-step process within a microwave irradiation. For this, we would suggest to use ethylene glycol as a solvent instead of water we used and control other parameter accordingly.
- The ferro/ferrimagnetic vortex-domain NPs with tunable size could be a promising candidates in significant enhancement of MRI T^*2 signal, which may overcome the drawbacks of conventional superparamagnetic imaging contrast agents. The T^*2 value strongly depends on the inhomogeneity of the local field surrounding the magnetic NPs which corresponds to the relative volume fraction, magnetic moment and susceptibility.

Owing to shape-induced vortex configuration and magnetic moment switching process (from vortex to onion and vice-versa), vortex nanostructures possess both high relative volume fraction and susceptibility, which result in the extremely large r^*2 value. In addition, the susceptibility difference between the inner and outer surface of NRs could result in the field inhomogeneity, which may also contribute to the enhancement of r^*2 value. Thus, we believe that vortex NPs can significantly enhance T^*2 -weighted MRI signals and have potential for cancer imaging applications.

- As the ferro/ferrimagnetic NPs can be oriented remotely via magnetic tuning under an external magnetic field. Taking an advantage of this property along with the prevention from undesired aggregation in iron oxide with vortex-configuration (for instance in NRs), we believe that the inner empty (hollow) space ascribe to the longer floating time while they rotate under magnetic modulation, whereas the solid magnetic NPs were more susceptible to the gravitational force and the floating time is very shorter. Thus, ring shape with gold(Au)/silver(Ag) coated magnetic NPs can be established as a potential candidate in biosensor leading to the reliable and reproducible detection. We would strongly suggest to utilize this system in localized surface plasmon resonance (LSPR) sensing in which higher sensitivity, lowers the noise in the sigmoidal fluctuation of extinction, and more tailorable dynamic range, than conventional LSPR sensing obtained using superparamagnetic NPs, are expected.
- We introduced iron oxide vortex NRs as a mechanotransducer based on the theoretical overview of the energy profile, dispersion/agglomeration capability, torque (τ) exerted and force applied to oppose the exerted magnetic torque (τ) in the present work. The experimental validate of the proposed work need to be investigated further at very low frequency set-up. Although the experimental work towards it is currently going on in our lab, we would like to encourage researchers to check out NRs as mechanotransducer in vitro and in vivo cancer destruction experiments.
- The hollow NPs were largely attentive in the biomedical field owing to their great potential in drug delivery taking an advantages of their unique structure such high surface-to-volume ratio, low material density, large cavities, controlled shell thickness and hierarchical pores. The as-prepared magnetic NTs can be heated in a magnetic field to trigger drug release and/or to produce hyperthermia/ablation of tissue simultaneously; thus can be utilized as a

dual mode nanosystem in diagnosis and therapy at the same time since hollow cavity incorporates to load the various drugs and bio-molecules inside and release them in a controlled manner. However, surface modification of these hollow NTs is suggested for the smart responsive release.

Chapter 9

Bibliography

(1) Cornell, R. M.; Schwertmann, U. Crystal Structure - The Iron Oxides: Structure, Properties, Reactions, Occurrences and Uses. **2006**, 707.

(2) Dunlop, D. J.; Berquó, T. S.; Dunlop, D. J.; Berquó, T. S.; Editors, G.; Feinberg, J.; Florindo, F.; Moskowitz, B.; Roberts, A. Morin Transition in Hematite: Size Dependence and Thermal Hysteresis. *Geochemistry, Geophys. Geosystems* **2008**, *9* (10), 10–11. https://doi.org/10.1029/2008GC002110.

(3) Bohra, M.; Agarwal, N.; Singh, V. A Short Review on Verwey Transition in Nanostructured Fe3O4 Materials. *J. Nanomater.* **2019**, *2019*. https://doi.org/10.1155/2019/8457383.

(4) Dronskowski, R. The Little Maghemite Story: A Classic Functional Material. https://doi.org/10.1002/1616-3028.

(5) Bowen, C. V.; Zhang, X.; Saab, G.; Gareau, P. J.; Rutt, B. K. Application of the Static Dephasing Regime Theory to Superparamagnetic Iron-Oxide Loaded Cells. *Magn. Reson. Med.* **2002**, *48* (1), 52–61. https://doi.org/10.1002/mrm.10192.

(6) Hergt, R.; Dutz, S.; Zeisberger, M.; Gawalek, W. Nanocrystalline Iron Oxide and Ba Ferrite Particles in the Superparamagnetism-Ferromagnetism Transition Range with Ferrofluid Applications. *J. Phys. Condens. Matter* **2006**, *18*, 2527–2542. https://doi.org/10.1088/0953-8984/18/38/S01.

(7) M. Benz. *Superparamagnetism : Theory and Applications*; 2012.

(8) Jönsson, P. E. Superparamagnetism and Spin Glass Dynamics of Interacting Magnetic Nanoparticle Systems. *Advances in Chemical Physics*. John Wiley and Sons Inc. October 29, 2004, pp 191–248. https://doi.org/10.1002/0471484237.ch3.

(9) Brown, W. F. Thermal Fluctuations of a Single-Domain Particle. *Phys. Rev.* **1963**, *130* (5), 1677–1686. https://doi.org/10.1103/PhysRev.130.1677.

(10) Papaefthymiou, G. C. Nanoparticle Magnetism. *Nano Today* **2009**, *4* (5), 438–447. https://doi.org/10.1016/j.nantod.2009.08.006.

(11) Benz, M. *Superparamagnetism : Theory and Applications-Discussion of Two Papers on Magnetic Nanoparticles*; 2012.

(12) Zheng, M.; Wu, X. C.; Zou, B. S.; Wang, Y. J. Magnetic Properties of Nanosized MnFe2O4

Particles. *J. Magn. Magn. Mater.* **1998**, *183* (1–2), 152–156. https://doi.org/10.1016/S0304-8853(97)01057-3.

(13) Vedantam, T. S.; Liu, J. P.; Zeng, H.; Sun, S. Thermal Stability of Self-Assembled FePt Nanoparticles. In *Journal of Applied Physics*; American Institute of PhysicsAIP, 2003; Vol. 93, pp 7184–7186. https://doi.org/10.1063/1.1558233.

(14) Skomski, R. Nanomagnetic Scaling. *J. Magn. Magn. Mater.* **2004**, *272–276*, 1476–1481. https://doi.org/10.1016/j.jmmm.2003.12.175.

(15) Kodama, R. . Magnetic Nanoparticles. *J. Magn. Magn. Mater.* **1999**, *200* (1–3), 359–372. https://doi.org/10.1016/S0304-8853(99)00347-9.

(16) Lifshitz, I. M.; Slyozov, V. V. The Kinetics of Precipitation from Supersaturated Solid Solutions. *J. Phys. Chem. Solids* **1961**, *19* (1–2), 35–50. https://doi.org/10.1016/0022-3697(61)90054-3.

(17) *Monte Carlo Methods in Statistical Physics*; Binder, K., Ed.; Topics in Current Physics; Springer Berlin Heidelberg: Berlin, Heidelberg, 1986; Vol. 7. https://doi.org/10.1007/978-3-642-82803-4.

(18) Jamet, M.; Wernsdorfer, W.; Thirion, C.; Dupuis, V.; Mélinon, P.; Pérez, A.; Mailly, D. Magnetic Anisotropy in Single Clusters. *Phys. Rev. B* **2004**, *69* (2), 024401. https://doi.org/10.1103/PhysRevB.69.024401.

(19) Eastham, D. A.; Kirkman, I. W. Highly Enhanced Orbital Magnetism on Cobalt Cluster Surfaces. *J. Phys. Condens. Matter* **2000**, *12* (31), L525–L532. https://doi.org/10.1088/0953-8984/12/31/101.

(20) Yanes, R.; Chubykalo-Fesenko, O.; Kachkachi, H.; Garanin, D. A.; Evans, R.; Chantrell, R. W. Effective Anisotropies and Energy Barriers of Magnetic Nanoparticles with Neel Surface Anisotropy. **2007**. https://doi.org/10.1103/PhysRevB.76.064416.

(21) Respaud, M.; Broto, J. M.; Rakoto, H.; Fert, A. R.; Thomas, L.; Barbara, B.; Verelst, M.; Snoeck, E.; Lecante, P.; Mosset, A.; Osuna, J.; Ely, T. O.; Amiens, C.; Chaudret, B. Surface Effects on the Magnetic Properties of Ultrafine Cobalt Particles. *Phys. Rev. B* **1998**, *57* (5), 2925–2935. https://doi.org/10.1103/PhysRevB.57.2925.

(22) Bødker, F.; Mørup, S.; Linderoth, S. Surface Effects in Metallic Iron Nanoparticles. *Phys. Rev. Lett.* **1994**, *72* (2), 282–285. https://doi.org/10.1103/PhysRevLett.72.282.

(23) Luis, F.; Torres, J. M.; García, L. M.; Bartolomé, J.; Stankiewicz, J.; Petroff, F.; Fettar, F.;

Maurice, J.-L.; Vaurès, A. Enhancement of the Magnetic Anisotropy of Nanometer-Sized Co Clusters: Influence of the Surface and of Interparticle Interactions. *Phys. Rev. B* **2002**, *65* (9), 094409. https://doi.org/10.1103/PhysRevB.65.094409.

(24) Parkin, S. S. P.; Hayashi, M.; Thomas, L. Magnetic Domain-Wall Racetrack Memory. *Science*. American Association for the Advancement of Science April 11, 2008, pp 190–194. https://doi.org/10.1126/science.1145799.

(25) Mermin, N. D. The Topological Theory of Defects in Ordered Media. *Rev. Mod. Phys.* **1979**, *51* (3), 591–648. https://doi.org/10.1103/RevModPhys.51.591.

(26) Braun, H.-B. Topological Effects in Nanomagnetism: From Superparamagnetism to Chiral Quantum Solitons. *Adv. Phys.* **2012**, *61* (1), 1–116. https://doi.org/10.1080/00018732.2012.663070.

(27) Feldtkeller, E.; Thomas, H. Struktur Und Energie von Blochlinien in Dünnen Ferromagnetischen Schichten. *Phys. der Kondens. Mater.* **1965**, *4* (1), 8–14. https://doi.org/10.1007/BF02423256.

(28) kosterlitz, J. M.; Thouless, D. J. Ordering, Metastability and Phase Transitions in Two-Dimensional Systems. *J. Phys. C Solid State Phys.* **1973**, *6* (7), 1181–1203. https://doi.org/10.1088/0022-3719/6/7/010.

(29) Zurek, W. H. Cosmological Experiments in Superfluid Helium? *Nature* **1985**, *317* (6037), 505–508. https://doi.org/10.1038/317505a0.

(30) Meier, Q. N.; Lilienblum, M.; Griffin, S. M.; Conder, K.; Pomjakushina, E.; Yan, Z.; Bourret, E.; Meier, D.; Lichtenberg, F.; Salje, E. K. H.; Spaldin, N. A.; Fiebig, M.; Cano, A. Global Formation of Topological Defects in the Multiferroic Hexagonal Manganites. *Phys. Rev. X* **2017**, *7* (4), 041014. https://doi.org/10.1103/PhysRevX.7.041014.

(31) Chmiel, F. P.; Price, N. W.; Johnson, R. D.; Lamirand, A. D.; Schad, J.; van der Laan, G.; Harris, D. T.; Irwin, J.; Rzchowski, M. S.; Eom, C.-B.; Radaelli, P. G. Observation of Magnetic Vortex Pairs at Room Temperature in a Planar {\alpha}-Fe2O3/Co Heterostructure. *Nat. Mater.* **2018**, *17* (7), 581–585. https://doi.org/10.1038/s41563-018-0101-x.

(32) Mermin, N. D.; Wagner, H. Absence of Ferromagnetism or Antiferromagnetism in One- or Two-Dimensional Isotropic Heisenberg Models. *Phys. Rev. Lett.* **1966**, *17* (22), 1133–1136. https://doi.org/10.1103/PhysRevLett.17.1133.

(33) Berezinski', V. L. DESTRUCTION OF LONG-RANGE ORDER IN ONE-DIMENSIONAL AND TWO-DIMENSIONAL SYSTEMS HAVING A CONTINUOUS SYMMETRY GROUP I. CLASSICAL SYSTEMS. *Sov. Phys. JEPT* **1971**, *32* (3).

(34) Moore, M. A. Additional Evidence for a Phase Transition in the Plane-Rotator and Classical Heisenberg Models for Two-Dimensional Lattices. *Phys. Rev. Lett.* **1969**, *23* (15), 861–863. https://doi.org/10.1103/PhysRevLett.23.861.

(35) Stanley, H. E. Dependence of Critical Properties on Dimensionality of Spins. *Phys. Rev. Lett.* **1968**, *20* (12), 589–592. https://doi.org/10.1103/PhysRevLett.20.589.

(36) Cowburn, R. P.; Koltsov, D. K.; Adeyeye, A. O.; Welland, M. E.; Tricker, D. M. Single-Domain Circular Nanomagnets. *Phys. Rev. Lett.* **1999**, *83* (5), 1042–1045. https://doi.org/10.1103/PhysRevLett.83.1042.

(37) Shinjo, T.; Okuno, T.; Hassdorf, R.; Shigeto, K.; Ono, T. Magnetic Vortex Core Observation in Circular Dots of Permalloy. *Science (80-.).* **2000**, *289* (5481), 930–932. https://doi.org/10.1126/science.289.5481.930.

(38) Guslienko, K. Y.; Novosad, V.; Otani, Y.; Shima, H.; Fukamichi, K. Field Evolution of Magnetic Vortex State in Ferromagnetic Disks. *Appl. Phys. Lett.* **2001**, *78* (24), 3848–3850. https://doi.org/10.1063/1.1377850.

(39) Guslienko, K. Y.; Novosad, V.; Otani, Y.; Shima, H.; Fukamichi, K. Magnetization Reversal Due to Vortex Nucleation, Displacement, and Annihilation in Submicron Ferromagnetic Dot Arrays. *Phys. Rev. B - Condens. Matter Mater. Phys.* **2002**, *65* (2), 244141–2441410. https://doi.org/10.1103/PhysRevB.65.024414.

(40) Ross, C. A.; Hwang, M.; Shima, M.; Cheng, J. Y.; Farhoud, M.; Savas, T. A.; Smith, H. I.; Schwarzacher, W.; Ross, F. M.; Redjdal, M.; Humphrey, F. B. Micromagnetic Behavior of Electrodeposited Cylinder Arrays. *Phys. Rev. B - Condens. Matter Mater. Phys.* **2002**, *65* (14), 1–8. https://doi.org/10.1103/PhysRevB.65.144417.

(41) Liu, X. L.; Yang, Y.; Ng, C. T.; Zhao, L. Y.; Zhang, Y.; Bay, B. H.; Fan, H. M.; Ding, J. Magnetic Vortex Nanorings: A New Class of Hyperthermia Agent for Highly Efficient In Vivo Regression of Tumors. *Adv. Mater.* **2015**, *27* (11), 1939–1944. https://doi.org/10.1002/adma.201405036.

(42) Yang, Y.; Liu, X.; Lv, Y.; Herng, T. S.; Xu, X.; Xia, W.; Zhang, T.; Fang, J.; Xiao, W.; Ding, J. Orientation Mediated Enhancement on Magnetic Hyperthermia of Fe_3O_4

Nanodisc. *Adv. Funct. Mater.* **2015**, *25* (5), 812–820. https://doi.org/10.1002/adfm.201402764.

(43) Kim, D.-H.; Rozhkova, E. A.; Ulasov, I. V.; Bader, S. D.; Rajh, T.; Lesniak, M. S.; Novosad, V. Biofunctionalized Magnetic-Vortex Microdiscs for Targeted Cancer-Cell Destruction. *Nat. Mater.* **2010**, *9* (2), 165–171. https://doi.org/10.1038/nmat2591.

(44) Gao, H.; Zhang, T.; Zhang, Y.; Chen, Y.; Liu, B.; Wu, J.; Liu, X.; Li, Y.; Peng, M.; Zhang, Y.; Xie, G.; Zhao, F.; Fan, H. M. Ellipsoidal Magnetite Nanoparticles: A New Member of the Magnetic-Vortex Nanoparticles Family for Efficient Magnetic Hyperthermia. *J. Mater. Chem. B* **2020**, *8* (3), 515–522. https://doi.org/10.1039/c9tb00998a.

(45) Ivanov, B.; Schnitzer, H.; Mertens, F.; Wysin, G. Magnon Modes and Magnon-Vortex Scattering in Two-Dimensional Easy-Plane Ferromagnets. *Phys. Rev. B - Condens. Matter Mater. Phys.* **1998**, *58* (13), 8464–8474. https://doi.org/10.1103/PhysRevB.58.8464.

(46) Guslienko, K. Y.; Ivanov, B. A.; Novosad, V.; Otani, Y.; Shima, H.; Fukamichi, K. Eigenfrequencies of Vortex State Excitations in Magnetic Submicron-Size Disks. *J. Appl. Phys.* **2002**, *91* (10 I), 8037–8039. https://doi.org/10.1063/1.1450816.

(47) Ferrero, R.; Manzin, A.; Barrera, G.; Celegato, F.; Coïsson, M.; Tiberto, P. Influence of Shape, Size and Magnetostatic Interactions on the Hyperthermia Properties of Permalloy Nanostructures. *Sci. Rep.* **2019**, *9* (1), 6591. https://doi.org/10.1038/s41598-019-43197-4.

(48) Wachowiak, A.; Wiebe, J.; Bode, M.; Pietzsch, O.; Morgenstern, M.; Wiesendanger, R. Direct Observation of Internal Spin Structure of Magnetic Vortex Cores. *Science (80-.).* **2002**, *298* (5593), 577–580. https://doi.org/10.1126/science.1075302.

(49) Choe, S. B.; Acremann, Y.; Scholl, A.; Bauer, A.; Doran, A.; Stöhr, J.; Padmore, H. A. Vortex Core-Driven Magnetization Dynamics. *Science (80-.).* **2004**, *304* (5669), 420–422. https://doi.org/10.1126/science.1095068.

(50) Kong, X. Y.; Ding, Y.; Yang, R.; Wang, Z. L. Single-Crystal Nanorings Formed by Epitaxial Self-Coiling of Polar Nanobelts. *Science (80-.).* **2004**, *303* (5662), 1348–1351. https://doi.org/10.1126/science.1092356.

(51) Tripp, S. L.; Pusztay, S. V.; Ribbe, A. E.; Wei, A. Self-Assembly of Cobalt Nanoparticle Rings. *J. Am. Chem. Soc.* **2002**, *124* (27), 7914–7915. https://doi.org/10.1021/ja0263285.

(52) Zhu, X.; Grütter, P.; Metlushko, V.; Ilic, B. Control of Domain Patterns in Square Shaped Nickel Rings. In *Journal of Applied Physics*; American Institute of PhysicsAIP, 2003; Vol.

93, pp 7059–7061. https://doi.org/10.1063/1.1557392.

(53) Zeng, H.; Li, J.; Wang, Z. L.; Liu, J. P.; Sun, S. Bimagnetic Core/Shell FePt/Fe3O4 Nanoparticles. *Nano Lett.* **2004**, *4* (1), 187–190. https://doi.org/10.1021/nl035004r.

(54) Zhu, X.; Grütter, P.; Metlushko, V.; Hao, Y.; Castaño, F. J.; Ross, C. A.; Ilic, B.; Smith, H. I. Construction of Hysteresis Loops of Single Domain Elements and Coupled Permalloy Ring Arrays by Magnetic Force Microscopy. In *Journal of Applied Physics*; American Institute of PhysicsAIP, 2003; Vol. 93, pp 8540–8542. https://doi.org/10.1063/1.1540129.

(55) Rothman, J.; Kläui, M.; Lopez-Diaz, L.; Vaz, C. A. F.; Bleloch, A.; Bland, J. A. C.; Cui, Z.; Speaks, R. Observation of a Bi-Domain State and Nucleation Free Switching in Mesoscopic Ring Magnets. *Phys. Rev. Lett.* **2001**, *86* (6), 1098–1101. https://doi.org/10.1103/PhysRevLett.86.1098.

(56) Jia, C.-J.; Sun, L.-D.; Luo, F.; Han, X.-D.; Heyderman, L. J.; Yan, Z.-G.; Yan, C.-H.; Zheng, K.; Zhang, Z.; Takano, M.; Hayashi, N.; Eltschka, M.; Kläui, M.; Rüdiger, U.; Kasama, T.; Cervera-Gontard, L.; Dunin-Borkowski, R. E.; Tzvetkov, G.; Raabe, J. Large-Scale Synthesis of Single-Crystalline Iron Oxide Magnetic Nanorings. *J. Am. Chem. Soc.* **2008**, *130* (50), 16968–16977. https://doi.org/10.1021/ja805152t.

(57) Wu, W.; Xiao, X.; Zhang, S.; Zhou, J.; Fan, L.; Ren, F.; Jiang, C. Large-Scale and Controlled Synthesis of Iron Oxide Magnetic Short Nanotubes: Shape Evolution, Growth Mechanism, and Magnetic Properties. *J. Phys. Chem. C* **2010**, *114* (39), 16092–16103. https://doi.org/10.1021/jp1010154.

(58) Yang, Y.; Liu, X. L.; Yi, J. B.; Yang, Y.; Fan, H. M.; Ding, J. Stable Vortex Magnetite Nanorings Colloid: Micromagnetic Simulation and Experimental Demonstration. *J. Appl. Phys.* **2012**, *111* (4). https://doi.org/10.1063/1.3684963.

(59) Zhu, F. Q.; Fan, D.; Zhu, X.; Zhu, J. G.; Cammarata, R. C.; Chien, C. L. Ultrahigh-Density Arrays of Ferromagnetic Nanorings on Macroscopic Areas. *Adv. Mater.* **2004**, *16* (23–24), 2155–2159. https://doi.org/10.1002/adma.200400675.

(60) Ding, H. F.; Schmid, A. K.; Li, D.; Guslienko, K. Y.; Bader, S. D. Magnetic Bistability of Co Nanodots. *Phys. Rev. Lett.* **2005**, *94* (15), 157202. https://doi.org/10.1103/PhysRevLett.94.157202.

(61) Córdoba-Camacho, W. Y.; Da Silva, R. M.; Vagov, A.; Shanenko, A. A.; Aguiar, J. A. Quasi-One-Dimensional Vortex Matter in Superconducting Nanowires. *Phys. Rev. B* **2018**,

98 (17), 174511. https://doi.org/10.1103/PhysRevB.98.174511.

(62) Fernandez-Roldan, J. A.; Del Real, R. P.; Bran, C.; Vazquez, M.; Chubykalo-Fesenko, O. Electric Current and Field Control of Vortex Structures in Cylindrical Magnetic Nanowires. *Phys. Rev. B* **2020**, *102* (2), 024421. https://doi.org/10.1103/PhysRevB.102.024421.

(63) Morgan-Wall, T.; Leith, B.; Hartman, N.; Rahman, A.; Marković, N. Measurement of Critical Currents of Superconducting Aluminum Nanowires in External Magnetic Fields: Evidence for a Weber Blockade. *Phys. Rev. Lett.* **2015**, *114* (7), 077002. https://doi.org/10.1103/PhysRevLett.114.077002.

(64) Córdoba, R.; Baturina, T. I.; Sesé, J.; Mironov, A. Y.; De Teresa, J. M.; Ibarra, M. R.; Nasimov, D. A.; Gutakovskii, A. K.; Latyshev, A. V.; Guillamón, I.; Suderow, H.; Vieira, S.; Baklanov, M. R.; Palacios, J. J.; Vinokur, V. M. Magnetic Field-Induced Dissipation-Free State in Superconducting Nanostructures. *Nat. Commun.* **2013**, *4* (1), 1–7. https://doi.org/10.1038/ncomms2437.

(65) Sorop, T. G.; De Jongh, L. J. Size-Dependent Anisotropic Diamagnetic Screening in Superconducting Sn Nanowires. *Phys. Rev. B - Condens. Matter Mater. Phys.* **2007**, *75* (1), 014510. https://doi.org/10.1103/PhysRevB.75.014510.

(66) Zhang, Y.; Wong, C. H.; Shen, J.; Sze, S. T.; Zhang, B.; Zhang, H.; Dong, Y.; Xu, H.; Yan, Z.; Li, Y.; Hu, X.; Lortz, R. Dramatic Enhancement of Superconductivity in Single-Crystalline Nanowire Arrays of Sn. *Sci. Rep.* **2016**, *6* (1), 1–10. https://doi.org/10.1038/srep32963.

(67) Kurtz, J. S.; Johnson, R. R.; Tian, M.; Kumar, N.; Ma, Z.; Xu, S.; Chan, M. H. W. Specific Heat of Superconducting Zn Nanowires. *Phys. Rev. Lett.* **2007**, *98* (24), 247001. https://doi.org/10.1103/PhysRevLett.98.247001.

(68) Brown, W. F. Criterion for Uniform Micromagnetization. *Phys. Rev.* **1957**, *105* (5), 1479–1482. https://doi.org/10.1103/PhysRev.105.1479.

(69) Heydon, G. P.; Hoon, S. R.; Farley, A. N.; Tomlinson, S. L.; Valera, M. S.; Attenborough, K.; Schwarzacher, W. Magnetic Properties of Electrodeposited Nanowires. *J. Phys. D. Appl. Phys.* **1997**, *30* (7), 1083–1093. https://doi.org/10.1088/0022-3727/30/7/004.

(70) Kröll, M.; Blau, W. J.; Grandjean, D.; Benfield, R. E.; Luis, F.; Paulus, P. M.; De Jongh, L. J. Magnetic Properties of Ferromagnetic Nanowires Embedded in Nanoporous Alumina Membranes. In *Journal of Magnetism and Magnetic Materials*; North-Holland, 2002; Vol.

249, pp 241–245. https://doi.org/10.1016/S0304-8853(02)00537-1.

(71) Jaccard, Y.; Guittienne, P.; Kelly, D.; Wegrowe, J.; Ansermet, J. P. Uniform Magnetization Rotation in Single Ferromagnetic Nanowires. *Phys. Rev. B - Condens. Matter Mater. Phys.* **2000**, *62* (2), 1141–1147. https://doi.org/10.1103/PhysRevB.62.1141.

(72) Wegrowe, J. E.; Kelly, D.; Franck, A.; Gilbert, S. E.; Ansermet, J. P. Magnetoresistance of Ferromagnetic Nanowires. *Phys. Rev. Lett.* **1999**, *82* (18), 3681–3684. https://doi.org/10.1103/PhysRevLett.82.3681.

(73) Wernsdorfer, W.; Doudin, B.; Mailly, D.; Hasselbach, K.; Benoit, A.; Meier, J.; Ansermet, J. P. H.; Barbara, B. Nucleation of Magnetization Reversal in Individual Nanosized Nickel Wires. *Phys. Rev. Lett.* **1996**, *77* (9), 1873–1876. https://doi.org/10.1103/PhysRevLett.77.1873.

(74) Li, S. P.; Peyrade, D.; Natali, M.; Lebib, A.; Chen, Y.; Ebels, U.; Buda, L. D.; Ounadjela, K. Flux Closure Structures in Cobalt Rings. *Phys. Rev. Lett.* **2001**, *86* (6), 1102–1105. https://doi.org/10.1103/PhysRevLett.86.1102.

(75) Hoffmann, H.; Steinbauer, F. Single Domain and Vortex State in Ferromagnetic Circular Nanodots. *J. Appl. Phys.* **2002**, *92* (9), 5463–5467. https://doi.org/10.1063/1.1510559.

(76) Vaz, C. A. F.; Athanasiou, C.; Bland, J. A. C.; Rowlands, G. Energetics of Magnetic Ring and Disk Elements: Uniform versus Vortex State. *Phys. Rev. B - Condens. Matter Mater. Phys.* **2006**, *73* (5). https://doi.org/10.1103/PhysRevB.73.054411.

(77) Goll, D.; MacKe, S.; Berkowitz, A. E.; Bertram, H. N. Magnetic Ground States and the Role of Vortices in Ferromagnetic Hollow Nanospheres. *Phys. B Condens. Matter* **2006**, *372* (1–2), 282–285. https://doi.org/10.1016/J.PHYSB.2005.10.067.

(78) Chicheł, A.; Skowronek, J.; Kubaszewska, M.; Kanikowski, M. Hyperthermia – Description of a Method and a Review of Clinical Applications. *Reports Pract. Oncol. Radiother.* **2007**, *12* (5), 267–275. https://doi.org/10.1016/S1507-1367(10)60065-X.

(79) GILCHRIST, R. K.; MEDAL, R.; SHOREY, W. D.; HANSELMAN, R. C.; PARROTT, J. C.; TAYLOR, C. B. Selective Inductive Heating of Lymph Nodes. *Ann. Surg.* **1957**, *146* (4), 596. https://doi.org/10.1097/00000658-195710000-00007.

(80) Bordelon, D. E.; Cornejo, C.; Grttner, C.; Westphal, F.; Deweese, T. L.; Ivkov, R. Magnetic Nanoparticle Heating Efficiency Reveals Magneto-Structural Differences When Characterized with Wide Ranging and High Amplitude Alternating Magnetic Fields. *J.*

Appl. Phys. **2011**, *109* (12), 124904. https://doi.org/10.1063/1.3597820.

(81) Belyanina, I.; Kolovskaya, O.; Zamay, S.; Gargaun, A.; Zamay, T.; Kichkailo, A. Targeted Magnetic Nanotheranostics of Cancer. *Molecules* **2017**, *22* (6). https://doi.org/10.3390/MOLECULES22060975.

(82) Hedayatnasab, Z.; Abnisa, F.; Daud, W. M. A. W. Review on Magnetic Nanoparticles for Magnetic Nanofluid Hyperthermia Application. *Mater. Des.* **2017**, *123*, 174–196. https://doi.org/10.1016/J.MATDES.2017.03.036.

(83) Johannsen, M.; Gneveckow, U.; Eckelt, L.; Feussner, A.; Waldöfner, N.; Scholz, R.; Deger, S.; Wust, P.; Loening, S. A.; Jordan, A. Clinical Hyperthermia of Prostate Cancer Using Magnetic Nanoparticles: Presentation of a New Interstitial Technique. *Int. J. Hyperthermia* **2005**, *21* (7), 637–647. https://doi.org/10.1080/02656730500158360.

(84) Clerc, P.; Jeanjean, P.; Hallalli, N.; Gougeon, M.; Pipy, B.; Carrey, J.; Fourmy, D.; Gigoux, V. Targeted Magnetic Intra-Lysosomal Hyperthermia Produces Lysosomal Reactive Oxygen Species and Causes Caspase-1 Dependent Cell Death. *J. Control. Release* **2018**, *270*, 120–134. https://doi.org/10.1016/J.JCONREL.2017.11.050.

(85) Carrey, J.; Mehdaoui, B.; Respaud, M. Simple Models for Dynamic Hysteresis Loop Calculations of Magnetic Single-Domain Nanoparticles: Application to Magnetic Hyperthermia Optimization. *J. Appl. Phys.* **2011**, *109* (8), 083921. https://doi.org/10.1063/1.3551582.

(86) Rosensweig, R. E. Heating Magnetic Fluid with Alternating Magnetic Field. *J. Magn. Magn. Mater.* **2002**, *252* (1-3 SPEC. ISS.), 370–374. https://doi.org/10.1016/S0304-8853(02)00706-0.

(87) Gavilán, H.; Avugadda, S. K.; Fernández-Cabada, T.; Soni, N.; Cassani, M.; Mai, B. T.; Chantrell, R.; Pellegrino, T. Magnetic Nanoparticles and Clusters for Magnetic Hyperthermia: Optimizing Their Heat Performance and Developing Combinatorial Therapies to Tackle Cancer. *Chem. Soc. Rev.* **2021**, *50* (20), 11614–11667. https://doi.org/10.1039/D1CS00427A.

(88) Sharma, S. K.; Shrivastava, N.; Rossi, F.; Tung, L. D.; Thanh, N. T. K. Nanoparticles-Based Magnetic and Photo Induced Hyperthermia for Cancer Treatment. *Nano Today* **2019**, *29*, 100795. https://doi.org/10.1016/J.NANTOD.2019.100795.

(89) Zhang, W.; Zuo, X.; Niu, Y.; Wu, C.; Wang, S.; Guan, S.; Silva, S. R. P. Novel

Nanoparticles with Cr3+ Substituted Ferrite for Self-Regulating Temperature Hyperthermia. *Nanoscale* **2017**, *9* (37), 13929–13937. https://doi.org/10.1039/c7nr02356a.

(90) Munoz-Menendez, C.; Conde-Leboran, I.; Baldomir, D.; Chubykalo-Fesenko, O.; Serantes, D. The Role of Size Polydispersity in Magnetic Fluid Hyperthermia: Average vs. Local Infra/over-Heating Effects. *Phys. Chem. Chem. Phys.* **2015**, *17* (41), 27812–27820. https://doi.org/10.1039/c5cp04539h.

(91) Nemati, Z.; Alonso, J.; Martinez, L. M.; Khurshid, H.; Garaio, E.; Garcia, J. A.; Phan, M. H.; Srikanth, H. Enhanced Magnetic Hyperthermia in Iron Oxide Nano-Octopods: Size and Anisotropy Effects. *J. Phys. Chem. C* **2016**, *120* (15), 8370–8379. https://doi.org/10.1021/acs.jpcc.6b01426.

(92) Dutz, S.; Hergt, R. Magnetic Nanoparticle Heating and Heat Transfer on a Microscale: Basic Principles, Realities and Physical Limitations of Hyperthermia for Tumour Therapy. *International Journal of Hyperthermia*. Informa Healthcare 2013, pp 790–800. https://doi.org/10.3109/02656736.2013.822993.

(93) Shah, R. R.; Davis, T. P.; Glover, A. L.; Nikles, D. E.; Brazel, C. S. Impact of Magnetic Field Parameters and Iron Oxide Nanoparticle Properties on Heat Generation for Use in Magnetic Hyperthermia. *J. Magn. Magn. Mater.* **2015**, *387*, 96–106. https://doi.org/10.1016/j.jmmm.2015.03.085.

(94) Martinez-Boubeta, C.; Simeonidis, K.; Makridis, A.; Angelakeris, M.; Iglesias, O.; Guardia, P.; Cabot, A.; Yedra, L.; Estradé, S.; Peiró, F.; Saghi, Z.; Midgley, P. A.; Conde-Leborán, I.; Serantes, D.; Baldomir, D. Learning from Nature to Improve the Heat Generation of Iron-Oxide Nanoparticles for Magnetic Hyperthermia Applications. *Sci. Rep.* **2013**, *3*. https://doi.org/10.1038/srep01652.

(95) Ho, D.; Sun, X.; Sun, S. Monodisperse Magnetic Nanoparticles for Theranostic Applications. *Acc. Chem. Res.* **2011**, *44* (10), 875–882. https://doi.org/10.1021/ar200090c.

(96) Usov, N. A.; Nesmeyanov, M. S.; Tarasov, V. P. Magnetic Vortices as Efficient Nano Heaters in Magnetic Nanoparticle Hyperthermia. *Sci. Rep.* **2018**, *8* (1), 1224. https://doi.org/10.1038/s41598-017-18162-8.

(97) Fan, H.-M.; Yi, J.-B.; Yang, Y.; Kho, K.-W.; Tan, H.-R.; Shen, Z.-X.; Ding, J.; Sun, X.-W.; Olivo, M. C.; Feng, Y.-P. Single-Crystalline MFe_2O_4 Nanotubes/Nanorings Synthesized by Thermal Transformation Process for Biological Applications. *ACS Nano* **2009**, *3* (9),

2798–2808. https://doi.org/10.1021/nn9006797.

(98) Gutierrez-Guzman, D. F.; Lizardi, L. I.; Otálora, J. A.; Landeros, P. Hyperthermia in Low Aspect-Ratio Magnetic Nanotubes for Biomedical Applications. *Appl. Phys. Lett.* **2017**, *110* (13), 133702. https://doi.org/10.1063/1.4979165.

(99) Haldar, A.; Adeyeye, A. O. Vortex Chirality Control in Circular Disks Using Dipole-Coupled Nanomagnets. *Appl. Phys. Lett.* **2015**, *106* (3). https://doi.org/10.1063/1.4906142.

(100) Dufrêne, Y. F.; Evans, E.; Engel, A.; Helenius, J.; Gaub, H. E.; Müller, D. J. Five Challenges to Bringing Single-Molecule Force Spectroscopy into Living Cells. *Nat. Methods* **2011**, *8* (2), 123–127. https://doi.org/10.1038/NMETH0211-123.

(101) Schoen, I.; Pruitt, B. L.; Vogel, V. The Yin-Yang of Rigidity Sensing: How Forces and Mechanical Properties Regulate the Cellular Response to Materials. *http://dx.doi.org/10.1146/annurev-matsci-062910-100407* **2013**, *43*, 589–618. https://doi.org/10.1146/ANNUREV-MATSCI-062910-100407.

(102) Vitol, E. A.; Novosad, V.; Rozhkova, E. A. Microfabricated Magnetic Structures for Future Medicine: From Sensors to Cell Actuators. *Nanomedicine (Lond).* **2012**, *7* (10), 1611–1624. https://doi.org/10.2217/NNM.12.133.

(103) Sixtus, K. J.; Tonks, L. Propagation of Large Barkhausen Discontinuities. *Phys. Rev.* **1931**, *37* (8), 930. https://doi.org/10.1103/PhysRev.37.930.

(104) Heisenberg, W. Zur Theorie Des Ferromagnetismus. *Zeitschrift für Phys.* **1928**, *49* (9–10), 619–636. https://doi.org/10.1007/BF01328601.

(105) Preisach, F. Untersuchungen Über Den Barkhauseneffekt. *Ann. Phys.* **1929**, *395* (6), 737–799. https://doi.org/10.1002/ANDP.19293950603.

(106) Hubert, A.; Schäfer, R. Introduction. *Magn. Domains* **1998**, 1–10. https://doi.org/10.1007/978-3-540-85054-0_1.

(107) Heisenberg, W. Zur Theorie Des Ferromagnetismus. *Zeitschrift für Phys. 1928 499* **1928**, *49* (9), 619–636. https://doi.org/10.1007/BF01328601.

(108) Brown, W. *Micromagnetics*; J. Wiley: New York ;;London, 1963.

(109) Landau, L. D.; Lifshitz, E. On the Theory of the Dispersion of Magnetic Permeability in Ferromagnetic Bodies. *Phys. Z. Sowjet.* **1935**, *8*, 153.

(110) Herring, C.; Kittel, C. On the Theory of Spin Waves in Ferromagnetic Media. *Phys. Rev.* **1951**, *81* (5), 869. https://doi.org/10.1103/PhysRev.81.869.

(111) Heisenberg, W. Zur Theorie Des Ferromagnetismus. *Zeitschrift für Phys. 1928 499* **1928**, *49* (9), 619–636. https://doi.org/10.1007/BF01328601.

(112) Brown, W. *Magnetostatic Principles in Ferromagnetism.*; North-Holland Pub. Co.;;Interscience Publishers,: Amsterdam,;New York, 1962.

(113) Bloch, F. Zur Theorie Des Austauschproblems Und Der Remanenzerscheinung Der Ferromagnetika. *Zeitschrift für Phys.* **1932**, *74* (5–6), 295–335. https://doi.org/10.1007/BF01337791.

(114) Gilbert, T. A Lagrangian Formulation of the Gyromagnetic Equation of the Magnetization Field. *Phys. Rev.* **1955**.

(115) Miltat, J. E.; Donahue, M. J. Numerical Micromagnetics: Finite Difference Methods. *Handb. Magn. Adv. Magn. Mater.* **2007**. https://doi.org/10.1002/9780470022184.HMM202.

(116) Schrefl, T.; Hrkac, G.; Bance, S.; Suess, D.; Ertl, O.; Fidler, J. Numerical Methods in Micromagnetics (Finite Element Method). *Handb. Magn. Adv. Magn. Mater.* **2007**. https://doi.org/10.1002/9780470022184.HMM203.

(117) Ferrero, R.; Manzin, A.; Barrera, G.; Celegato, F.; Coïsson, M.; Tiberto, P. Influence of Shape, Size and Magnetostatic Interactions on the Hyperthermia Properties of Permalloy Nanostructures. *Sci. Reports 2019 91* **2019**, *9* (1), 1–12. https://doi.org/10.1038/s41598-019-43197-4.

(118) Victora, R. H. Micromagnetic Predictions for Barium Ferrite Particles (Invited). *J. Appl. Phys.* **1998**, *63* (8), 3423. https://doi.org/10.1063/1.340755.

(119) Fukunaga, H.; Inoue, H. Effect of Intergrain Exchange Interaction on Magnetic Properties in Isotropic Nd-Fe-B Magnets. *Jpn. J. Appl. Phys.* **1992**, *31* (5 R), 1347–1352. https://doi.org/10.1143/JJAP.31.1347/XML.

(120) Kittel, C. On the Theory of Ferromagnetic Resonance Absorption. *Phys. Rev.* **1948**, *73* (2), 155. https://doi.org/10.1103/PhysRev.73.155.

(121) The Go Programming Language https://go.dev/ (accessed Dec 28, 2021).

(122) CUDA Toolkit Documentation https://docs.nvidia.com/cuda/index.html (accessed Dec 28, 2021).

(123) Rave, W.; Fabian, K.; Hubert, A. Magnetic States of Small Cubic Particles with Uniaxial Anisotropy. *J. Magn. Magn. Mater.* **1998**, *190*, 332–348.

(124) Bowden, S. R.; Ahmed, K. K. L.; Gibson, U. J. Longitudinal Magneto-Optic Kerr Effect Detection of Latching Vortex Magnetization Chirality in Individual Mesoscale Rings. *Appl. Phys. Lett.* **2007**, *91* (23), 232505. https://doi.org/10.1063/1.2822814.

(125) Jain, S.; Adeyeye, A. O. Probing the Magnetic States in Mesoscopic Rings by Synchronous Transport Measurements in Ring-Wire Hybrid Configuration. *Appl. Phys. Lett.* **2008**, *92* (20), 202506. https://doi.org/10.1063/1.2936089.

(126) Mawass, M. A.; Richter, K.; Bisig, A.; Reeve, R. M.; Krüger, B.; Weigand, M.; Stoll, H.; Krone, A.; Kronast, F.; Schütz, G.; Kläui, M. Switching by Domain-Wall Automotion in Asymmetric Ferromagnetic Rings. *Phys. Rev. Appl.* **2017**, *7* (4), 044009. https://doi.org/10.1103/PHYSREVAPPLIED.7.044009/FIGURES/7/MEDIUM.

(127) Schneider, M.; Hoffmann, H.; Zweck, J. Lorentz Microscopy of Circular Ferromagnetic Permalloy Nanodisks. *Appl. Phys. Lett.* **2000**, *77* (18), 2909–2911. https://doi.org/10.1063/1.1320465.

(128) Dimian, M.; Lefter, C. Analysis of Magnetization Switching via Vortex Formation in Soft Magnetic Nanoparticles. *Adv. Electr. Comput. Eng.* **2013**, *13* (1), 53–58. https://doi.org/10.4316/AECE.2013.01009.

(129) Coey, J. M. D. Magnetism and Magnetic Materials. *Magn. Magn. Mater.* **2010**, *9780521816144*, 1–617. https://doi.org/10.1017/CBO9780511845000.

(130) Karatutlu, A.; Sapelkin, A. Liquid-Phase Synthesis of Nanoparticles and Nanostructured Materials. *Emerg. Appl. Nanoparticles Archit. Nanostructures* **2018**, 1–28. https://doi.org/10.1016/B978-0-323-51254-1.00001-4.

(131) Alivisatos, A. P. Semiconductor Clusters, Nanocrystals, and Quantum Dots. *Science (80-.).* **1996**, *271* (5251), 933–937. https://doi.org/10.1126/science.271.5251.933.

(132) Charitidis, C. A.; Georgiou, P.; Koklioti, M. A.; Trompeta, A.-F.; Markakis, V. Manufacturing Nanomaterials: From Research to Industry. *Manuf. Rev.* **2014**, *1*, 11. https://doi.org/10.1051/mfreview/2014009.

(133) Gutsch, A.; Mühlenweg, H.; Krämer, M. Tailor-Made Nanoparticles via Gas-Phase Synthesis. *Small* **2004**, *1* (1), 30–46. https://doi.org/10.1002/smll.200400021.

(134) Feng, J.; Biskos, G.; Schmidt-Ott, A. Toward Industrial Scale Synthesis of Ultrapure Singlet Nanoparticles with Controllable Sizes in a Continuous Gas-Phase Process. *Sci. Rep.* **2015**, *5* (1), 15788. https://doi.org/10.1038/srep15788.

(135) Charitidis, C. A.; Georgiou, P.; Koklioti, M. A.; Trompeta, A.-F.; Markakis, V. Manufacturing Nanomaterials: From Research to Industry. *Manuf. Rev.* **2014**, *1*, 11. https://doi.org/10.1051/mfreview/2014009.

(136) Nadagouda, M. N.; Speth, T. F.; Varma, R. S. Microwave-Assisted Green Synthesis of Silver Nanostructures. *Acc. Chem. Res.* **2011**, *44* (7), 469–478. https://doi.org/10.1021/ar1001457.

(137) Kou, J.; Varma, R. S. Beet Juice-Induced Green Fabrication of Plasmonic AgCl/Ag Nanoparticles. *ChemSusChem* **2012**, *5* (12), 2435–2441. https://doi.org/10.1002/cssc.201200477.

(138) Virkutyte, J.; Varma, R. S. Green Synthesis of Metal Nanoparticles: Biodegradable Polymers and Enzymes in Stabilization and Surface Functionalization. *Chem. Sci.* **2011**, *2* (5), 837–846. https://doi.org/10.1039/C0SC00338G.

(139) Polshettiwar, V.; Nadagouda, M. N.; Varma, R. S. Microwave-Assisted Chemistry: A Rapid and Sustainable Route to Synthesis of Organics and Nanomaterials. *Aust. J. Chem.* **2009**, *62*, 16–26. https://doi.org/10.1071/CH08404.

(140) Galema, S. A. Microwave Chemistry. *Chem. Soc. Rev.* **1997**, *26* (3), 233. https://doi.org/10.1039/cs9972600233.

(141) Bilecka, I.; Niederberger, M. Microwave Chemistry for Inorganic Nanomaterials Synthesis. *Nanoscale* **2010**, *2* (8), 1358. https://doi.org/10.1039/b9nr00377k.

(142) Kappe, C. O. Controlled Microwave Heating in Modern Organic Synthesis. *Angew. Chemie Int. Ed.* **2004**, *43* (46), 6250–6284. https://doi.org/10.1002/anie.200400655.

(143) Baghbanzadeh, M.; Carbone, L.; Cozzoli, P. D.; Kappe, C. O. Microwave-Assisted Synthesis of Colloidal Inorganic Nanocrystals. *Angew. Chemie Int. Ed.* **2011**, *50* (48), 11312–11359. https://doi.org/10.1002/anie.201101274.

(144) Gawande, M. B.; Shelke, S. N.; Zboril, R.; Varma, R. S. Microwave-Assisted Chemistry: Synthetic Applications for Rapid Assembly of Nanomaterials and Organics. *Acc. Chem. Res* **2014**, *47* (4), 1338–1348. https://doi.org/10.1021/ar400309b.

(145) Mingos, D. M. P.; Baghurst, D. R. Tilden Lecture. Applications of Microwave Dielectric Heating Effects to Synthetic Problems in Chemistry. *Chem. Soc. Rev.* **1991**, *20* (1), 1. https://doi.org/10.1039/cs9912000001.

(146) Tsuji, M.; Hashimoto, M.; Nishizawa, Y.; Kubokawa, M.; Tsuji, T. Microwave-Assisted

Synthesis of Metallic Nanostructures in Solution. *Chem. - A Eur. J.* **2005**, *11* (2), 440–452. https://doi.org/10.1002/chem.200400417.

(147) Nüchter, M.; Ondruschka, B.; Bonrath, W.; Gum, A. Microwave Assisted Synthesis – a Critical Technology Overview. *Green Chem.* **2004**, *6* (3), 128–141. https://doi.org/10.1039/B310502D.

(148) Gabriel, C.; Gabriel, S.; H. Grant, E.; H. Grant, E.; S. J. Halstead, B.; Michael P. Mingos, D. Dielectric Parameters Relevant to Microwave Dielectric Heating. *Chem. Soc. Rev.* **1998**, *27* (3), 213. https://doi.org/10.1039/a827213z.

(149) Gedye, R. N.; Smith, F. E.; Westaway, K. C. The Rapid Synthesis of Organic Compounds in Microwave Ovens. *Can. J. Chem.* **1988**, *66* (1), 17–26. https://doi.org/10.1139/v88-003.

(150) de la Hoz, A.; Díaz-Ortiz, A.; Moreno, A. Microwaves in Organic Synthesis. Thermal and Non-Thermal Microwave Effects. *Chem. Soc. Rev.* **2005**, *34* (2), 164–178. https://doi.org/10.1039/b411438h.

(151) Perreux, L.; Loupy, A. Â. A Tentative Rationalization of Microwave Effects in Organic Synthesis According to the Reaction Medium, and Mechanistic Considerations. *Tetrahedron* **2001**, *57*, 9199–9223. https://doi.org/10.1016/s0040-4020(01)00905-x.

(152) Stass, D. V.; Woodward, J. R.; Timmel, C. R.; Hore, P. J.; McLauchlan, K. A. Radiofrequency Magnetic Field Effects on Chemical Reaction Yields. *Chem. Phys. Lett.* **2000**, *329* (1–2), 15–22. https://doi.org/10.1016/S0009-2614(00)00980-5.

(153) Dąbrowska, S.; Chudoba, T.; Wojnarowicz, J.; Łojkowski, W.; Dąbrowska, S.; Chudoba, T.; Wojnarowicz, J.; Łojkowski, W. Current Trends in the Development of Microwave Reactors for the Synthesis of Nanomaterials in Laboratories and Industries: A Review. *Crystals* **2018**, *8* (10), 379. https://doi.org/10.3390/cryst8100379.

(154) Nishioka, M.; Miyakawa, M.; Daino, Y.; Kataoka, H.; Koda, H.; Sato, K.; Suzuki, T. M. Single-Mode Microwave Reactor Used for Continuous Flow Reactions under Elevated Pressure. *Ind. Eng. Chem. Res.* **2013**, *52* (12), 4683–4687. https://doi.org/10.1021/ie400199r.

(155) Öhrngren, P.; Fardost, A.; Russo, F.; Schanche, J.-S.; Fagrell, M.; Larhed, M. Evaluation of a Nonresonant Microwave Applicator for Continuous-Flow Chemistry Applications. *Org. Process Res. Dev.* **2012**, *16* (5), 1053–1063. https://doi.org/10.1021/op300003b.

(156) Morschhäuser, R.; Krull, M.; Kayser, C.; Boberski, C.; Bierbaum, R.; Püschner, P. A.;

Glasnov, T. N.; Kappe, C. O. Microwave-Assisted Continuous Flow Synthesis on Industrial Scale. *Green Process. Synth.* **2012**, *1* (3). https://doi.org/10.1515/gps-2012-0032.

(157) Park, H. J.; McConnell, J. T.; Boddohi, S.; Kipper, M. J.; Johnson, P. A. Synthesis and Characterization of Enzyme-Magnetic Nanoparticle Complexes: Effect of Size on Activity and Recovery. *Colloids Surf. B. Biointerfaces* **2011**, *83* (2), 198–203. https://doi.org/10.1016/j.colsurfb.2010.11.006.

(158) Cahn, R. W. (Robert W. . Concise Encyclopedia of Materials Characterization. **2005**, 1096.

(159) TOPAS V4 General profile and structural analysis software for powder diffraction data - Google Search https://www.google.com/search?q=TOPAS+V4+General+profile+and+structural+analysis+software+for+powder+diffraction+data&sxsrf=AOaemvIB4Ttr4iT2z4ezCvcQ1FCitEoJeQ%3A1641301278161&ei=HkXUYYKLCdCG9u8PyoWT4As&ved=0ahUKEwiCkp3dk5j1AhVQg_0HHcrCBLwQ4dUDCA4&uact=5&oq=TOPAS+V4+General+profile+and+structural+analysis+software+for+powder+diffraction+data&gs_lcp=Cgdnd3Mtd2l6EAM6BwgjELADECc6BwgAEEcQsAM6BwgjELACECdKBAhBGABKBAhGGABQ5ApYvSpgrC1oAXACeACAAaoDiAHNC5IBCTIuNS4xLjAuMZgBAKABAcgBCcABAQ&sclient=gws-wiz (accessed Jan 4, 2022).

(160) Toby, B. H.; Von Dreele, R. B. GSAS-II: The Genesis of a Modern Open-Source All Purpose Crystallography Software Package. *J. Appl. Crystallogr.* **2013**, *46* (2), 544–549. https://doi.org/10.1107/S0021889813003531.

(161) Williams, D. B.; Carter, C. B. Transmission Electron Microscopy. **1996**. https://doi.org/10.1007/978-1-4757-2519-3.

(162) Carter, C. B.; Williams, D. B. Transmission Electron Microscopy: Diffraction, Imaging, and Spectrometry. *Transm. Electron Microsc. Diffraction, Imaging, Spectrom.* **2016**, 1–518. https://doi.org/10.1007/978-3-319-26651-0.

(163) Spence, J. C. H. Experimental High-Resolution Electron Microscopy. **1988**, 427.

(164) Murr, L. E. Electron and Ion Microscopy and Microanalysis : Principles and Applications. **1991**, 837.

(165) Brück, E. *Handbook of Magnetic Materials*, 1st ed.; 2018; Vol. 27.

(166) Lichte, H.; Lehmann, M. Electron Holography—Basics and Applications. *Reports Prog. Phys.* **2007**, *71* (1), 016102. https://doi.org/10.1088/0034-4885/71/1/016102.

(167) Christian Reichardt. Solvents and Solvent Effects in Organic Chemistry, 3rd, Updated and Enlarged Edition. **2006**.

(168) Castle, J. E. Practical Surface Analysis by Auger and X-Ray Photoelectron Spectroscopy. D. Briggs and M. P. Seah (Editors). John Wiley and Sons Ltd, Chichester, 1983, 533 Pp., £44.50. *Surf. Interface Anal.* **1984**, *6* (6), 302–302. https://doi.org/10.1002/SIA.740060611.

(169) Briggs, D. Handbook of X-Ray Photoelectron Spectroscopy C. D. Wanger, W. M. Riggs, L. E. Davis, J. F. Moulder and G. E.Muilenberg Perkin-Elmer Corp., Physical Electronics Division, Eden Prairie, Minnesota, USA, 1979. 190 Pp. $195. *Surf. Interface Anal.* **1981**, *3* (4), v–v. https://doi.org/10.1002/SIA.740030412.

(170) Golʹdanskiĭ, V. I. (Vitaliĭ I.; Herber, R. H. Chemical Applications of Mössbauer Spectroscopy,. **1968**, 701.

(171) Mössbauer, R. L. The Discovery of the Mössbauer Effect. *Hyperfine Interact. 2000 1261* **2000**, *126* (1), 1–12. https://doi.org/10.1023/A:1012620106837.

(172) Mössbauer Spectroscopy. **1975**, *5*. https://doi.org/10.1007/3-540-07120-2.

(173) Brand, R. A. Normos Mössbauer fit Program; Laboratorium für Angewandte Physick: Duisburg, Germany, 1990. - Google Search https://www.google.com/search?q=Normos+Mössbauer+fit+Program%3B+Laboratorium+für+Angewandte+Physick%3A+Duisburg%2C+Germany%2C+1990.&oq=Normos+Mössbauer+fit+Program%3B+Laboratorium+für+Angewandte+Physick%3A+Duisburg%2C+Germany%2C+1990.&aqs=chrome..69i57.880j0j7&sourceid=chrome&ie=UTF-8 (accessed Feb 1, 2022).

(174) MossWinn - Mossbauer spectrum analysis and database software http://www.mosswinn.com/ (accessed Feb 1, 2022).

(175) Tesche, C. D. Analysis of a Double-Loop Dc SQUID. *J. Low Temp. Phys.* **1982**, *47* (5–6), 385–410. https://doi.org/10.1007/BF00683981.

(176) van der PAUW, L. J. A METHOD OF MEASURING SPECIFIC RESISTIVITY AND HALL EFFECT OF DISCS OF ARBITRARY SHAPE. *Semicond. Devices Pioneer. Pap.* **1991**, 174–182. https://doi.org/10.1142/9789814503464_0017.

(177) Hergt, R.; Andrae, W.; d'Ambly, C. G.; Hilger, I.; Kaiser, W. A.; Richter, U.; Schmidt, H. G. Physical Limits of Hyperthermia Using Magnetite Fine Particles. *IEEE Trans. Magn.* **1998**, *34* (5 pt 2), 3745–3754. https://doi.org/10.1109/20.718537.

(178) Ma, M.; Wu, Y.; Zhou, J.; Sun, Y.; Zhang, Y.; Gu, N. Size Dependence of Specific Power Absorption of Fe3O4 Particles in AC Magnetic Field. *J. Magn. Magn. Mater.* **2004**, *268* (1–2), 33–39. https://doi.org/10.1016/S0304-8853(03)00426-8.

(179) Kallumadil, M.; Tada, M.; Nakagawa, T.; Abe, M.; Southern, P.; Pankhurst, Q. A. Suitability of Commercial Colloids for Magnetic Hyperthermia. *J. Magn. Magn. Mater.* **2009**, *321* (10), 1509–1513. https://doi.org/10.1016/J.JMMM.2009.02.075.

(180) Babes, L.; Denizot, B.; Tanguy, G.; Le Jeune, J. J.; Jallet, P. Synthesis of Iron Oxide Nanoparticles Used as MRI Contrast Agents: A Parametric Study. *J. Colloid Interface Sci.* **1999**, *212* (2), 474–482. https://doi.org/10.1006/jcis.1998.6053.

(181) Shokouhimehr, M.; Piao, Y.; Kim, J.; Jang, Y.; Hyeon, T. A Magnetically Recyclable Nanocomposite Catalyst for Olefin Epoxidation. *Angew. Chemie - Int. Ed.* **2007**, *46* (37), 7039–7043. https://doi.org/10.1002/anie.200702386.

(182) Hertel, R. Magnetic Nanostructures: Vortex States à La Carte. *Nat. Nanotechnol.* **2013**, *8* (5), 318–320. https://doi.org/10.1038/nnano.2013.81.

(183) Jung, H.; Choi, Y.-S.; Lee, K.-S.; Han, D.-S.; Yu, Y.-S.; Im, M.-Y.; Fischer, P.; Kim, S.-K. Logic Operations Based on Magnetic-Vortex-State Networks. *ACS Nano* **2012**, *6* (5), 3712–3717. https://doi.org/10.1021/nn3000143.

(184) Kumar, D.; Barman, S.; Barman, A. Magnetic Vortex Based Transistor Operations. *Sci. Rep.* **2014**, *4* (1), 1–8. https://doi.org/10.1038/srep04108.

(185) Mi, C.; Zhang, J.; Gao, H.; Wu, X.; Wang, M.; Wu, Y.; Di, Y.; Xu, Z.; Mao, C.; Xu, S. Multifunctional Nanocomposites of Superparamagnetic (Fe3O4) and NIR-Responsive Rare Earth-Doped up-Conversion Fluorescent (NaYF4 : Yb,Er) Nanoparticles and Their Applications in Biolabeling and Fluorescent Imaging of Cancer Cells. *Nanoscale* **2010**, *2* (7), 1141. https://doi.org/10.1039/c0nr00102c.

(186) Muthukumaran, T.; Philip, J. Effect of Phosphate and Oleic Acid Capping on Structure, Magnetic Properties and Thermal Stability of Iron Oxide Nanoparticles. *J. Alloys Compd.* **2016**, *689*, 959–968. https://doi.org/10.1016/j.jallcom.2016.08.067.

(187) Muthukumaran, T.; Pati, S. S.; Singh, L. H.; de Oliveira, A. C.; Garg, V. K.; Philip, J. Comparison of Magnetic Properties and High-Temperature Phase Stability of Phosphate- and Oleic Acid-Capped Iron Oxide Nanoparticles. *Appl. Nanosci.* **2018**, *8* (4), 593–608. https://doi.org/10.1007/s13204-018-0715-y.

(188) Hu, X.; Yu, J. C.; Gong, J.; Li, Q.; Li, G. α-Fe2O3 Nanorings Prepared by a Microwave-Assisted Hydrothermal Process and Their Sensing Properties. *Adv. Mater.* **2007**, *19* (17), 2324–2329. https://doi.org/10.1002/adma.200602176.

(189) Jia, C.-J.; Sun, L.-D.; Luo, F.; Han, X.-D.; Heyderman, L. J.; Yan, Z.-G.; Yan, C.-H.; Zheng, K.; Zhang, Z.; Takano, M.; Hayashi, N.; Eltschka, M.; Kläui, M.; Rüdiger, U.; Kasama, T.; Cervera-Gontard, L.; Dunin-Borkowski, R. E.; Tzvetkov, G.; Raabe, J. Large-Scale Synthesis of Single-Crystalline Iron Oxide Magnetic Nanorings. *J. Am. Chem. Soc.* **2008**, *130* (50), 16968–16977. https://doi.org/10.1021/ja805152t.

(190) Kim, S. H.; Lee, S. Y.; Yi, G. R.; Pine, D. J.; Yang, S. M. Microwave-Assisted Self-Organization of Colloidal Particles in Confining Aqueous Droplets. *J. Am. Chem. Soc.* **2006**, *128* (33), 10897–10904. https://doi.org/10.1021/ja063528y.

(191) Jia, C.-J.; Sun, L.-D.; Yan, Z.-G.; You, L.-P.; Luo, F.; Han, X.-D.; Pang, Y.-C.; Zhang, Z.; Yan, C.-H. Single-Crystalline Iron Oxide Nanotubes. *Angew. Chemie Int. Ed.* **2005**, *44* (28), 4328–4333. https://doi.org/10.1002/anie.200463038.

(192) Zhang, R.; Khalizov, A.; Wang, L.; Hu, M.; Xu, W. Nucleation and Growth of Nanoparticles in the Atmosphere. *Chem. Rev.* **2012**, *112* (3), 1957–2011. https://doi.org/10.1021/cr2001756.

(193) Thanh, N. T. K.; Maclean, N.; Mahiddine, S. Mechanisms of Nucleation and Growth of Nanoparticles in Solution. *Chem. Rev.* **2014**, *114* (15), 7610–7630. https://doi.org/10.1021/cr400544s.

(194) Huang, X. Intersection of Isotherms for Phosphate Adsorption on Hematite. *J. Colloid Interface Sci.* **2004**, *271* (2), 296–307. https://doi.org/10.1016/J.JCIS.2003.12.007.

(195) Sharifi Dehsari, H.; Halda Ribeiro, A.; Ersöz, B.; Tremel, W.; Jakob, G.; Asadi, K. Effect of Precursor Concentration on Size Evolution of Iron Oxide Nanoparticles. *CrystEngComm* **2017**, *19* (44), 6694–6702. https://doi.org/10.1039/c7ce01406f.

(196) Huang, J.-H.; Parab, H. J.; Liu, R.-S.; Lai, T.-C.; Hsiao, M.; Chen, C.-H.; Sheu, H.-S.; Chen, J.-M.; Tsai, D.-P.; Hwu, Y.-K. Investigation of the Growth Mechanism of Iron Oxide Nanoparticles via a Seed-Mediated Method and Its Cytotoxicity Studies. *J. Phys. Chem. C* **2008**, *112* (40), 15684–15690. https://doi.org/10.1021/jp803452j.

(197) Zieliński, J.; Zglinicka, I.; Znak, L.; Kaszkur, Z. Reduction of Fe2O3 with Hydrogen. *Appl. Catal. A Gen.* **2010**, *381* (1–2), 191–196. https://doi.org/10.1016/j.apcata.2010.04.003.

(198) Lv, B.; Xu, Y.; Wu, D.; Sun, Y. Preparation and Properties of Magnetic Iron Oxide Nanotubes. *Particuology* **2008**, *6* (5), 334–339. https://doi.org/10.1016/j.partic.2008.04.006.

(199) Singh, D.; Gautam, R. K.; Kumar, R.; Shukla, B. K.; Shankar, V.; Krishna, V. Citric Acid Coated Magnetic Nanoparticles: Synthesis, Characterization and Application in Removal of Cd(II) Ions from Aqueous Solution. *Journal of Water Process Engineering*. Elsevier Ltd 2014, pp 233–241. https://doi.org/10.1016/j.jwpe.2014.10.005.

(200) Elzinga, E. J.; Sparks, D. L. Phosphate Adsorption onto Hematite: An in Situ ATR-FTIR Investigation of the Effects of PH and Loading Level on the Mode of Phosphate Surface Complexation. *J. Colloid Interface Sci.* **2007**, *308* (1), 53–70. https://doi.org/10.1016/j.jcis.2006.12.061.

(201) Tejedor-Tejedor, M. I.; Anderson, M. A. Protonation of Phosphate on the Surface of Goethite As Studied by CIR-FTIR and Electrophoretic Mobility. *Langmuir* **1990**, *6* (3), 602–611. https://doi.org/10.1021/la00093a015.

(202) CULLITY, B. D. . C. D. G. *Introduction to Magnetic Materials -Cap 6 FERRIMAGNETISM*; IEEE press Wiely, 2009.

(203) Lyubutin, I. S.; Lin, C. R.; Korzhetskiy, Y. V.; Dmitrieva, T. V.; Chiang, R. K. Mössbauer Spectroscopy and Magnetic Properties of Hematite/Magnetite Nanocomposites. *J. Appl. Phys.* **2009**, *106* (3). https://doi.org/10.1063/1.3194316.

(204) Valstyn, E. P.; Hanton, J. P.; Morrish, A. H. Ferromagnetic Resonance of Single-Domain Particles. *Phys. Rev.* **1962**, *128* (5), 2078–2087. https://doi.org/10.1103/PhysRev.128.2078.

(205) Salazar-Alvarez, G.; Qin, J.; Šepelák, V.; Bergmann, I.; Vasilakaki, M.; Trohidou, K. N.; Ardisson, J. D.; Macedo, W. A. A.; Mikhaylova, M.; Muhammed, M.; Baró, M. D.; Nogués, J. Cubic versus Spherical Magnetic Nanoparticles: The Role of Surface Anisotropy. *J. Am. Chem. Soc.* **2008**, *130* (40), 13234–13239. https://doi.org/10.1021/ja0768744.

(206) Brown, W. F. Theory of the Approach to Magnetic Saturation. *Phys. Rev.* **1940**, *58* (8), 736–743. https://doi.org/10.1103/PhysRev.58.736.

(207) Dunlop, D. J. Theory and Application of the Day Plot (M_{Rs} / M_s versus H_{Cr} / H_c) 1. Theoretical Curves and Tests Using Titanomagnetite Data. *J. Geophys. Res.* **2002**, *107* (B3), 2056. https://doi.org/10.1029/2001JB000486.

(208) Dias, C. S. B.; Hanchuk, T. D. M.; Wender, H.; Shigeyosi, W. T.; Kobarg, J.; Rossi, A. L.;

Tanaka, M. N.; Cardoso, M. B.; Garcia, F. Shape Tailored Magnetic Nanorings for Intracellular Hyperthermia Cancer Therapy. *Sci. Rep.* **2017**, *7* (1), 14843. https://doi.org/10.1038/s41598-017-14633-0.

(209) VERWEY, E. J. W. Electronic Conduction of Magnetite (Fe3O4) and Its Transition Point at Low Temperatures. *Nature* **1939**, *144* (3642), 327–328. https://doi.org/10.1038/144327b0.

(210) Santoyo Salazar, J.; Perez, L.; De Abril, O.; Truong Phuoc, L.; Ihiawakrim, D.; Vazquez, M.; Greneche, J. M.; Begin-Colin, S.; Pourroy, G. Magnetic Iron Oxide Nanoparticles in 10-40 Nm Range: Composition in Terms of Magnetite/Maghemite Ratio and Effect on the Magnetic Properties. *Chem. Mater.* **2011**, *23* (6), 1379–1386. https://doi.org/10.1021/cm103188a.

(211) Schrettle, F.; Krohns, S.; Lunkenheimer, P.; Brabers, V. A. M.; Loidl, A. Relaxor Ferroelectricity and the Freezing of Short-Range Polar Order in Magnetite. *Phys. Rev. B - Condens. Matter Mater. Phys.* **2011**, *83* (19). https://doi.org/10.1103/PhysRevB.83.195109.

(212) Shepherd, J. P.; Koenitzer, J. W.; Aragn, R.; Spalek, J.; Honig, J. M. Heat Capacity and Entropy of Nonstoichiometric Magnetite Fe3(1-)O4: The Thermodynamic Nature of the Verwey Transition. *Phys. Rev. B* **1991**, *43* (10), 8461–8471. https://doi.org/10.1103/PhysRevB.43.8461.

(213) Goya, G. F.; Berquó, T. S.; Fonseca, F. C.; Morales, M. P. Static and Dynamic Magnetic Properties of Spherical Magnetite Nanoparticles. *J. Appl. Phys.* **2003**, *94* (5), 3520–3528. https://doi.org/10.1063/1.1599959.

(214) Daniels, J. M.; Rosencwaig, A. Mössbauer Spectroscopy of Stoichiometric and Non-Stoichiometric Magnetite. *J. Phys. Chem. Solids* **1969**, *30* (6), 1561–1571. https://doi.org/10.1016/0022-3697(69)90217-0.

(215) Guigue-Millot, N.; Keller, N.; Perriat, P. Evidence for the Verwey Transition in Highly Nonstoichiometric Nanometric Fe-Based Ferrites. *Phys. Rev. B - Condens. Matter Mater. Phys.* **2001**, *64* (1), 124021–124024. https://doi.org/10.1103/PhysRevB.64.012402.

(216) Choe, S. B.; Acremann, Y.; Scholl, A.; Bauer, A.; Doran, A.; Stöhr, J.; Padmore, H. A. Vortex Core-Driven Magnetization Dynamics. *Science (80-.).* **2004**, *304* (5669), 420–422. https://doi.org/10.1126/SCIENCE.1095068.

(217) Van Waeyenberge, B.; Puzic, A.; Stoll, H.; Chou, K. W.; Tyliszczak, T.; Hertel, R.; Fähnle,

M.; Brückl, H.; Rott, K.; Reiss, G.; Neudecker, I.; Weiss, D.; Back, C. H.; Schütz, G. Magnetic Vortex Core Reversal by Excitation with Short Bursts of an Alternating Field. *Nat. 2006 4447118* **2006**, *444* (7118), 461–464. https://doi.org/10.1038/nature05240.

(218) Hertel, R.; Gliga, S.; Fähnle, M.; Schneider, C. M. Ultrafast Nanomagnetic Toggle Switching of Vortex Cores. *Phys. Rev. Lett.* **2007**, *98* (11), 117201. https://doi.org/10.1103/PhysRevLett.98.117201.

(219) Pigeau, B.; Loubens, G. de; Klein, O.; Riegler, A.; Lochner, F.; Schmidt, G.; Molenkamp, L. W.; Tiberkevich, V. S.; Slavin, A. N. A Frequency-Controlled Magnetic Vortex Memory. *Appl. Phys. Lett.* **2010**, *96* (13), 132506. https://doi.org/10.1063/1.3373833.

(220) Niraula, G.; Coaquira, J. A. H.; Aragon, F. H.; Bakuzis, A. F.; Villar, B. M. G.; Garcia, F.; Muraca, D.; Zoppellaro, G.; Ayesh, A. I.; Sharma, S. K. Stoichiometry and Orientation- and Shape-Mediated Switching Field Enhancement of the Heating Properties of Fe 3 O 4 Circular Nanodiscs . *Phys. Rev. Appl.* **2021**, *15* (1), 014056. https://doi.org/10.1103/physrevapplied.15.014056.

(221) Liu, X.; Yan, B.; Li, Y.; Ma, X.; Jiao, W.; Shi, K.; Zhang, T.; Chen, S.; He, Y.; Liang, X. J.; Fan, H. Graphene Oxide-Grafted Magnetic Nanorings Mediated Magnetothermodynamic Therapy Favoring Reactive Oxygen Species-Related Immune Response for Enhanced Antitumor Efficacy. *ACS Nano* **2020**, *14* (2), 1936–1950. https://doi.org/10.1021/acsnano.9b08320.

(222) Niraula, G.; Toneto, D.; Joshy, E.; Coaquira, J. A. H.; Ayesh, A. I.; Garcia, F.; Muraca, D.; Denardin, J. C.; Goya, G. F.; Sharma, S. K. Energy Evolution, Stabilization, and Mechanotransducer Properties of Fe3O4 Vortex Nanorings and Nanodisks. *Phys. Rev. Appl.* **2021**, *16* (2), 024002. https://doi.org/10.1103/PhysRevApplied.16.024002.

(223) Gregurec, D.; Senko, A. W.; Chuvilin, A.; Reddy, P. D.; Sankararaman, A.; Rosenfeld, D.; Chiang, P. H.; Garcia, F.; Tafel, I.; Varnavides, G.; Ciocan, E.; Anikeeva, P. Magnetic Vortex Nanodiscs Enable Remote Magnetomechanical Neural Stimulation. *ACS Nano* **2020**, *14* (7), 8036–8045. https://doi.org/10.1021/acsnano.0c00562.

(224) Wolf, M. S.; Badea, R.; Berezovsky, J. Fast Nanoscale Addressability of Nitrogen-Vacancy Spins via Coupling to a Dynamic Ferromagnetic Vortex. *Nat. Commun. 2016 71* **2016**, *7* (1), 1–7. https://doi.org/10.1038/ncomms11584.

(225) Pinilla-Cienfuegos, E.; Mañas-Valero, S.; Forment-Aliaga, A.; Coronado, E. Switching the

Magnetic Vortex Core in a Single Nanoparticle. *ACS Nano* **2016**, *10* (2), 1764–1770. https://doi.org/10.1021/acsnano.5b06776.

(226) Lacroix, L.-M.; Lachaize, S.; Hue, F.; Gatel, C.; Blon, T.; Tan, R. P.; Carrey, J.; Warot-Fonrose, B.; Chaudret, B. Stabilizing Vortices in Interacting Nano-Objects: A Chemical Approach. *Nano Lett.* **2012**, *12* (6), 3245–3250. https://doi.org/10.1021/NL3012616.

(227) Goiriena-Goikoetxea, M.; Guslienko, K. Y.; Rouco, M.; Orue, I.; Berganza, E.; Jaafar, M.; Asenjo, A.; Fernández-Gubieda, M. L.; Barquín, L. F.; García-Arribas, A. Magnetization Reversal in Circular Vortex Dots of Small Radius. *Nanoscale* **2017**, *9* (31), 11269–11278. https://doi.org/10.1039/C7NR02389H.

(228) Kim, S.-K.; Yoo, M.-W.; Lee, J.; Lee, H.-Y.; Lee, J.-H.; Gaididei, Y.; Kravchuk, V. P.; Sheka, D. D. Resonantly Excited Precession Motion of Three-Dimensional Vortex Core in Magnetic Nanospheres. *Sci. Reports 2015 51* **2015**, *5* (1), 1–9. https://doi.org/10.1038/srep11370.

(229) Kim, S.-K.; Yoo, M.-W.; Lee, J.; Lee, J.-H.; Kim, M.-K. Resonant Vortex-Core Reversal in Magnetic Nano-Spheres as Robust Mechanism of Efficient Energy Absorption and Emission. *Sci. Reports 2016 61* **2016**, *6* (1), 1–8. https://doi.org/10.1038/srep31513.

(230) Senn, M. S.; Wright, J. P.; Attfield, J. P. Charge Order and Three-Site Distortions in the Verwey Structure of Magnetite. *Nat. 2011 4817380* **2011**, *481* (7380), 173–176. https://doi.org/10.1038/nature10704.

(231) Zhang, F.; Chan, S.-W.; Spanier, J. E.; Apak, E.; Jin, Q.; Robinson, R. D.; Herman, I. P. Cerium Oxide Nanoparticles: Size-Selective Formation and Structure Analysis. *Appl. Phys. Lett.* **2002**, *80* (1), 127. https://doi.org/10.1063/1.1430502.

(232) Kim, T.; Lim, S.; Hong, J.; Kwon, S. G.; Okamoto, J.; Chen, Z. Y.; Jeong, J.; Kang, S.; Leiner, J. C.; Lim, J. T.; Kim, C. S.; Huang, D. J.; Hyeon, T.; Lee, S.; Park, J. G. Giant Thermal Hysteresis in Verwey Transition of Single Domain Fe3O4 Nanoparticles. *Sci. Rep.* **2018**, *8* (1). https://doi.org/10.1038/s41598-018-23456-6.

(233) Mitra, A.; Mohapatra, J.; Meena, S. S.; Tomy, C. V.; Aslam, M. Verwey Transition in Ultrasmall-Sized Octahedral Fe3O4 Nanoparticles. *J. Phys. Chem. C* **2014**, *118* (33), 19356–19362. https://doi.org/10.1021/JP501652E.

(234) Goya, G. F.; Berquó, T. S.; Fonseca, F. C.; Morales, M. P. Static and Dynamic Magnetic Properties of Spherical Magnetite Nanoparticles. **2003**. https://doi.org/10.1063/1.1599959.

(235) Piekarz, P.; Parlinski, K.; Oleś, A. M. Mechanism of the Verwey Transition in Magnetite. *Phys. Rev. Lett.* **2006**, *97* (15), 156402. https://doi.org/10.1103/PhysRevLett.97.156402.

(236) Bickford, L. R. The Low Temperature Transformation in Ferrites. *Rev. Mod. Phys.* **1953**, *25* (1), 75. https://doi.org/10.1103/RevModPhys.25.75.

(237) Niraula, G.; Coaquira, J. A. H.; Zoppellaro, G.; Villar, B. M. G.; Garcia, F.; Bakuzis, A. F.; Longo, J. P. F.; Rodrigues, M. C.; Muraca, D.; Ayesh, A. I.; Sinfrônio, F. S. M.; Menezes, A. S. de; Goya, G. F.; Sharma, S. K. Engineering Shape Anisotropy of Fe3O4-γ-Fe2O3 Hollow Nanoparticles for Magnetic Hyperthermia. *ACS Appl. Nano Mater.* **2021**, *4* (3), 3148–3158. https://doi.org/10.1021/ACSANM.1C00311.

(238) Muxworthy, A. R.; Williams, W. Critical Single-Domain/Multidomain Grain Sizes in Noninteracting and Interacting Elongated Magnetite Particles: Implications for Magnetosomes. *J. Geophys. Res. Solid Earth* **2006**, *111* (B12), 12–12. https://doi.org/10.1029/2006JB004588.

(239) Jubert, P. O.; Allenspach, R. Analytical Approach to the Single-Domain-to-Vortex Transition in Small Magnetic Disks. *Phys. Rev. B - Condens. Matter Mater. Phys.* **2004**, *70* (14), 144402. https://doi.org/10.1103/PhysRevB.70.144402.

(240) Guslienko, K. Y.; Metlov, K. L. Evolution and Stability of a Magnetic Vortex in a Small Cylindrical Ferromagnetic Particle under Applied Field. *Phys. Rev. B - Condens. Matter Mater. Phys.* **2001**, *63* (10), 4. https://doi.org/10.1103/PhysRevB.63.100403.

(241) Guslienko, K. Y.; Scholz, W.; Chantrell, R. W.; Novosad, V. Vortex-State Oscillations in Soft Magnetic Cylindrical Dots. *Phys. Rev. B - Condens. Matter Mater. Phys.* **2005**, *71* (14), 144407. https://doi.org/10.1103/PhysRevB.71.144407.

(242) Zhu, X.; Grütter, P.; Metlushko, V.; Ilic, B. Magnetic Force Microscopy Study of Electron-Beam-Patterned Soft Permalloy Particles: Technique and Magnetization Behavior. *Phys. Rev. B* **2002**, *66* (2), 024423. https://doi.org/10.1103/PhysRevB.66.024423.

(243) Zhu, X.; Grütter, P.; Metlushko, V.; Hao, Y.; Castaño, F. J.; Ross, C. A.; Ilic, B.; Smith, H. I. Construction of Hysteresis Loops of Single Domain Elements and Coupled Permalloy Ring Arrays by Magnetic Force Microscopy. *J. Appl. Phys.* **2003**, *93* (10), 8540. https://doi.org/10.1063/1.1540129.

(244) Bonevich, J. E.; Harada, K.; Matsuda, T.; Kasai, H.; Yoshida, T.; Pozzi, G.; Tonomura, A. Electron Holography Observation of Vortex Lattices in a Superconductor. *Phys. Rev. Lett.*

1993, *70* (19), 2952. https://doi.org/10.1103/PhysRevLett.70.2952.

(245) Hasegawa, S.; Matsuda, T.; Endo, J.; Osakabe, N.; Igarashi, M.; Kobayashi, T.; Naito, M.; Tonomura, A.; Aoki, R. Magnetic-Flux Quanta in Superconducting Thin Films Observed by Electron Holography and Digital Phase Analysis. *Phys. Rev. B. Condens. Matter* **1991**, *43* (10), 7631–7650. https://doi.org/10.1103/PHYSREVB.43.7631.

(246) Midgley, P. A.; Dunin-Borkowski, R. E. Electron Tomography and Holography in Materials Science. *Nat. Mater. 2009 84* **2009**, *8* (4), 271–280. https://doi.org/10.1038/nmat2406.

(247) Gatel, C.; Bonilla, F. J.; Meffre, A.; Snoeck, E.; Warot-Fonrose, B.; Chaudret, B.; Lacroix, L. M.; Blon, T. Size-Specific Spin Configurations in Single Iron Nanomagnet: From Flower to Exotic Vortices. *Nano Lett.* **2015**, *15* (10), 6952–6957. https://doi.org/10.1021/ACS.NANOLETT.5B02892/SUPPL_FILE/NL5B02892_SI_001.PDF.

(248) Dunin-Borkowski, R. E.; Kasama, T.; Wei, A.; Tripp, S. L.; Hytch, M. J.; Snoeck, E.; Harrison, R. J.; Putnis, A. Off-Axis Electron Holography of Magnetic Nanowires and Chains, Rings, and Planar Arrays of Magnetic Nanoparticles. *Microsc. Res. Tech.* **2004**, *64* (5–6), 390–402. https://doi.org/10.1002/JEMT.20098.

(249) Tanigaki, T.; Takahashi, Y.; Shimakura, T.; Akashi, T.; Tsuneta, R.; Sugawara, A.; Shindo, D. Three-Dimensional Observation of Magnetic Vortex Cores in Stacked Ferromagnetic Discs. *Nano Lett.* **2015**, *15* (2), 1309–1314. https://doi.org/10.1021/NL504473A.

(250) Kazakova, O.; Hanson, M.; Blixt, A. M.; Hjörvarsson, B. Domain Structure of Circular and Ring Magnets. In *Journal of Magnetism and Magnetic Materials*; 2003; Vol. 258–259, pp 348–351. https://doi.org/10.1016/S0304-8853(02)01057-0.

(251) Subramani, A.; Geerpuram, D.; Domanowski, A.; Baskaran, V.; Metlushko, V. Vortex State in Magnetic Rings. *Phys. C Supercond.* **2004**, *404* (1–4), 241–245. https://doi.org/10.1016/J.PHYSC.2003.11.044.

(252) Muscas, G.; Concas, G.; Cannas, C.; Musinu, A.; Ardu, A.; Orrù, F.; Fiorani, D.; Laureti, S.; Rinaldi, D.; Piccaluga, G.; Peddis, D. Magnetic Properties of Small Magnetite Nanocrystals. *J. Phys. Chem. C* **2013**, *117* (44), 23378–23384. https://doi.org/10.1021/jp407863s.

(253) Qiu, H.; Pan, L.; Li, L.; Zhu, H.; Zhao, X.; Xu, M.; Qin, L.; Xiao, J. Q. Microstructure and

Magnetic Properties of Magnetite Thin Films Prepared by Reactive Sputtering. *J. Appl. Phys.* **2007**, *102* (11), 113913. https://doi.org/10.1063/1.2817644.

(254) Chang, M.-T.; Chou, L.-J.; Hsieh, C.-H.; Chueh, Y.-L.; Wang, Z. L.; Murakami, Y.; Shindo, D. Magnetic and Electrical Characterizations of Half-Metallic Fe3O4 Nanowires. *Adv. Mater.* **2007**, *19* (17), 2290–2294. https://doi.org/10.1002/adma.200602330.

(255) Redl, F. X.; Black, C. T.; Papaefthymiou, G. C.; Sandstrom, R. L.; Yin, M.; Zeng, H.; Murray, C. B.; O'Brien, S. P. Magnetic, Electronic, and Structural Characterization of Nonstoichiometric Iron Oxides at the Nanoscale. *J. Am. Chem. Soc.* **2004**, *126* (44), 14583–14599. https://doi.org/10.1021/ja046808r.

(256) Reddy, L. H.; Arias, J. L.; Nicolas, J.; Couvreur, P. Magnetic Nanoparticles: Design and Characterization, Toxicity and Biocompatibility, Pharmaceutical and Biomedical Applications. *Chemical Reviews*. November 14, 2012, pp 5818–5878. https://doi.org/10.1021/cr300068p.

(257) Dutz, S.; Hergt, R. Magnetic Particle Hyperthermia - A Promising Tumour Therapy? *Nanotechnology*. Institute of Physics Publishing November 14, 2014, p 452001. https://doi.org/10.1088/0957-4484/25/45/452001.

(258) Périgo, E. A.; Hemery, G.; Sandre, O.; Ortega, D.; Garaio, E.; Plazaola, F.; Teran, F. J. Fundamentals and Advances in Magnetic Hyperthermia. *Applied Physics Reviews*. American Institute of Physics Inc. December 1, 2015, p 041302. https://doi.org/10.1063/1.4935688.

(259) Habib, A. H.; Ondeck, C. L.; Chaudhary, P.; Bockstaller, M. R.; McHenry, M. E. Evaluation of Iron-Cobalt/Ferrite Core-Shell Nanoparticles for Cancer Thermotherapy. *J. Appl. Phys.* **2008**, *103* (7), 07A307. https://doi.org/10.1063/1.2830975.

(260) Simeonidis, K.; Martinez-Boubeta, C.; Balcells, L.; Monty, C.; Stavropoulos, G.; Mitrakas, M.; Matsakidou, A.; Vourlias, G.; Angelakeris, M. Fe-Based Nanoparticles as Tunable Magnetic Particle Hyperthermia Agents. *J. Appl. Phys.* **2013**, *114* (10), 103904. https://doi.org/10.1063/1.4821020.

(261) Khurshid, H.; Alonso, J.; Nemati, Z.; Phan, M. H.; Mukherjee, P.; Fdez-Gubieda, M. L.; Barandiarán, J. M.; Srikanth, H. Anisotropy Effects in Magnetic Hyperthermia: A Comparison between Spherical and Cubic Exchange-Coupled FeO/Fe3O4 Nanoparticles. *J. Appl. Phys.* **2015**, *117* (17), 17A337. https://doi.org/10.1063/1.4919250.

(262) Lee, J. H.; Jang, J. T.; Choi, J. S.; Moon, S. H.; Noh, S. H.; Kim, J. W.; Kim, J. G.; Kim, I. S.; Park, K. I.; Cheon, J. Exchange-Coupled Magnetic Nanoparticles for Efficient Heat Induction. *Nat. Nanotechnol.* **2011**, *6* (7), 418–422. https://doi.org/10.1038/nnano.2011.95.

(263) Das, R.; Alonso, J.; Nemati Porshokouh, Z.; Kalappattil, V.; Torres, D.; Phan, M. H.; Garaio, E.; García, J. Á.; Sanchez Llamazares, J. L.; Srikanth, H. Tunable High Aspect Ratio Iron Oxide Nanorods for Enhanced Hyperthermia. *J. Phys. Chem. C* **2016**, *120* (18), 10086–10093. https://doi.org/10.1021/acs.jpcc.6b02006.

(264) Gutierrez-Guzman, D. F.; Lizardi, L. I.; Otálora, J. A.; Landeros, P. Hyperthermia in Low Aspect-Ratio Magnetic Nanotubes for Biomedical Applications. *Appl. Phys. Lett.* **2017**, *110* (13). https://doi.org/10.1063/1.4979165.

(265) Nemati, Z.; Das, R.; Alonso, J.; Clements, E.; Phan, M. H.; Srikanth, H. Iron Oxide Nanospheres and Nanocubes for Magnetic Hyperthermia Therapy: A Comparative Study. *J. Electron. Mater.* **2017**, *46* (6), 3764–3769. https://doi.org/10.1007/s11664-017-5347-6.

(266) Muela, A.; Muñoz, D.; Martín-Rodríguez, R.; Orue, I.; Garaio, E.; Abad Díaz De Cerio, A.; Alonso, J.; García, J. Á.; Fdez-Gubieda, M. L. Optimal Parameters for Hyperthermia Treatment Using Biomineralized Magnetite Nanoparticles: Theoretical and Experimental Approach. *J. Phys. Chem. C* **2016**, *120* (42), 24437–24448. https://doi.org/10.1021/acs.jpcc.6b07321.

(267) Hu, X.; Yu, J. C.; Gong, J.; Li, Q.; Li, G. α-Fe2O3 Nanorings Prepared by a Microwave-Assisted Hydrothermal Process and Their Sensing Properties. *Adv. Mater.* **2007**, *19* (17), 2324–2329. https://doi.org/10.1002/adma.200602176.

(268) Chueh, Y.-L.; Lai, M.-W.; Liang, J.-Q.; Chou, L.-J.; Wang, Z. L. Systematic Study of the Growth of Aligned Arrays of α-Fe2O3 and Fe3O4 Nanowires by a Vapor–Solid Process. *Adv. Funct. Mater.* **2006**, *16* (17), 2243–2251. https://doi.org/10.1002/adfm.200600499.

(269) Zhang, S.; Wu, W.; Xiao, X.; Zhou, J.; Ren, F.; Jiang, C. Preparation and Characterization of Spindle-like Fe3O4 Mesoporous Nanoparticles. *Nanoscale Res. Lett.* **2011**, *6* (1), 1–9. https://doi.org/10.1186/1556-276X-6-89.

(270) Dunlop, D. J. Coercive Forces and Coercivity Spectra of Submicron Magnetites. *Earth Planet. Sci. Lett.* **1986**, *78* (2–3), 288–295. https://doi.org/10.1016/0012-821X(86)90068-3.

(271) Stacey, F.; Wise, K. Crystal Dislocations and Coercivity in Fine Grained Magnetite. *Aust. J. Phys.* **1967**, *20* (5), 507. https://doi.org/10.1071/ph670507.

(272) Heider, F.; Dunlop, D. J.; Sugiura, N. Magnetic Properties of Hydrothermally Recrystallized Magnetite Crystals. *Science (80-.).* **1987**, *236* (4805), 1287–1290. https://doi.org/10.1126/science.236.4806.1287.

(273) Chiu, W. S.; Radiman, S.; Abd-Shukor, R.; Abdullah, M. H.; Khiew, P. S. Tunable Coercivity of CoFe2O4 Nanoparticles via Thermal Annealing Treatment. *J. Alloys Compd.* **2008**, *459* (1–2), 291–297. https://doi.org/10.1016/j.jallcom.2007.04.215.

(274) Raabe, J.; Pulwey, R.; Sattler, R.; Schweinböck, T.; Zweck, J.; Weiss, D. Magnetization Pattern of Ferromagnetic Nanodisks. *J. Appl. Phys.* **2000**, *88* (7), 4437–4439. https://doi.org/10.1063/1.1289216.

(275) Novosad, V.; Guslienko, K. Y.; Shima, H.; Otani, Y.; Kim, S. G.; Fukamichi, K.; Kikuchi, N.; Kitakami, O.; Shimada, Y. Effect of Interdot Magnetostatic Interaction on Magnetization Reversal in Circular Dot Arrays. *Phys. Rev. B - Condens. Matter Mater. Phys.* **2002**, *65* (6), 1–4. https://doi.org/10.1103/PhysRevB.65.060402.

(276) Usov, N. A.; Nesmeyanov, M. S.; Tarasov, V. P. Magnetic Vortices as Efficient Nano Heaters in Magnetic Nanoparticle Hyperthermia. *Sci. Rep.* **2018**, *8* (1), 1224. https://doi.org/10.1038/s41598-017-18162-8.

(277) Aharoni, A. *Introduction to the Theory of Ferromagnetism*; Clarendon Press ;;Oxford University Press: Oxford ;New York, 1996.

(278) Ross, C. A.; Hwang, M.; Shima, M.; Cheng, J. Y.; Farhoud, M.; Savas, T. A.; Smith, H. I.; Schwarzacher, W.; Ross, F. M.; Redjdal, M.; Humphrey, F. B. Micromagnetic Behavior of Electrodeposited Cylinder Arrays. *Phys. Rev. B - Condens. Matter Mater. Phys.* **2002**, *65* (14), 1–8. https://doi.org/10.1103/PhysRevB.65.144417.

(279) d'Albuquerque e Castro, J.; Altbir, D.; Retamal, J. C.; Vargas, P. Scaling Approach to the Magnetic Phase Diagram of Nanosized Systems. *Phys. Rev. Lett.* **2002**, *88* (23), 2372021–2372024. https://doi.org/10.1103/PhysRevLett.88.237202.

(280) Porrati, F.; Huth, M. Diagram of the States in Arrays of Iron Nanocylinders. *Appl. Phys. Lett.* **2004**, *85* (15), 3157–3159. https://doi.org/10.1063/1.1805697.

(281) Metlov, K. L.; Guslienko, K. Y. Stability of Magnetic Vortex in Soft Magnetic Nano-Sized Circular Cylinder. *J. Magn. Magn. Mater.* **2001**, *242–245*, 1015–1017. https://doi.org/10.1016/S0304-8853(01)01360-9.

(282) Li, L.; Mak, K. Y.; Leung, C. W.; Chan, K. Y.; Chan, W. K.; Zhong, W.; Pong, P. W. T.

Effect of Synthesis Conditions on the Properties of Citric-Acid Coated Iron Oxide Nanoparticles. *Microelectron. Eng.* **2013**, *110*, 329–334. https://doi.org/10.1016/j.mee.2013.02.045.

(283) Mamiya, H.; Jeyadevan, B. Hyperthermic Effects of Dissipative Structures of Magnetic Nanoparticles in Large Alternating Magnetic Fields. *Sci. Rep.* **2011**, *1*. https://doi.org/10.1038/srep00157.

(284) Ma, M.; Zhang, Y.; Guo, Z.; Gu, N. Facile Synthesis of Ultrathin Magnetic Iron Oxide Nanoplates by Schikorr Reaction. *Nanoscale Res. Lett.* **2013**, *8* (1), 1–7. https://doi.org/10.1186/1556-276X-8-16.

(285) Carrey, J.; Mehdaoui, B.; Respaud, M. Simple Models for Dynamic Hysteresis Loop Calculations of Magnetic Single-Domain Nanoparticles: Application to Magnetic Hyperthermia Optimization. *J. Appl. Phys.* **2011**, *109* (8), 083921. https://doi.org/10.1063/1.3551582.

(286) Usov, N. A.; Liubimov, B. Y. Dynamics of Magnetic Nanoparticle in a Viscous Liquid: Application to Magnetic Nanoparticle Hyperthermia. *J. Appl. Phys.* **2012**, *112* (2), 023901. https://doi.org/10.1063/1.4737126.

(287) Mamiya, H. Recent Advances in Understanding Magnetic Nanoparticles in Ac Magnetic Fields and Optimal Design for Targeted Hyperthermia. *J. Nanomater.* **2013**, *2013*. https://doi.org/10.1155/2013/752973.

(288) Landeros, P.; Escrig, J.; Altbir, D.; Laroze, D.; D'Albuquerque E Castro, J.; Vargas, P. Scaling Relations for Magnetic Nanoparticles. *Phys. Rev. B - Condens. Matter Mater. Phys.* **2005**, *71* (9), 094435. https://doi.org/10.1103/PhysRevB.71.094435.

(289) Wu, W.; He, Q.; Jiang, C. Magnetic Iron Oxide Nanoparticles: Synthesis and Surface Functionalization Strategies. *Nanoscale Res. Lett.* **2008**, *3* (11), 397–415. https://doi.org/10.1007/s11671-008-9174-9.

(290) Hurley, K. R.; Ring, H. L.; Etheridge, M.; Zhang, J.; Gao, Z.; Shao, Q.; Klein, N. D.; Szlag, V. M.; Chung, C.; Reineke, T. M.; Garwood, M.; Bischof, J. C.; Haynes, C. L. Predictable Heating and Positive MRI Contrast from a Mesoporous Silica-Coated Iron Oxide Nanoparticle. **2016**. https://doi.org/10.1021/acs.molpharmaceut.5b00866.

(291) Ravichandran, M.; Oza, G.; Velumani, S.; Ramirez, J. T.; Garcia-Sierra, F.; Andrade, N. B.; Vera, A.; Leija, L.; Garza-Navarro, M. A. Plasmonic/Magnetic Multifunctional

Nanoplatform for Cancer Theranostics. *Sci. Rep.* **2016**, *6* (1), 1–15. https://doi.org/10.1038/srep34874.

(292) Das, R.; Cardarelli, J. A.; Phan, M. H.; Srikanth, H. Magnetically Tunable Iron Oxide Nanotubes for Multifunctional Biomedical Applications. *J. Alloys Compd.* **2019**, *789*, 323–329. https://doi.org/10.1016/j.jallcom.2019.03.024.

(293) Lee, J. H.; Jang, J. T.; Choi, J. S.; Moon, S. H.; Noh, S. H.; Kim, J. W.; Kim, J. G.; Kim, I. S.; Park, K. I.; Cheon, J. Exchange-Coupled Magnetic Nanoparticles for Efficient Heat Induction. *Nat. Nanotechnol.* **2011**, *6* (7), 418–422. https://doi.org/10.1038/nnano.2011.95.

(294) Horev-Azaria, L.; Baldi, G.; Beno, D.; Bonacchi, D.; Golla-Schindler, U.; Kirkpatrick, J. C.; Kolle, S.; Landsiedel, R.; Maimon, O.; Marche, P. N.; Ponti, J.; Romano, R.; Rossi, F.; Sommer, D.; Uboldi, C.; Unger, R. E.; Villiers, C.; Korenstein, R. Predictive Toxicology of Cobalt Ferrite Nanoparticles: Comparative in-Vitro Study of Different Cellular Models Using Methods of Knowledge Discovery from Data. *Part. Fibre Toxicol.* **2013**, *10* (1), 32. https://doi.org/10.1186/1743-8977-10-32.

(295) Crossgrove, J.; Zheng, W. Manganese Toxicity upon Overexposure. *NMR in Biomedicine*. NMR Biomed December 2004, pp 544–553. https://doi.org/10.1002/nbm.931.

(296) Pham, X. N.; Nguyen, T. P.; Pham, T. N.; Tran, T. T. N.; Tran, T. V. T. Synthesis and Characterization of Chitosan-Coated Magnetite Nanoparticles and Their Application in Curcumin Drug Delivery. *Adv. Nat. Sci. Nanosci. Nanotechnol.* **2016**, *7* (4), 045010. https://doi.org/10.1088/2043-6262/7/4/045010.

(297) Tai, M. F.; Lai, C. W.; Abdul Hamid, S. B. Facile Synthesis Polyethylene Glycol Coated Magnetite Nanoparticles for High Colloidal Stability. *J. Nanomater.* **2016**, *2016*. https://doi.org/10.1155/2016/8612505.

(298) Chen, X.; Klingeler, R.; Kath, M.; El Gendy, A. A.; Cendrowski, K.; Kalenczuk, R. J.; Borowiak-Palen, E. Magnetic Silica Nanotubes: Synthesis, Drug Release, and Feasibility for Magnetic Hyperthermia. *ACS Appl. Mater. Interfaces* **2012**, *4* (4), 2303–2309. https://doi.org/10.1021/am300469r.

(299) Zulfiqar; Afzal, S.; Khan, R.; Zeb, T.; Rahman, M. ur; Burhanullah; Ali, S.; Khan, G.; Rahman, Z. ur; Hussain, A. Structural, Optical, Dielectric and Magnetic Properties of PVP Coated Magnetite (Fe3O4) Nanoparticles. *J. Mater. Sci. Mater. Electron.* **2018**, *29* (23), 20040–20050. https://doi.org/10.1007/s10854-018-0134-6.

(300) Li, S. P.; Peyrade, D.; Natali, M.; Lebib, A.; Chen, Y.; Ebels, U.; Buda, L. D.; Ounadjela, K. Flux Closure Structures in Cobalt Rings. *Phys. Rev. Lett.* **2001**, *86* (6), 1102–1105. https://doi.org/10.1103/PhysRevLett.86.1102.

(301) Maldonado, A. C. M.; Winkler, E. L.; Raineri, M.; Córdova, A. T.; Rodríguez, L. M.; Troiani, H. E.; Pisciotti, M. L. M.; Mansilla, M. V.; Tobia, D.; Nadal, M. S.; Torres, T. E.; De Biasi, E.; Ramos, C. A.; Goya, G. F.; Zysler, R. D.; Lima, E. Free-Radical Formation by the Peroxidase-Like Catalytic Activity of MFe2O4 (M = Fe, Ni, and Mn) Nanoparticles. *J. Phys. Chem. C* **2019**, *123* (33), 20617–20627. https://doi.org/10.1021/acs.jpcc.9b05371.

(302) A Mechanism of Magnetic Hysteresis in Heterogeneous Alloys. *Philos. Trans. R. Soc. London. Ser. A, Math. Phys. Sci.* **1948**, *240* (826), 599–642. https://doi.org/10.1098/rsta.1948.0007.

(303) Niraula, G.; Coaquira, J. A. H.; Aragon, F. H.; Galeano Villar, B. M.; Mello, A.; Garcia, F.; Muraca, D.; Zoppellaro, G.; Vargas, J. M.; Sharma, S. K. Tuning the Shape, Size, Phase Composition and Stoichiometry of Iron Oxide Nanoparticles: The Role of Phosphate Anions. *J. Alloys Compd.* **2020**, 156940. https://doi.org/10.1016/j.jallcom.2020.156940.

(304) Coelho, B. C. P.; Siqueira, E. R.; Ombredane, A. S.; Joanitti, G. A.; Chaves, S. B.; Da Silva, S. W.; Chaker, J. A.; Longo, J. P. F.; Azevedo, R. B.; Morais, P. C.; Sousa, M. H. Maghemite-Gold Core-Shell Nanostructures (γ-Fe2O3@Au) Surface-Functionalized with Aluminium Phthalocyanine for Multi-Task Imaging and Therapy. *RSC Adv.* **2017**, *7* (19), 11223–11232. https://doi.org/10.1039/c6ra27539g.

(305) Topić, M.; Moguš-Milanković, A.; Day, D. E. Study of Polarization Mechanisms in Sodium Iron Phosphate Glasses by Partial Thermally Stimulated Depolarization Current. *J. Non. Cryst. Solids* **2000**, *261* (1), 146–154. https://doi.org/10.1016/S0022-3093(99)00601-8.

(306) Pasquini, L.; Wacrenier, O.; Vona, M. L. D.; Knauth, P. Hydration and Ionic Conductivity of Model Cation and Anion-Conducting Ionomers in Buffer Solutions (Phosphate, Acetate, Citrate). *J. Phys. Chem. B* **2018**, *122* (50), 12009–12016. https://doi.org/10.1021/acs.jpcb.8b08622.

(307) Stus, N. V.; Lisnyak, V. V.; Nagornyi, P. G. Crystal Structure and Ionic Conductivity of a Novel Indium and Sodium Phosphate Na7(InP2O7)4PO4. *J. Alloys Compd.* **2001**, *314* (1–2), 62–66. https://doi.org/10.1016/S0925-8388(00)01207-X.

(308) Horikoshi, S.; Osawa, A.; Abe, M.; Serpone, N. On the Generation of Hot-Spots by

Microwave Electric and Magnetic Fields and Their Impact on a Microwave-Assisted Heterogeneous Reaction in the Presence of Metallic Pd Nanoparticles on an Activated Carbon Support. *J. Phys. Chem. C* **2011**, *115* (46), 23030–23035. https://doi.org/10.1021/jp2076269.

(309) Vreeland, E. C.; Watt, J.; Schober, G. B.; Hance, B. G.; Austin, M. J.; Price, A. D.; Fellows, B. D.; Monson, T. C.; Hudak, N. S.; Maldonado-Camargo, L.; Bohorquez, A. C.; Rinaldi, C.; Huber, D. L. Enhanced Nanoparticle Size Control by Extending LaMer's Mechanism. *Chem. Mater.* **2015**, *27* (17), 6059–6066. https://doi.org/10.1021/acs.chemmater.5b02510.

(310) Becker, P.; Heizmann, J. J.; Baro, R. Relations Topotaxiques Entre Des Cristaux Naturels d'hématite et Le Magnétite Qui En Est Issue Par Réduction à Basse Température. *J. Appl. Crystallogr.* **1977**, *10* (2), 77–78. https://doi.org/10.1107/s0021889877012941.

(311) Bursill, L. A.; Withers, R. L. On the Multiple Orientation Relationships between Hematite and Magnetite. *J. Appl. Crystallogr.* **1979**, *12* (3), 287–294. https://doi.org/10.1107/s0021889879012486.

(312) Cullity, B. D.; Graham, C. D. *Introduction to Magnetic Materials*; John Wiley & Sons, Inc., 2008. https://doi.org/10.1002/9780470386323.

(313) James, M. A.; Hibma, T. (Formula Presented)-Assisted Molecular-Beam Epitaxy of (Formula Presented) (Formula Presented) and (Formula Presented) Thin Films on Mgo(100). *Phys. Rev. B - Condens. Matter Mater. Phys.* **1999**, *60* (15), 11193–11206. https://doi.org/10.1103/PhysRevB.60.11193.

(314) Tong, S.; Quinto, C. A.; Zhang, L.; Mohindra, P.; Bao, G. Size-Dependent Heating of Magnetic Iron Oxide Nanoparticles. *ACS Nano* **2017**, *11* (7), 6808–6816. https://doi.org/10.1021/acsnano.7b01762.

(315) Guibert, C. C.; Dupuis, V.; Peyre, V.; Jérô Me Fresnais, J. Hyperthermia of Magnetic Nanoparticles: Experimental Study of the Role of Aggregation. **2015**. https://doi.org/10.1021/acs.jpcc.5b07796.

(316) Simeonidis, K.; Morales, M. P.; Marciello, M.; Angelakeris, M.; de la Presa, P.; Lazaro-Carrillo, A.; Tabero, A.; Villanueva, A.; Chubykalo-Fesenko, O.; Serantes, D. In-Situ Particles Reorientation during Magnetic Hyperthermia Application: Shape Matters Twice. *Sci. Rep.* **2016**, *6* (1), 38382. https://doi.org/10.1038/srep38382.

(317) Gao, Y.; Lim, J.; Teoh, S. H.; Xu, C. Emerging Translational Research on Magnetic

Nanoparticles for Regenerative Medicine. *Chem. Soc. Rev.* **2015**, *44* (17), 6306–6329. https://doi.org/10.1039/c4cs00322e.

(318) Gobbo, O. L.; Sjaastad, K.; Radomski, M. W.; Volkov, Y.; Prina-Mello, A. Magnetic Nanoparticles in Cancer Theranostics. *Theranostics* **2015**, *5* (11), 1249–1263. https://doi.org/10.7150/thno.11544.

(319) Stephen, Z. R.; Kievit, F. M.; Zhang, M. Magnetite Nanoparticles for Medical MR Imaging. *Mater. Today* **2011**, *14* (7–8), 330–338. https://doi.org/10.1016/S1369-7021(11)70163-8.

(320) Cheng, Y.; Morshed, R. A.; Auffinger, B.; Tobias, A. L.; Lesniak, M. S. Multifunctional Nanoparticles for Brain Tumor Imaging and Therapy. *Adv. Drug Deliv. Rev.* **2014**, *66*, 42–57. https://doi.org/10.1016/j.addr.2013.09.006.

(321) Goiriena-Goikoetxea, M.; Muñoz, D.; Orue, I.; Fernández-Gubieda, M. L.; Bokor, J.; Muela, A.; García-Arribas, A. Disk-Shaped Magnetic Particles for Cancer Therapy. *Applied Physics Reviews*. American Institute of Physics Inc. March 1, 2020, p 011306. https://doi.org/10.1063/1.5123716.

(322) Mannix, R. J.; Kumar, S.; Cassiola, F.; Montoya-Zavala, M.; Feinstein, E.; Prentiss, M.; Ingber, D. E. Nanomagnetic Actuation of Receptor-Mediated Signal Transduction. *Nat. Nanotechnol.* **2008**, *3* (1), 36–40. https://doi.org/10.1038/nnano.2007.418.

(323) Chen, M.; Wu, J.; Ning, P.; Wang, J.; Ma, Z.; Huang, L.; Plaza, G. R.; Shen, Y.; Xu, C.; Han, Y.; Lesniak, M. S.; Liu, Z.; Cheng, Y. Remote Control of Mechanical Forces via Mitochondrial-Targeted Magnetic Nanospinners for Efficient Cancer Treatment. *Small* **2020**, *16* (3), 1905424. https://doi.org/10.1002/smll.201905424.

(324) Mansell, R.; Vemulkar, T.; Petit, D. C. M. C.; Cheng, Y.; Murphy, J.; Lesniak, M. S.; Cowburn, R. P. Magnetic Particles with Perpendicular Anisotropy for Mechanical Cancer Cell Destruction. *Sci. Rep.* **2017**, *7* (1), 1–7. https://doi.org/10.1038/s41598-017-04154-1.

(325) Leulmi, S.; Chauchet, X.; Morcrette, M.; Ortiz, G.; Joisten, H.; Sabon, P.; Livache, T.; Hou, Y.; Carrière, M.; Lequien, S.; Dieny, B. Triggering the Apoptosis of Targeted Human Renal Cancer Cells by the Vibration of Anisotropic Magnetic Particles Attached to the Cell Membrane. *Nanoscale* **2015**, *7* (38), 15904–15914. https://doi.org/10.1039/c5nr03518j.

(326) Rahm, M.; Schneider, M.; Biberger, J.; Pulwey, R.; Zweck, J.; Weiss, D.; Umansky, V. Vortex Nucleation in Submicrometer Ferromagnetic Disks. *Appl. Phys. Lett.* **2003**, *82* (23), 4110–4112. https://doi.org/10.1063/1.1581363.

(327) McMichael, R. D.; Maranville, B. B. Edge Saturation Fields and Dynamic Edge Modes in Ideal and Nonideal Magnetic Film Edges. *Phys. Rev. B - Condens. Matter Mater. Phys.* **2006**, *74* (2). https://doi.org/10.1103/PhysRevB.74.024424.

(328) Altbir Drullinsky, D. R.; Escrig Murua, J. E.; Kamenetskii, E. O.; Landeros Silva, P. M. *ELECTROMAGNETIC, MAGNETOSTATIC, AND EXCHANGE-INTERACTION VORTICES IN CONFINED MAGNETIC STRUCTURES*; TRANSWORLD RESEARCH NETWORK: Kerala, India, 2008.

(329) Landeros, P.; Suarez, O. J.; Cuchillo, A.; Vargas, P. Equilibrium States and Vortex Domain Wall Nucleation in Ferromagnetic Nanotubes. *Phys. Rev. B - Condens. Matter Mater. Phys.* **2009**, *79* (2), 024404. https://doi.org/10.1103/PhysRevB.79.024404.

(330) Escrig, J.; Landeros, P.; Altbir, D.; Vogel, E. E.; Vargas, P. Phase Diagrams of Magnetic Nanotubes. *J. Magn. Magn. Mater.* **2007**, *308* (2), 233–237. https://doi.org/10.1016/j.jmmm.2006.05.019.

(331) Goiriena-Goikoetxea, M.; García-Arribas, A.; Rouco, M.; Svalov, A. V.; Barandiaran, J. M. High-Yield Fabrication of 60 Nm Permalloy Nanodiscs in Well-Defined Magnetic Vortex State for Biomedical Applications. *Nanotechnology* **2016**, *27* (17). https://doi.org/10.1088/0957-4484/27/17/175302.

(332) Chung, S. H.; McMichael, R. D.; Pierce, D. T.; Unguris, J. Phase Diagram of Magnetic Nanodisks Measured by Scanning Electron Microscopy with Polarization Analysis. *Phys. Rev. B - Condens. Matter Mater. Phys.* **2010**, *81* (2), 024410. https://doi.org/10.1103/PhysRevB.81.024410.

(333) Montoncello, F.; Giovannini, L.; Nizzoli, F.; Tanigawa, H.; Ono, T.; Gubbiotti, G.; Madami, M.; Tacchi, S.; Carlotti, G. Magnetization Reversal and Soft Modes in Nanorings: Transitions between Onion and Vortex States Studied by Brillouin Light Scattering. *Phys. Rev. B - Condens. Matter Mater. Phys.* **2008**, *78* (10), 104421. https://doi.org/10.1103/PhysRevB.78.104421.

(334) Wang, Z. K.; Lim, H. S.; Liu, H. Y.; Ng, S. C.; Kuok, M. H.; Tay, L. L.; Lockwood, D. J.; Cottam, M. G.; Hobbs, K. L.; Larson, P. R.; Keay, J. C.; Lian, G. D.; Johnson, M. B. Spin Waves in Nickel Nanorings of Large Aspect Ratio. *Phys. Rev. Lett.* **2005**, *94* (13), 137208. https://doi.org/10.1103/PhysRevLett.94.137208.

(335) Zhang, W.; Haas, S. Phase Diagram of Magnetization Reversal Processes in Nanorings.

Phys. Rev. B - Condens. Matter Mater. Phys. **2010**, *81* (6), 064433. https://doi.org/10.1103/PhysRevB.81.064433.

(336) Castaño, F. J.; Ross, C. A.; Frandsen, C.; Eilez, A.; Gil, D.; Smith, H. I.; Redjdal, M.; Humphrey, F. B. Metastable States in Magnetic Nanorings. *Phys. Rev. B - Condens. Matter Mater. Phys.* **2003**, *67* (18), 184425. https://doi.org/10.1103/PhysRevB.67.184425.

(337) Goll, D.; Berkowitz, A. E.; Bertram, H. N. Critical Sizes for Ferromagnetic Spherical Hollow Nanoparticles. *Phys. Rev. B - Condens. Matter Mater. Phys.* **2004**, *70* (18), 1–10. https://doi.org/10.1103/PhysRevB.70.184432.

(338) Zaharko, O.; Oppeneer, P. M.; Grimmer, H.; Horisberger, M.; Mertins, H. C.; Abramsohn, D.; Schäfers, F.; Bill, A.; Braun, H. B. Exchange Coupling in Fe/NiO/Co Film Studied by Soft x-Ray Resonant Magnetic Reflectivity. *Phys. Rev. B - Condens. Matter Mater. Phys.* **2002**, *66* (13), 1–10. https://doi.org/10.1103/PhysRevB.66.134406.

(339) Kharmouche, A.; Chérif, S. M.; Bourzami, A.; Layadi, A.; Schmerber, G. Structural and Magnetic Properties of Evaporated Co/Si(100) and Co/Glass Thin Films. *J. Phys. D. Appl. Phys.* **2004**, *37* (18), 2583–2587. https://doi.org/10.1088/0022-3727/37/18/014.

(340) Paritosh; Srolovitz, D. J. Shadowing Effects on the Microstructure of Obliquely Deposited Films. *J. Appl. Phys.* **2002**, *91* (3), 1963–1972. https://doi.org/10.1063/1.1432125.

(341) Vopsaroiu, M.; Georgieva, M.; Grundy, P. J.; Fernandez, G. V.; Manzoor, S.; Thwaites, M. J.; O'Grady, K. Preparation of High Moment CoFe Films with Controlled Grain Size and Coercivity. In *Journal of Applied Physics*; American Institute of PhysicsAIP, 2005; Vol. 97, p 10N303. https://doi.org/10.1063/1.1855276.

(342) Tu, K. N.; Gusak, A. M.; Sobchenko, I. Linear Rate of Grain Growth in Thin Films during Deposition. *Phys. Rev. B - Condens. Matter Mater. Phys.* **2003**, *67* (24), 245408. https://doi.org/10.1103/PhysRevB.67.245408.

(343) Rijks, T. G. S. M.; Lenczowski, S.; Coehoorn, R. In-Plane and out-of-Plane Anisotropic Magnetoresistance in Thin Films. *Phys. Rev. B - Condens. Matter Mater. Phys.* **1997**, *56* (1), 362–366. https://doi.org/10.1103/PhysRevB.56.362.

(344) Bryan, M. T.; Atkinson, D.; Cowburn, R. P. Experimental Study of the Influence of Edge Roughness on Magnetization Switching in Permalloy Nanostructures. *Appl. Phys. Lett.* **2004**, *85* (16), 3510–3512. https://doi.org/10.1063/1.1806566.

(345) Kläui, M.; Vaz, C. A. F.; Bland, J. A. C.; Sinnecker, E. H. C. P.; Guimarạes, A. P.;

Werndorfer, W.; Faini, G.; Cambril, E.; Heyderman, L. J.; David, C. Switching Processes and Switching Reproducibility in Ferromagnetic Ring Structures. *Appl. Phys. Lett.* **2004**, *84* (6), 951–953. https://doi.org/10.1063/1.1640451.

(346) Casey Uhlig, W.; Shi, J. Systematic Study of the Magnetization Reversal in Patterned Co and NiFe Nanolines. *Appl. Phys. Lett.* **2004**, *84* (5), 759–761. https://doi.org/10.1063/1.1645332.

(347) Garcia, F.; Westfahl, H.; Schoenmaker, J.; Carvalho, E. J.; Santos, A. D.; Pojar, M.; Seabra, A. C.; Belkhou, R.; Bendounan, A.; Novais, E. R. P.; Guimarães, A. P. Tailoring Magnetic Vortices in Nanostructures. *Appl. Phys. Lett.* **2010**, *97* (2), 022501. https://doi.org/10.1063/1.3462305.

(348) Caputo, J. G.; Gaididei, Y.; Kravchuk, V. P.; Mertens, F. G.; Sheka, D. D. Effective Anisotropy of Thin Nanomagnets: Beyond the Surface-Anisotropy Approach. *Phys. Rev. B - Condens. Matter Mater. Phys.* **2007**, *76* (17), 174428. https://doi.org/10.1103/PhysRevB.76.174428.

(349) Pylypovskyi, O. V.; Sheka, D. D.; Kravchuk, V. P.; Gaididei, Y. Effects of Surface Anisotropy on Magnetic Vortex Core. *J. Magn. Magn. Mater.* **2014**, *361*, 201–205. https://doi.org/10.1016/j.jmmm.2014.02.094.

(350) Scholz, W.; Guslienko, K. Y.; Novosad, V.; Suess, D.; Schrefl, T.; Chantrell, R. W.; Fidler, J. Transition from Single-Domain to Vortex State in Soft Magnetic Cylindrical Nanodots. In *Journal of Magnetism and Magnetic Materials*; North-Holland, 2003; Vol. 266, pp 155–163. https://doi.org/10.1016/S0304-8853(03)00466-9.

(351) Feldtkeller, E.; Thomas, H. Struktur Und Energie von Blochlinien in Dünnen Ferromagnetischen Schichten. *Phys. der Kondens. Mater.* **1965**, *4* (1), 8–14. https://doi.org/10.1007/BF02423256.

(352) Leulmi, S.; Joisten, H.; Dietsch, T.; Iss, C.; Morcrette, M.; Auffret, S.; Sabon, P.; Dieny, B. Comparison of Dispersion and Actuation Properties of Vortex and Synthetic Antiferromagnetic Particles for Biotechnological Applications. *Appl. Phys. Lett.* **2013**, *103* (13), 132412. https://doi.org/10.1063/1.4821854.

(353) Stutzin, A.; Hoffmann, E. K. Swelling-Activated Ion Channels: Functional Regulation in Cell-Swelling, Proliferation and Apoptosis. *Acta Physiol.* **2006**, *187* (1–2), 27–42. https://doi.org/10.1111/j.1748-1716.2006.01537.x.

(354) Lang, F.; Föller, M.; Lang, K. S.; Lang, P. A.; Ritter, M.; Gulbins, E.; Vereninov, A.; Huber, S. M. Ion Channels in Cell Proliferation and Apoptotic Cell Death. *Journal of Membrane Biology*. Springer June 2005, pp 147–157. https://doi.org/10.1007/s00232-005-0780-5.

(355) Martinac, B. Mechanosensitive Ion Channels: Molecules of Mechanotransduction. *J. Cell Sci.* **2004**, *117* (12), 2449–2460. https://doi.org/10.1242/jcs.01232.

(356) Hu, W.; Wilson, R. J.; Koh, A.; Fu, A.; Faranesh, A. Z.; Earhart, C. M.; Osterfeld, S. J.; Han, S.-J.; Xu, L.; Guccione, S.; Sinclair, R.; Wang, S. X. High-Moment Antiferromagnetic Nanoparticles with Tunable Magnetic Properties. *Adv. Mater.* **2008**, *20* (8), 1479–1483. https://doi.org/10.1002/adma.200703077.

GOPAL NIRAULA
Doctoral Student in Condensed Matter Physics
Functional Nanomaterial Laboratory
Post Graduate Research Program in Physics- PPGF
Federal University of Maranhão - UFMA, São Luís, Brazil
Email: gopalniraula891@gmail.com
Phone: (+55) 61991460621
ORCID: https://orcid.org/0000-0002-8776-7794

Research Interest:

- Magnetic vortex nanoparticles; surface interface effect; magnetic and photothermal hyperthermia; theoretical modelling and magnetic simulations for vortex nanoparticles; magneto-mechanical transducer for cancer therapy; cell culture; in vitro experiments.

Professional Visit during Ph.D.:

- 23 November 2021 – 27 January 2022, Institute of Nanoscience and Materials of Argon, University of Zaragoza, Zaragoza, Spain.
- March- April, 2020, Department of Genetics & Morphology, Institute of Biological Sciences, University of Brasilia, Brazil.
- September- October 2019, Brazilian Center for Research in Physics - CBPF, Rio de Janeiro, RJ, Brazil
- March, 2019 – Present, Laboratory of Magnetic Materials, NFA, Institute of Physics, University of Brasilia, Brazil
- November-December, 2018, Group of Thermal Nanomedicine, Institute of Physics, Federal University of Goias, Goiania, Brazil.

Training/Workshop/Teaching assistant/Programming Skills:

- 08-19 November 2021, ***1st Latin American Tutorial in Magnetism*** conducted by Latin American Association of Magnetism-ALMA
- May 2021***, Minicourse on "Magnetic Particle Imaging: Tracing Design and Application, II Advance School on Nanomedicine"***, Institute of Physics, Federal University of Goias- UFG, Brazil.
- May 2021, ***Minicourse on "Application of Iron Oxide Nanoparticles for Cancer Hyperthermia and Immunotherapy"***, II Advance ***School on Nanomedicine***, Institute of Physics, Federal University of Goias- UFG, Brazil.
- May 2021, ***Minicourse on "Combining Photothermal Nanoparticles with Immunotherapies", II Advance School on Nanomedicine***, Institute of Physics, Federal University of Goias- UFG, Brazil.

- March 2019- Present, monitoring undergraduate students as a ***'Teaching Assistant'*** with involving in materials synthesis and their different characterizations at Laboratory of Magnetic Materials, NFA, Institute of Physics, University of Brasilia, Brazil
- August 2019, ***Minicourse on "Introduction to Atomic Force Microscopy"*** (Hours: 4h). Brazilian Society of Microscopy and Microanalysis, SBMM, Brazil
- May 2019***, I Advance School on Nanomedicine*** (Hours: 18h). Institute of Physics, Federal University of Goias- UFG, Brazil.
- Scientific programing with ***Python, Mathematica*** *and* ***GNU plot***.
- Expertise in programming ***Normos*** *and* ***Fit; O*** for Mossbauer spectroscopic analysis and ***GSAS*** for X-ray diffraction Rietveld analysis.
- Transmission Electron Microscopy (TEM) analysis with ***Gatan DigitalMicrograph*** software.
- Expertise in ***computational micromagnetic modelling*** for the study of magnetic behavior of materials via Mumax 3.0

Research Skills:

- **Synthesis:** hydrothermal/solvothermal and microwave assisted hydrothermal methods
- **Characterization techniques:** X-ray diffraction; Reitveld analysis; thermal annealing/reduction; Fourier transform infrared radiation (FT-IR); scanning electronic microscopy (SEM); transmission electronic microscopy including Lorentz microscopy(TEM/LTEM); superconducting quantum interference device (SQUID); Mossbauer spectroscopy; X-ray photoelectron spectroscopy; calorimetry-based hyperthermia.
- Experience on handling the cryogen liquid (LN2 and LHe) to perform magnetic and electrical experiment at low cryogenic temperatures.
- Experience on 'Gas Sensing' experiment.
- Micro magnetic Simulation using **Mumax3.9**

Publication- Articles:

1. **NIRAULA**, **GOPAL**; DENILSON TONETO; GERARDO F. GOYA; GIORGIO ZOPPELLARO; JOSE A. H. COAQUIRA; DIEGO MURACA; JULIANO C. DENARDIN; TREVOR P. ALMEIDA; MARCELO KNOBEL AND SURENDER K. SHARMA, "Evidence of Magnetic Vortex Configuration and Loss of Stoichiometry in Submicrometer Fe_3O_4 Nanospheres" Submitted.

2. **NIRAULA, GOPAL**; TONETO, DENILSON; JOSHY, ELMA; COAQUIRA, JOSE AH; FLAVIO; MURACA, DIEGO; AYESH, AHMAD I.; DENARDIN, JULIANO; GOYA, GERARDO F.; SHARMA, SURENDER K, "Energy Evolution, Stabilization, and Mechanotransducer Properties of Fe_3O_4 Vortex Nanorings and Nanodiscs" ***Physical Review Applied***, ***v. 16, p.024002, 2021*** (10.1103/PhysRevApplied.16.024002) [IF= 4.985, Quartile = Q1]

3. **NIRAULA, GOPAL**; COAQUIRA, JOSE AH; ZOPPELLARO, GIORGIO; VILLAR, BIANCA MG; GARCIA, FLAVIO; BAKUZIS, ANDRIS F.; LONGO, JOÃO PF;

RODRIGUES, MOSAR C.; MURACA, DIEGO; AYESH, AHMAD I.; SINFRÔNIO, FRANCISCO SÁVIOM.; DE MENEZES, ALAN S.; GOYA, GERARDO F.; SHARMA, SURENDER K. Engineering Shape Anisotropy of Fe_3O_4 -γ-Fe_2O_3 Hollow Nanoparticles for Magnetic Hyperthermia. ***ACS Applied Nano Materials, v.4, 3, 3148–3158, 2021.*** [IF= 5.097, Quartile = Q1, Citation = 1]

4. **NIRAULA, GOPAL**; COAQUIRA, JOSE AH; ARAGON, FERMIN H.; BAKUZIS, ANDRIS F.; VILLAR, BIANCA MG; GARCIA, FLAVIO; MURACA, DIEGO; ZOPPELLARO, GIORGIO; AYESH, AHMAD I.; SHARMA, SURENDER K. Stoichiometry and Orientation and Shape-Mediated Switching Field Enhancement of the Heating Properties of Fe_3O_4. ***Physical Review Applied, v. 15, p.014056, 2021.*** [IF= 4.985, Quartile = Q1, Citation = 1]

5. **NIRAULA, GOPAL**; COAQUIRA, JOSE AH; ARAGON, FERMIN H.; GALEANO VILLAR, BIANCA M.; MELLO, ALEXANDRE; GARCIA, FLAVIO; MURACA, DIEGO; ZOPPELLARO, GIORGIO; VARGAS, JOSE M.; SHARMA, SURENDER K. Tuning the shape, size, phase composition and stoichiometry of iron oxide nanoparticles: The role of phosphate anions. ***Journal of Alloys and Compounds, v. 856, p. 156940, 2021.*** [IF= 5.316, Quartile = Q1]

Publication- Book Chapters:

1. **NIRAULA, GOPAL**; JASON J. A. MEDRANO; MOHAN C. MATHPAL; JERO-R MAZE; JOSE A. H. COAQUIRA AND SURENDER K. SHARMA, "X-rays Based Bioimaging Techniques and Scintillating Materials", **(in production).**

2. FAEZEH, MOZAFARI; HAMID, RASHIDZADEH; MURAT, BARSBAY; MOHAMMADREZA, GHAFFARLOU; MARZIYEH, SALEHIABAR; ALI, RAMAZANI; MORTEZA, ABAZARI; MOHAMMAD-AMIN, RAHMATI; **NIRAULA, GOPAL**, SHARMA, SURENDER K. AND HOSSEIN DANAFAR, "Application of Nanoradioprotective Agents in Cancer Therapy", **(in production).**

3. **NIRAULA, GOPAL**; MATHPAL, MOHAN C.; HERRERA, EDHER Z.; SOLER, MARIA A.G.; COAQUIRA, JOSE A.H.; SHARMA, SURENDER K. Magnetic Nanoflowers: Synthesis, Formation Mechanism and Hyperthermia Application. Accepted in Springer Nature, Switzerland: Springer International Publishing, S.K. Sharma Eds., 2021. [ISBN: 978-3-030-79959-5; https://doi.org/10.1007/978-3-030-79960-1_6]

4. **NIRAULA, GOPAL**; MATHPAL, MOHAN C.; HERRERA, EDHER Z.; SOLER, MARIA A.G.; COAQUIRA, JOSE A.H.; VERMA, RAMESH; SHARMA, SURENDER K. Superparamagnetic Iron Oxide Based Nanomaterials for Magnetic Resonance Imaging. Accepted in Springer Nature, Switzerland: Springer International Publishing, S.K. Sharma Eds., 2021. [ISBN: 978-3-030-79959-5; https://doi.org/10.1007/978-3-030-79960-1_7]

5. MATHPAL, MOHAN C.; **NIRAULA, GOPAL**; CHAND MAHESH; KUMAR, PRAMOD; SINGH, MANISH K.; SHARMA, SURENDER K.; SOLER, MARIA A.G.; SWART, H. C. Ferrite as an Alternative Source of Renewable Energy for hydroelectric cell. Springer International Publishing, S.K. Sharma Eds., 2021. [ISBN: 978-3-030-79959-5; https://doi.org/10.1007/978-3-030-79960-1_13]

6. MATHPAL, MOHAN C.; **NIRAULA, GOPAL**; CHAND MAHESH; KUMAR, PRAMOD; SINGH, MANISH K.; SHARMA, SURENDER K.; SOLER, MARIA A.G.; SWART, H. C. State of Art of Spinel Ferrites Enabled Humidity Sensor. Accepted in Springer Nature, Switzerland: Springer International Publishing, S.K. Sharma Eds., 2021. [ISBN: 978-3-030-79959-5; https://doi.org/10.1007/978-3-030-79960-1_14]

7. **NIRAULA, GOPAL**; SHRIVASTAVA, NAVADEEP; AKHTAR, KANWAL; JAVED, YASIR; COAQUIRA, JAH; SHARMA, SURENDER K. Liquid-Phase Synthesis of Multifunctional Nanomaterials: A Recent Update. Nanomedicine and Nanotoxicology. First ed. Switzerland: Springer International Publishing, 2020, v., P. 1-56 [Citation = 1]

Conference and Travel Grants during Ph.D.:

1 Received a collective travel grant from CAPES(Brazil) and MAGNA group at INMA, University of Zaragoza (Spain) for 2-month research collaboration with MAGNA group at INMA, UZ, Spain.
2 Received a travel grant from FAPEMA to visit the University of Brasilia, November-2020.
3 Received a conference participation grant from FAPEMA to participate 5th "3NANO International Conference" in Brasilia, December-2020.
4 Received a travel grant from PPGF/UFMA and FAPEMA to visit the Brazilian Centre for Research in Physics, Rio de Janeiro, August-2019.
5 Received a travel grant from FAPEMA to visit the University of Brasilia, October-2018.

Talk/Presentation/Participation in National and International Meetings/Conferences/ Congress during Ph.D.:

1 A **talk** on "Synthesis of Magnetic Vortex Nanoparticles for Therapeutic Applications" at Institute for Advanced Material and Mathematics, Public University of Pamplona, Pamplona - Spain (14-01-2022)

2 A **talk** on "Synthesis of Magnetic Vortex Nanoparticles and their thermal Properties" at Institute of Nanoscience and Materials of Argon, University of Zaragoza, Spain (06-12-2021)

3 A **talk** on "Synthesis of Magnetic Vortex Nanoparticles and their thermal Properties" at Institute of Nanoscience and Materials of Argon, University of Zaragoza, Spain (30-11-2021)

4 65th Virtual Conference on Magnetism and Magnetic Materials (MMM 2020), 02-06, November 2020, Virginia, USA. Switching Field, Orientation and Geometry Contribution on Magneto-hyperthermia of Fe_3O_4 (**Oral Presentation**).

5 XI scientific meeting of applied physics, UFES, Vitoria-ES, 01-04 December 2020. Nucleation Field, Orientation and Geometry Based Anisotropic Contribution on Magneto-hyperthermia of Fe_3O_4. (**Oral Presentation**).

6 1st Brazilian Congress of Nanomedicine, 8-10, December 2019 Brasilia (**Participation**).

7 27th Congress of Brazilian Microscopy and Microanalysis Society, 26-28, August 2019, Rio de Janeiro, Brazil. "Design of Magnetic Nanoparticles: Nanorods and Nanodisc for Magnetic Hyperthermia Applications" (**Poster Presentation**).

8 5th International Conference on Nanoscience, Nanotechnology, and Nanobiotechnology. "Role of Size, Morphology, Surface Composition on Magnetic Vortex State and Hyperthermia Properties of Iron Oxide Nanoparticles", 2019. (**Poster Presentation**).

9 A **talk** on "Size, Morphology, Surface Composition on Magnetic Vortex State and their Hyperthermia Properties" at Brazilian Center for Research in Physics- CBPF, Rio de Janeiro, Brazil (30-10-2019)

10 A **talk** on "Magnetic Vortex Nanoparticles and their Biomedical Application" at the Institute of Physics, University of Brasilia, Brazil (12-04-2019)

11 1st International Conference of Nanoscience and Nanobiotechnology, 23-25, October 2018, Brasilia. 2018. (**Participation**)

Stoichiometry and Orientation- and Shape-Mediated Switching Field Enhancement of the Heating Properties of Fe_3O_4 Circular Nanodiscs

Gopal Niraula,[1,2] Jose A. H. Coaquira,[2] Fermin H. Aragon,[3] Andris F. Bakuzis,[4] Bianca M. G. Villar,[5] Flavio Garcia,[5] Diego Muraca,[6] Giorgio Zoppellaro,[7] Ahmad I. Ayesh,[8,9] and Surender K. Sharma[1,10,*]

[1] *Department of Physics, Federal University of Maranhao, Sao Luis, Brazil*
[2] *Laboratory of Magnetic Materials, NFA, Institute of Physics, University of Brasilia, Brasilia, Brazil*
[3] *Laboratory of Thin Films, School of Physics, National University of Saint Augustine, Arequipa 001, Peru*
[4] *Institute of Physics, Federal University of Goias, 74690-900, Goiania, GO, Brazil*
[5] *Brazilian Center for Research in Physics - CBPF, Rio de Janeiro, RJ, Brazil*
[6] *Institute of Physics "Gleb Wataghin" (IFGW), University of Campinas, Campinas, Brazil*
[7] *Regional Centre of Advanced Technologies and Materials, Faculty of Science, Palacky University in Olomouc, Slechtitelu 11, 78371 Olomouc, Czech Republic*
[8] *Center for Sustainable Development, Qatar University, P. O. Box 2713, Doha, Qatar*
[9] *Department of Mathematics, Statistics and Physics, Qatar University, P. O. Box 2713, Doha, Qatar*
[10] *Department of Physics, Central University of Punjab, Bathinda, India*

(Received 9 July 2020; revised 6 November 2020; accepted 14 December 2020; published 28 January 2021)

The generation of topological magnetic vortex-domain structures in iron-oxide nanomaterials has promising applications in biomedical scenarios, such as heat generators for hyperthermia treatments. In this report we describe alternative kinds of magnetic-vortex nanoparticles, circular Fe_3O_4 nanodiscs (NDs), and dissect their heating properties by in-depth investigation of their shape and size, stoichiometry, orientations, and switching field "H_S" behaviors, through experiments and theoretical simulation. We find that the stoichiometric NDs show better heating performance than nonstoichiometric materials because of the significant electron hopping between Fe^{3+} and Fe^{2+} ion. The higher heating efficiency (in terms of specific absorption rate, SAR) is observed only for the higher switching field regime, an effect that is associated with the parallel and perpendicular alignment of nanodiscs with respect to low and high ac magnetic field, respectively. A higher SAR of approximately 270 W/g is observed at a higher switching field (approximately 700 Oe) for NDs of diameter 770 nm, which increases by a factor of 4 at a switching field of approximately 360 Oe for NDs of diameter 200 nm. The reported results suggest that the heating efficiency in these systems can be enhanced by controlling the switching field, which is, in turn, tuned by size, shape, and orientation of circular magnetic vortex nanodiscs.

DOI: 10.1103/PhysRevApplied.15.014056

ACS APPLIED NANO MATERIALS

www.acsanm.org Article

Engineering Shape Anisotropy of Fe_3O_4-γ-Fe_2O_3 Hollow Nanoparticles for Magnetic Hyperthermia

Gopal Niraula, Jose A. H. Coaquira, Giorgio Zoppellaro, Bianca M. G. Villar, Flavio Garcia, Andris F. Bakuzis, João P. F. Longo, Mosar C. Rodrigues, Diego Muraca, Ahmad I. Ayesh, Francisco Sávio M. Sinfrônio, Alan S. de Menezes, Gerardo F. Goya, and Surender K. Sharma*

Cite This: ACS Appl. Nano Mater. 2021, 4, 3148−3158 Read Online

ACCESS | Metrics & More | Article Recommendations | Supporting Information

ABSTRACT: The use of microwave-assisted synthesis (in water) of α-Fe_2O_3 nanomaterials followed by their transformation onto iron oxide Fe_3O_4-γ-Fe_2O_3 hollow nanoparticles encoding well-defined sizes and shapes [nanorings (NRs) and nanotubes (NTs)] is henceforth described. The impact of experimental variables such as concentration of reactants, volume of solvent employed, and reaction times/temperatures during the shape-controlled synthesis revealed that the key factor that gated generation of morphologically diverse nanoparticles was associated to the initial concentration of phosphate anions employed in the reactant mixture. All the nanomaterials presented were fully characterized by powder X-ray diffraction, field emission scanning electron microscopy, Fourier transform infrared, Mössbauer spectroscopy, and superconducting quantum interference device (SQUID). The hollow nanoparticles that expressed the most promising magnetic responses, NTs and NRs, were further tested in terms of efficiencies in controlling the magnetic hyperthermia, in view of their possible use for biomedical applications, supported by their excellent viability as screened by *in vitro* cytotoxicity tests. These systems NTs and NRs expressed very good magneto-hyperthermia properties, results that were further validated by micromagnetic simulations. The observed specific absorption rate (SAR) and intrinsic loss power of the NRs and NTs peaked the values of 340 W/g and 2.45 nH m^2 kg^{-1} (NRs) and 465 W/g and 3.3 nH m^2 kg^{-1} (NTs), respectively, at the maximum clinical field 450 Oe and under a frequency of 107 kHz and are the highest values among those reported so far in the hollow iron-oxide family. The higher SAR in NTs accounts the importance of magnetic shape anisotropy, which is well-predicted by the modified dynamic hysteresis (β-MDH) theoretical model.

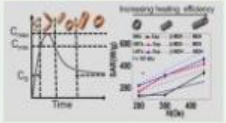

KEYWORDS: *Fe_3O_4-γ-Fe_2O_3 hollow nanoparticles, shape anisotropy, magnetic hyperthermia, micromagnetic simulation, modified dynamic hysteresis model*

Energy Evolution, Stabilization, and Mechanotransducer Properties of Fe_3O_4 Vortex Nanorings and Nanodisks

Gopal Niraula,[1,2] Denilson Toneto,[3] Elma Joshy,[4] Jose A. H. Coaquira,[2] Ahmad I. Ayesh,[5,6] Flavio Garcia,[7] Diego Muraca,[8] Juliano C. Denardin,[9] Gerardo F. Goya,[10] and Surender K. Sharma[1,4,*]

[1] *Department of Physics, Federal University of Maranhao, Sao Luis 65080-805, Brazil*
[2] *Laboratory of Magnetic Materials, NFA, Institute of Physics, University of Brasilia, Brasilia 70910-900, Brazil*
[3] *Departamento de Física, Universidade Federal de Santa Maria, UFSM, Santa Maria, RS 97105-900, Brazil*
[4] *Department of Physics, Central University of Punjab, Bathinda, 151401, India*
[5] *Center for Sustainable Development, Qatar University, P.O. Box 2713, Doha, Qatar*
[6] *Department of Mathematics, Statistics and Physics, Qatar University, P.O. Box 2713, Doha, Qatar*
[7] *Brazilian Center for Research in Physics - CBPF, Rio de Janeiro - RJ, 22290-180, Brazil*
[8] *Institute of Physics "Gleb Wataghin" (IFGW), University of Campinas, Campinas, Brazil*
[9] *CEDENNA and Departamento de Física, Universidad de Santiago de Chile (USACH), Santiago 9170124, Chile*
[10] *Instituto de Nanociencia y Materiales de Aragón (INMA), Universidad de Zaragoza, 50018, Zaragoza, Spain*

(Received 24 March 2021; revised 23 June 2021; accepted 12 July 2021; published 2 August 2021)

Recent reports on spin structures produced in nanomaterials due to confinement of spins imposed by geometrical restrictions are at the center of rising scientific interest. Topological curling magnetic structures (vortices) exhibit unique properties, regarding the energy profile, good colloidal stability in suspensions, manipulation under a low-frequency magnetic field, and torque exertion. The last property provides the potential to mechanically eradicate cancer cells via magnetomechanical actuation using remote ac magnetic fields. Here, we study, theoretically and by micromagnetic simulations, the magnetic energy evolutions for vortex nanosystems, i.e., Fe_3O_4 nanodisks (NDs) and nanorings (NRs). The obtained results for magnetic energy, magnetic susceptibility, and magnetization reversal confirm that the vortex-domain structure in NRs exhibits better stability and avoids agglomeration in solution, owing to the presence of a central hole, whereas the presence of a vortex core in NDs induces magnetic remanence. Although NDs are found to exert slightly higher torques than NRs, this weakness can be compensated for by a small increase (i.e., approximately equals 20%) in the amplitude of the applied field. Our results provide evidence of the magnetic stability of the curling ground states in NRs and open the possibility of applying these systems to magnetomechanical actuation on single cells for therapeutics in biomedicine, such as cancer-cell destruction by low-frequency torque transduction.

DOI: 10.1103/PhysRevApplied.16.024002

Journal of Alloys and Compounds 856 (2021) 158040

Contents lists available at ScienceDirect

Journal of Alloys and Compounds

journal homepage: http://www.elsevier.com/locate/jalcom

Tuning the shape, size, phase composition and stoichiometry of iron oxide nanoparticles: The role of phosphate anions

Gopal Niraula [a], Jose A.H. Coaquira [b], Fermin H. Aragon [c], Bianca M. Galeano Villar [d], Alexandre Mello [d], Flavio Garcia [d], Diego Muraca [e], Giorgio Zoppellaro [f], Jose M. Vargas [g], Surender K. Sharma [a, h, *]

[a] Department of Physics, Federal University of Maranhao, Sao Luis, Brazil
[b] Laboratory of Magnetic Materials, NFA, Institute of Physics, University of Brasilia, Brazil
[c] Universidad Nacional de San Agustin de Arequipa Avenida Independencia s/n, Arequipa, Perú
[d] Brazilian Centre for Research in Physics - CBPF, Rio de Janeiro- RJ, Brazil
[e] Institute of Physics "Gleb Wataghin" (IFGW), University of Campinas, Campinas, Brazil
[f] Regional Centre of Advanced Technologies and Materials, Faculty of Science, Palacky University in Olomouc, Slechtitelu 11, 78371, Olomouc, Czech Republic
[g] Imagion Biosystems Inc, San Diego, CA, 92121, USA
[h] Department of Physics, Central University of Punjab, Bathinda, India

ARTICLE INFO

Article history:
Received 14 May 2020
Received in revised form
26 July 2020
Accepted 28 August 2020
Available online 17 September 2020

Keywords:
Iron oxide nanoparticles
Magnetic vortex state
Verwey transition
Stoichiometry

ABSTRACT

This work describes a microwave synthetic approach for the controlled assembly of α-Fe_2O_3 nanosystems with defined morphologies, such as hollow nanotubes (NTs), solid nanorods (NRs) and nanodisks (NDs). The morphological control is aided during the crystallization processes by using phosphate anions as key surfactants in solution. Furthermore, the thermal reduction under H_2 atmosphere of these NTs, NRs and NDs α-Fe_2O_3 systems to the correspondent Fe_3O_4 nanomaterials preserved their initial morphologies. It was observed that the concentration of phosphate anions and volume of solvent had significant impact not only on controlling the shapes and sizes, but also phase composition and stoichiometry of the NTs, NRs and NDs nanoparticles. X-ray Rietveld refinement analysis of the NTs, NRs and NDs systems, after reduction in H_2, revealed the presence of zero-valent iron (Fe^0) in the final materials, with Fe^0 fractions that decreased gradually in **X** from NTs (~16**X**), NRs (~11**X**) to NDs (~0**X**) upon increasing amount of phosphate anions. Bulk magnetic susceptibility measurements showed clear alterations of the Verwey transition temperatures (T_V) and the development of unusual magnetic phenomena, such as magnetic vortex states in NDs, which was subsequently verified by micro-magnetic simulations. From the combination of XRD analysis, bulk magnetic susceptibility and Mössbauer results, we provide herein a detailed mechanistic description of the chemical processes that gated the development of shape-controlled synthesis of NTs, NRs and NDs and give a detailed correlation between specific morphology and magneto-electronic behaviors.